The Development of Enzyme Based Printable Glucose Sensors

by

Sundus A. Al-Zuhairi

A THESIS SUBMITTED TO THE UNIVRSITY OF NEWCASTLE
FOR THE DEGREE OF
DOCTOR OF PHILOSOPHY
IN PHYSICS
March 2021

THE UNIVERSITY OF
NEWCASTLE
AUSTRALIA

Declaration

I hereby certify that the work embodied in the thesis is my own work, conducted under normal supervision.

The thesis contains published scholarly work of which I am a co-author. For each such work a written statement, endorsed by my co-authors, attesting to my contribution to the joint work has been included.

The thesis contains no material which has been accepted, or is being examined, for the award of any other degree or diploma in any university or other tertiary institution and, to the best of my knowledge and belief, contains no material previously published or written by another person, except where due reference has been made in the text. I give consent to the final version of my thesis being made available worldwide when deposited in the University's Digital Repository, subject to the provisions of the Copyright Act 1968 and any approved embargo.

_____

Sundus Al-Zuhairi

9 March 2021

Dedication

To souls of my father, Abdulrazzaq, and my nephews, Nabil, and Adam, who left early before achieving their dreams in this life, and to my mother, brothers, and sisters, who taught me nothing is impossible. Patience, positivity, caring and happiness have come from you and your unfailing support.

Acknowledgements

First and foremost, I would like to express my utmost gratitude to my supervisor, Professor Paul Dastoor, for his continued guidance, encouragement, and support during my PhD study. He and genuinely conveyed a spirit of adventure regarding my research progress and this thesis. I could not have imagined having a better supervisor for my PhD studies. If I ever achieve anything in science, all the credit should rest on his shoulders.

My sincerest thanks go to my co-supervisors, Dr Warwick Belcher and Dr Daniel Elkington, for the many hours of discussion and advice, for taking the time to listen to my ideas and helping me reject the wrong ones and pick some with potential. During my PhD journey, we discussed many challenging topics. I also thank them for dedicating many hours to review my written chapters. Their help was immeasurable in this regard.

I must acknowledge Associate Professor John Holdsworth for his contribution in reviewing my research and encouraging me in times when the dark tunnel seemed endless. Thank you to Dr Xiaojing Zhou for the help and the support.

Thank you to the Ministry of Higher Education and Scientific Research in Iraq for providing me with a PhD scholarship; this support meant that I could focus on my work without the worries of financial hardship which I know to be a common setback for research students. I would like to thank the University of Anbar, Iraq for permitting me to complete a PhD. I would like to express most sincere to Dr Saeed Al Rashid and Dr Ali Khalaf at Department physics (Education for Pure Science), University of Anbar – Iraq for their great

motivation, vital encouragement, endless support to me all the time during the PhD journey.

My special thanks go out to Dr Oun Al-iedani / Post-doctoral Research Fellow at Hunter Medical Research Institute for his motivation, encouragement, and valuable advice. Despite of his heavy clinical research workload at different projects, he was always there to support and give advice and take care of me. You always encouraged me to be a better person. I doubt that I will ever be able to convey my full appreciation.

I also acknowledge Dr Pankaj Kumar, Dr Tim Lewis, Dr Swee Lim, Dr Galiya Sharafutdinova, Dr Levi Tegge, Dr Rhea Barnett, Dr Joel Martens and Mr Michael Cventanovski for helping and intellectual contribution. All the above provided me with advice at times of critical need, which helped enrich the experience.

Thank you to all the other members of the Centre for Organic Electronics that I haven't mentioned yet, you made the group such a helpful learning environment to complete my PhD. I would like to thank Dr Nathan Cooling, whose large batches of active materials allowed me to produce large batches of particles. I would like to thank ANFF members: Dr Adam Fahy and Dr Matt Barr for their effort helping and teaching me how to use the equipment.

Special thanks also go to Alaa Yousif and Riku Chowdhury who are great colleagues and friends for their sharing of ideas, advice, general concern, and laughter during those stressful times.

Finally, I would like to thank my family for the support, especially my older sister Amina and brother Wisam who were always there for me. They have provided for me through my entire life, and I must acknowledge their continual support in the challenging times in my PhD journey and especially during those

hard and trying times when courage dwindled. I can rejoice in my accomplishment with them.

Table of Contents

Chapter 1: Introduction 1

1.1 Background 1

1.2 Organic Thin Film Transistors 4

1.3 Biosensors 5

1.3.1 Types of Biosensor 6

1.3.1.1 Amperometric sensors 6

1.3.1.2 Potentiometric sensors 7

1.3.1.3 Optical sensors 8

1.3.1.4 Piezoelectric sensors 8

1.3.1.5 Calorimetric sensors 9

1.3.1.6 Impedimetric sensors 10

1.4 Printable sensors 11

1.5 Applications of Biosensors 12

1.6 Glucose Biosensors 14

1.7 Saliva 17

1.8 Motivations and Aims 18

Chapter 2: Experimental Procedure and Materials 19

2.1 Materials 19
2.1.1 P3HT 19
2.1.2 PEDOT: PSS 22
2.1.3 Nafion 23
2.1.4 Polyacrylonitrile 25
2.1.5 Glucose oxidase 26
2.1.6 Indium-tin-oxide (ITO) 29
2.2 Device Fabrication 30
2.2.1 Device Architecture 32
2.2.2 Spin-coating 34
2.3 Physical Material Characterisation 35
2.3.1 Profilometry 35
2.3.2 Scanning Electron Microscopy (SEM) 36
2.3.3 Atomic Force Microscope (AFM) 37
2.4 Electrical Device Characterisation 41
2.4.1 Transistor Characterisation 41
2.4.2 Sensor Characterisation 43
Chapter 3: Standard Fabrication and Figure of Merit 45
3.1 Introduction 45
3.2 Transistor Characterisation 48
3.2.1 Structure 48

3.2.2 Electrical Characterisation 52
3.3 Modifying the Transistor Architecture 54
3.3.1 Replacing PEDOT with Nafion 55
3.3.2 Replacing PVPy with PVP 58
3.3.4 Introduction of GOX to the sensor structure 62
3.4 OTFTs as a saliva glucose sensor 64
3.4.1 Response of sensor to glucose concentration (current vs time) 65
3.4.2 Improving response time by removing the PVP layer 74
3.5 Data Analysis 78
3.5.1 Determining a suitable figure of merit (FOM) 79
3.6 Summary 81
Chapter 4: Investigating the Effect of Fabrication Conditions on P3HT and Nafion Films and their Interface within the Sensor 82
4.1 Introduction 82
4.1.1 Aim 83
4.1.2 Experimental 83
4.2 P3HT Film Characterisation 84
4.2.1 P3HT film thickness as a function of deposition conditions 84
4.2.2 Electrical properties of P3HT films as a function of annealing temperature 86
4.3 Nafion Film Characterisation 91
4.3.1 Nafion film thickness as a function of deposition conditions 91
4.3.2 Electrical properties of Nafion as a function of annealing temperature 93

4.4 P3HT/Nafion Bilayer Characterisation 95

4.4.1 Electrical properties of P3HT/Nafion Bilayer as a function of annealing temperature 96

4.5 Characterising the Effect of the Addition of Water to the Component Layers..... 102

4.5.1 Characterising the effect of the addition of water on P3HT films 103

4.5.2 Characterising the effect of the addition of water on Nafion films 107

4.5.3 Characterising the effect of the addition of water on the P3HT/Nafion bilayers. 109

4.6 Characterising the Effect on Sensor Characteristics of Device Annealing Temperature. 113

4.7 Conclusion 116

Chapter 5: PAN Film Fabrication and PAN-mediated Devices 118

5.1 Introduction..... 118

5.2 Experimental 124

5.2.1 Materials and method 124

5.2.2 Preparation of the polymer (PAN) membrane 125

5.2.2.1 Preparation of wet PAN films using spin coating 125

5.2.2.2 Preparation of wet PAN films using the drawing bar technique 128

5.3 Controlling and characterising the properties of the PAN film 130

5.4 Effects of PAN on the response of devices to glucose solution addition 150

5.5 Conclusion 153

Chapter 6: Modifying the Approach to Glucose Sensing to Mitigate Variance in Device Response..... 154

6.1 Introduction 154

6.1.1 Potential sources of variation in device response 155

6.1.2 Possible approaches for mitigating sensor variation 158

6.2 Description of the adopted approach 160

6.2.1 Experimental 161

6.3 Dual Device Data With/Without PAN (DD1 and DD2) 162

6.4 Dual Device Data with Isolated Devices (DD3) 174

6.5 Conclusion 183

Chapter 7: Conclusions and Future work 184

7.1 Conclusions 184

7.2 Future work 185

7.3 Summary 187

References 188

Abstract

The main goal of this thesis is to develop an easy to fabricate and sensitive biosensor based on organic materials capable of monitoring saliva glucose concentration in people with diabetes.

In Chapter 3 we focus on designing, fabricating and characterising flexible organic thin film transistor- (OTFT-) based sensors suitable for salivary glucose sensing. We employed different device architectures utilising poly-3-hexylthiophene (P3HT) as the semiconductor layer, dielectric layers of either poly(vinyl-pyridine) (PVPy) or poly(vinyl-phenol) (PVP) and poly(3,4-ethylenedioxythiophene) poly(styrenesulfonate) (PEDOT:PSS) as a gate material, to produce trial OTFTs. Our results demonstrated that compared with the initial architecture of ITO/P3HT/PVPy/PEDOT:PSS, when PVPy was replaced with PVP the off current was increased. Nafion was chosen as an appropriate replacement for PEDOT: PSS in the final (ITO/P3HT/Nafion:GOX) sensor device due to the acidity of PEDOT:PSS, with the dielectric layer being removed to improve device response time. The mechanism of signal transduction in these devices is via protonic doping of the P3HT channel and thus acidic PEDOT:PSS leads to a large off current in the device. Upon the replacement of PEDOT:PSS by the Nafion:GOX mixture, a working prototype sensor was produced of architecture ITO/P3HT/PVP/Nafion:GOX.

Chapter 4 focuses on the establishing the mechanisms behind the formation and the effect of mixed interlayers between the Nafion proton transport layer and P3HT semiconductor material. Surprisingly high conductivity was obtained for P3HT/Nafion bilayers, in excess of the native conductivity of either pristine

material, due to intermixing of the materials and doping of the P3HT. Our results suggested that the annealing condition giving the best device performance is a postproduction treatment at 50 °C. A full study of the effect of thermal annealing and the addition of water to pristine P3HT and Nafion and bilayers was undertaken.

Chapter 5 explores the use of a porous capping layer to encapsulate GOX in the device and control the volume and location of added analyte. The phase inversion technique was used to produce the porous polyacrylonitrile (PAN) films for this purpose. Scanning electron microscopy (SEM) and atomic force microscopy (AFM) techniques were employed to investigate the resultant membrane morphology of the PAN films. Our results show that the PAN films are highly porous and suitable for the capping application and ITO/P3HT/Nafion:GOX/PAN devices showed improved sensitivity to glucose in to the range of salivary glucose levels (SGL) in humans.

Finally, in Chapter 6, the device architecture was redesigned to incorporate a non-GOX containing reference sensor in an attempt to mitigate device-based variation. Sources of sensor output variation is discussed and we observe that the addition of a reference sensor seems to merely add an additional source of variance.

Chapter 7 summarises results and discusses potential further studies.

List of Figures

Figure 1.1: Schematic showing the layer structure of OTFTs where Vgs is the gate-source voltage and Vds is the drain-source voltage ..……2

Figure 1.2: External system is one of the main components of a biosensor. …….....5

Figure 1.3: Iterative glucose biosensor development plan……18

Figure 2.1: Chemical structure of P3HT……20

Figure 2.2: Chemical structure of poly(3,4-ethylenedioxythiophene) doped with poly(styrene sulfonate) (PEDOT:PSS) used as a transport conductive polymer……...22

Figure 2.3: Chemical structure of Nafion……..23

Figure 2.4: Chemical structure of PAN…… 25

Figure 2.5: Glucose oxidase structure …… 27

Figure 2.6: Schematic depicting FAD being reduced to $FADH_2$…… 27

Figure 2.7: Schematic depicting the $FADH_2$ is oxidized to FAD…… 28

Figure 2.8: Photograph of the patterned ITO coated glass substrates used for fabrication of OTFTs and sensors…… 30

Figure 2.9: A schematic representation of the fabrication of a standard glucose biosensor…….32

Figure 2.10: WS-400A-6NPP/LITE spin coater……34

Figure 2.11: DektakXT stylus profiler used to measure the thickness of films ……36

Figure 2.12: Photograph of the Zeiss Sigma ZP-FE-SEM……37

Figure 2.13: Schematic diagram of the AFM in tapping mode…….40

Figure 2.14: AFM from Asylum Research (Cypher scanning microscope) used in this project……..40

Figure 2.15: Keithley 2400 Source Meters used for transistor measurement…42

Figure 2.16: Schematic illustrating (a) The Typical output characteristic of the transistor fabrication from P3HT solution in chloroform, (b) The transfer curve of the same device……..42

Figure 2.17: Schematic illustrating output characteristic of electrical sensor……..44

Figure 2.18: Schematic representing current response versus time for water ……44

Figure 3.1: Different thin film transistors architectures: (a) bottom-gate bottom contact, (b) bottom-gate top-contact, (c) top-gate bottom-contact, (d) top-gate top-contact ……49

Figure 3.2: Basic device architecture and dielectric (PVPy)……..……50

Figure 3.3: Schematic diagram shows steps of the fabricated OTFTs device...50

Figure 3.4: Chemical structure of the poly(3,4-ethylenedioxthiophene)-phene): poly (styrene) sulfonate (PEDOT: PSS) ……51

Figure 3.5: Standard OTFTs device (PVPy dielectric) with PEDOT: PSS gate electrode. (a) Output characteristic with (V_{DS}) = 0 V to -1.9 V and (V_{GS}) = 0.4 V to -1.4 V (b) Transfer characteristics (V_{GS}) = 0 V to -1.5 V and (V_{DS}) = -1.4 V. (c) Gate leakage with (V_{DS}) = 0 V to -1.9 V and (V_{GS}) = 0.4 V to -1.4 V. ……53

Figure 3.6: The off-set gate structure of device with Nafion……56

Figure 3.7: Standard OTFTs device (PVPy dielectric) with Nafion gate electrode. (a) output characteristic with (V_{DS}) = 0 V to -1.9 and (V_{GS}) = 0.4 V to -2.4 V. (b) Transfer characteristics with (V_{GS}) = 0 V to -2.4 V and (V_{DS}) = -2.4 V. (c) Gate leakage current with (V_{DS}) = 0 V to -1.9 V and (V_{GS}) = 0.4 V to -2.4 V.……57

Figure 3.8: Chemical structure of PVP (a) and PVPy (b)……..58

Figure 3.9: Standard OTFTs device of materials used. (a) (PVP dielectric), (b) (PVPy dielectric) ……59

Figure 3.10: (a) Standard OTFTs device (PVP dielectric) with PEDOT: PSS gate electrode. (a) output characteristic with (V_{DS}) = 0 V to – 1.9 V and (V_{GS}) = 0V to – 1.4 V (b) Transfer characteristics with (V_{GS}) = 0 V to - 1.4 V and (V_{DS}) = - 1.4 V. (c) Gate leakage current with (V_{DS}) = 0 V to – 1.9 V and (V_{GS}) = 0 V to -1.4 V……..61

Figure 3.11: Photo of OTFTs based glucose sensors (P3HT/PVP/GOX: Nafion)……63

Figure 3.12: Schematic representation of the cross section view of the (P3HT/PVP/GOX: Nafion) ……63

Figure 3.13: Device arcticture of ITO / P3HT/PVP/ Nafion: GOX……..66

Figure 3.14: Figure 3.14: a, b, c and d show duplicate current (- I_D) vs time outputs for these devices for the 0.01, 0.1, 1 and 10 mM glucose solutions, respectively. Arrows are represented the event at 300s……..68

Figure 3.15: a) Figure 3.15: (a) Typical 0.01 mM, 0.1 mM, 1 mM and 10 mM current-time responses for the ITO/P3HT/PVP/Nafion:GOX device structure, whilst (b) shows the same data normalised to 0 µA at t = 280 second, just prior to the addition of the analyte. (c) shows the change in current after 1800 s as a function of glucose concentration. Arrows are shown the plateau current location on the curve.……..……...71

Figure 3.16: Simplified diagram for OTFT glucose sensing mechanism . a) Glucose diffuses to the GOX in the Nafion matrix whereupon H_2O_2 generated . b) The H_2O_2 is oxidised and protons are generated . c) : Protons then diffuse to and dope the P3HT channel……73

Figure 3.17: Schematic of OTFTs based sensor of ITO/P3HT/Nafion:GOX ……74

Figure 3.18: (a) Typical 0.01 mM, 0.1 mM, 1 mM and 10 mM current-time responses for the ITO/P3HT/Nafion: GOX device structure, whilst (b) shows the same data normalised to 0 µA at t = 280 second, just prior to the addition of the analyte. (c) shows the change in current after 1800 s as a function of glucose concentration.……..76

Figure 3.19: Current-time responses for the ITO/P3HT/Nafion:GOX device structure highlighting the improvement in response time normalised data for the 1 mM glucose PVP and Non–PVP devices……77

Figure 4.1: P3HT film thickness at different concentrations as presented in Table 4.1……87

Figure 4.2: Device configuration for P3HT two-terminal measurements ……87

Figure 4.3: Figure 4.3: I-V characteristics of the 71 nm P3HT film with varying annealing temperatures (50 ºC, 70 ºC, 90 ºC, 110 ºC, 150 ºC, 200 ºC and 250 ºC) …..……88

Figure 4.4: I-V characteristics of the 113 nm P3HT film with varying annealing temperatures (50 ºC, 70 ºC, 90 ºC, 110 ºC, 150 ºC, 200 ºC and 250 ºC)

…….……...89

Figure 4.5: I-V characteristics of the 135 nm P3HT film with varying annealing temperatures (50 ºC, 70 ºC, 90 ºC, 110 ºC, 150 ºC, 200 ºC and 250 ºC)

……..…….90

Figure 4.6: Thickness for spin-coated Nafion film as a function of spin-speed……..92

Figure 4.7: Device configuration for Nafion two-terminal measurements …….....94

Figure 4.8: I-V characteristics of Nafion films with varying annealing 2temperatures (50 ºC, 70 ºC, 90 ºC, 110 ºC, 150 ºC, 200 ºC and 250 ºC). ……...94

Figure 4.9: Device configuration for Nafion/P3HT two-terminal

measurements……95

Figure 4.10: Output characteristics of the P3HT/Nafion at 71 nm with varying the temperatures (50 ºC, 70 ºC, 90 ºC, 110 ºC, 150 ºC, 200 and 250 ºC)……..97

Figure 4.11: Output characteristics of the P3HT/Nafion at 113 nm with varying the temperatures (50 ºC, 70 ºC, 90 ºC, 110 ºC, 150 º C, 200 ºC and 250 ºC)……..98

Figure 4.12: Output characteristics of the P3HT/Nafion, 135 nm with varying the temperatures (50 ºC, 70 ºC, 90 ºC, 110 ºC, 150 ºC, 200 ºC and 250 ºC). ……99

Figure 4.13: Schematic diagrams illustrating the difference in current pathways between devices with thick and thin P3HT layers: (a) thinner P3HT layer device and (b) thicker P3HT layer device……100

Figure 4.14: IV Characteristic of P3HT/Nafion bilayer film annealed at 50 °C

with P3HT thickness 71 nm, 113 nm and 135 nm….....101

Figure 4.15: Relationship between thickness of P3HT and the P3HT/Nafion bilayer resistance. The resistance error is estimated to be 10 %.....102

Figure 4.16: Cross-sectional schematic of P3HT sample with water addition as used in this study……..103

Figure 4.17: Output characteristics of the bilayers film P3HT/Water, P3HT 71 nm at the following annealing temperatures: 50 ºC, 70 ºC, 90 ºC, 110 ºC, 150 ºC, 200 ºC and 250 ºC……...105

Figure 4.18: Output characteristics of the bilayers film P3HT/Water, P3HT 113 nm at the following annealing temperatures: 50 ºC, 70 ºC, 90 ºC, 110 ºC, 150 ºC, 200 ºC and 250 ºC……...106

Figure 4.19: Output characteristics of the bilayers film P3HT/Water, P3HT 135 nm at the following annealing temperatures: 50 ºC, 70 ºC, 90 ºC, 110 ºC, 150 ºC, 200 ºC and 250 ºC……...107

Figure 4.20: Cross-sectional schematic of Nafion samples with water addition as used in this study……..108

Figure 4.21: Output characteristics of the bilayers film Nafion/ Water with varying the temperatures (50 ºC, 70 ºC, 90 ºC,110 ºC,150 ºC,200 ºC and 250 ºC)……109

Figure 4.22: Cross-sectional schematic of P3HT/Nafion samples with water addition as used in this study……110

Figure 4.23: I-V characteristics of the P3HT/Nafion bilayer with /water addition for a 71 nm thick P3HT film. The bilayer was annealed at50 ºC, 70 ºC, 90 ºC, 110 ºC, 150 ºC, 200 ºC and 250 ºC……111

Figure 4.24: I-V characteristics of the P3HT/Nafion bilayer with /water addition for a 113 nm thick P3HT film. The bilayer was annealed at 50 ºC, 70 ºC, 90 ºC, 110 ºC, 150 ºC, 200 ºC and 250 ºC……..112

Figure 4.25: I-V characteristics of the P3HT/Nafion bilayer with water addition for a 135 nm thick P3HT film. The bilayer was annealed at 50 ºC, 70 ºC, 90 ºC, 110 ºC, 150 ºC, 200 ºC and 250 ºC……...113

Figure 4.26: Plots of $I_{D\ (max)}$-$I_{D\ (800s)}$ as a function of glucose concentration (0 mM, 0.01 mM, 0.1 mM, 1 mM and 10 mM) for P3HT / Nafion: GOX devices annealed at a) 50°C, b) 90°C, c) 150°C and d) 200°C. Error bars represent one standard deviation for a minimum of 6 replicate measurements……..115

Figure 5.1: Chemical structure of PAN……...119

Figure 5.2: (a) Dimethyl sulfoxide (DMSO). (b) N, N-Dimethylformamide (DMF)……...125

Figure 5.3: Schematic depicting the steps of preparing a thick phase inverted, porous PAN film……..127

Figure 5.4: Schematic of the draw bar technique……129

Figure 5.5: Schematic representation of the cross-section view of the draw bar technique……..129

Figure 5.6: 5 µm × 5 µm scale topography and corresponding phase images of acetone treated PAN films by AFM in tapping mode (a) PAN-DMF and PAN-DMF 3D (b) PAN-DMSO and PAN -DMSO 3D……132

Figure 5.7: 5 µm × 5 µm scale topography and corresponding phase images of chloroform treated PAN films by AFM in tapping mode (a) PAN-DMF and PAN- DMF 3D (b) PAN-DMSO and PAN -DMSO 3D……..133

Figure 5.8: 5 µm × 5 µm scale topography and corresponding phase images of propanol treated PAN films by AFM in tapping mode (a) PAN-DMF and PAN-DMF 3D (b) PAN-DMSO and PAN -DMSO 3D……134

Figure 5.9: 5 µm × 5 µm scale topography and corresponding phase images of deionised water treated PAN films by AFM in tapping mode (a) PAN-DMF and PAN- DMF 3D (b) PAN-DMSO and PAN -DMSO…….……...135

Figure 5.10: 5 µm × 5 µm scale topography and corresponding phase images of methanol treated PAN films by AFM in tapping mode (a) PAN-DMF and PAN-DMF 3D (b) PAN-DMSO and PAN -DMSO 3D……..……..136

Figure 5.11: 5 µm × 5 µm scale topography and corresponding phase images of ethanol treated PAN films by AFM in tapping mode (a) PAN-DMF and PAN-DMF 3D (b) PAN-DMSO and PAN -DMSO 3D……137

Figure 5.12: SEM micrographs (at 2 kV and 200, 000 x magnification) of PAN films using DMF as a solvent and water as a non – solvent annealed at: (a) 35 ºC (scale bar is 100 nm), (b) 50 ºC (Scale bar is 200 nm), (c) 100 ºC (scale bar is 100 nm), (d) 150 ºC (scale bar is 200 nm)…….141

Figure 5.13: SEM micrographs (at 2 kV and 100, 000 x magnification) of PAN films using DMF as a solvent and water as a non – solvent annealed at: (a) 35 ºC (scale bar is 100 nm), (b) 50 ºC (scale bar is 200 nm), (c) 100 ºC (scale bar is 100 nm), (d) 150 ºC (scale bar is 200 nm)……142

Figure 5.14: SEM micrographs (at 2 kV and the scale bars are 1 µm) of PAN films using DMF as a solvent and water as a non – solvent annealed at: (a) 35

ºC (magnification is 50, 000 x), (b) 50 ºC (magnification is 20, 000 x), (c) 100 ºC (magnification is 50, 000 x), (d) 150 ºC (magnification is 50, 000 x) ……143

Figure 5.15: Cross-sectional SEM micrographs (at 2 kV) of PAN films using DMF as a solvent and water as a non-solvent annealed at: (a) 50 °C (magnification is 10, 000 x and the scale bar is 2 μm), (b) 100 °C (magnification is 10, 000 x and the scale bar is 1 μm) and (c) 150 °C (magnification is 12, 000 x and the scale bar is 2 μm)……..144

Figure 5.16: Effect of annealing on PAN membranes. a) Photograph of the PAN annealed at 50˚C, b) Photograph of the PAN annealed at 100˚C, c) Photograph of the PAN annealed at 150˚C d) Photograph of the PAN annealed at 200˚C, e) Photograph of the PAN annealed at 250˚C ……..……145

Figure 5.17: Effect of the volume of PAN solution on the thickness of spin coated PAN films. Errors are one standard deviation for a minimum of 5 measurements……148

Figure 5.18: Effect of the number of layers of tape used in the draw bar guide rails on the thickness of PAN membrane. Errors are one standard deviation for a minimum of 5 measurements……149

Figure 5.19: Typical I_D vs t curves for PAN containing glucose sensors treated with glucose of concentrations 0 μm to 10 μm……151

Figure 5.20: Calibration for PAN containing glucose sensors treated with glucose of concentrations 0 μm to 10 μm normalised to $I_{D\,(240s)}$ = 0 A and using the I_D at t = 800 s as the FOM……...152

Figure 6.1: Device configuration for DD1 showing a single PAN layer spanning the full substrate. One of the sides contains GOX and the other side has no GOX. One drop of glucose analyte (0 Mm, 0.01 Mm, 0.1 mM, 1 mM and 10 mM) is deposited in the centre of the PAN layer.……..163

Figure 6.2: Top-down view of DD1. …….....163

Figure 6.3: Typical I_D versus time for glucose concentrations a (0 mM), b (0.01 mM), c (0.1 mM), d (1 mM) and e (10 mM) (0 mM, 0.01 mM, 0.1 mM, 1 mM and 10 mM) where the glucose analyte is dropped in the middle of DD1 at t = 200s……...166

Figure 6.4: Typical DD1 current response versus time for glucose concentrations of; a 0 mM, b 0.01 mM, c 0.1 mM, d 1 mM and e 10 mM. The reference data has been subtracted from the test data and the resulting plot is normalised to I_D = 0 A at t = 240s seconds, just before glucose analyte addition……167

Figure 6.5: Typical ΔI_D vs t curves normalised to t = 240s for DD1……...168

Figure 6.6: Calibration curve for DD1 glucose testing using the change in current at Av $\Delta I_{D,T=800s} - \Delta I_{D,t=240s}$ A after addition of 0 mM, 0.01 mM, 0.1 mM, 1 mM and 10 mM glucose analyte, for a minimum of 6 tests at each glucose concentration. The error bars represent one standard deviation from the average……..168

Figure 6.7: Device configuration for DD2. One of the sides contains GOX and the other side no GOX. One drops of glucose analyte (0 mM, 1 mM, 0.01 mM, 0.1 mM, 1 mM and 10 mM) is deposited on the top of each side of the device……169

Figure 6.8: Top-down view of DD2. One of the sides contains GOX and the other side No GOX……...170

Figure 6.9: Typical DD2 current response versus time for glucose concentrations of; a 0 mM, b 0.01 mM, c 0.1 mM, d 1 mM and e 10 mM. The reference data has been subtracted from the test data and the resulting plot is normalised to I_D = 0 A at t = 240s seconds, just before glucose analyte addition……171

Figure 6.10: Typical ΔI_D vs t curves normalised to t = 240s for DD2..……...172

Figure 6.11: Calibration curve for DD2 glucose testing using the change in current at Av $\Delta I_{D,T=800s} - \Delta I_{D,t=240s}$ A after addition of 0 mM, 0.01 mM, 0.1 mM, 1 mM and 10 mM glucose analyte, for a minimum of 6 tests at each glucose concentration. The error bars represent one standard deviation from the average……..173

Figure 6.12: Device configuration for DD3 showing PAN layer on both sides. One of the sides contains GOX and the other side No GOX. One drop of glucose analyte (0 mM, 0.01 mM, 0.1, 1 mM and 10 mM) is deposited on the top of the PAN on each side of the separated device……174

Figure 6.13: Top-down view of DD3……...175

Figure 6.14: Typical DD3 current response versus time for glucose concentrations of; a 0 mM, b 0.01 mM, c 0.1 mM, d 1 mM and e 10 mM. The reference data has been subtracted from the test data and the resulting plot is normalised to I_D = 0 A at t = 240s seconds, just before glucose analyte addition……176

Figure 6.15: Typical ΔI_D vs t curves normalised to t = 240s for DD3. ……..177

Figure 6.16: Calibration curve for DD3 glucose testing using the change in current at Av $\Delta I_{D,T=800s} - \Delta I_{D,t=240s}$ A after addition of 0 mM, 0.01 mM, 0.1 mM, 1 mM and 10 mM glucose analyte, for a minimum of 6 tests at each glucose concentration. The error bars represent one standard deviation from the average……..177

Figure 6.17: Comparison of glucose calibration curves for DD1 (yellow dots), DD2 (orange dots), DD3 (red dots) and the optimised device presented in Chapter 5 (maroon dots). Error bars have been removed for clarity and dotted lines have been added to aid the eye…….181

Figure 6.18: 1 standard deviation of the average I_D values as a function of glucose concentration for the data points presented in Figure 6.17 ...……..181

Figure 6.19: Data in Figure 6.20 presented as a percentage error of the data presented in Figure 6.17……182

List of Tables

Table 4.1: Average P3HT film thickness for films spun from different concentrations in chloroform……..85

Table 4.2: Thickness for spin-coated Nafion films as a function of spin-speed……...92

Table 4.3: The average current and resistance of P3HT/Nafion bilayers with different P3HT thickness at V=1 V……..101

Table 6.1: The variations observed B2B = batch to batch variation; D2D = device to device variation……158

List of Abbreviations

OLEDs	organic light-emitting diodes
OTFTs	organic thin-film transistors
P3HT	poly (3-hexylthiophene)
Si-NW	silicon nano-wires
ZnO	zinc oxide
V_{DS}	drain source voltage
I_D	drain current
Au	gold
Pt	platinum
C	carbon
Ag	silver
AgCl	silver chloride
GOX	glucose oxidase
ISE	ion-selective electrode
BW	bulk wave
SAW	surface acoustic wave
QCM	quartz-crystal microbalances
DNA	redox proteins (cytochrome)
GluOx	glucose oxidase
BGL	blood glucose levels
GDH	glucose dehydrogenase
SGL	salivary glucose level
UV - vis	UV- visible spectroscopy
OPV	organic photovoltaic
Mw	weight average molecular weight

Mn	number average molecular weight
COE	Centre for Organic Electronics
PAN	polyacrylonitrile
FAD	flavin adenine dinucleotide
Ω	ohm
nm	nano metre
°C	degree celsius
rpm	revolutions per minute
PVP	poly (4 - vinyl phenol)
PVPy	poly (vinyl - pyridine)
SEM	scanning electron microscopy
AFM	atomic force microscopy
µL	micro
PoC	point of care
ITO	indium tin oxide
I - V	current - voltage
V	voltage
mM	molar
DD1	dual device unbroken with pan, single drop of analyte
DD2	dual device unbroken without pan, two drops
DD3	dual device broken with pan, two drops
PET	polyethylene terephthalate
cm	centimetre
DMSO	dimethyl sulfonate
DMF	N, N-dimethylformamide
C_3H_6O	acetone

$CHCl_3$	chloroform
CH_3OH	methanol
C_3H_8O	isopropanol
CH_5OH	ethanol
T_g	glass transition temperature

Chapter 1: Introduction

1.1 Background

Conductive polymers are a new class of organic materials which have the optical and electronic properties of metals and semiconductors [1]. The discovery of them in the 1970s opened the way for the use of organic semiconducting or conducting materials as the active material in many organic device applications [2] and, as a result, Heeger, MacDiarmid and Shirakawa were awarded the Nobel Prize for chemistry in 2000 “for the discovery and development of conductive polymers”. They showed that charge carriers can be introduced into polyacetylene by chemical doping of the material, which results in a dramatic increase in electrical conductivity [3].

Subsequently, organic electronics has gained enormous attention with activities encompassing the fabrication and development of electronic devices that use semiconducting and conducting organic materials. These materials can be either non-polymeric materials such as small molecule semiconductors like pentacene, carbon allotropes such as graphene and carbon nanotubes [4], or conducting polymers, where these are now used in many applications encompassing, lightweight batteries, solar cells, sensors, and electrochemical devices [5]. Soluble conductive polymers can be employed to print organic electronic devices such as electro-chromic displays, organic light-emitting diodes (OLEDs) and organic thin-film transistors (OTFTs) [6].

The first thin film organic transistor (OTFT) fabricated by inkjet printing was introduced in 2000 [7]. Thin film transistors (TFTs) are multilayered devices

consisting of source and drain electrodes contacting a semiconducting material and with the gate electrode in contact with the opposite side of a dielectric layer, as shown in Figure 1.1. The properties of OTFTs depend largely on the properties of the interface between the dielectric and semiconducting layers. There are many different semiconducting materials available (organic or inorganic) which can be solution processed and printed to form the semiconducting layer of the device, including poly (3-hexylthiophene) (P3HT), silicon nano-wires (Si-NW), zinc oxide (ZnO) and graphene. There are also many printing techniques such as screen printing, gravure printing and inkjet printing which can be employed to fabricate printed electronics and bioactive products from the conducting polymers available [8].

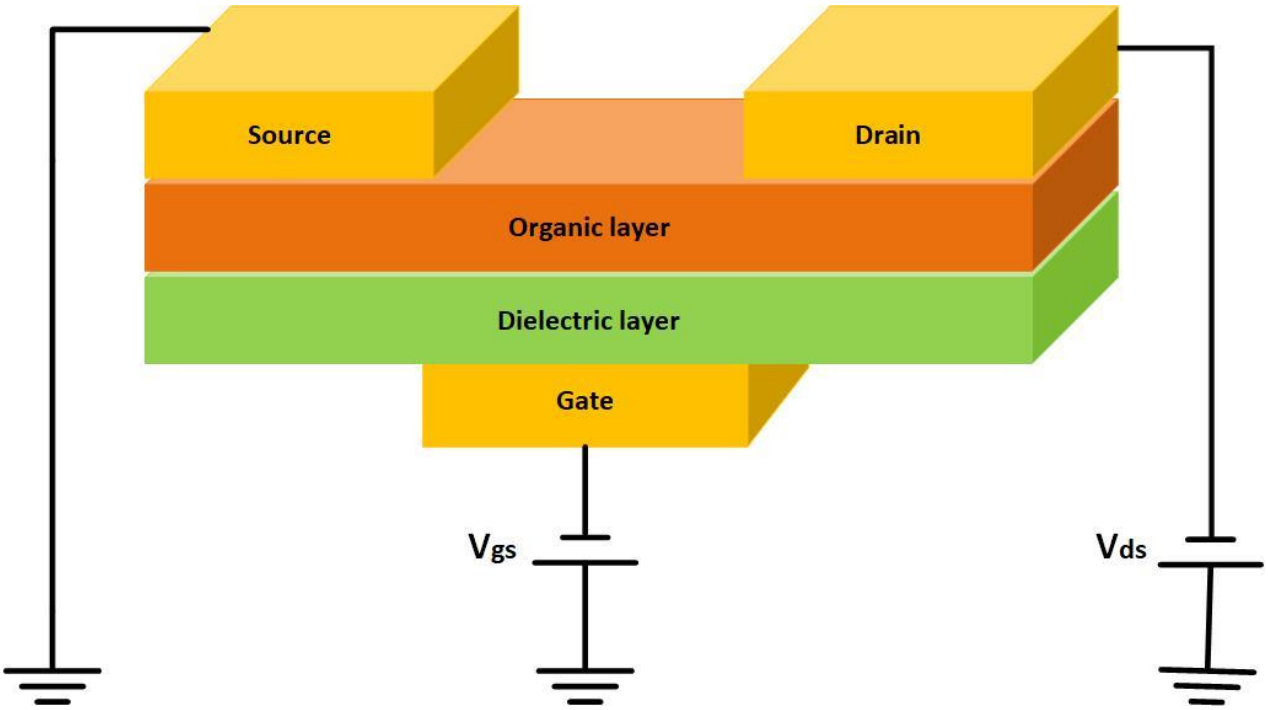

1.1: Schematic showing the layer structure of OTFTs where Vgs is the gate-source voltage and Vds is the drain- source voltage.

The biocompatibility of conducting polymers has enabled their use in biosensors [2] where this growing application has seen them employed in different fields ranging from environmental monitoring to clinical diagnostics [9, 10]. Biosensors represent an emerging direction in the detection of species such as glucose, cholesterol, urea and lactate which are molecules of significance in clinical diagnostics[9, 10] .

Glucose biosensors have been commonly employed for the diagnosis and management diabetes, a serious disease that can lead to higher risks of heart disease, blindness or kidney failure among the afflicted, arising from the body failing to regulate blood glucose levels appropriately[11]. Efficient and sensitive glucose detection is therefore important in the treatment and management of diabetes to aid glucose regulation by diet or self-medication. Consequently, a range of biosensors have been proposed for glucose monitoring based on electrochemical and fluorescence detection methods and mechanisms [12-14].

Electrochemical sensing is a particularly desirable technique due to its high selectivity and sensitivity, rapid response time, low cost and potential for sensor portability [15]. Advances in nanotechnology have enabled researchers to develop non-invasive methods for glucose detection [16]. Currently, the conventional method of measuring blood glucose level (BGL) involves obtaining a small sample of blood through finger-pricking, which is painful, uncomfortable and invasive. Blood glucose concentration measurements can be made by using accessible bodily fluids, such as saliva and tears, to avoid the pain and complication of blood based techniques [17, 18]. Tears, however, have some limiting factors associated with them that makes the detection of glucose difficult. It is time consuming to collect enough tears and glucose concentration in tears is lower than that in blood [19].

Recently, interest in using saliva as the sampling medium for glucose biosensors has been increasing due to the advantages of non-invasive and painless collection, as well as the observation that glucose concentration in saliva is proportional to blood glucose concentration [16]. Saliva is 99% water, but the remaining 1% contains many significant substances, such as electrolytes and mucus that the body needs to digest food, as well as antibacterial compounds to aid dental health [20]. However, there are some disadvantages associated with the use of saliva, including that, while a representative proportion, the glucose concentration in saliva is much lower that the concentration of glucose in blood [16].

1.2 Organic Thin Film Transistors

There are many devices made using organic electronic materials, which are used for sensing applications. One of these devices is the OTFT, which has a wide range of sensing applications, for instance, food monitoring, medical diagnostics and detection of chemicals [9, 21, 22]. An OTFT has three basic components, which are a) a thin semiconductor film, b) an insulating layer, and c) three electrodes. The source and drain are two electrodes that are in contact with semiconductor layer. The gate (the third electrode) is then separated by the insulating layer from the semiconductor layer (Figure 1.1) [23]. The source and drain electrode are separated by a region which is known as the channel of the transistor. Current flow between the source and drain electrodes is controlled by a voltage that is applied between the gate electrode and the source electrode (V_{GS}). As V_{GS} is modulated, the current flowing into the drain electrode of the device (I_D) changes. The exact mechanism for charge modulation defines the category of transistor – for example, organic field-effect transistors (OFETs) are a specific type of OTFTs in which the current modulation mechanism is driven

by an electric field caused by the application of V_{GS} to the device, as in conventional TFTs.

OTFTs have advantages over the other types of devices as they have the potential for use as a transducer due to their capability to amplify signals. Furthermore, their affordability, and ease of fabrication also makes them an excellent candidate for sensor use [24, 25].

1.3 Biosensors

The term biosensor was proposed by Cammann in 1977 [26], when he stated that a biosensor is a device with a biological sensing element which allows recognition and quantification of an analyte in a sample. In general, biological recognition is based on a chemical approach where a sensing element "recognises" the analyte through a specific chemical reaction. This reaction is connected to a transducer that converts the chemical or physical change to a measurable signal, often an electric signal [27]. A biosensor, then, has three main components: biological recognition elements, a transducer and a signal

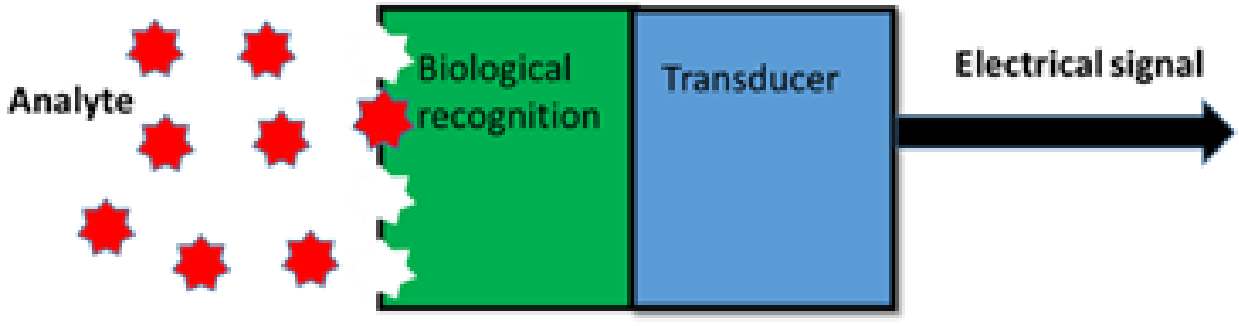

Figure 1.2: External system is one of the main components of a biosensor.

processing system, where the biological element is employed for the recognition of a specific analyte and the transducer transforms the signal or biorecognition incident into an easily measurable signal, which the signal processor then transforms into a mode readable by an external system [28]. Figure 1.2 shows the typical architecture of a biosensor, where the biological recognition element of the biosensor could be an enzyme, antibodies, nucleic acids, or other biomolecules [29].

1.3.1 Types of Biosensor

There are different types of biosensor based on the particular detection principle employed which include amperometric, potentiometric, piezoelectric, calorimetric and optical detection. These will be discussed below.

1.3.1.1 Amperometric sensors

In electrochemistry, amperometry refers to the measurement of the current produced by the oxidation or reduction of an electroactive species in a chemical reaction which depends on the concentration of an reactant [30]. In the biochemical realm, this current will depend on the concentration of the target analyte and be generated by the reaction of a biochemical species.

Typically, amperometry would be conducted using an electrochemical cell, which consists of a working electrode, often formed from gold (Au), platinum (Pt), or carbon (C), a reference electrode, often made from silver (Ag) or silver chloride (AgCl), and a counter or auxiliary electrode. When a constant potential is applied between the working electrode and a reference electrode, a current is generated by oxidation or reduction of an electroactive species, the analyte, at the surface of the working electrode. The electrical signal generated is

dependent on the concentration of the analyte electroactive species diffusing to the surface of the working electrode. A loss of sensitivity and damage to the electrode surface may result from continuous use[31].

Amperometric biosensors may use a device structure similar to an electrochemical cell in order to detect a particular species. The amperometric biosensor is the most researched of all biosensors for glucose detection, where the enzyme glucose oxidase (GOX) is mostly employed to catalyse the transformation of glucose to gluconic acid with a concurrent current generation [32]. Additionally, the amperometric technique has been used for the detection of antigens for the identification and diagnosis of disease and nucleic acids [33-36]. Furthermore, the amperometric biosensor has significant applications in environmental monitoring of pesticides [37].

Collectively, amperometric biosensors are the most commonly used electrochemical biosensors, because they are highly sensitive, may be manufactured at low cost and offer rapid detection [38]. However, amperometric biosensors have some issues wherein a transducer can give a false current reading caused by the presence of electroactive interference in the sample matrix [30].

1.3.1.2 Potentiometric sensors

Potentiometric biosensors operate by measuring the potential between two electrodes, one of which is functionalised to interact with the biological analyte. This functionalisation may be in the form of an ion-selective electrode (ISE) [39] or a recognition element immobilised on to the electrode. ISEs are chemical sensing elements which have a huge number of applications, and have found widespread use in sensing applications [40]. Their utility is not surprising since these types of devices are fast, inexpensive, selective and offer maintenance free measurement [41, 42]. In short, they are preferred as a

biosensors because of these features. In potentiometric sensors, the recognition process converts the analyte molecule interaction with the biological recognition element applied to the functionalised surface into a potential providing an analytical signal unique to the presence of the analyte molecule [32].

1.3.1.3 Optical sensors

Optical biosensors are based on measurement of emitted or absorbed light as a result of a biochemical reaction[43]. Optical biosensors are a powerful alternative to conventional analytical techniques because of their particularly high sensitivity, specificity, portability and affordability [44, 45]. Thus, rapid advances have been made in this area and optical biosensors have great potential in many important areas including food safety, life science, security, medicine and environmental monitoring [5]. Optical biosensors are capable of providing parallel and real time label free detection of many biological substances and chemicals [46, 47]. Integration of surface plasmon resonance or fluorescence with optical fibre methods is quickly gaining popularity for optical-based biosensing [48]. Optical fibre based sensors are attracting much research interest due to their convenience as probes and they are being used in numerous biosensor studies[30].

1.3.1.4 Piezoelectric sensors

Piezoelectric biosensors work on the principle that an oscillating crystal resonates at a natural resonance frequency [49] and this frequency may change in the presence of target molecules. The most widely utilized transducer in piezoelectric biosensors is quartz due to its low cost [50]. There are two major types of piezoelectric crystal devices: bulk wave (BW) and surface acoustic

wave (SAW) [51]. BW devices are employed in gravimetric devices known as quartz-crystal microbalances (QCM). SAW devices involve an acoustic wave being transferred along a crystal face from one position to another. Piezoelectric transducers have some issues which need to be overcome, such as sensitivity, as well as excessive interference and lack of specificity [30]. Piezoelectric biosensors are commonly used for immune sensing applications. Several studies propose that the piezoelectric transducer is convenient for protein and DNA detection with a detection limit of 1 ng/cm² [52]. A recent review showed that the application range of the quartz crystal has progressively developed and that new measuring techniques that use the quartz crystal as a transducer for chemical sensors and biosensors have also been advanced [53].

A piezoelectric biosensor surface can be sensitised by coating it with a recognition element (biological substance e.g. antibody) before being placed in a medium containing an analyte. An interaction of the analyte with the recognition element leads to a mass change on the piezoelectric crystal surface and a resultant altered frequency of oscillation [32]. Piezoelectric crystal devices have major advantages as they are cost effective, easy to use sensors and they facilitate direct measurement without the need for analyte labelling [49]. Piezoelectric sensors have been utilized for the measurement of ammonia, carbon, monoxide, nitrous oxide and other organophosphorus compounds [54].

1.3.1.5 Calorimetric sensors

Calorimetric biosensors operate by the measurement of heat change arising from the reaction between an analyte and a biorecognition element. This change in temperature is related to the amount of substance consumed or present [55].

Typically, the heat change in these types of biosensors is measured using either a thermopile (usually a ceramic semiconductor) or a thermistor (usually a metal oxide) [30]. The generation and absorption of heat are major features of most chemical and biochemical processes. In addition, a calorimetric biosensor can be sensitised by coating with an appropriate enzyme bioreceptor, which react with the analyte and generate a heat change [32].

Calorimetric biosensors have great advantages such as high sensitivity and stability [56]. Recent research has shown that a range of biological molecules (i.e. urea, glucose) can be detected by utilizing a calorimetric based biosensor [32]. Furthermore, a recent survey demonstrated that calorimetric transduction can be used to detect DNA hybridization [57-60]. Nowadays, calorimetric transduction is being heavily employed in the environmental and food industries [30].

1.3.1.6 Impedimetric sensors

Electrochemical Impedance spectroscopy (EIS) has been widely used technique for electrochemical sensing. It used to study the electrode – electrolyte interface because it is a strong AC method based technique. (EIS) is including a small sinusoidal potential that is applied across the interface by measuring the current at the working electrode [61, 62]. Owing to their advantages such as enhanced sensitivities, low operating sample volumes, low detection and user friendly interfaces that can be making them ideal platforms for performing detection in a point of need or point of use manner[63]. Furthermore, Electrochemical impedimetric biosensors have gained significant attention from food safety scientists and administrators. EIBs has been used for detecting and measuring target molecules with no sample preparation requirement thereby, it used for inline monitoring of hazards in the food supply chain. Due to it has a good sensitivity that better than of other biosensors and

conventional methods so it used for detecting and measuring of food hazard[64].It is interesting that Electrochemical impedance spectroscopy has a lot of advantages compare with other electrochemical methods[65, 66]. Such as a lebel free and nandisruptive technique depend on the conformational changes of aptamers on an electrode in response to the target molecule. Which is measured by change transfer resistance[67]. It is simple and inexpensive and allow the fast biological molecules , quantification of metal ions as well as whole cells[68-70].The strategy of enzyme immobilization, the construction and morphology of transducer is the important part of a biosensor design[71-75] .Furthermore, the surface interactions at the transducer to reduce interferents . For this reason , nanostructured semiconducting metal oxides have focused in the bioanalytical area due to their advantages such as simple to fabricate, good optical transmission in the visible region, high surface area, chemical stability and unique ability to promote electron transfer between active site of desired enzyme and electrode[76, 77].

1.4 Printable sensors

With the rapid development of miniaturized portable and stretchable electronic devices and flexible[78]. The development of wearable sensors on polymer substrates demands a compatible manufacturing process with the thermal and chemical properties of the substrates. Printing technologies are the most promising manufacturing for these developments that deposit solution based functional materials at coveted positions with lower processing steps[79-83] Furthermore, printing is a fast increasing field for the fabrication of electronics and sensors on non-planner substrates. Which includes position specific deposition of functional materials from their chemical solutions or colloidal[83]. Printing is a bottom -up manufacturing approach. It involves adding materials layer in fabrication steps. Owing this a dvantage of this manufacturing the printing process will be cost and simple to fabricate

compared to conventional microfabrication rinting techniques are of two types based on contact and non contact of the printing medium with the target substrates [80].In the contact based the printing medium with designed structures on the surface is inked and brought in physical contact with the target substrate. These techniques includes screen printing, pad printing, stamp assisted, flexographic printing and gravure printing[80, 84]. In non contact based approach the printing materials are ejected in the from of micro droplets or a continuous jet, facilited by miniaturized printing nozzle heads. Which droplets / jet are ejected on demand which is called digital manufacturing[83, 85]. Such techniques involve electrohydrodynamic inkjet printing, piezoelectric inkjet printing, aerosol jet printing and slot die[80, 86].Non contact techniques have a lot of attractive due to they are versatile and lead to fast changes in the designed structures via computer controlled software[87].

1.5 Applications of Biosensors

Biosensors have a wide range of applications in various fields, such as environmental monitoring, genetics, medical diagnostics and clinical detection. For example, current cancer screening methods are invasive and as a result, participation rates in screening programs can be low [88]. Additionally, at the early stages of the disease, biopsies can fail to locate localised cancer cells. In clinical testing, biosensor-based detection has several potential advantages over conventional diagnosis methods, such as speed, being less invasive, less expensive and less technically demanding than microarray or proteomic analysis[89]. Moreover, biosensors are suitable for multi-array testing in cancer diagnosis which would be advantageous for multi-marker analysis [90]. Another application of biosensors in the medical field is for cholesterol measurement in

patients with cardiovascular diseases. Cholesterol biosensors are used to estimate free cholesterol and total cholesterol, primarily using devices based upon cholesterol oxidase (Choux) as the sensing elements [90]. DNA biosensors are another medical application of enormous significance where the low cost, short response time and simple design [91] of the DNA biosensor allows unprecedented screening.

A further growth area for biosensors is in environmental applications [92] where, for example, an environmental biosensor may use bacteria as a detector for toxicity within different environmental mediums such as soil, sediment, and water. By mingling the bacteria with a transducer, a cellular response may be converted into a detectable signal. Engineering of bacterial biosensors requires the pairing of a reporter gene, providing signal generation, with a contaminant-sensing component that responds to physical or chemical change, such as exposure to a specific analyte.

Biosensors are commercially available for applications in the food industries to measure acids, alcohols and carbohydrates and are, for example, utilized in the production of soft drinks, wine, beer and yoghurt. These types of biosensor are mostly employed in quality assurance. Such detectors can be used in laboratories or “in-line”, connected to the processing line by a flow injection analysis system. Possible implementations of enzyme-based biosensors for food quality control involve measurement of alcohols, gases, amino acids and phenols[93, 94]. Immunosensors, which are another type of biosensor, have potential applications in ensuring food safety through detecting pathogenic organisms in fish or fresh meat [95].

One significant application in biomedical diagnosis is in monitoring blood glucose levels (BGL) using glucose oxidase (GOX) based sensors. These

sensors are extensively employed by individuals suffering from diabetes to monitor BGL [95]. The most widely used devices are the amperometric glucose biosensors [32]. The devices are based upon interactions with one of the following enzymes: hexokinase, GOX or glucose dehydrogenase (GDH) [96, 97]. Glucose biosensors will be discussed in more detail in the next section.

1.6 Glucose Biosensors

The standard enzyme for glucose biosensors is the highly selective GOX. This enzyme´s ability to tolerate high extremes of pH, temperature and ionic strength makes it better than other enzymes because it allows for less strict conditions during the process of manufacturing and easy storage requirements for biosensor users [32, 98, 99]. The electrochemistry of the GOX-glucose interaction is well established. When glucose is oxidised selectively by GOX, this reaction will generate gluconolactone and hydrogen peroxide (H_2O_2) as products as described in the equation below:

$$\text{Glucose} + O_2 \rightarrow \text{Gluconolactone} + H_2O_2 \quad (1)$$

Subsequently, when H_2O_2 is oxidised at 0.7 V, it will break down electrochemically into protons, oxygen and electrons as described in the following equation [100]:

$$H_2O_2 \rightarrow O_2 + 2H^+ + 2e^- \quad (2)$$

GOX has many other applications for measurement in different fields such as food production, industrial chemistry, pharmaceuticals, clinical chemistry, biotechnology and other industries. By using co-immobilized enzymes, there

are many improvements that can be anticipated such as better stability, handling, improved control of reaction expectancy, continuous operation, high purity and product yields and economical processes [101].

In 1962 the initial concept of glucose-sensing electrodes was introduced by Clark and Lyons when they implanted GOX into an electrode of an electrochemical cell [102]. In more recent years, glucose sensor development has grown rapidly due to the increased incidence of diabetes worldwide. Management of diabetes mellitus can be achieved by glucose monitoring for diabetic patients, which requires them to monitor their BGL multiple times daily in order to know the best times to eat and exercise [100] .The monitoring of BGL as a management tool was established back in the 1960s, however, it could only be conducted by a qualified practitioner. This early device was based on a cellulose strip incorporating peroxide, glucose oxidise and a chromogen (dye). The presence of these chemicals allowed the strip to change colours when a drop of blood was deposited onto it. The change in colour of the strip could then be compared to a colour chart that gave an estimate of BGL. In 1978, Peterson et al. made it possible for diabetic patients to test their blood glucose at home [103]. In the 1980s, Sen and Sarin showed the existence of a relationship between BGL and glucose levels in tears [104], and later studies by Baca et al. 2007 also confirmed this relationship [105]. Furthermore, studies have now shown that there is a linear relationship between BGL and the concentration of glucose in saliva, indicating that saliva could be the basis for an alternative to blood testing. However, the typical salivary glucose level (SGL) is approximately 8-200 μM, while the range of concentration for glucose in blood is between 3.3-8.3mM [17, 106].

Chengcheng Liu et al. have developed and generated a novel dual enzyme biosensor composed of glucose oxidase (GOX) and Pistol like DNAzyme (PLDZ) to detect glucose levels in tears and saliva. They found the relationship

between glucose concentration and the cleavage rates of PLDZ was simulated by a Double Boltzmann equation. The design GOX-PLDZ 1.0 biosensor is able to determine glucose levels in tears and saliva as a nano invasive glucose biosensor which is important for diabetic patients with continuous glucose monitoring requirements [107].

In 2014 Elkington et al. integrated GOX into an OTFT, and the results showed a monotonic response for the sensor across four decades of glucose concentration covering both blood and saliva glucose concentration levels. The key determinant of the device response time was shown to be glucose diffusion [100]. This work acts as a proof of concept for the integration of functioning biomolecules (such as enzymes) directly into organic electronic devices and the feasibility for low cost printed biosensors for salivary glucose.

Yamaguchi et al. constructed a saliva analysing system that uses an enzyme sensor by which determination of SGL from 0.1 to 1.0 mg/dL was possible. They show the correlation between BGL and SGL and then present an approach that uses an enzyme sensor system to noninvasively measure blood glucose using saliva which would greatly contribute to the clinical treatment of diabetes patients[17]. Macaya, D.J., et al. reports a simple glucose biosensor with micromolar sensitivity. The transistor utilized the conducting polymer poly(3,4-ethylenedioxythiphene):poly(styrene sulfonate) (PEDOT:PSS) as a semiconductor layer and the enzyme GOX to allow specificity [108]. This study shows a fast response by the sensor to glucose within the clinical range of glucose levels in human saliva. Recently, Freckmann et al. has shown that several commercial blood glucose sensors suffer from poor accuracy in the high and low blood glucose concentration ranges [109].

In a study by Wenjun Zhang et al. a unique disposable saliva nano biosensor was developed [110]. These sensors showed excellent clinical accuracy compared to saliva glucose analysis obtained by UV spectrophotometry. In addition, a good correlation of glucose levels in saliva and in blood before and

two hours after glucose intake was observed. In a separate study, Jian Liu et al. have developed a unique, disposable saliva nano-biosensor with a detection limit of 0.003 mM glucose. They added the interferent species of uric acid, lactate and ascorbic in 0.5 mM glucose to evaluate the selectivity of the biosensor. A thirty-person clinical trial was conducted by real time monitoring of blood glucose and salivary glucose levels. The result showed a close correlation between glucose levels in blood and saliva [111].

1.7 Saliva

Blood is the most direct and widely used source of testable biomarkers. However, blood analyses are often high cost and require breaking of the skin for analyte collection; an invasive procedure which is painful and opens a pathway to infection in the body. Saliva is a biological fluid containing components that can provide an indication of a subject's neurologic, hormonal, metabolic and nutritional state[112] . Saliva comprises 98 % water, but the other 2 % is composed of substances such as electrolytes, mucus, antibacterial compounds and various enzymes [113]. A number of reports have revealed that there is a good correlation between blood glucose levels (which range from 3.3 to 8.3 mM [114]) and the concentration of glucose in saliva [17, 115], which ranges from 8 to 200 μM[17] . As such, saliva is an attractive alternative medium for medical diagnostics in non-invasive glucose sensing [116]. Indeed, chemical biomarkers in human body fluids, such as urine, sweat, tears or saliva have all been used as analytes by currently studies due to the non-invasive nature of their collection [117, 118]. In particular, saliva is attractive as an non-invasive alternative analyte for blood analysis in the monitoring of metabolism and stress in individuals [119]. Saliva is easily collected from humans with minimal discomfort to the subject. Glucose level measurement is one of a large number of diagnostic analyses which can be conducted on saliva [120, 121].

Incorporating sensors into daily dental platforms, such as dentures, mouth guards and new devices, such as dental tattoos, is a new and evolving methodology for the continuous and non-invasive detection of glucose in saliva [122, 123].

1.8 Motivations and Aims

This thesis will focus on the design and development of a glucose biosensor utilising an OTFT architecture for detection of glucose in saliva. The aim will be to design and fabricate a sensor that has a low detection limit and presents a high degree of biocompatibility allowing direct contact between the subject and the sensor. This iterative process is depicted in Figure 1. *3*.

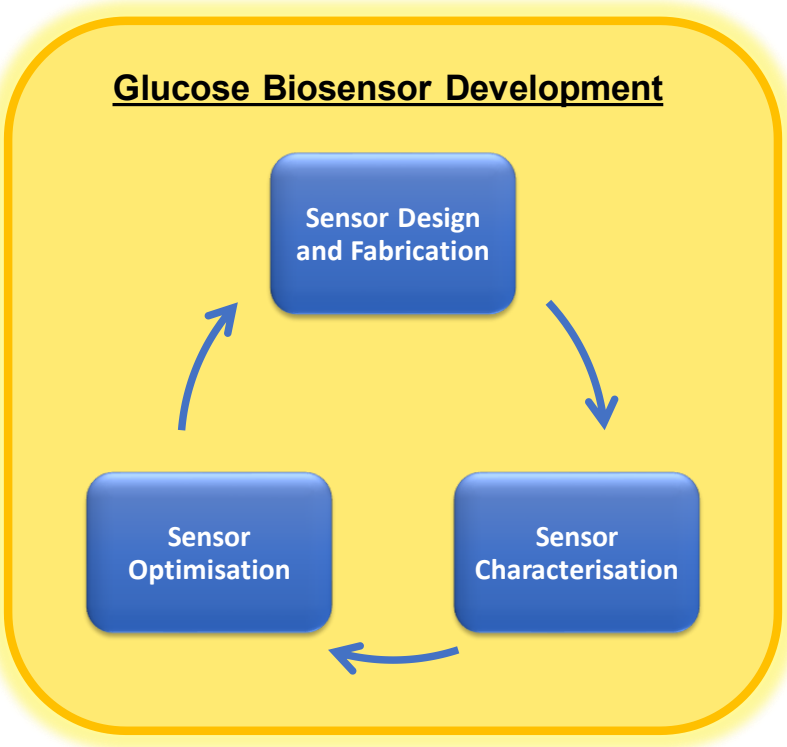

Figure 1. 3: Iterative glucose biosensor development plan

The success of this project will allow for portable and rapid point of care testing. Organic electronic printable biosensors are particularly desirable as they have the potential to be inexpensive, easy to produce and accurate. Printable sensors have the potential to be produced *a mass* for a low per-sensor cost using a variety of existing printing techniques such as screen printing, inkjet printing and flexographic printing.

Chapter 2: Experimental Procedure and Materials

2.1 Materials

This section will detail the main materials used for the fabrication of organic thin-film transistors (OTFTs) and biosensors throughout this thesis.

2.1.1 P3HT

Poly (3-hexylthiophene) (P3HT) is one of the most widely used semiconducting polymer in organic electronics. It has been applied in devices : organic photovoltaic (OPV) cells and organic field transistors(OFETs)[124-126] due to its good processability, high charge carrier mobility up to ~0.2 cm^2/Vs [127] and excellent stability to photo degradation [128]. One of the most significant

properties of P3HT polymer is available in quantities over ten kg compared to other polymers[129].Thus, P3HT polymer has already been widely designed and used for commercial purpose of OPV. Interestingly, it has been commonly used and demonstrated in large-area applications such as roll-to-roll printed solar cells. Moreover, P3HT polymer with semi-crystalline nature mostly has a unique in setting an appropriate morphology scale for bulk heterojunction OPV from a different range of solvents and processing conditions, additionally, with high quality of charge transport properties [130-132]. The highest efficiency for P3HT was 4.4 % and standard efficiencies of 3-4% with P3HT manufactured at Plextronics by the grignard metathesis (GRIM) method [133]. P3HT can also self-assemble into nanofibers [134, 135]. However, due to differences in the flexibility of the backbone compared to the side chains, achieving highly crystalline domains of P3HT is challenging [136]. Recently, a report has demonstrated that there is a strong relationship between the electronic properties of P3HT and its molecular weight as demonstrated by changes to charge carrier mobility [137-139] . Other studies have also reported by Brabec.et al on the relationship of P3HT molecular weight and organic field effect transistor (OFET) performance[140]. The P3HT (Mw = 32600 g/ moL, Mn = 23000, PDI = 1.42) in the current study was provided by Dr Nathan Cooling, a member of the COE group in the Physics department, University of Newcastle. The chemical structure of P3HT can be seen in Figure 2.1.

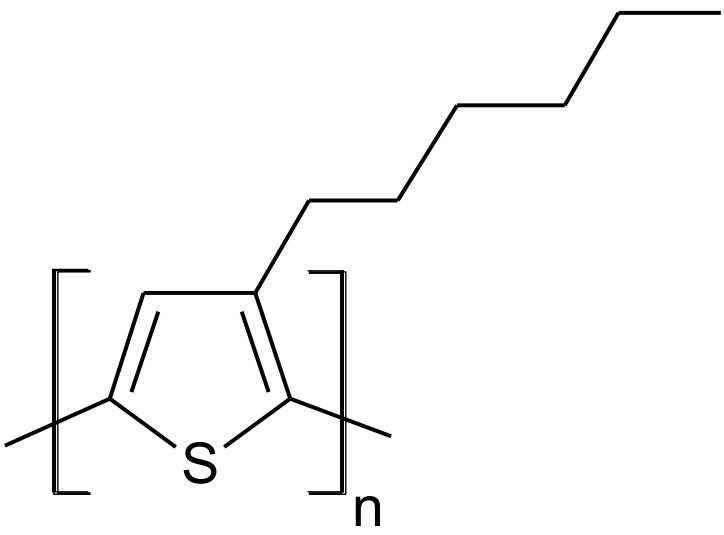

Figure 2.1: Chemical structure of P3HT

The morphology of P3HT films can determine the device field effect mobility, which can vary by several order of magnitude [141-143]. In recent years, reports have been published on the relationship between the number and size of highly ordered P3HT domains and its molecular weight of P3HT used [140, 144]. Furthermore, the performance of bulk heterojunction OPV cells have been demonstrated to be strongly affected by P3HT regioregularity. High regioregularity leads to better solid state packing upon annealing and higher photovoltaic power conversion efficiency [145]. It is evident that the backbone conformation of the P3HT chains is the most important parameter that controls both charge carrier mobility (important for OFETs) and efficiency of bulk heterojunction solar cells and determines the packing within the bulk material.
In this study, P3HT is used as the semiconductor material in the fabrication of organic transistors and sensors.

2.1.2 PEDOT: PSS

Poly(3,4–ethylenedioxythiophene) doped with poly(styrene) sulfonate (PEDOT:PSS) is one of the most important conducting polymers for photovoltaic cells, thermoelectric and organic field effect transistor (OFET) applications [146, 147]. Its molecular structure is shown in Figure 2.2. PEDOT.PSS has excellent advantages such as thermal stability, high transparency in the visible range, practically the tunable and improved conductivity by secondary doping [148, 149]. Interestingly, the maximum value of conductivity is 4380 S cm^{-1} with four orders of magnitude improvement compared to untreated PEDOT: PSS film. Thereby, the high conductivity and transparency of PEDOT:PSS films can play a role replacing ITO in different applications such light-emitting diodes, solar cells, and field -effect transistors [150-152]. Previously, several studies have reported that thermal and light treatment [153, 154], have significantly correlated with the conductivity of PEDOT:PSS. Additionally, treatments of organic solvents, ionic liquids, surfactants, and salts, have also considerably enhanced the conductivity of PEDOT: PSS [150, 155-157]. PEDOT:PSS film has also been employed as novel an electrode material in electrochemical applications such as fuel cells, batteries, capacitors and sensors. PEDOT: PSS has been selected for the OTFTs in this study due to its high conductivity and processability compared with other polymers. The poly(3,4-ethylenedioxythiophene): poly(styrene) sulfonate (PEDOT: PSS) hole transport layer material was purchased as a suspended with a solid content of 1.3-1.7 wt % from Heraeus Deutschland GmbH and Co, Germany. This solution was Clevios PVP A14083.

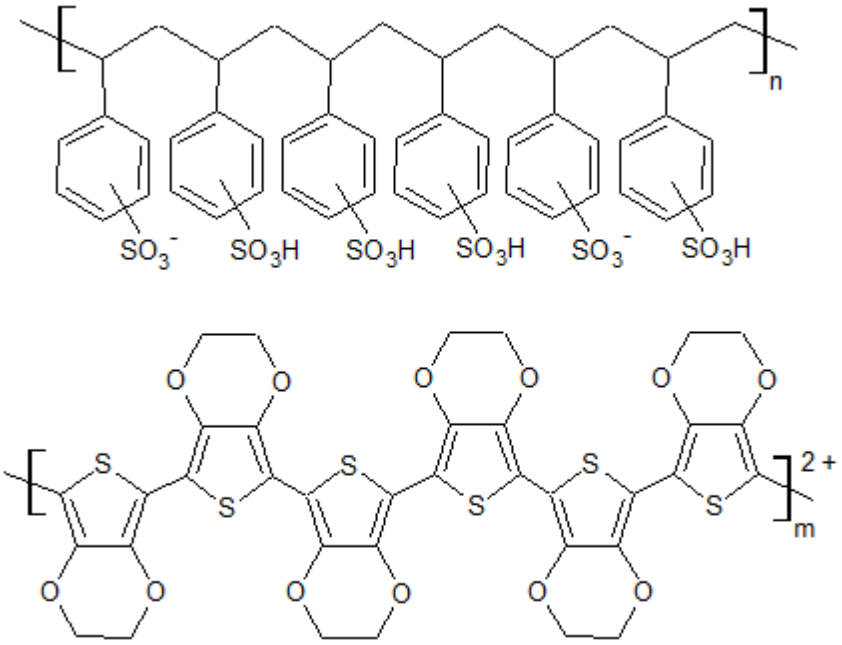

Figure 2.2: Chemical structure of poly(3,4-ethylenedioxythiophene) doped with poly (styrene sulfonate) (PEDOT: PSS) used as a transport conductive polymer.

2.1.3 Nafion

Nafion is a polymeric perfluorinated sulfonated cation exchange material and was developed by the E. I. DuPont Company in the 1960s [158]. Nafion allows proton conduction but neither electronic nor anionic conduction making it well suited for use in fuel cells [159]. The polymer consists of polytetrafluoroethyl as a polymer backbone with sulfonated end groups as pendent chains (Figure 2.3). Under humid conditions, the hydrophilic end groups separate into nano-sized clusters that cause swelling of the ionomer. Several studies have reported on the phase separated morphology and ionic conducting mechanisms of Nafion [159-161]. In particular, interconnected acidic domains formed from the water clusters are thought to be a major path for proton transport using the Grotthuss mechanism [161, 162]. The hydration level increases both the swelling and

proton conductivity and is known to govern the mechanical behaviour of Nafion [162]. Nafion responds dynamically to hydration and stress related changes due to its high viscoelasticity [163] Upon absorption of water the polymer membrane swells causing considerable stress, the resultant stress can cause thinning of a Nafion film, and may lead to contact problems between Nafion and electrodes [163, 164] .

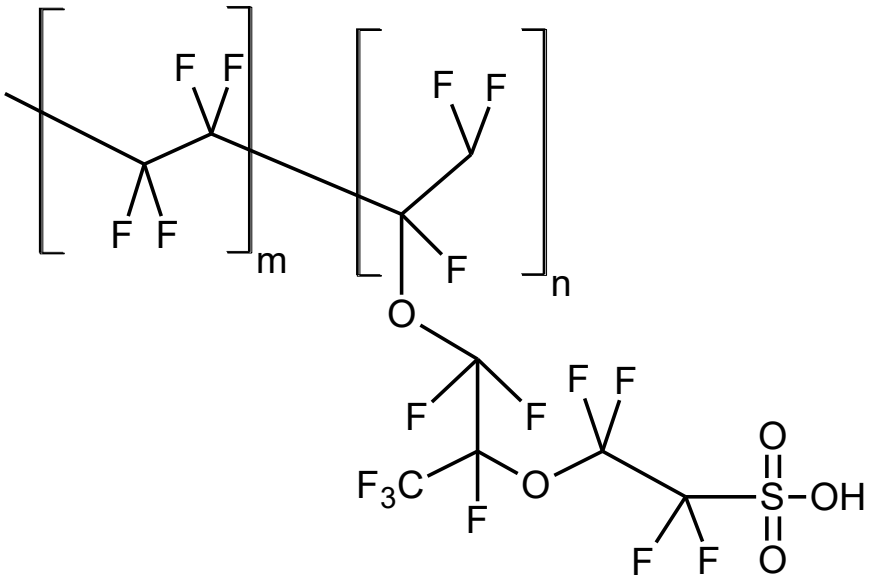

Figure 2.3: Chemical structure of Nafion.

Many sensing applications of Nafion-coated electrodes have been reported, such as for the detection of phenol [165], parathion [166], doxazosin [167], estrogen [168], and its use in many immunoassays [169]. Specific chemical properties such as chemical inertness, mechanical strength and thermal stability make it a highly suitable component material for use in sensors [170]. The electrical and mechanical properties of Nafion are sensitive to temperature and humidity. In the temperature and relative humidity range of 25 to 95 °C and 0 to 100 % [171], respectively, studies have reported on the measurement of mass uptake [172, 173] , water permeation and tensile strength [163] of Nafion films. The unique ion exchange properties, chemical resistance and biocompatibility of Nafion make it suitable for electrode surfaces and amperomatric biosensor

construction [174-176]. In this study, Nafion is used as a proton transport material. Nafion was purchased in a solution of propanol and water from Sigma-Aldrich and was used without additional purification. It has a more neutral pH than the PEDOT:PSS solution providing a biocompatible environment for GOX, thereby reducing the likelihood or denaturation. Nafion mixed with GOX as well as Nafion situated below a GOX film will be employed in the sensors presented here and this will be discussed in more details in Chapter 3.

2.1.4 Polyacrylonitrile

Polyacrylonitrile (PAN) is an organic polymer resin with a linear formula $(C_3H_3N)_n$, the chemical structure for which is shown in Figure 2.4. It is a very versatile polymer used in the the manufacture of a range of fibres spanning fibres for textiles, carbon fibres, medicated nanofibres and fibres for reverse osmosis [177, 178]. Polymer membranes can be produced using PAN, which can be dissolved in polar solvents such as N, N–dimethyl acetamide (DMAc), dimethyl formamide (DMF), ethylene carbonate (EC), and dimethyl sulfoxide (DMSO) and subsequently processed [179-182]. These kinds of membranes are often used in water ultrafiltration processes due to their high porosity and , therefore, higher water permeability [183].

PAN fibres are widely used as a precursor to carbon fibres due to their reasonable carbon yield and high strength [184]. Furthermore, PAN is one of the most widely used polymers in the biomedical field because of its excellent mechanical, chemical and thermal properties as well as low cost [185]. In addition, PAN is easily fabricated into nanofibers by electrospinning producing porous high surface area materials [186].

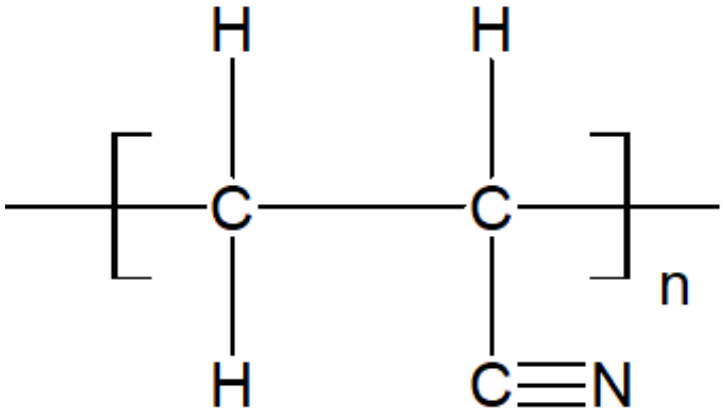

Figure 2.4: Chemical structure of PAN.

In this study, PAN is used in a novel way as an enzyme-containing porous membrane in the fabrication of organic sensors to improve device response.. The polyacrylonitrile (Mw = 150,000 typical) was purchased as a powder from Sigma Aldrich (product No. 181315-100G).

2.1.5 Glucose oxidase

The majority of enzymes that it is beneficial in the production of electrochemical energy were made using electrons transferred with enzyme-catalyzed reactions [187-189]. In the biofuel cell research area, the glucose/ glucose oxidase (GOX) couple has been widely used as the fuel and the catalyst due to its availability in nature in high rate percentages [189-191].

GOX has several properties which are favourable for use in a glucose sensor design such as a high turnover rate, good thermal stability, low cost, reasonable pH stability and excellent selectivity [192], which have made it a benchmark system within biosensor development [193-195] . As such, GOX requires less

stringent conditions than many other enzymes as it can withstand a wide variation in pH, temperature and ionic strength [196, 197].

The activity of GOX is affected by pH, temperature and humidity [192]. Where the temperature and pH govern the stability of glucose oxidase, in general, lyophilised GOX is very stable, and can be stored for long times at -15 °C, but is destabilised when temperatures exceed 40°C. Thermal denaturation can be prevented to some extent by the addition of stabilising polyhydric alcohols like glycerol [192]. At high (> 8) and low (< 2) pH, GOX is rapidly denatured [192] , with a pH of between 7 and 8 being optimal depending on the source [197-199]. At physiological pH,the enzyme GOX is negatively charged and its isoelectric point is 4.2 [192]. A molecular structure of glucose oxidase can be seen in Figure 2.5.

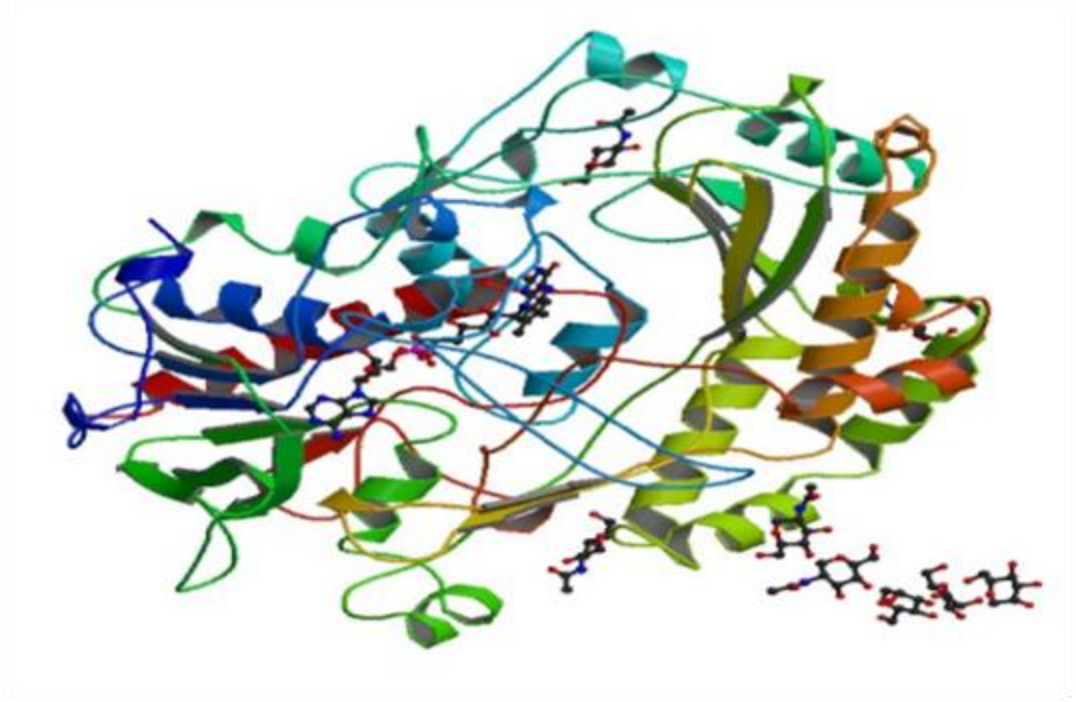

Figure 2.5: Glucose oxidase structure[200]

In our studies, GOX was employed as the functional part of the biosensors. GOX is composed of two identical subunits and one flavin adenine dinucleotide (FAD), coloured red in Figure 2.5, is the active site in GOX. FAD plays major

role as the electron accepter due to of its reversible electrochemistry. It is essential for glucose oxidation [189, 192, 200]. The FAD cofactor, as an electron accepter, requires the addition of two hydrogen atoms to reduce to $FADH_2$ and produce gluconolactone during the reaction as shown in Figure 2.6 and Figure 2.7.

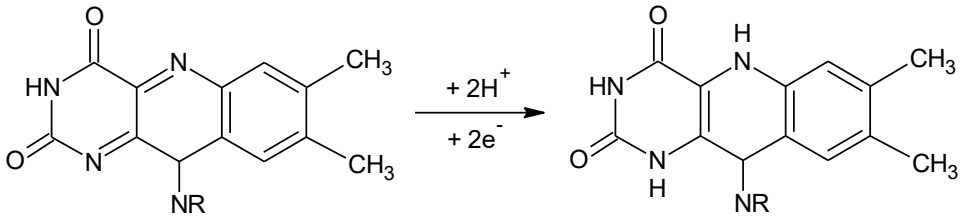

Figure 2.6: Schematic depicting FAD being reduced to $FADH_2$

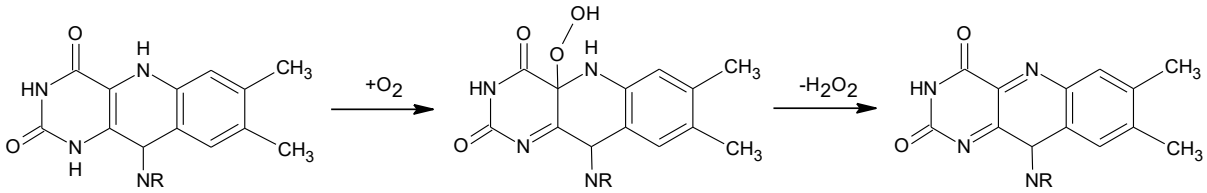

Figure 2.7: Schematic depicting the $FADH_2$ is oxidized to FAD.

The overall oxidation reaction of glucose by GOX (FAD) can be described by the following chemical and electrochemical steps [12, 201].

FAD works as the preliminary electron acceptor and is reduced to $FADH_2$.

$$Glucose + GOX - FAD^{+} \rightarrow Glucolactone + GOX - FADH_2 \quad (1)$$

Subsequently, Oxygen, the acceptor oxidizes the $FADH_2$ back to FAD with hydrogen peroxide (H_2O_2) is produced of the reaction.

$$GOX - FADH_2 + O_2 \rightarrow GOX - FAD + H_2O_2 \quad (2)$$

Hydrogen peroxide is classically oxidized at a platinum anode.

$$H_2O_2 \rightarrow 2H^+ + O_2 + 2e \quad (3)$$

Due to its favourable properties, GOX is widely used in biosensor platforms. Glucose biosensors generally have a wide linear range, high reliability and high sensitivity and are being increasingly used in clinical diagnosis, food processing and industrial quality analysis [202, 203]. The immobilisation of GOX can be an important factor in biosensor preparation [204]. The embedded redox centre can make it difficult for glucose and the GOX to interact, moreover when the enzyme is absorbed or embedded on to an electrode surface, the shape of enzyme can shift slightly exacerbating this problem [197, 205]. For this present study, glucose oxidase from Aspergillus Niger purchased from Sigma -Aldrich (product No. G7141-250 KU) was used. It was a type X.S, lyophilized powder containing 100,000-250,000 g/moL.

2.1.6 Indium-tin-oxide (ITO)

Indium-tin-oxide (ITO) is a widely used transparent electrode in many optoelectronic devices such as organic light -emitting diodes (OLETs), flat panel displays, photovoltaic cells (OPVs) and sensors [206-208], due to its good conductivity and high transparency [209-211].Additionally, ITO has very low resistivity which is $2\times10^{-4}\ \Omega$ cm when deposited on glass [212].In this study, ITO was used for the electrodes of the organic transistors and sensors. ITO coated glass substrates (12.5 × 17.5 × 0.7mm) were purchased from Xinyan Technology Ltd., China. (Pattern No. XY0310) pre-patterned in the design as shown in Figure 2.8. The thickness of ITO was (102 ± 2 nm) and the sheet resistivity was 150 ohm/sq. and the gap between the source and drain electrodes is 20 μm.

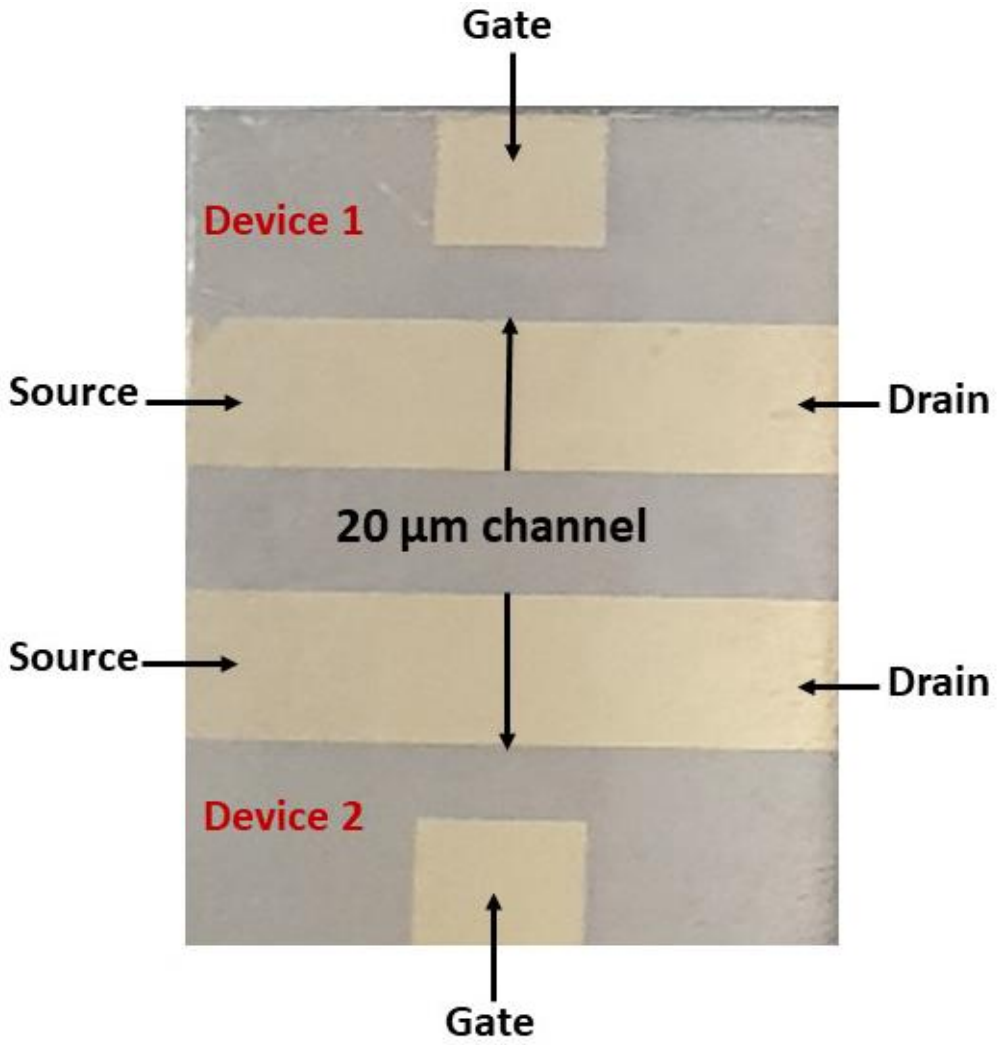

Figure 2.8: Photograph of the patterned ITO coated glass substrates used for fabrication of OTFTs and sensors.

2.2 Device Fabrication

OTFTs were fabricated on pre-patterned ITO-on-glass substrates from Xinyan Technology Ltd. The substrates were cleaned before use to remove debris and impurities by the following procedure:

a) Washing the substrates with detergent solution (Liquid Pyroneg).
b) Cleaning the pre-patterned ITO substrates was done using an ultrasonic bath and rinsing in Milli-Q water for 5 min.
c) This was followed by using acetone in an ultrasonic bath for 5 minutes.

d) The ITO substrates were then placed in IPA in an ultrasonic bath for 5 minutes.
e) The ITO substrates were immersed in Milli-Q water for 10 minutes.
f) The last step of substrate cleaning is heating of the substrates on a hot plate at 85 °C for 5 minutes to ensure that there are no residual cleaning solvents left on the substrates. Any residual solvent left on the substrates will evaporate at 85˚C.

The fabrication of a typical glucose sensor is described here as an example of the techniques used in the fabrication of the various types of device structure presented in this thesis. Variations to this procedure are described in the relevant sections. The fabrication process of a standard glucose sensor is illustrated in Figure 2.9.

P3HT was dissolved in chloroform at a concentration of 20 mg/mL and sonicated for ~1 hour or until the material was entirely dissolved. 100 µL of the P3HT solution was then spin-coated onto the cleaned ITO-on-glass substrate at 2000 rpm at an acceleration 1596 rpm/s for 60 s to deposit an approximately 100 nm thick P3HT layer (as measured by profilometry). The film was then patterned manually using a chloroform-soaked cotton tip to expose the source and drain electrodes and allow enough space to deposit the Nafion layer. They were annealed for 10 minutes at 50 °C in air to remove excess solvent. A Nafion solution was spin-coated for 120 s at 500 rpm and an acceleration of 1330 rpm/s on top of the P3HT layer, to form a film with a thickness of approximately 500 nm (as measured by profilometry), and again patterned manually using acetone. The P3HT/Nafion bilayer structure was annealed for 10 minutes at 50 °C in air to remove any remaining solvents. GOX solution (12 mg/mL in DI water) was drop-cast on the top of the Nafion film above the source-drain channel area and allowed to dry at room temperature. Devices were used immediately where possible and, where not were stored in a N_2-filled chamber.

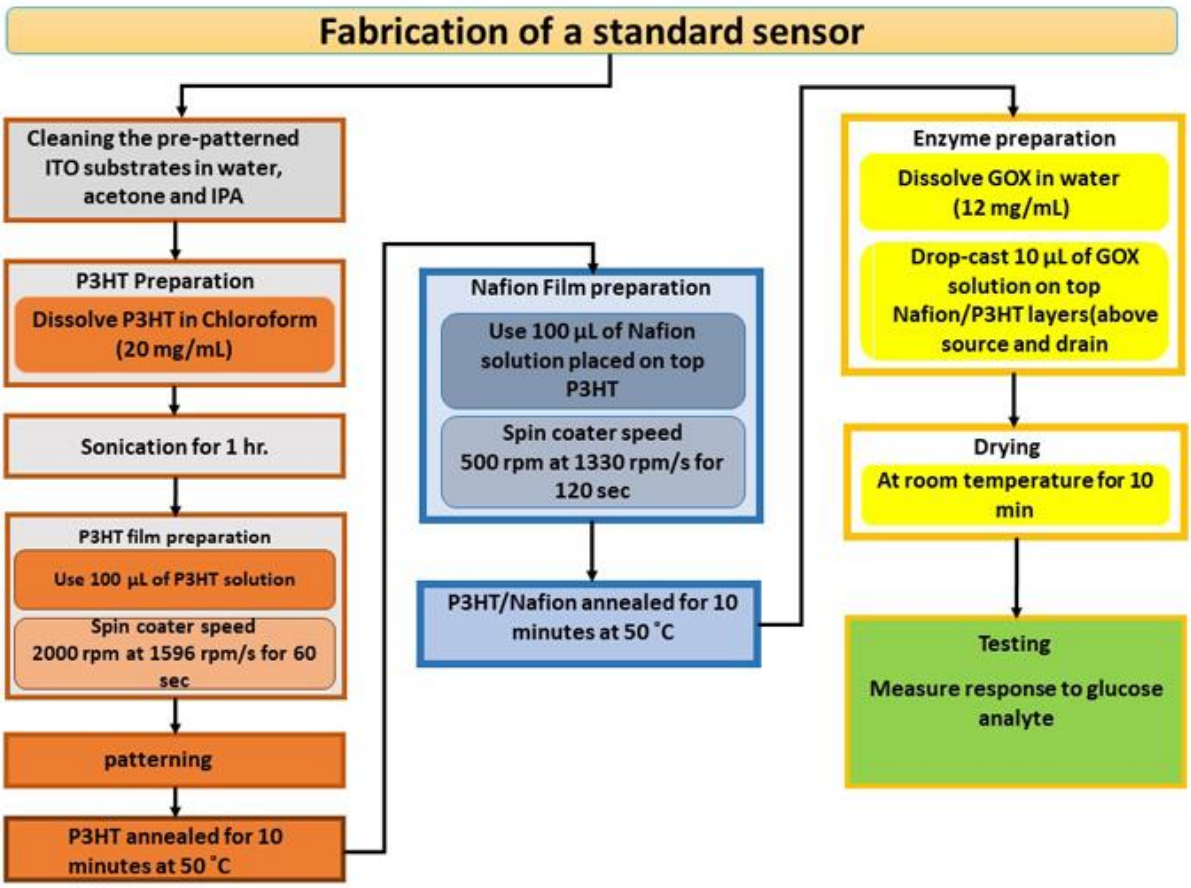

Figure 2.9: A schematic representation of the fabrication of a standard glucose biosensor

2.2.1 Device Architecture

This thesis is focused on the fabrication of three devices with conventional architecture which are transistors, sensors and two terminal measurements. Generally, there are four architecture types to fabricate OTFTs that are categorised according to the location of the gate and the source/drain contacts. These categorises are namely, bottom-gate bottom contact; bottom-gate top contact; top-gate bottom contact and top-gate top contact, relative to the

semiconductor layer. The fabrication methods and the materials used are descried in detail in chapter three. The OTFTs device architecture in this chapter is top-gate-bottom contact using ITO for the source and drain electrodes. The OTFTs design architecture requires the compatibility of solvents to ensure that previously deposited layers are not dissolving as upper layers are applied. The device design comprised a glass substrate with indium tin oxide (ITO) as the bottom electrodes, a poly-3-hexylthiophene (P3HT) semiconductor layer, with, either poly(4-vinylphenol) (PVP) or poly (vinyl-pyridine) (PVPy) as a dielectric layer and poly(3,4-ethylenedioxy-thiophene) poly(styrenesulforate) (PEDOT:PSS) as a gate electrode. The current output performance of these OTFs devices with ITO/P3HT/PVPy/PEDOT:PSSand ITO/P3HT/PVP/PEDOT: PSS has been measured and compared.

The second conventional architecture studied was a PTFT device as a glucose sensor. An OTFTs device incorporated GOX into the device structure (ITO/P3HT/Nafion: GOX) and an assessment of how the incorporation changed the electronic properties of the device stack was made. GOX was introduced into the Nafion gate electrode instead of the PEDOT: PSS due to reason that will be discussed in chapter 3. The device architecture (ITO/P3HT/Nafion: GOX) was used with a different glucose solution concentration to evaluate device performance in the sensor application, such as for glucose levels in saliva and many other applications.

The third conventional architecture is a diode comprising two terminals. This device architecture was comprised of ITO/P3HT, ITO/P3HT/Nafion, ITO/Nafion, ITO/P3HT/Nafion/ Water and ITO/Nafion/Water. These conventional architectures were employed to investigate the electrical properties of the materials annealed with different temperatures. The full description of design and effect of these properties on the device performance will be discussed.

2.2.2 Spin-coating

Uniform thin films are commonly fabricated using the spin-coating technique[213]. A small amount of a solution is deposited onto the centre of a substrate and then the substrate is rotated at high speed to spread the fluid to, and off, the edge of the substrate (driven by centrifugal force). The solute forms a uniform thin film as the solvent is removed. Subsequently, excess solvent is eliminated from the coated films by a drying process.

The spin-coating parameters such as rotation speed, acceleration, the solution concentration and the nature of the solvent, determine the final film thickness which is typically in the nano- to micro-metre range. The solution starts drying immediately as the surface area increases and hence controlling the acceleration accurately is very important to achieving consistent film formation. In addition, the final film coating depends on the nature of the solution such as concentration surface tension and inherent drying rate. In this work, the films were fabricated on a Laurell WS-400A-6NPP/LITE as shown in Figure 2.10.

Figure 2.10: WS-400A-6NPP/LITE spin coater

2.3 Physical Material Characterisation

2.3.1 Profilometry

The thickness of the films deposited by spin-coating were measured by stylus profilometry. The profilometer works by scanning a diamond tip stylus across the film's surface and vertical movement is recorded as a height trace. Film thickness can be determined by scanning across a scratch which has been deliberately placed in the film. The stylus applies a predetermined and adjustable force (0.03-15 mg). Since the organic films that we are measuring are soft, care is taken not to cause damage by excess force applied by the stylus. The profiler measurement head integrates a high-resolution video camera to be used for setting the gap between the stylus tip and the sample surface. When determining film thickness, multiple measurements are recorded and average values, as well as errors (σ), are reported. All profilometry measurements in this thesis were conducted using a Bruker DektakXT XT surface profilometer, shown in Figure 2.11.

Figure 2.11: DektakXT stylus profiler used to measure the thickness of films.

2.3.2 Scanning Electron Microscopy (SEM)

Scanning electron microscopy (SEM) is a microscopic technique for high resolution imaging of materials. Fundamentally, SEM works by raster scanning the specimen surface with a focused beam of electrons. Electrons that are backscattered from the specimen surface and secondary electrons are detected to generated images of the specimen, where these images of the specimen provide topographical information on the morphology and roughness of PAN films. In this work, SEM micrographs were produced by Dr. Natalie Holmes using a Zeiss Sigma ZP field emission (FE) SEM, as shown in Figure 2.12, at accelerating voltages of 1 to 2 kV and magnifications of up 200,000 x. SEM samples were prepared by spin coating of Polyacrylonitrile(PAN) µL (500 rpm, 1 minute, acceleration 1330 rpm/s) Silicon was used as substrate so as to

prevent charge accumulation during measurement and subsequent damage the specimen.

.

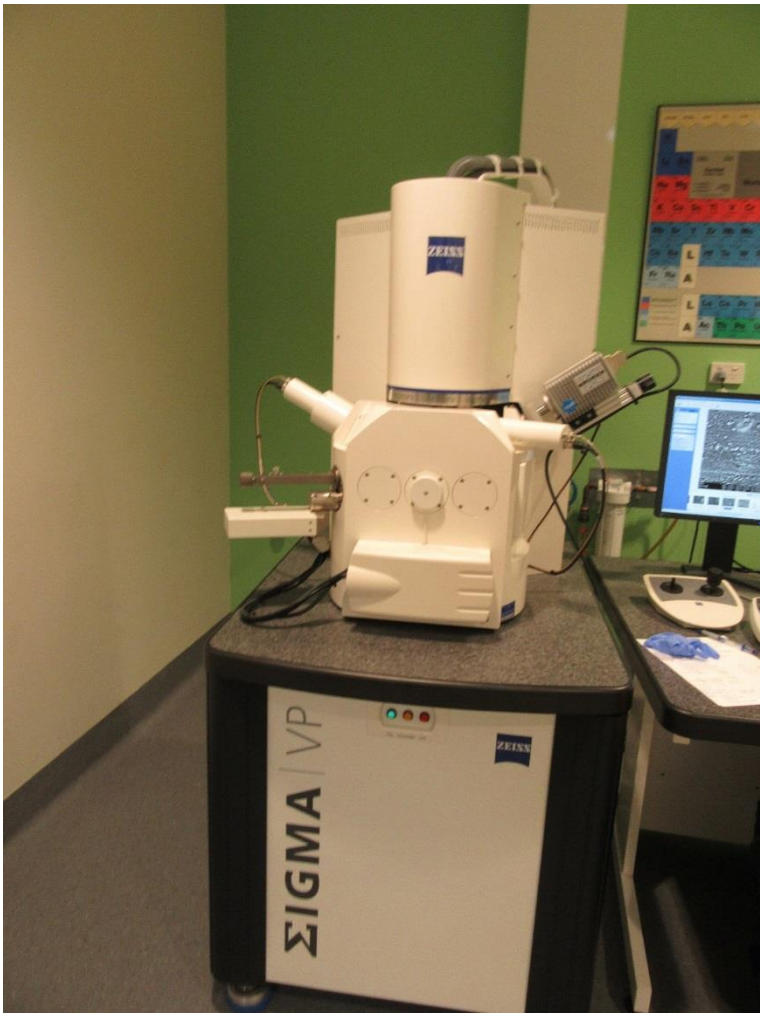

Figure 2.12: Photograph of the Zeiss Sigma ZP-FE-SEM

2.3.3 Atomic Force Microscope (AFM)

Atomic force microscopy (AFM) is a common scanning probe microscopy (SPM) technique, that gives the opportunity to study sample surface topography in nanoscale range and provide images with resolution of fraction of a nanometres [214]. The AFM technique was introduced by Binnig et al. in

1986[215] based on concept combining scanning tunnelling microscopy with stylus profilometer. This technique is applicable to OTFTs devices for investigating the morphology of films prepared from PAN. In this thesis, the AFM used to characteristic PAN films as well as to investigate the morphology and roughness in PAN films. The major components of AFM include a piezoelectric holder, a cantilever with a sharp tip, laser and a photodetector. The cantilever mounted tip is brought close to the surface under piezo-electric control. When sufficiently close for the tip electrons to interact with the electrons on the sample surface, the cantilever will bend, with this motion amplified by an optical lever of the laser bouncing off the tip and onto a position sensitive detector, to generate an electrical signal. The continuous "contact" mode of the tip on the surface, as outlined, generates a signal representative of the surface contour by keeping the cantilever force constant. This mode can cause damage to material surfaces due to the close proximity, ˜ 1 nm, of surface and tip. The other technique that can produce AFM topography images is tapping mode where the tip is vibrated at a frequency and, topography images is tapping mode where the tip is vibrated at a frequency and, when in proximity of the surface, the amplitude of the vibration changes, and a laser is bounced off the tip. Change of the reflection angles of the laser is associated with change in the position of the cantilever. Additionally, the reflected laser will be collected by a sensitive optical detector that measure the change in the deflection of the cantilever then convert it into an electric signal.

There are mainly two techniques that can be used to produce AFM topography images: contact mode and tapping mode. These track the tip on sample and monitoring the directional deviations of the cantilever. The working principle of the AFM in contact mode is transformation the deflection variations of the cantilever into a constant force. Whilst in tapping mode (Figure 2.13), the prop tip is hold lase to the specimen surface by oscillating the cantilever with a

known resonance on the surface by the piezoelectric actuator. The resonance can be turned via the set-up drive frequency in order to be near the cantilever resonance outcome the tip will be as a net repulsive force during the imaging. The produced oscillations will be collected by a sensitive in the deflection of the cantilever then convert it into an electric signal. This signal is used by computer for the maintain either a constant force or a constant height above the sample. In this thesis, AFM investigations were performed on PAN films using an Asylum Research (AR) Cypher AFM (oxford instruments) in tapping mode with AR Scanning Probe Microscopy software for analysing image. AFM offers surface images with atomic scale resolution and produce quantitative data of surface roughness in PAN films. Tips for the AFM were purchased from Budget Sensors Co. Model Tap 300Al-G tips coated with 30 nm aluminium were used in tapping mode where the tapping vibration had a resonant frequency of 300 KHz. AFM device as shown in Figure 2.14 has been used to exam the morphology and roughness for PAN films.

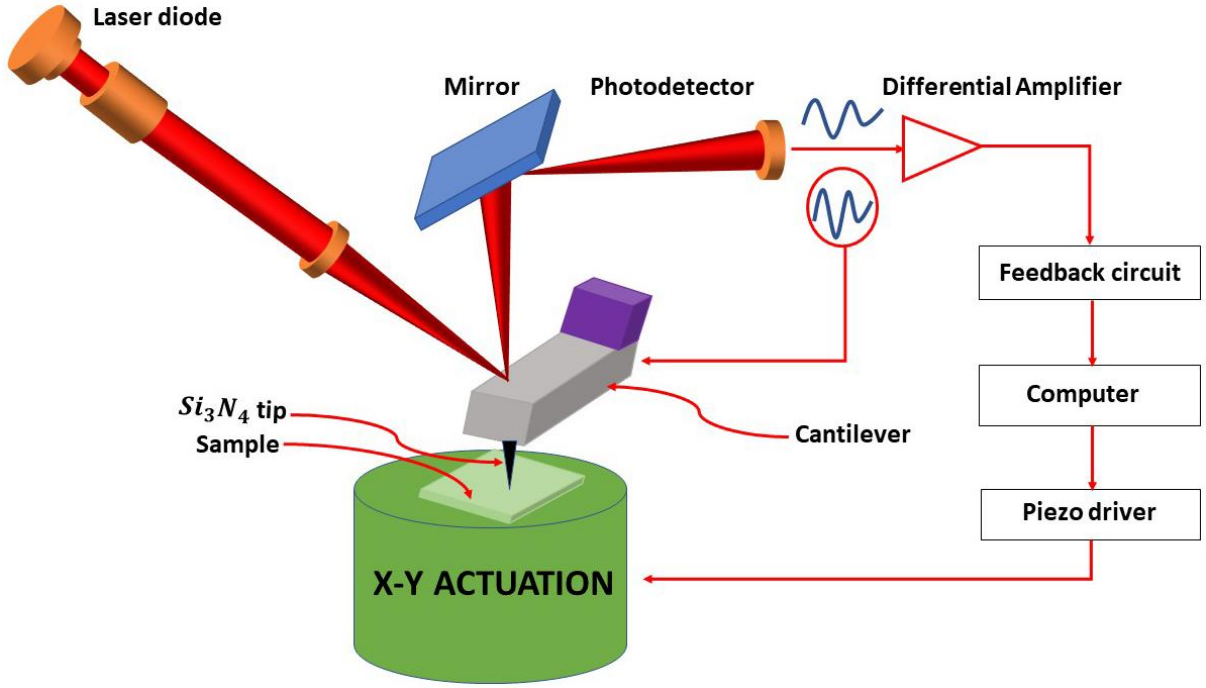

Figure 2.13: Schematic diagram of the AFM in tapping mode.

Figure 2.14: AFM from Asylum Research (Cypher scanning microscope) used in this project.

2.4 Electrical Device Characterisation

In all the electrical measurements, the specimen is tested on a grounded plate and coaxial or triaxle cables are used for contacting the metal electrodes on the samples. All electrical measurements for devices were performed in air, at room temperature.

2.4.1 Transistor Characterisation

The current – voltage characteristics of the devices, such as the output and transfer characteristics of the transistors, was measured using two Keithley 2400 SourceMeters (see Figure 2.15) controlled by a program written in National Instruments LabVIEW development environment. The output characteristics (Figure 2.16 a) were measured as follows. The drain current was measured as proportional to the drain voltage. For a given value of gate -source voltage ($V_{GS)}$, the drain -source voltage ($V_{DS)}$ was swept over a range and I_D and I_G were recorded while the gate voltage was kept constant. This repeated for a series of different V_{GS} values. The transfer characteristics (Figure 2.16 b) is a plot of I_D as a function of gate source voltage (V_{GS}) for a given value of $V_{DS,}$ which was measured in similar method to the output characteristic with a LabVIEW program controlling the two Keithley SourceMeters. The V_{GS} is swept over a range of values both increasing and decreasing, with the measurement carried out for both a small and large drain voltage in order to record the drain current in the linear regime and the saturation regime (Figure 2.16 b). The sweep starts from a V_{GS} value of (0V) to the end value, to observe if any hysteresis exists in the I-V curve of the device. Measuring both the output characteristics and transfer characteristics, is a useful measure of device performance.

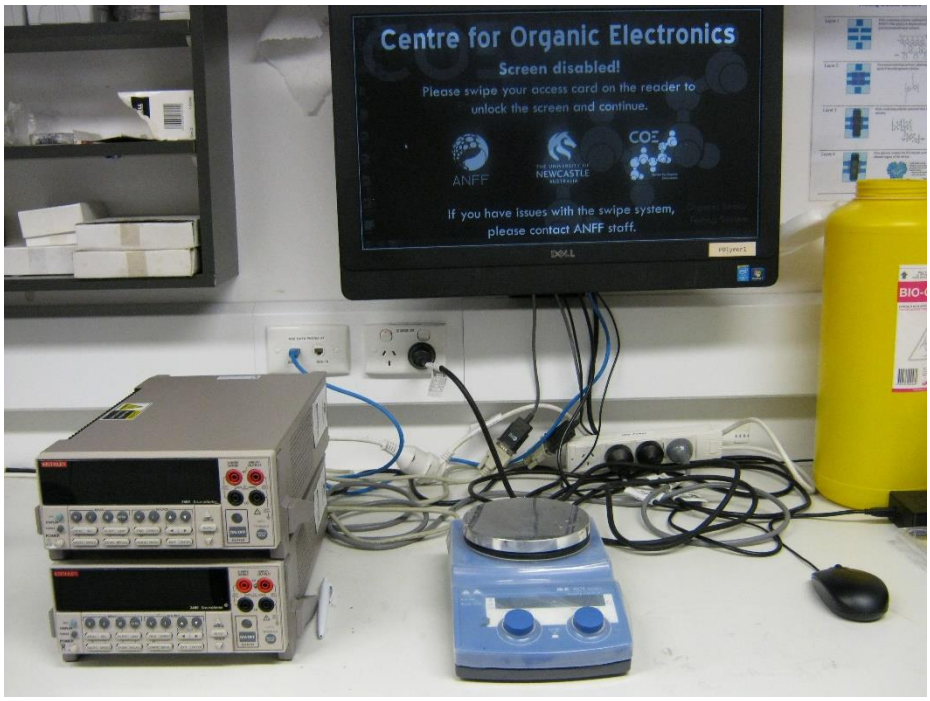

Figure 2.15: Keithley 2400 Source Meters used for transistors measurement.

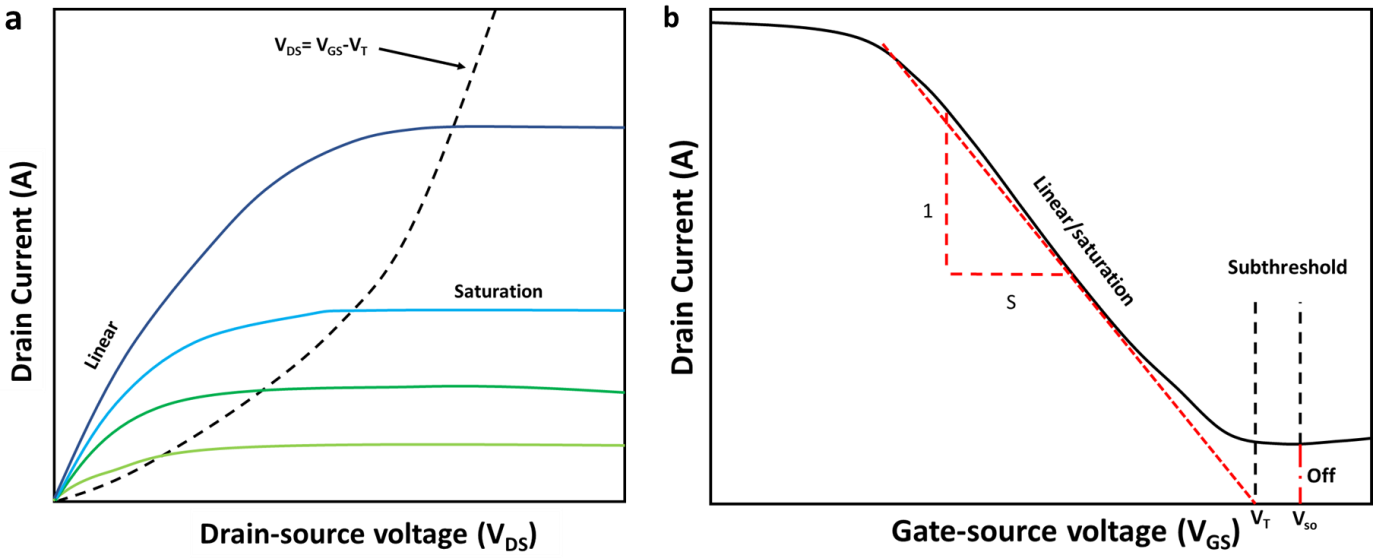

Figure 2.16: Schematic illustrating (a) The Typical output characteristic of the transistor, fabricated from P3HT solution in chloroform, (b) The transfer curve of the same device.

2.4.2 Sensor Characterisation

The electrical characteristics of the sensors were evaluated using two Keithley 2400 SourceMeters. The gate leakage current in all the devices was negligible. The output characteristics were obtained by measuring drain current as a function of drain voltage. In the experiments conducted to record the output characteristics, the voltage applied to the gate V_{GS} was (0.3 V). Figure 2.17 shows schematically the output characteristics of standard architecture device. The device transistor response was observed in both linear and saturation regions and V_{GS} modulated I_D. The transfer characteristic data were collected in a similar way, using a LabVIEW program controlling the two Keithley SourceMeters. Samples of deionized (DI) water and 0 mM glucose were deposited over the source (S) and drain (D) electrodes of the standard glucose sensor as described elsewhere in this thesis and the drain source current (I_{DS}) was measured versus gate voltage as represented by the schematic in Figure 2.18.

The I_{DS} - V_{GS} curves were measured until the response to the glucose analyte reached saturation. Change in the electrical output can be detected in the presence of the analyte, with the electrical output dependent upon the analyte concentration, composition and the OTFT bias conditions [216].

The goal of this chapter was not to describe the manufacture of the transistors and sensors using various materials and methods, but to provide a general description of how the transistor and sensor are fabricated as well as how they can electrically characterised, which will lay the foundation for optimisation of transistor and sensor utilisation.

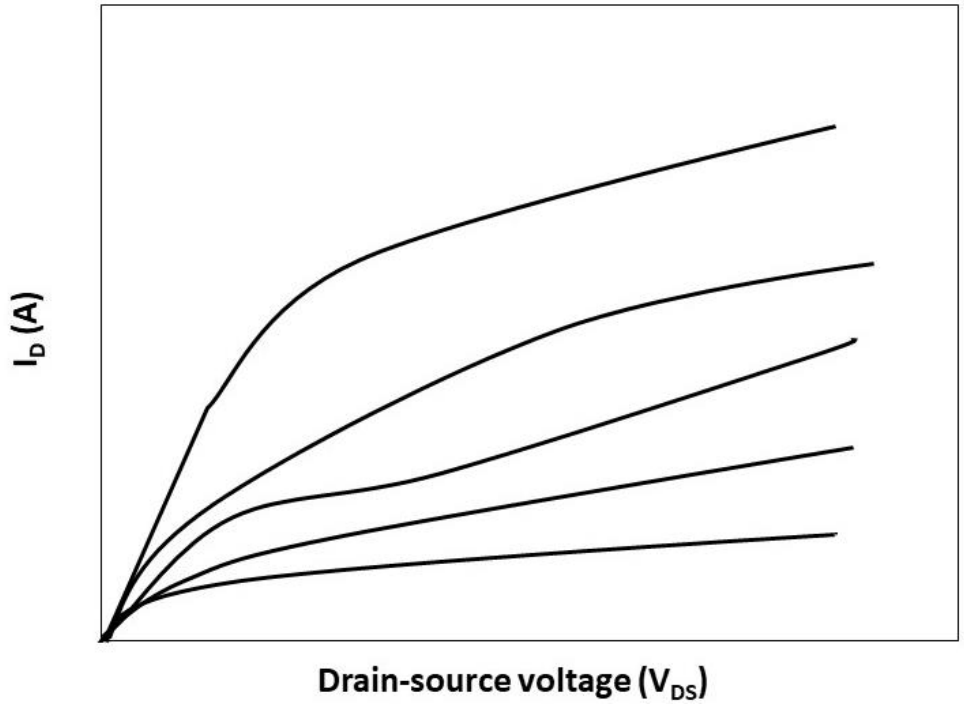

Figure 2.17: Schematic illustrating output characteristic of electrical sensor

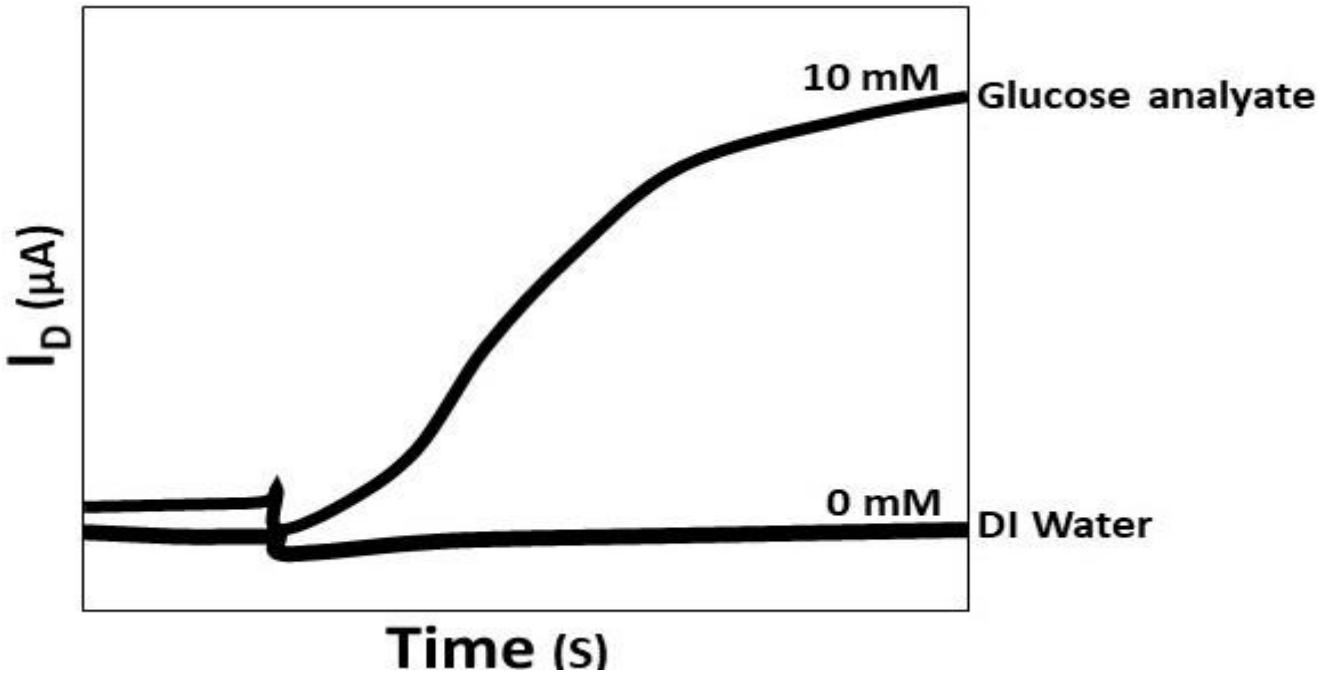

Figure 2.18: Schematic representing Current response versus time for water.

Chapter 3: Standard Fabrication and Figure of Merit

3.1 Introduction

The organic thin film transistor (OTFT) is now a mature technology that has shown impressive progress during the last twenty years. OTFTs are simple electronic devices consisting of three terminals, in which a voltage applied between two electrodes (the gate and source) controls the electrical current flowing between the source and drain electrodes. Because OTFTs are based on organic molecules, they can be flexible and biocompatible. As such, they are attractive for a vast number of applications such as smart cards, flexible displays and in particular, they are suitable for use in chemical and biological sensors [217-219]. OTFT-based sensors have already attracted attention in many applications such as *in-situ* medical diagnostics [108], environmental monitoring [220], detection of chemical warfare agents and food storage [216]. OTFTs have the unique ability to be engineered so as to allow analytes to be in direct contact with organic materials [221]. In contrast, in silicon-based technology sensing occurs at the gate or the gate / insulator interface and by indirect modulation of the drain current through capacitive coupling.

In addition, OTFTs have the advantage of being inexpensive to manufacture, due the ease of processability of the materials used. Consequently, they are increasingly being investigated for a wide range of new disposable healthcare products, using point of care (PoC) devices in order to allow people to diagnose or monitor illness very easily (in applications such as hygiene tests for life sciences, pregnancy tests and food handling [222].

Transistors can be used as building blocks in the design of sensors to transduce a given physical signal into an electrical current and/or to amplify a low-level electrical input signal. A traditional transistor-based sensor combines a sensing element with transduction and amplification giving the potential for high sensitivity [223, 224]. OTFTs have the significant advantage that they can be produced at low cost on flexible materials by utilising conventional printing techniques with a high device density [225, 226].

In recent years, there has been an increasing demand for glucose sensing devices due to the rise in diabetes worldwide, especially Type 2 diabetes mellitus. According to the estimates of the International Diabetes Federation, the number of sufferers of diabetes worldwide was 6.4 % in 2010, was estimated to be 7.5 % (374 million) in 2019 and is predicted to rise to 8.6 % (548 million) by 2045 [227, 228]. People suffering from both Type 1 and Type 2 diabetes require multiple daily measurements of their blood glucose concentration to regulate their daily activities and correctly administer insulin where required. However, conventional glucose monitors require that the users measure their blood glucose level (BGL) directly and this method relies on blood sampling by finger pricking. Unfortunately, this method is painful, causes anxiety and is inconvenient. Furthermore, repeated measurements to ensure glucose concentration levels are a big problem when dealing with children. In addition, Freckmann et al. has shown that many commercial blood glucose sensors lack accuracy in the low and high blood glucose concentration ranges causing major problems in the clinical treatment of patients [109]. Glucose sensing started in 1841 when the correlation between glucose in blood plasma and urine was established but the glucose measurements were inconsistent [110, 229]. In the 1960s the Ames reflectance meter (ARM) was developed as a method of measuring the blood glucose level. The ARM was based on a strip of cellulose containing glucose oxidise, peroxidise and chromogen. When blood

samples were deposited on the strip, the strip would change colour according to the amount of glucose in the blood. The method could be made quantitative by measuring the amount of light reflected from the strip using a photoelectric cell [230, 231].

Over the past 50 years the finger-prick method has remained the most widely-used method for glucose monitoring for sufferers of diabetes [232, 233]. A variety of techniques have been used to monitor blood glucose including fluorescence spectroscopy, infrared spectroscopy and surface plasmon resonance[110]. However, these techniques rely on correlation with direct blood glucose measurements to provide a quantitative measure of BGL. Additionally, the reliability and sensitivity of finger prick tests are limited by skin thickness and spectral signal to noise [110]. In addition, the finger-prick blood glucose test only provides information as a single snapshot in time. Therefore, periods of hyper- or hypoglycaemia can be missed with possible fatal consequences [234]. As a result, continuous glucose monitoring is advantageous in some circumstances.

Recently, many studies have focused on the development of organic-based devices for glucose sensing. The first organic semiconductor-based glucose sensor was demonstrated by Contractor et al. [235] in which glucose oxidase was immobilised in polyaniline as the active layer. A typical glucose sensor must be fast and accurate, with a reversible response to a change of glucose concentration being highly desirable for continuous monitoring of glucose levels.

In this study, we have optimised a glucose biosensor design based on an organic thin film transistor with a GOX modified Nafion charge transport layer for detection of glucose. This biosensor should provide non-invasive, fast, reliable, detection of glucose at low concentrations (0.01mM or less). In particular, in this chapter we will detail the fabrication and characterisation of OTFTs and

OTFT-based sensors saliva glucose determination. In particular, the chapter will detail the procedures for fabrication, characterisation and optimisation.

3.2 Transistor Characterisation

3.2.1 Structure

In this work OTFTs can be fabricated as one of four different architecture types consisting of three electrodes (gate, drain and source), an organic semiconductor layer and a dielectric layer. These architectures are named depending on the position of the source, drain and gate: bottom-gate bottom-contact, top-gate top-contact, top-gate bottom contact and bottom-gate top-contact (Figure 3.1). Each of these configurations has particular advantages and drawbacks and the materials and fabrication processes which are utilised, as well as the intended application, play a crucial role in determining the best architecture. The OTFTs which are presented in this thesis are all of a top-gate bottom-contact configuration. The main reasons for selecting this architecture (Figure 3.1 c) in this work is due to both the desire to modify the dielectric layer for use as a recognition element in sensors and the relative ease of manufacture with the fabrication techniques available. Later in this chapter, we will introduce a "staggered" (offset gate) structure which is a modification to the top-gate bottom-contact configuration for the purpose of transitioning the device to a glucose sensor [236, 237].

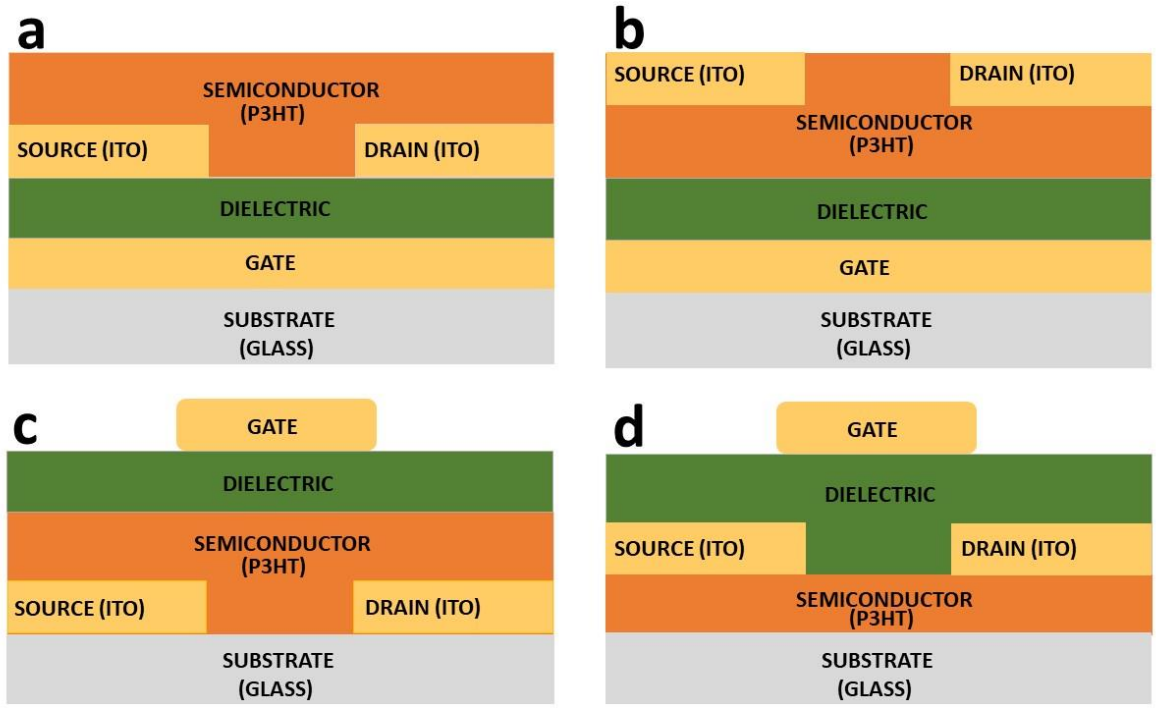

Figure 3.1: Different thin film transistors architectures: (a) bottom-gate bottom contact, (b) bottom-gate top-contact, (c) top-gate bottom-contact, (d) top-gate top-contact.

In this thesis, all OTFT and sensor devices were prepared on cleaned glass substrates with pre-patterned indium-tin-oxide (ITO) source and drain electrodes. A 100 nm thick P3HT layer was deposited by spin coating from a chloroform solution (20 mg/mL) as described in Chapter 2. This film was wiped out with a dry cotton tip soaked in chloroform to expose the source and drain electrodes (allowing enough space for the dielectric layer to entirely cover the P3HT layer whilst leaving the electrodes exposed Figure 3.2) and was then annealed for 10 minutes at 50 °C in air. A 500 nm thick PVPy dielectric layer was then deposited by spin-coating and patterned with ethyl acetate to again expose the electrodes (see Chapter 2 for further details). The P3HT/PVPy bilayers then were annealed for 10 minutes at 85 °C in air to remove excess solvent. Finally, a PEDOT: PSS (AL4083, Heraeus, used as received) gate electrode was deposited by drop-casting and the complete device was then dried

for 10 minutes at 50 °C in air to give a device with cross-section as shown in Figure 3.2. The steps of the fabricated OTFTs device can be seen in Figure 3.3.

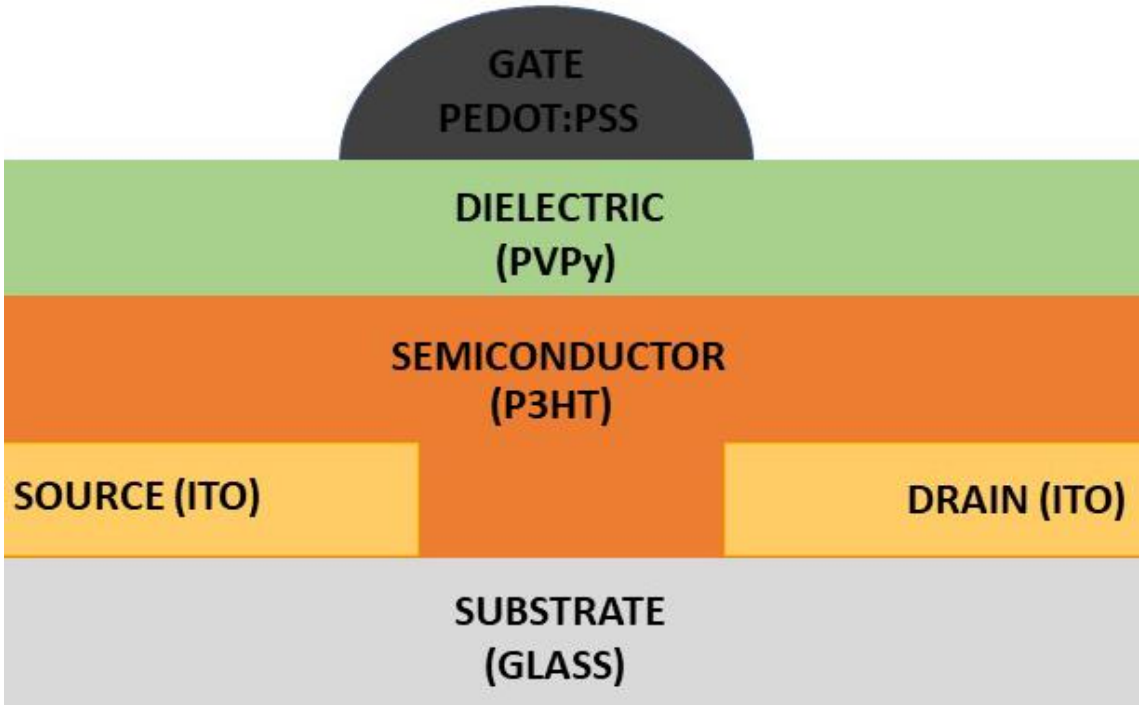

Figure 3.2: Basic device architecture and dielectric (PVPy) used.

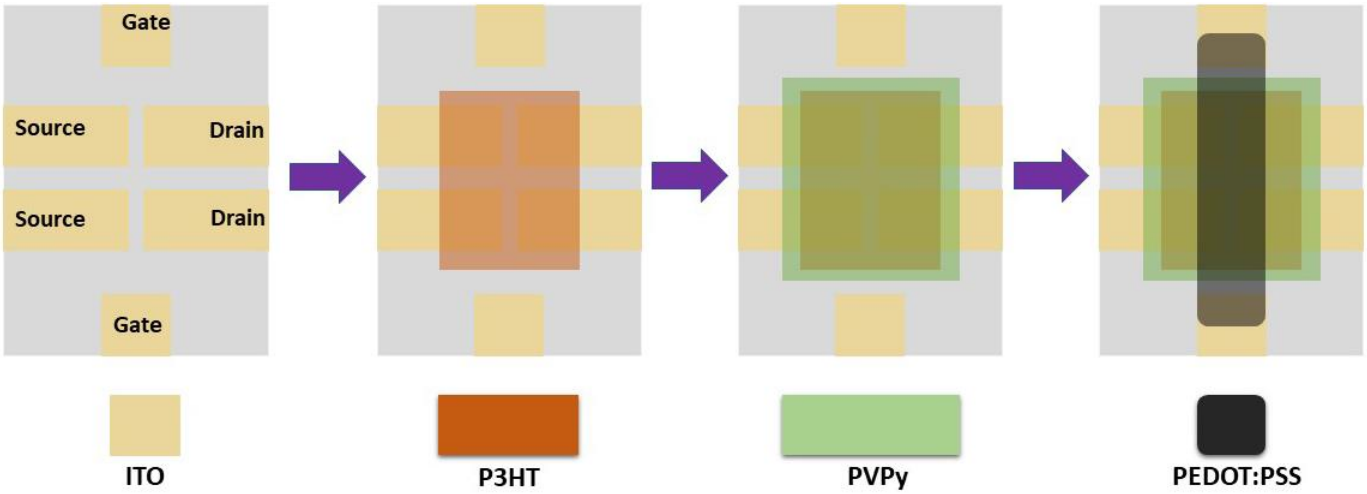

Figure 3.3: Schematic diagram shows steps of the fabricated OTFTs device.

PEDOT:PSS was initially used as the gate electrode in the OTFTs presented in this thesis due to its high conductivity and ability to be processed via a wide range of deposition techniques [238]. PEDOT: PSS has been widely used in sensors over the past decade [151, 239]. However, PEDOT:PSS is highly acidic, which can have a major impact on other materials in the device [240-242]. In particular, the protons that PEDOT:PSS introduces to the OTFTs can participate in the devices operation through movement within the dielectric layer and doping of the semiconductor between source and drain [243]. The chemical structure of PEDOT: PSS is depicted in Figure 3.4.

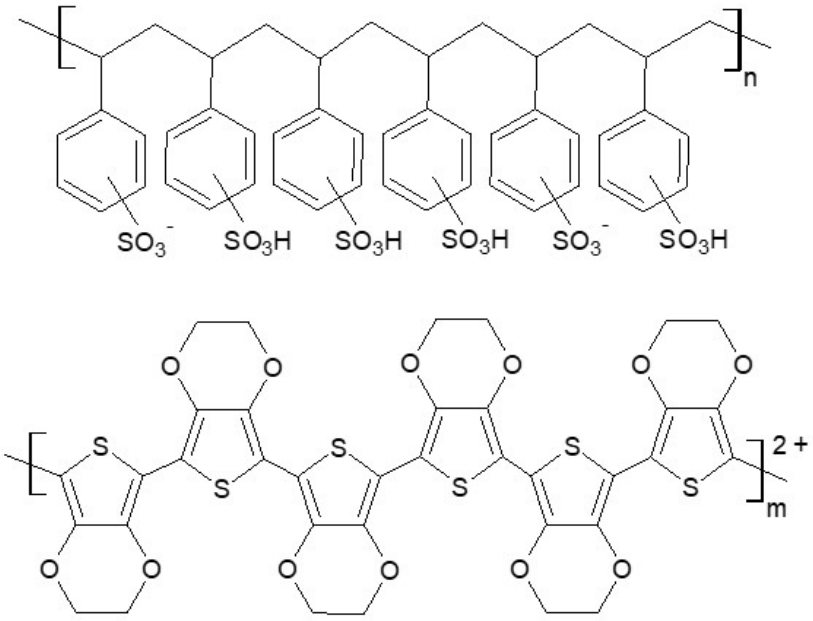

Figure 3.4: Chemical structure of the poly (3,4 – ethylenedioxthiophene – phene): poly (styrene) sulfonate (PEDOT: PSS).

The PVPy layer is physically situated between the PEDOT:PSS and the P3HT layer and acts as a dielectric between these layers. PVPy is weakly basic and thus acts as a proton acceptor and was chosen here to reduce the initial doping effect of the PEDOT:PSS on the P3HT, ensuring that the drain current (I_D) is as low as possible in the device's off state [244]. Specifically, a significant fraction of the protons is immobilised as pyridinium cations and therefore dopant anions

in the devices are immobilised due to ion pairing. It is important to use orthogonal solvents when depositing the dielectric and gate electrode layers in order to prevent dissolution of layers deposited previously [245].

3.2.2 Electrical Characterisation

There are two characterisation methods that play an important role in the performance evaluation of OTFTs: the output characteristic and the transfer characteristic. In the output characteristic, the drain current (I_D) is plotted as a function of the drain-source voltage (V_{DS}) across a range of gate-source voltage (V_{GS}) values (as seen in the Figure 3.5). Output characteristics of the transistors were recorded using two Keithley 2400 SourceMeters controlled by a program written in the National Instruments Lab VIEW development environment. For a given value of V_{GS}, V_{DS} was swept over a specified range (typically between 0 V and -2 V) and both I_D and I_G were recorded. We observe that the magnitude of I_D increases monotonically with V_{DS} and that there are linear and saturation regions in the output characteristic (as expected for a transistor [246]). The transfer characteristics of a standard P3HT/PVPy/PEDOT:PSS device were also obtained from the output characteristics at V_{DS} = -1.4 V, for V_{GS} = 0 to -1.5 V. The gate leakage current (I_G at I_D = 0 A) was also recorded at V_{DS} = 0 V to -1.9 V (Figure 3.5).

In these measurements it is also important to record the gate (or leakage) current (I_G) values to determine the amount of current that flows through the dielectric layer (PVPy) of the devices and be able to compare the I_D to I_G ratio to give an indication of how well the dielectric is performing as an electrical isolator. We observe that both I_D and I_G nonlinearly decrease as V_{GS} decreases, with I_G (~10^{-8} A) being about an order of magnitude smaller than I_D (~10^{-7} A).

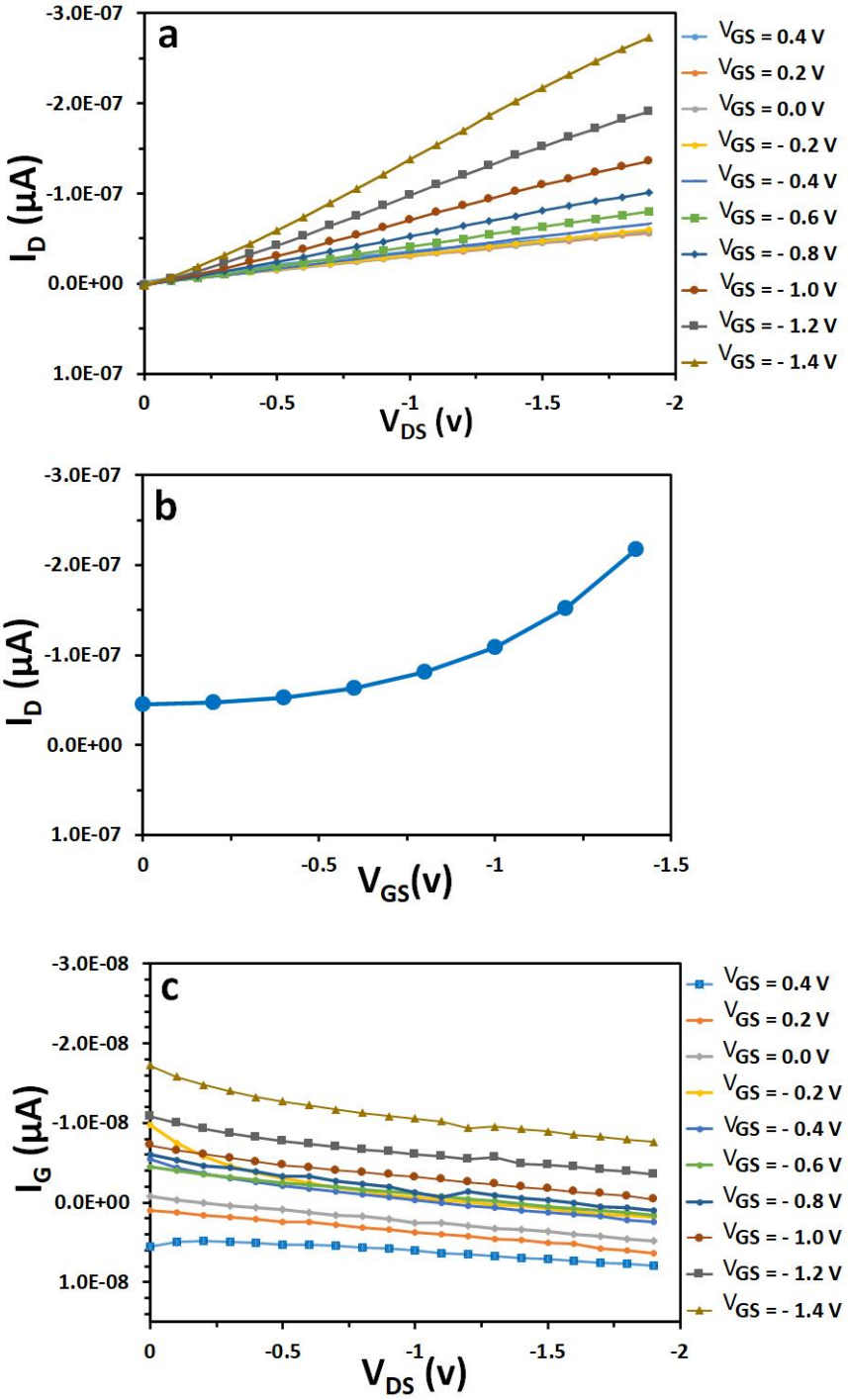

Figure 3.5: Standard OTFTs device (PVPy dielectric) with PEDOT: PSS gate electrode. (a) Output characteristic with (V_{DS}) = 0 V to -1.9 V and (V_{GS}) = 0.4 V to -1.4 V (b) Transfer characteristics (V_{GS}) = 0 V to -1.5 V and (V_{DS}) = -1.4 V. (c) Gate leakage with (V_{DS}) = 0 V to -1.9 V and (V_{GS}) = 0.4 V to -1.4 V.

3.3 Modifying the Transistor Architecture

The aim of the work presented in this section is to optimise the method of modifying an existing OTFT architecture to create a device which can be used for glucose sensing by incorporating the enzyme glucose oxidase (GOX). In order to achieve this aim, the standard OTFT structure as described above was modified as follows:

The PEDOT: PSS gate electrode was replaced with the proton transport material Nafion. Since we intend to incorporate GOX into the devices, having an acidic material such as PEDOT:PSS situated in this position would have two negative effects. Firstly, the acidity of the PEDOT:PSS could act to denature the enzyme and, secondly, since the mechanism of sensing will rely on proton generation, the acidity of the PEDOT:PSS could impede the response of the devices to glucose [247]. With this change, the devices become more accurately described as offset-gate electrochemical transistors as the Nafion layer is not a gate electrode in the traditional sense and the ITO pad situated adjacent to the device is now the gate electrode of the device. Secondly, the PVPy dielectric was replaced with a poly-4-vinylphenol (PVP) dielectric material. PVPy is a weakly basic material and as such acts to inhibit proton transport in the device [248]. Again, since the mechanism is proton driven, the presence of PVPy could reduce the apparent sensitivity to glucose. By contrast, PVP is neutral (very weakly acidic) and can facilitate proton transport making it suitable for inclusion here. Finally, GOX was added to the device in the area above the source-drain channel to facilitate selective glucose detection.

3.3.1 Replacing PEDOT with Nafion

Whilst it is a high-performance electrode material, PEDOT:PSS has several disadvantages for this sensing application. In particular, PEDOT:PSS is acidic and is known to adversely affect acid-sensitive materials [249, 250]. As such, PEDOT:PSS may not be suitable for use in a biosensor in which it will be in direct contact with the biological recognition element, which may be pH sensitive. Furthermore, PEDOT:PSS may not be suitable for devices which rely on the generation of protons as a transduction mechanism between analyte and signal, such as those presented in this thesis. If the biological recognition element (i.e. GOX) is to be incorporated onto or in the device, the surrounding materials must be capable of conducting protons to the semiconductor interface but also be biocompatible with the enzyme.

Previous studies in organic photovoltaic (OPV) devices have shown that replacing PEDOT:PSS with Nafion (5 wt. % in lower aliphatic alcohols and water, contains 15-20% water, Sigma-Aldrich) improves device stability because of the lower acidity of the Nafion [251, 252]. In this work, we replaced PEDOT: PSS with Nafion to create an offset-gate transistor where an ITO electrode situated adjacent to the rest of the device is the gate electrode (Figure 3.6). Nafion was chosen to replace PEDOT:PSS because it is more compatible with biological recognition elements due to its neutral pH and OTFTs were fabricated and tested using this new structure. Figure 3.7 shows the output characteristics at V_{DS} = 0 V to -1.9 V, transfer characteristics at V_{GS} = 0 V to -1.4 V and the gate leakage current at V_{DS} = - 1.9 V.

When compared to the PEDOT: PSS device characterised in Figure 3.5, the Nafion device shows an order of magnitude increase in the I_D values recorded (from ~10^{-7} to 10^{-6} A), whilst the gate current (I_G) remains almost the same

across the comparable V_{GS} range. In addition, the output characteristics show a notable saturation region at V_{DS} ranging from ~-0.25 V at V_{GS} = 0V to ~-1.25 V at V_{GS} = 2.0V. The ten-fold increase observed in I_D, seen by comparing Figure 3.5(a) to Figure 3.7(a), is promising for increased sensitivity of subsequent sensors based on this architecture.

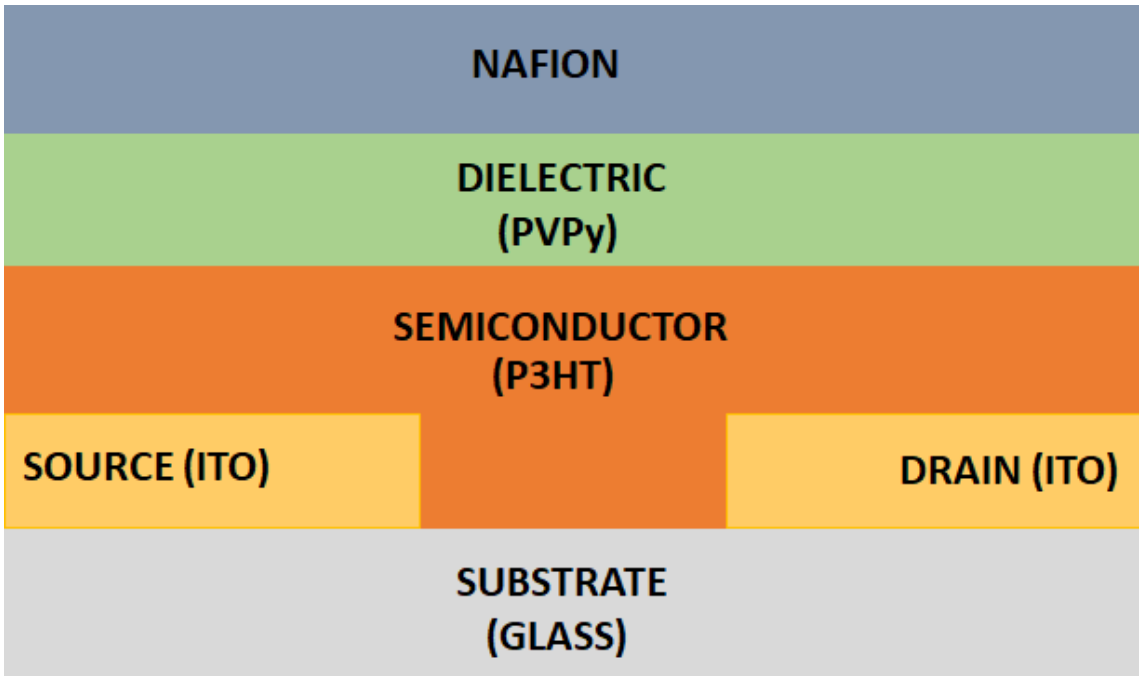

Figure 3.6: The off-set gate structure of device with Nafion.

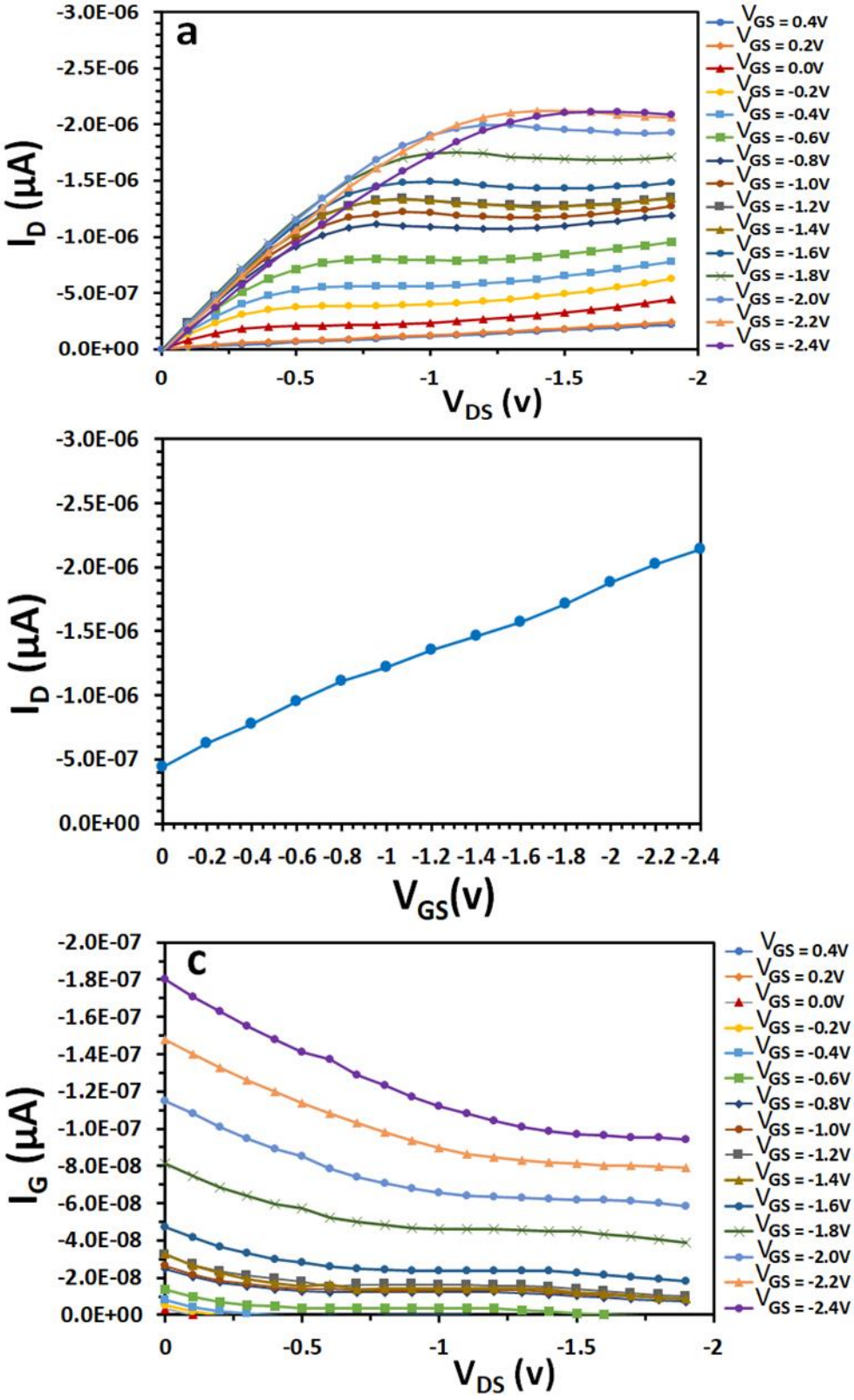

Figure 3.7: Standard OTFTs device (PVPy dielectric) with Nafion gate electrode. (a) output characteristic with (V_{DS}) = 0 V to -1.9 and (V_{GS}) = 0.4 V to -2.4 V. (b) Transfer characteristics with (V_{GS}) = 0 V to -2.4 V and (V_{DS}) = -2.4 V. (c) Gate leakage current with (V_{DS}) = 0 V to -1.9 V and (V_{GS}) = 0.4 V to -2.4 V.

3.3.2 Replacing PVPy with PVP

Because our final target sensor architecture relies on the generation and transport of protons through the device, replacing PVPy with a dielectric material which is a better proton conductor was also identified as a key step towards the final sensor design. This work is key to the creation of effective organic thin film sensor and acts as a stepping stone in the optimisation of such devices. Poly (4-vinylphenol) (PVP) was chosen as a dielectric material to replace PVPy. PVP is a very poorly acidic dielectric layer which more freely allows internal movement of protons as compared to PVPy where the basic pyridyl group introduces chemical interactions will have an effect on proton movement and therefore device performance. The chemical structure of PVP and PVPy are shown in Figure 3.8. The standard devices of PVP and PVPy are shown in Figure 3.9. OTFTs were fabricated, as per the standard procedure, and tested using this new structure, with a PVP layer of thickness ~560 nm replacing the PVPy layer.

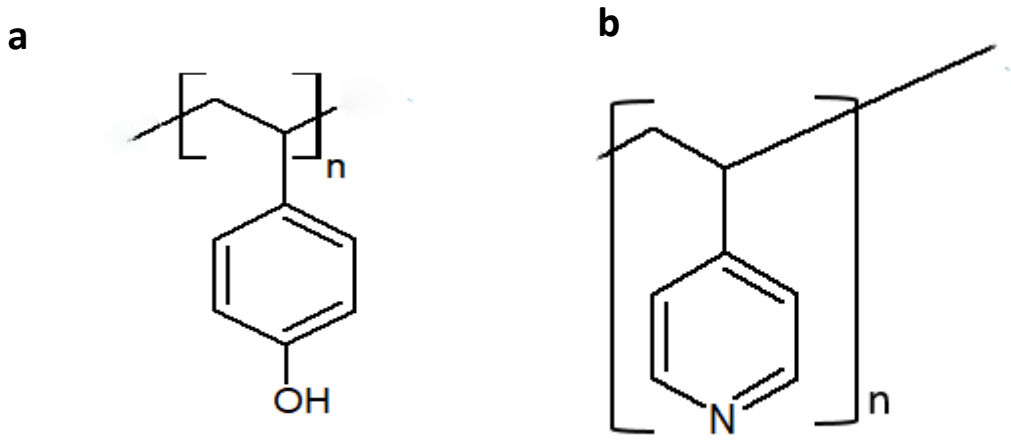

Figure 3.8: Chemical structure of PVP (a) and PVPy (b).

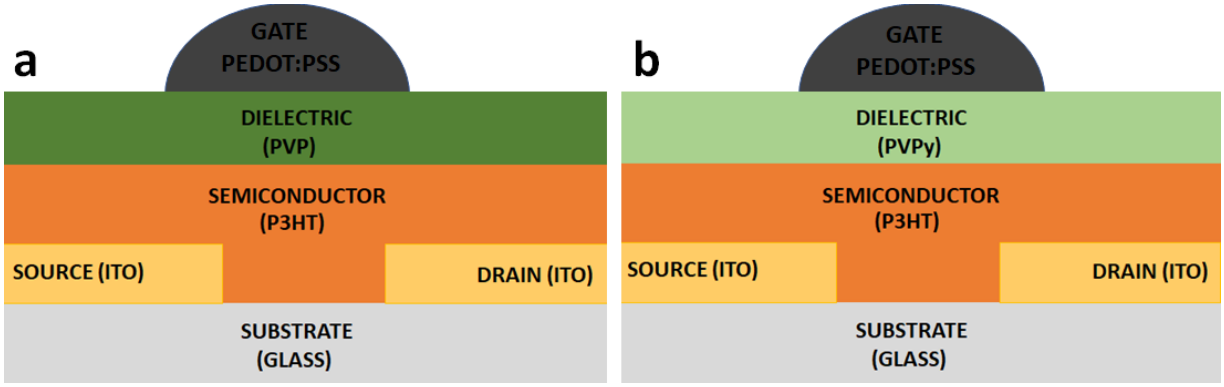

Figure 3.9: Standard OTFTs device of materials used. (a) (PVP dielectric), (b) (PVPy dielectric).

Figure 3.10(a) shows the output characteristic of a typical PVP OTFT measured in air and shows that there is current modulation within the whole range of gate voltage V_{GS}. For these values of V_{DS} a saturation region is not observed in the data. In general, the I_D values in these devices are higher than those for the PVPy devices (more than an order of magnitude greater), reflecting the greater mobility of protons in this architecture.

Figure 3.10 (b) shows the transfer curves, from the same device measured in ambient air, that were obtained from the output characteristics at V_{DS} = -1.9 V. This data shows that there is higher modulation of the output current between V_{GS} = 0 and -1.4 V. Sandberg et.al. have reported that current modulation in P3HT and PVP based ″HIFETs″ is prevented when measuring in a dry nitrogen medium with a gold gate but that modulation does occur under ambient conditions, as observed here [243, 253]. Nonetheless while these devices operate at 0 V to -2V and have maximum output currents (I_{ON}) comparable with conventional OFET operating at many tens of volts [254, 255]. The transfer curves for all devices operated from 0V to -1.4 V was consistent with the low voltage of P3HT/PVP layers in non-cross-linked hygroscopic transistors [243, 256, 257]. Notably, each of these transistors demonstrate large gate leakage currents of the order of 10 % of the drain current which highlights the importance of the contribution of ion current to the devices electric current

[244]. Gate leakage current was measured at at V_{DS} = -1.9 V. The high leakage current as a result of ionic species in the active leads to a modulation ratio of less than 50, but adds to the current, increasing I_D.

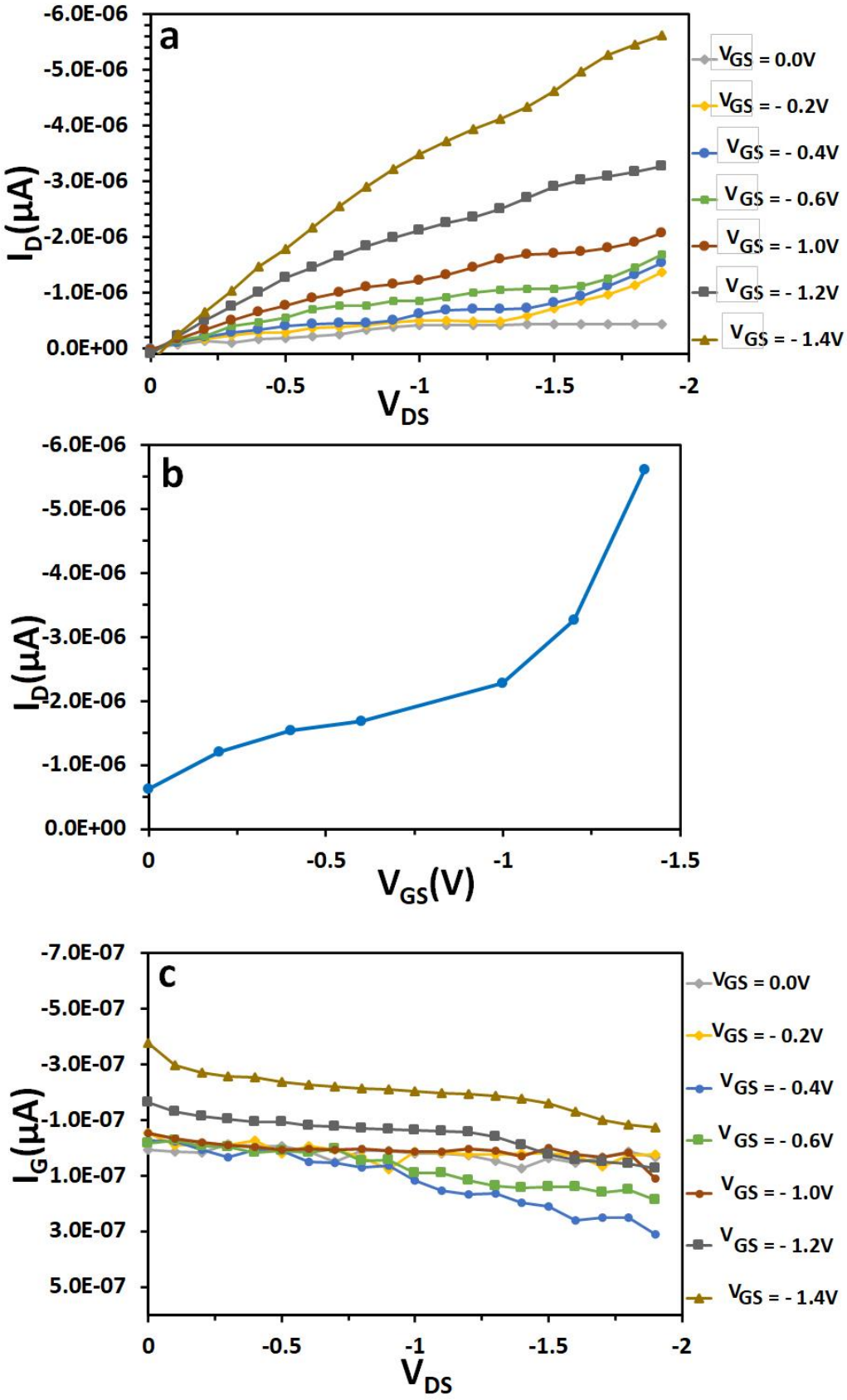

Figure 3.10: (a) Standard OTFTs device (PVP dielectric) with PEDOT: PSS gate electrode. (a) output characteristic with (V_{DS}) = 0 V to – 1.9 V and (V_{GS}) = 0V to – 1.4 V (b) Transfer characteristics with (V_{GS}) = 0 V to - 1.4 V and (V_{DS}) = - 1.4 V. (c) Gate leakage current with (V_{DS}) = 0 V to – 1.9 V and (V_{GS}) = 0 V to -1.4 V.

3.3.4 Introduction of GOX to the sensor structure

The final step in the development of the OTFT structure as a glucose sensor is the incorporation of GOX into the device structure. GOX was introduced into the Nafion gate electrode to trap the enzyme within the device structure. Several studies have been carried out to study the effect of GOX embedded in a Nafion film. Sirois was one the first researchers who presented results for embedding GOX in Nafion [258]. She drops cast suspensions of GOX in Nafion onto ITO-on-glass substrates, which were used as working electrodes in a three terminal electrochemical cell. Different concentrations of solutions of glucose were utilized in a phosphate buffer solution as the electrolyte in the cell. The GOX embedded in Nafion showed potential as a sensing element. Elkington et al. [259] developed a glucose sensor by embedding GOX enzyme within Nafion films which were then incorporated into a transistor design. The authors propose that the glucose sensing is based on protonic doping of the transistor channel and demonstrated that the main determinant of the device response times was the diffusion of glucose. Their findings are evidence of a proof of concept for low-cost printed biosensors for glucose. The study presented in this chapter attempts to expand on the previous work by embedding Nafion with GOX on OTFTs to obtain signal transduction and to achieve optimal glucose sensing performance.

Our goal here is to show that incorporation of GOX does not adversely affect the electronic function of the device and that it can therefore be used as the basis for a glucose biosensor. The standard sensor architecture which we used in this work was ITO as source and drain electrodes, a semiconductor layer of P3HT, dielectric layer of PVP and Nafion with GOX embedded as a gate electrode, as shown in Figure 3.11 and Figure 3.12. Early work by Elkington et

al. showed that quantitative glucose detection could be realised using OTFT devices based on the related architecture; poly(3,4ethylenedioxthiophene) P3HT/PVP/Nafion:GOX [260].

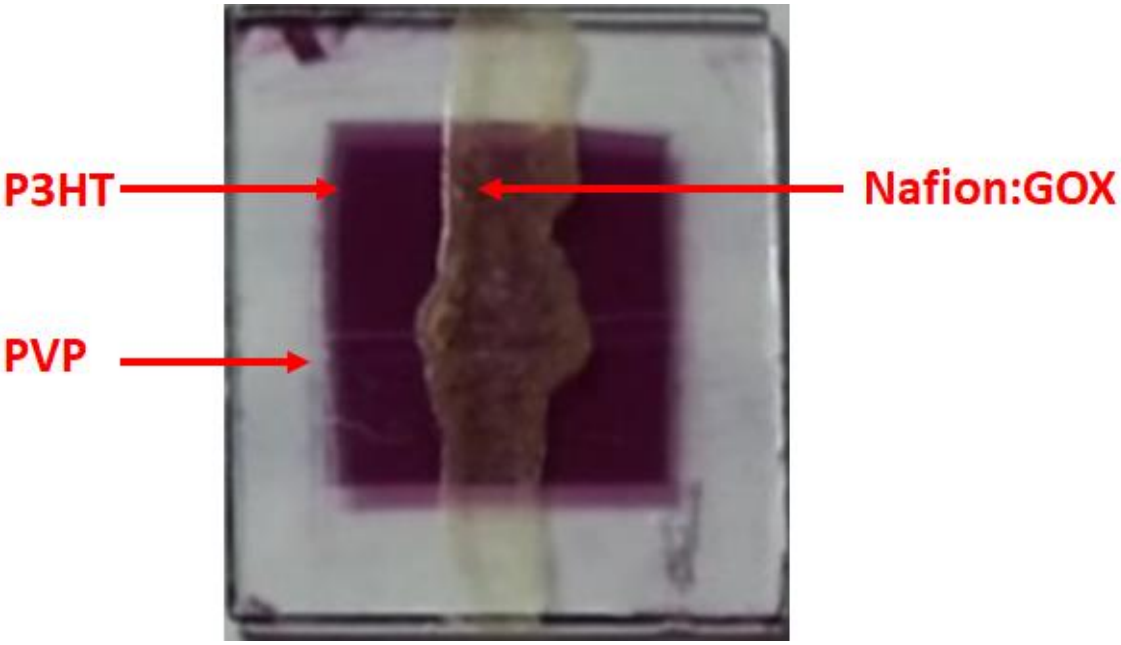

Figure 3.11: Photo of OTFTs based glucose sensors (P3HT/PVP/ Nafion:GOX)

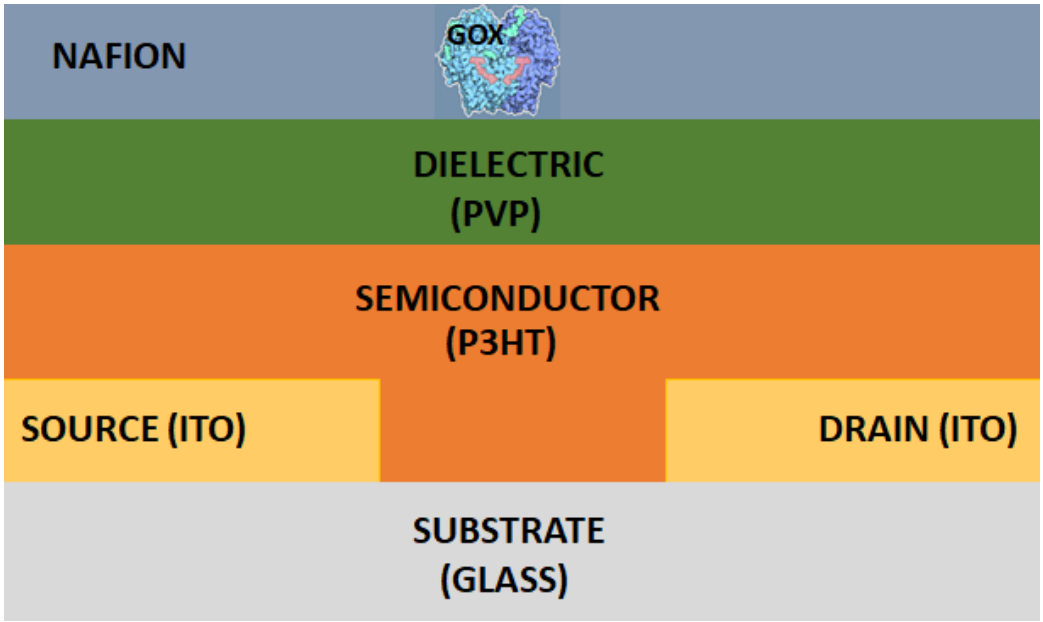

Figure 3.12: Schematic representation of the cross section view of the (P3HT/PVP/ Nafion:GOX).

As previously mentioned in Chapter 2, GOX has many extremely useful favourable attributes in a sensor, such as high sensitivity, low cost and good

thermal stability [192]. The high biocompatibility of glucose oxidase with some organic materials is the main reason for using the enzyme as a catalyst in the oxidation of glucose in our work. It is important to immobilise the GOX on the electrode surface when fabricating the glucose biosensor to maximise sensor output, although problems can arise due to the embed redox centre becoming inaccessible to the glucose analyte [197]. The glucose oxidase catalyses the oxidation of glucose to gluconolactone and hydrogen peroxide [28]. This catalytic process is explained in Chapter 2 Section 2.1.5.

3.4 OTFTs as a saliva glucose sensor

In this work, the Nafion:GOX films were prepared by drop–casting mixtures of 20 mg/mL GOX in as-received Nafion solution on to the ITO/P3HT/PVP stack in the region between the source and drain electrodes and connected to the gate electrode. The film is then allowed to dry at 50 °C. Having discussed in Section 3.3.3 that addition of GOX to the organic transistor stack should not adversely affect device performance, the glucose sensor was now systematically tested with glucose samples made from D-(+)-glucose (Sigma-Aldrich G5767) in Milli-Q purified water (18.2 MΩ cm^{-1}) across the known range for salivatory glucose in humans (8 to 200 mM). For all subsequent glucose sensing experiments in this thesis, the same materials were used to prepare glucose solutions.

For the detection of glucose, 10 µL of analyte solutions with different concentrations were dropped above the source-drain channel and the current was monitored as a function of time for a fixed V_{DS}. An increase in the conductivity of the semiconductor proportional to the glucose concentration is reflected by a corresponding increase in I_D. Measurements were conducted on the same day as fabrication so that variation in devices response because of

fabrication conditions, humidity and temperature were minimised. An initial period of 300 s was allowed prior to analyte addition to ensure stabilisation of the sensor device. The device output was recorded for 1500 s after glucose addition to allow for glucose diffusion within the device, reaction with the enzyme and subsequent doping of the source-drain channel. After this time, it was noted that I_D had reached a plateau maximum in the majority of experiments, resulting in total accounting of the analyte response.

In each case, a significant increase in current at higher glucose concentrations is observed, especially at 10 mM, the highest analyte concentrations. This observation is consistent with previous work which has shown large increases in current and faster response of devices and diffusion of enzyme on the surface at 10 mM glucose [10]. A linear response of current has previously been shown for glucose concentrations over 1 mM [11-13] with the current beginning to increase for glucose concentrations above 0.1 mM [14]. A significant advantage of the OTFTs architecture utilised in this experiment is its low voltage operation (<1 V) which is well suited for operating with aqueous analytes, since water undergoes oxidation at voltages above 1.2 V [15, 16].

3.4.1 Response of sensor to glucose concentration (current vs time)

This study is a culmination of the creation of an effective prototype glucose sensor for monitoring applications and acts as a steppingstone in the optimisation of fabricating conditions for such devices.

The work presented here demonstrates a standard sensor architecture comprising (ITO) source and drain electrodes on glass substrates. The channel width and length are 20 μm and 3 mm, respectively. A poly(3-hexylthiophere)

(P3HT) semiconductor layer was spin-coated (60 s at 2000 rpm) from a solution in chloroform at a concentration of 20 mg/mL to give a layer thickness of 113 nm. A poly(4–vinylphenol) (PVP) dielectric layer was the deposited by spin-coating (60 s at 2000 rpm) from a solution in in ethanol at a concentration of 80 mg/mL to a layer thickness of approximately 500 nm. Finally, a drop cast layer of Nafion mixed with GOX was deposited as shown in Figure 3.13. In order to test the effectiveness of the prototype glucose sensor described in section 3.3.3 to detect glucose across the saliva glucose range, a series of experiments were conducted. A series of current versus time plots for different glucose concentrations (0 mM, 0.01 mM, 0.1 mM, 1 mM and 10 mM) were recorded. The device architecture is depicted in Figure 3.13.

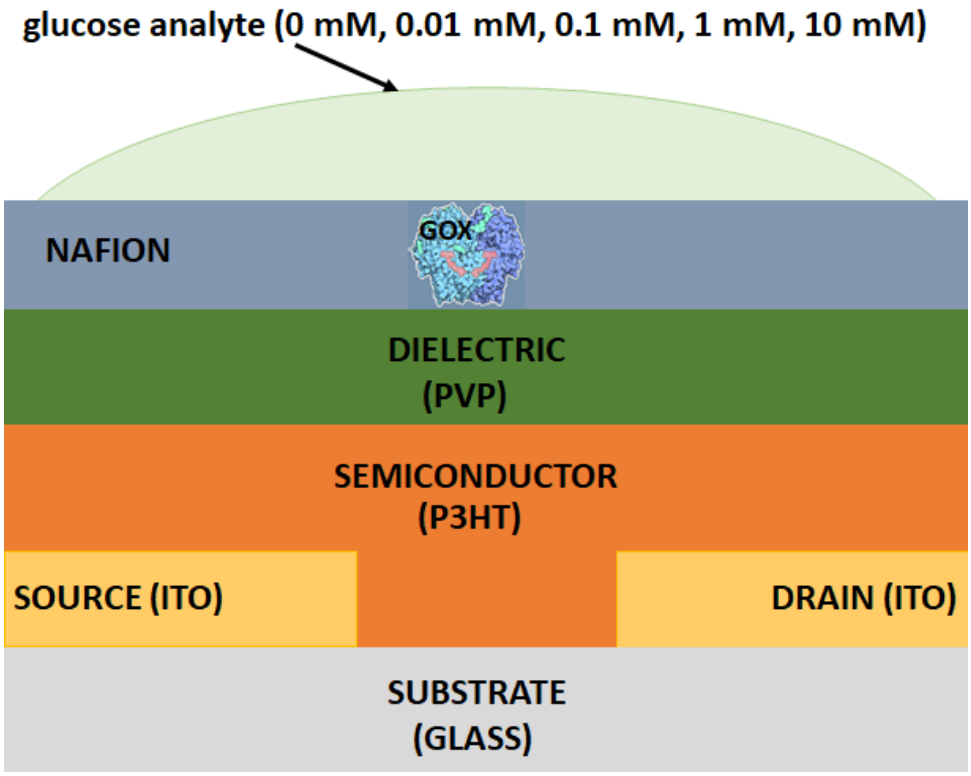

Figure 3.13: Device arcticture of ITO /P3HT /PVP/ Nafion:GOX

Each experiment was conducted as follows. Initially, the drain current of the devices was recorded for 300 seconds to allow the native device response to stabilise. A 10 µL drop of analyte was then placed on the Nafion:GOX electrode

in order to measure the response of the P3HT/PVP/Nafion:GOX device. V_{DS} was set at -1 V and V_{GS} at -0.3 V. The device drain current (I_D) was then monitored as a function of time [260]. The device voltages were chosen to ensure three important points:

1. above the threshold for reduction of H_2O_2 to produce H^+
2. below the threshold for oxidation of water
3. and within the relatively flat saturation region of the P3HT/PVP/Nafion:GOX device.

The devices were then exposed to samples of glucose in DL water at concentrations of 0 mM, 0.01 mM, 0.1 mM, 1mM, and 10 mM glucose and monitoring of the drain current was continued for a further 1500 seconds.

Our observation was that when the analyte solution was added at t = 300 second there was an initial drop in current followed by an increase as the glucose reacts. (Figure 3.14 a-d).

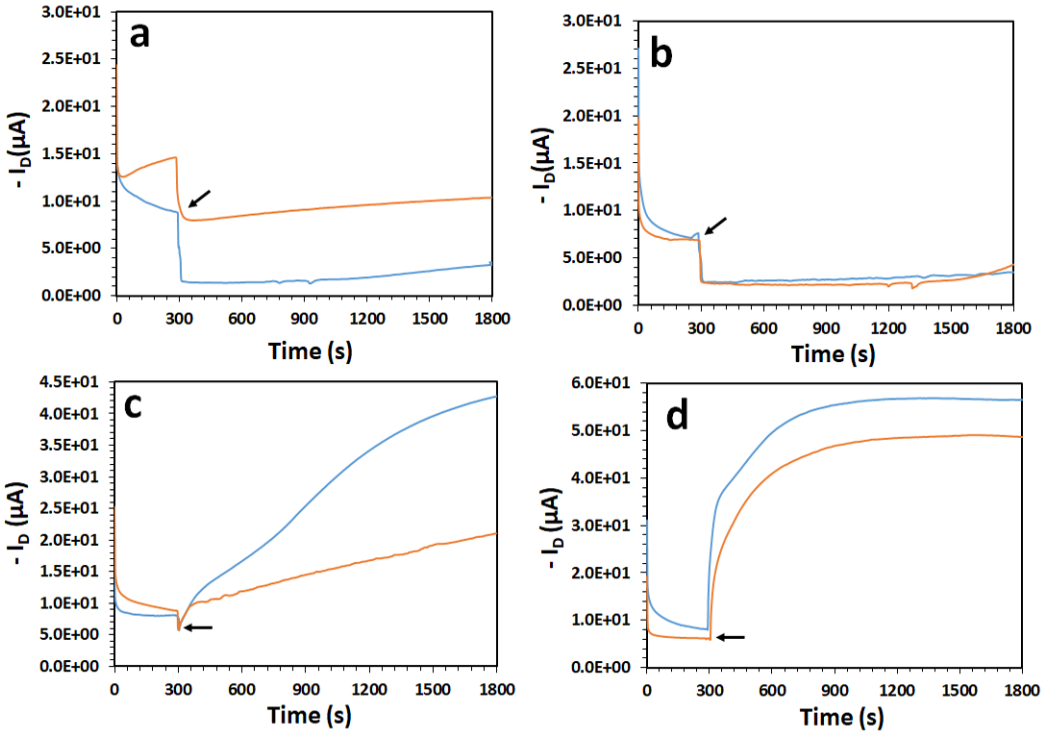

Figure 3.14: a, b, c and d show duplicate current (- I_D) vs time outputs for these devices for the 0.01, 0.1, 1 and 10 mM glucose solutions, respectively. Arrows are represented the event at 300s.

Addition of the analyte results in an initial drop in current followed by an increase as the glucose reacts. The observed decrease in I_D upon the addition of the analyte or deionised water suggests that the initial action of the addition of the analyte solution is a dedoping of the channel material. This observation also confirms that the operating of the OTFT sensor is below the threshold for oxidation of water to H_2O_2 and that it is not until the oxidation of glucose by the GOX that peroxide is generated and an increase in I_D observed. It is noticeable that duplicate measurements show not only variance in the device response to the analyte (small for the low concentration glucose samples (~ 1 µA) but increasing for the higher concentration samples (~20 µA at 1 mM glucose and ~ 8 µA at 10 mM glucose)) but also significant differences in the initial pre-analyte addition I_D value. This is indicative of device variations in the device fabrication.

Figure 3.15a shows typical 0.01 mM, 0.1 mM, 1 mM, and 10 mM responses for the same device structure. Examination of the current prior to analyte addition shows the variance in the stable current for the native device. This variance is of the order of ~0.3 μA for the devices shown, which is insignificant compared to the responses of the 1 mM and 10 mM analyte solutions but is comparable to the total responses of the 0.01 mM and 0.1 mM analyte solutions. The experiments were carried out on the same day so that observation the variations in device response cannot be attributed to the ambient conditions in the laboratory such as humidity and temperature. Consequently, in order to mitigate this variance, the responses were normalised to 0 μA at t = 380 seconds, just prior to addition of the analyte (Figure 3.15b). The plots clearly show that the magnitude of I_D increases systematically with increasing glucose concentration with the output current ranging from a few μA to > 50 μA across the range of glucose concentrations measured.

At 10 mM the increase is rapid, and a plateau current is reached after approximately 600 seconds. For the lower concentrations a plateau current is not reached, and I_D continues to increase across the full duration of the monitoring. The slow stabilisation of the I_D signal is an area that may need to be addressed and improved, if $I_{D(plateau)}$ or $I_{D(max)}$ is to be used as the device output, in order to minimise device response time. The plots show that the variance in the output current is small for the low concentration glucose samples (~ 1 μA) but increase for the higher concentration samples (≥10 μA at 1 mM and 10 mM glucose).

Figure 3.15c shows a calibration curve for the chosen glucose concentrations obtained at an experiment time of 1800 s from the normalised data presented in Figure 3.16b. The plot shows a sigmoidal monotonically increasing relationship between glucose concentration and I_D at 1800 s. The sigmoidal shape suggests poorer sensitivity of the sensor at concentrations below 0.1 mM and also

suggests that a device saturation limit is approached as the glucose concentration approaches 10 mM. Saturation could be a result of a doping limit for the P3HT channel material (where further addition of protons no longer modifies the channel conductivity) or alternatively be a result of total consumption of the glucose analyte. However, since the lower concentration analytes do not reach a plateau (or do so slower that at higher concentrations) total consumption of the analyte is unlikely.

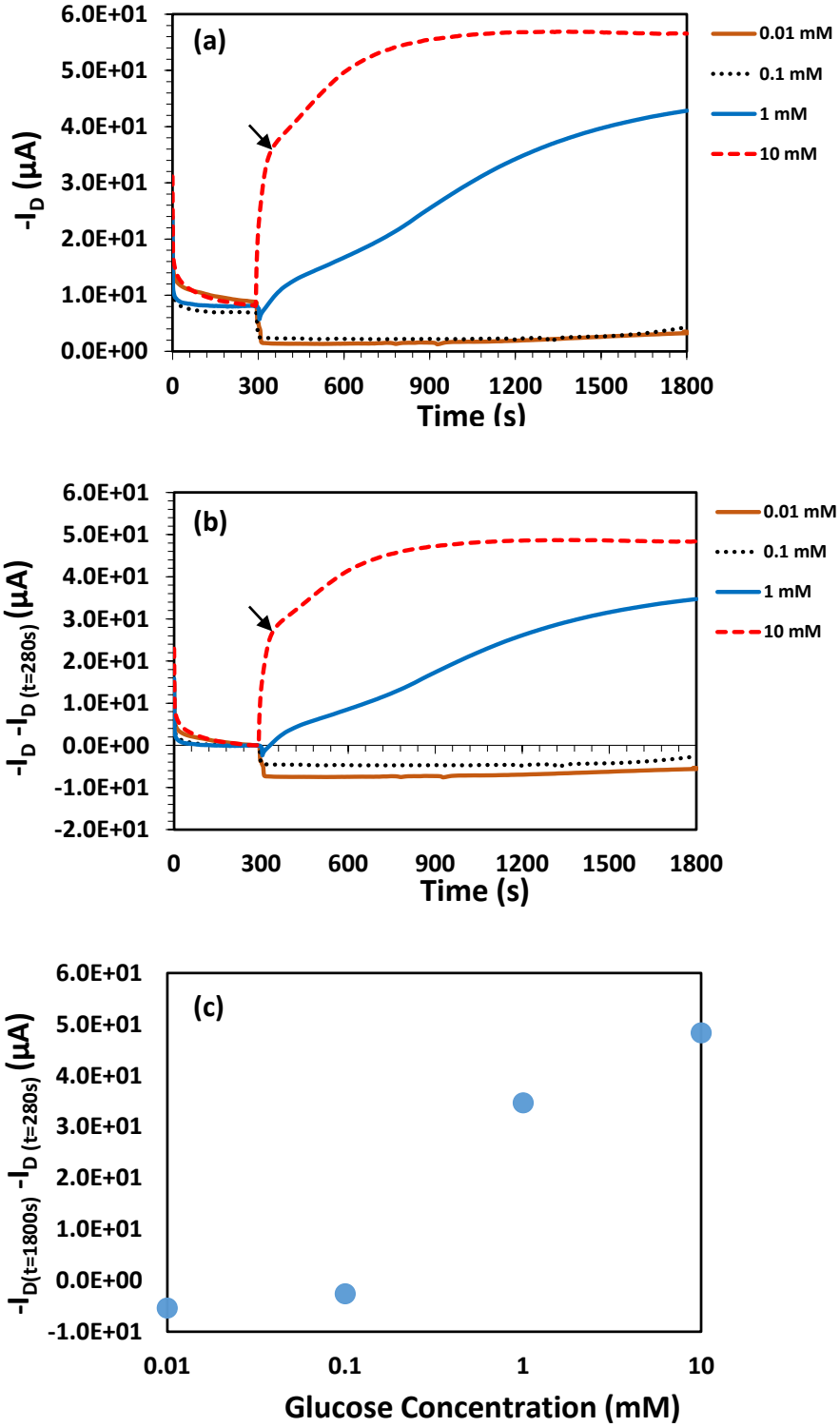

Figure 3.15: (a) Typical 0.01 mM, 0.1 mM, 1 mM and 10 mM current-time responses for the ITO/P3HT/PVP/Nafion:GOX device structure, whilst (b) shows the same data normalised to 0 µA at t = 280 second, just prior to the addition of the analyte. (c) shows the change in current after 1800 s as a function of glucose concentration. Arrows are shown the plateau current location on the curve.

The generation of charge carriers by the reaction of glucose with the GOX enzyme plays a significant role in the current generated in hygroscopic OTFT devices and is produced by the diffusion of protons through the dielectric layer to dope the channel material [244, 260, 261]. Glucose diffusion through the Nafion gate is initially slow and it is then rapidly oxidised at the GOX to produce gluconolactone and H_2O_2 [262] (Equation (1)).

$$\text{Glucose} + O_2 \rightarrow \text{gluconolactone} + H_2O_2 \qquad (1)$$

The peroxide produced is then rapidly electrochemically oxidised into protons, oxygen and electrons at the operating voltage of the device.

Above a threshold voltage (~ 0.7 V versus a standard calomel electrode) hydrogen peroxide oxidises as described in the following equation (2):

$$H_2O_2 \rightarrow O_2 + 2H^+ + 2e^- \qquad (2)$$

The generated protons then move under the electric field of the device to the channel material where doping of the conducting polymer occurs.

This mechanism is further discussed in Chapter two but repeated to assist understanding.

Thus, proton generation and diffusion to the dielectric – semiconductor interface plays a significant role in the mechanism of these OTFT sensing devices [34] (as shown in Figure 3.16: a, b and c). As such the PVP dielectric plays a critical role in modulating the current (I_D) in these devices. It is proposed that for PVP (a highly hydrated sol-gel material) the enzymatically produced protons will transfer from across the PVP to the PVP/P3HT interface by the Grotthuss mechanism [263]. This migration must play a major role in the response time of the device.

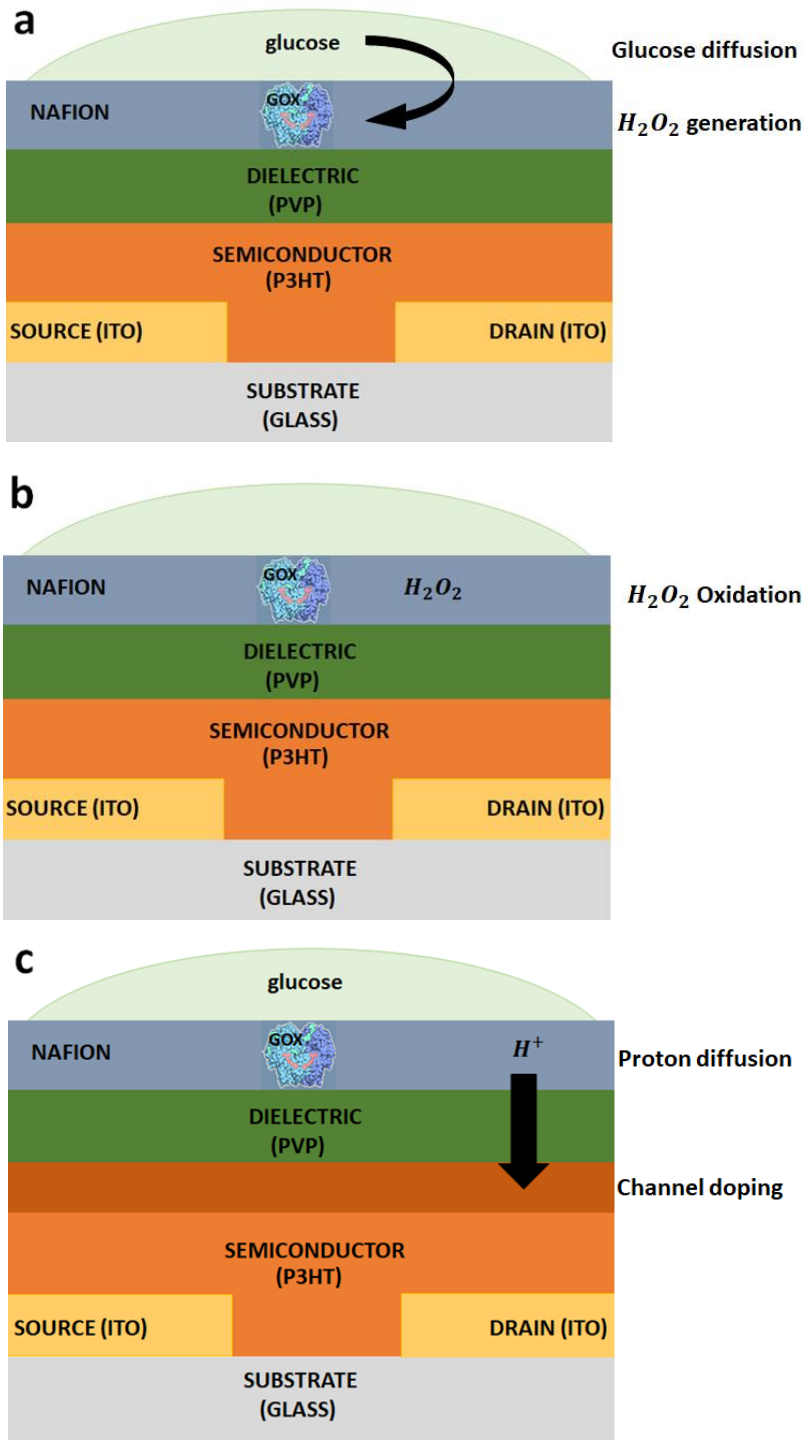

Figure 3.16: Simplified diagram for OTFT glucose sensing mechanism . a) Glucose diffuses to the GOX in the Nafion matrix whereupon H_2O_2 generated . b) The H_2O_2 is oxidised and protons are generated . c) : Protons then diffuse to and dope the P3HT channel.

3.4.2 Improving response time by removing the PVP layer

In Section 3.4.2 a slow response time for the P3HT/PVP/Nafion:GOX glucose sensor was observed with a wait time of >600 s required for the device to reach a plateau I_D output at 10 mM analyte concentration. In Section 3.4.2 we also hypothesised that proton diffusion across the PVP "dielectric" layer must play a significant role in the slow response time. The presence of a PVP layer is in reality a conceptual leftover from the initial OTFT design; the devices presented here do not act via a conventional field effect transistor mechanism where a dielectric material is required in order to create a capacitive layer at the channel. In these devices current modulation in the channel is instead a result of proton transport to the channel and subsequent doping of this material. As such, the PVP layer may not be required for device function, and even though it is a good proton transport material, the PVP may merely act to increase the response time. Consequently, in this section our ambition was to investigate modify the device response time through removal the dielectric layer PVP. The standard sensor architecture used in Section 3.4.2 was modified as shown in Figure 3.17.

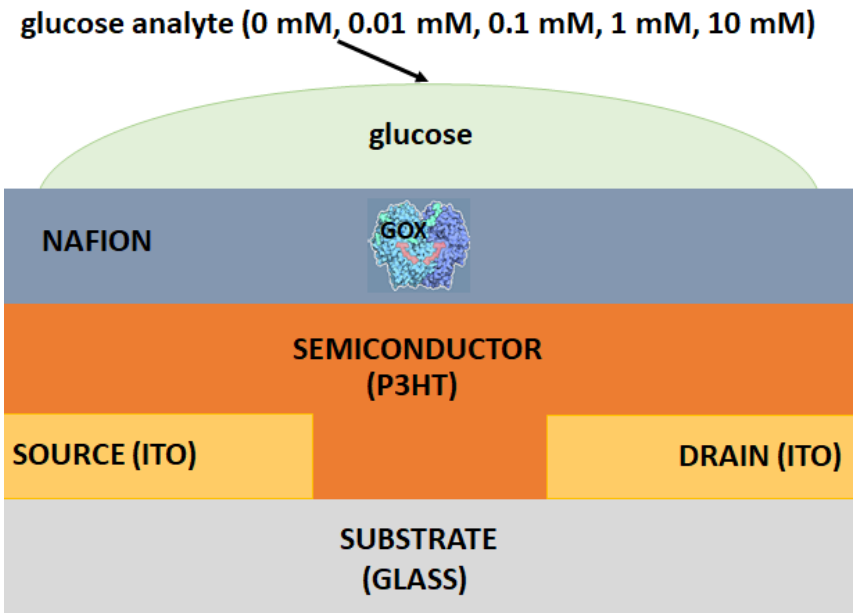

Figure 3.17: Schematic of OTFTs based sensor of ITO/P3HT/Nafion:GOX.

V_{DS} and V_{GS} were again set to (-0.3 V and -1.0 V) for these experiments and the same range of concentrations of glucose analyte mixed with DI water (0.01 mM, 0.1 mM, 1 mM, 10 mM) were used as above. The devices were allowed to stabilise under the set voltages for 300 s and then the samples were dropped onto the Nafion: GOX between the source and drain electrodes. I_D was then measured for a further 1500 s as before. Figure 3.18a shows typical I_D vs time plots for the four glucose concentrations, whilst Figure 3.18b shows the data normalised to the current just prior to analyte addition (at t = 280 s). Figure 3.18c shows the resultant calibration curve using the I_D values at 1800 s for each analyte concentration.

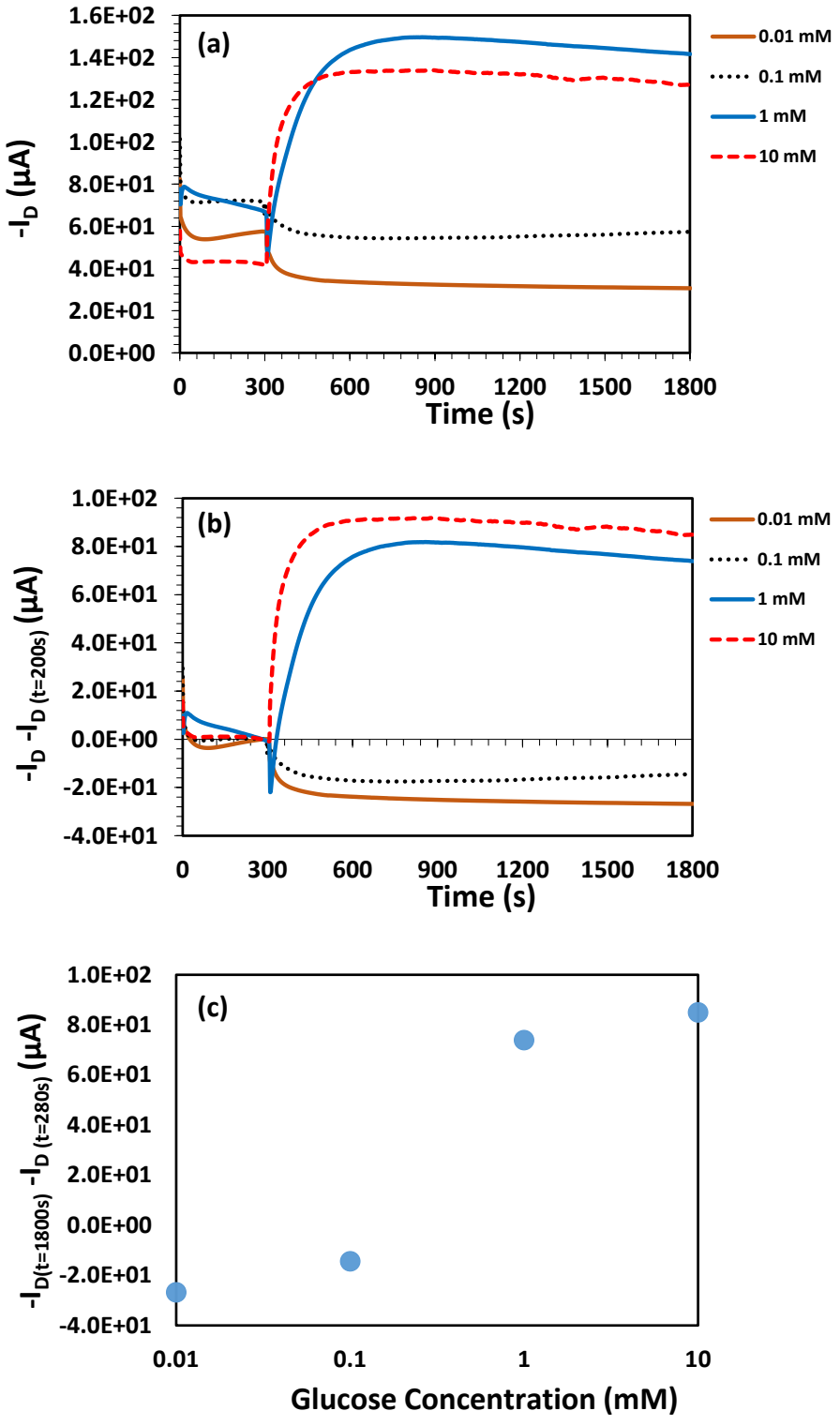

Figure 3.18: (a) Typical 0.01 mM, 0.1 mM, 1 mM and 10 mM current-time responses for the ITO/P3HT/Nafion:GOX device structure, whilst (b) shows the same data normalised to 0 µA at t = 280 second, just prior to the addition of the analyte. (c) shows the change in current after 1800 s as a function of glucose concentration.

Qualitatively the data is very similar to that observed for devices in Section 3.4.2 with two significant differences. Firstly, the magnitude of the I_D output current in the "non-PVP" devices is nearly twice that of the corresponding "PVP" devices at 1800 seconds, implying that more doping of the P3HT channel occurs in the absence of the PVP. Secondly, and most significantly, devices exposed to both 1 mM and 10 mM glucose samples reach a plateau I_D current within 300 seconds of analyte addition. To further probe this apparent improvement in response time normalised data for the 1 mM glucose PVP and non-PVP devices has been plotted on the same axes and the slope of the data has been determined by fitting a tangent to the first 150 seconds of response post analyte addition (Figure 3.19).

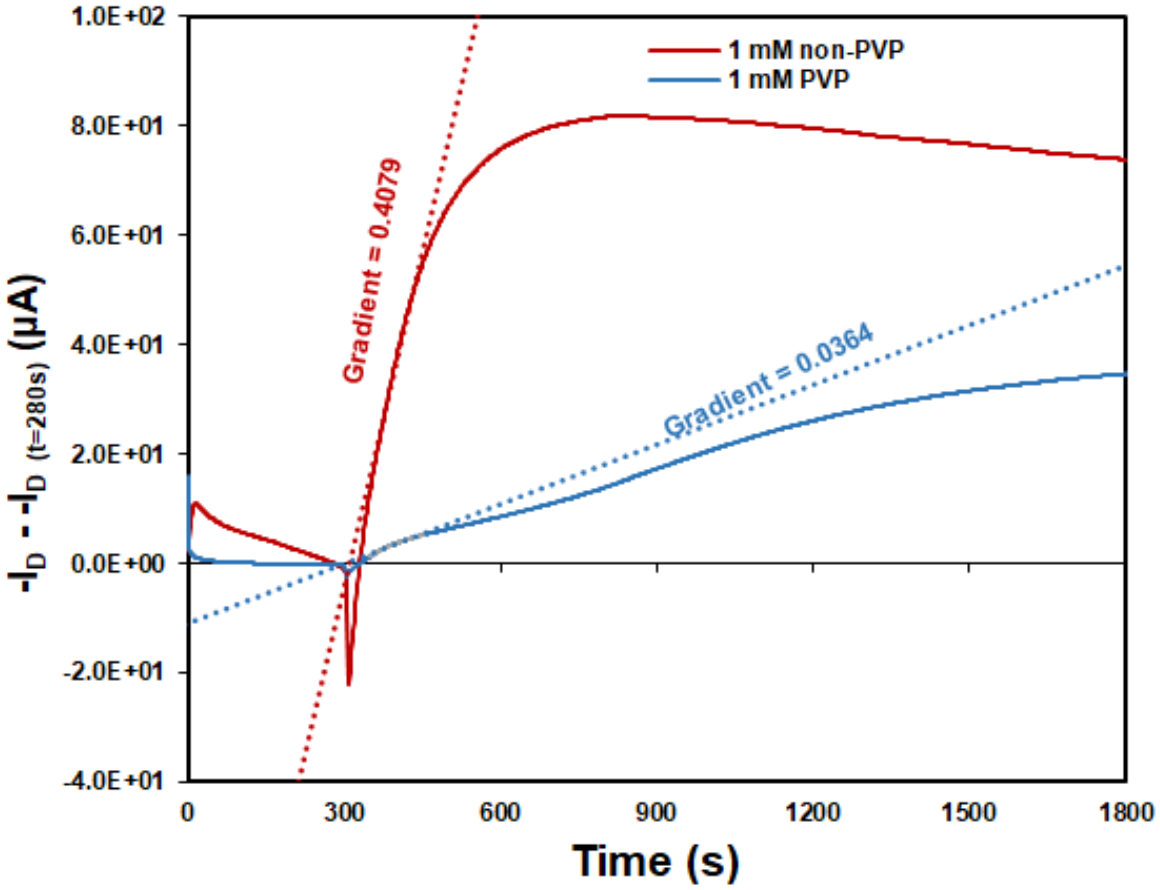

Figure 3.19: Current-time responses for the ITO/P3HT/Nafion:GOX device structure highlighting the improvement in response time normalised data for the 1 mM glucose PVP and Non–PVP devices.

The data shows a more than ten-fold decrease in response time upon the removal of the PVP layer. This observation, in conjunction with the observed increase in the magnitude of the output current, supports our initial hypothesis that PVP serves to slow down proton migration, and therefore increases device response time. Consequently, all subsequent device designs did not include a PVP layer. Notably, the sensor devices are again sensitive to a wide range of concentrations to glucose analyte within the saliva glucose range [260] and this work serves as a promising proof of concept for the proposed organic glucose sensor..

3.5 Data Analysis

In order to be used as a sensor device, a quantifiable output or property of the device which changes upon addition of the analyte must be measured and reliably correlated to the analyte concentration. In the case of the glucose sensors presented here the property which changes is the conductivity of the P3HT channel material, and this change is observed as a change in I_D of the device. Whilst this change is the basis of the device response, analysis of the raw output data is required to determine the actual quantified property of the change which best correlates to the glucose concentration. This requires the determination of a figure of merit (FOM) for the system. A figure of merit is a quantity used to characterise the performance of a device, system, or method, relative to its alternatives. For example, in engineering, FOM are often defined for materials or devices in order to determine their relative utility for an application. In the following section we will discuss and justify the FOM chosen in this work for the devices presented in this thesis.

3.5.1 Determining a suitable figure of merit (FOM)

In order to determine a suitable FOM for devices the shape and nature of the data output must be understood and considered. The devices presented here give a plot of I_D vs time as their initial raw data output. Upon addition of the glucose analyte, we observe an increase in the I_D signal which at higher glucose concentrations reaches an upper saturation limit.

As discussed in Section 3.4.2 an initial period of 300 second is allowed for the I_D to stabilise prior to analyte addition. We observe considerable variation of the I_D curves and magnitude between devices in this region. These variations are totally independent of the analyte and are instead indicative of variations in the device fabrication. As such, the I_D data was normalised to 0 A at t = 280 s, just prior to analyte addition, thus mitigating the variation inherent in the device structure.

Immediately upon analyte addition a significant drop in I_D is observed for all glucose concentrations (including the addition of pure deionised water). This observation implies that the addition of deionised water results in some dedoping of the P3HT channel material. Again. this is a change in ID which is independent of the glucose analyte and which could theoretically be removed from the data set via a normalisation (such as subtracting a standard signal for a deionised water response in the device). However, the change in I_D is rapid upon analyte addition and the response (both magnitude and rate) due to the glucose is highly dependent on the concentration of the analyte. The complexity of this region combined with the natural variations in device performance means that no effort was made to remove this dedoping effect and it was retained in the ongoing data analysis.

Two main values present themselves as candidates as a FOM for these devices. These are $I_{D(x)}$; the I_D value at some constant time from analyte addition (x) or $I_{D(max)}$; the maximum value of I_D reached by the device after analyte addition. We have observed that at high glucose concentrations, I_D reaches a plateau value, suggesting that there is a maximum doping of the channel. In addition, at lower glucose concentrations, we observe an I_D value which gradually increases throughout the measurement lifetime. Consequently, $I_{D\,(x),}$ where x is the upper limit of the time axis, should be equal to $I_{D\,(max)}$ for all analyte concentrations. If this is not true, it suggests some random device variation has occurred. As such, a normalised $I_{D\,(1800s)}$ value was utilised in this analysis as the device FOM.

Two others potential FOM values were considered for the analysis. The first was the area under the I_D vs time plot – essentially a measurement of the total charge transferred by the current. This value combines the rate at which doping occurs at the channel with the total doping which occurs. However, a study of the I_D vs time curves shows that there are often significant deviations in the shape of the curve prior to reaching a current plateau and as such, the normalised $I_{D\,(1800s)}$ value was preferred. Secondly, the initial slope of I_D increase was considered as a possible FOM. Again, a study of the data shows that there is a correlation between the initial slope and the analyte concentration, with increasing concentrations resulting in steeper slopes. However, the initial dedoping effect of analyte addition complicates this measurement and consequently it was not used in this study.

3.6 Summary

In this Chapter, through a journey of discovery and understanding we have developed a proof-of-concept glucose sensor based on the initial source: drain/P3HT/PVPy/PEDOT:PSS/gate architecture. The device shows good sensitivity in the 0.1 – 1 mM glucose concentration range, with lower sensitivity below 0.1 mM and a device saturation limit appears to be approached as the concentration increases from 1 to 10 mM glucose.

A series of architecture modifications were used to improve the initial device output. Initially, PEDOT: PSS was replaced with Nafion. PEDOT: PSS is an acidic polymer and since the mechanism of the devices relies upon proton generation, the removal of replacement of PEDOT: PSS by neutral Nafion was deemed sensible. PVPy was replaced by PVP for a similar reason. Basic PVPy was initially used to mitigate the acidity of PEDOT: PSS. With the removal of PEDOT: PSS it was considered that PVPy would only serve to hinder the mobility of protons within the device. Consequently, PVPy was replaced by neutral PVP. In both of these cases an increase in the current output of the device (I_D) of more than one order of magnitude was observed.

Finally, PVP was removed from the device to create a final device architecture of source:drain/P3HT/Nafion:GOX/gate. The inclusion of the PVP layer dates from the initial OFET architectural design concept where a dielectric layer was required for device function. Since protonic doping of the channel is the key mechanism of these devices, a dielectric layer is not required and serves only to slow the device response. Removal of the PVP layer resulted in a more than ten-fold decrease in response time of the device, greatly improving the viability of the device.

Finally we discussed and justified the selection of a FOM for the device, settling on a normalised $I_{D(1800s)}$ value in these experiments.

Chapter 4: Investigating the Effect of Fabrication Conditions on P3HT and Nafion Films and their Interface within the Sensor

4.1 Introduction

In order to develop a more robust understanding of the operation of the glucose sensor, the P3HT semiconductor layer and the Nafion proton transport layer, as well as the interface that they form in the sensor, will be thoroughly characterised here. In this chapter, the main attention is focused on characterisation and optimisation of the elements that make up the design of the biosensor. It is very important to control the interface between the proton transport material and the organic semiconductor due to the key role that this interface plays in determining the electrical characteristics of the devices [264-266]. Both film thickness and thermal annealing are expected to have a significant influence on the electrical characteristics for this type of device. Therefore, in order to achieve control of the interfacial properties and improve the performance of the sensor, the focus of this study is to determine the effect of film thickness and thermal annealing on device performance.

In this study, the following structures were fabricated on ITO electrode pairs (as in Chapter 3) and their electrical properties were characterised as a function of annealing temperature and film thickness (where applicable) with and without the addition of water above the gap between the electrodes:

- P3HT
- Nafion
- P3HT/Nafion

4.1.1 Aim

The aims of this chapter are threefold: 1) To determine the effect of annealing temperature on the electrical properties of P3HT films, Nafion films and P3HT/Nafion bilayers; 2) To determine the effect of film thickness on the electrical properties of P3HT films, Nafion films and P3HT/Nafion bilayers; 3) To discuss the possible mechanisms of enhanced conductivity in P3HT/Nafion bilayers and relate this to interface composition.

4.1.2 Experimental

P3HT layers of varying thickness were prepared from a range of concentrations of P3HT in chloroform solution. Solutions of 10 mg/mL, 15 mg/mL, 20 mg/mL, 25 mg/mL and 30 mg/mL of P3HT (synthesised by Dr Nathan Cooling, The University of Newcastle) in chloroform (Sigma Aldrich, anhydrous 99.8%) were prepared. Note that 20 mg/mL is the concentration utilised in a standard device in the context of this thesis. The solutions were sonicated for 1 hour to complete dissolution and ensure that the polymer solution was homogeneous before spin coating. P3HT films were prepared by spin coating 80 μL of the solution at 2000 rpm for 60 seconds onto a cleaned ITO substrate. The films were heated at 50 ºC for 10 minutes to eliminate any remaining solvent. The P3HT layer film thickness was determined by making a scratch in the film and measuring the height difference between the substrate and the top of the film via profilometry using a DektakXT stylus profilometer.

Nafion films were prepared by spin coating 75 μL of as received Nafion solution (Sigma-Aldrich, 5 % wt. in propanol and water) at 500 rpm onto a cleaned ITO substrate [267, 268]. The films were thermally treated at 50 ºC for 10 minutes. The average film thickness was determined over three measurements using profilometry. The average thickness of the Nafion film was measured to be 575 ± 15 nm. The P3HT/Nafion bilayers were prepared by deposition of a P3HT layer and drying, followed by deposition of a Nafion layer, as described for the single film cases above.

4.2 P3HT Film Characterisation

4.2.1 P3HT film thickness as a function of deposition conditions

Organic semiconductor thickness has been shown previously to have a significant impact on the electrical characteristics of OTFTs [269, 270]. The effect on devices of P3HT thickness was studied previously by Osterbacka's group [261], where a systematic drop in the conductance of channels in devices with a poly(4-vinylphenol) (PVP) dielectric layer was observed for P3HT thicknesses below 50 nm. In addition, Lee et al. found that, whilst the threshold voltage for pentacene-based OTFTs did not change significantly when film thickness was decreased from 90 to 16 nm, charge mobility did increase [271]. A calibration curve figure 4.2 of film thickness as a function of P3HT solution concentration was established here in order to allow fabrication of films with specific thicknesses going forward.

As mentioned in Chapter 2, the thickness of the P3HT layers can be controlled by modifying the concentration of P3HT in the chloroform solution. Different concentrations of P3HT in chloroform solution were prepared and the thickness was measured using profilometry. In the current study, we noted that the thickness of the P3HT films increased linearly with increasing concentration (R^2

= 0.9) as shown in Table 4.1 and Figure 4.1. The 20 mg/mL solution, which produced a thickness of 113 ± 8 nm was selected to produce P3HT films for the standard devices throughout the remainder of the thesis.

Table 4.1: Average P3HT film thickness for films spun from different concentrations in chloroform.

P3HT Concentration (mg/mL)	**Average Thickness (nm)**
6	25 ± 9
10	42 ± 8
15	71 ± 6
20	113 ± 8
25	135 ± 10
30	172 ± 9
35	225 ± 9
40	250 ± 12

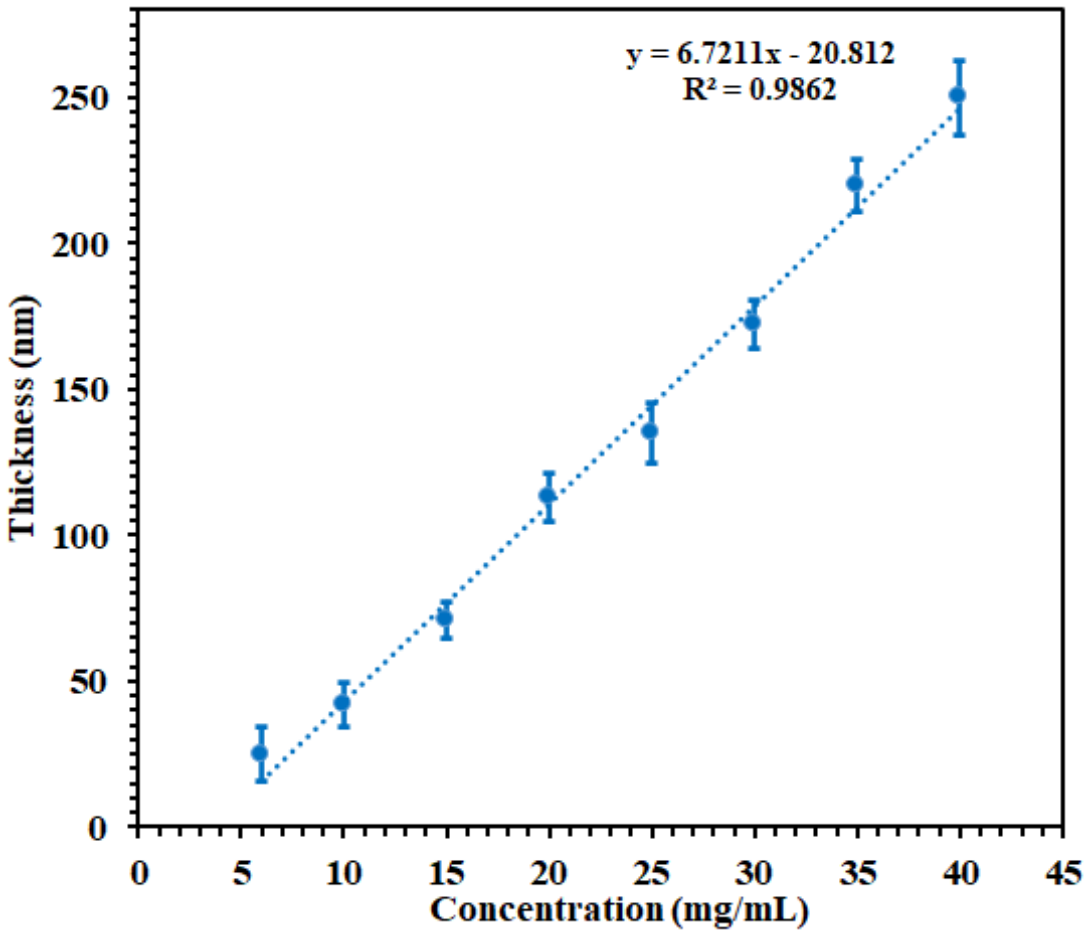

Figure 4.1: P3HT film thickness at different concentrations as presented in Table 4.1

4.2.2 Electrical properties of P3HT films as a function of annealing temperature

The aim of this experiment was to measure the electric properties of P3HT films as a function of annealing conditions. The structure of the measurement architecture is displayed in Figure 4.2. The effect of temperature on P3HT has been studied previously, showing increasing charge carrier mobility with increasing temperature [272]. At higher temperatures the polymer becomes more fluid and rubbery which leads to change in viscosity and density because of the thermally activated translational and rotational modes of motion of the polymer backbone [273, 274]. The temperature at which this starts to occur is

the glass transition temperature (T_g). Above the T_g, intermolecular rearrangement will increase with increasing temperature which results in a decrease in viscosity and allows polymer chains to rearrange and relax towards thermodynamic equilibrium [275-278] .

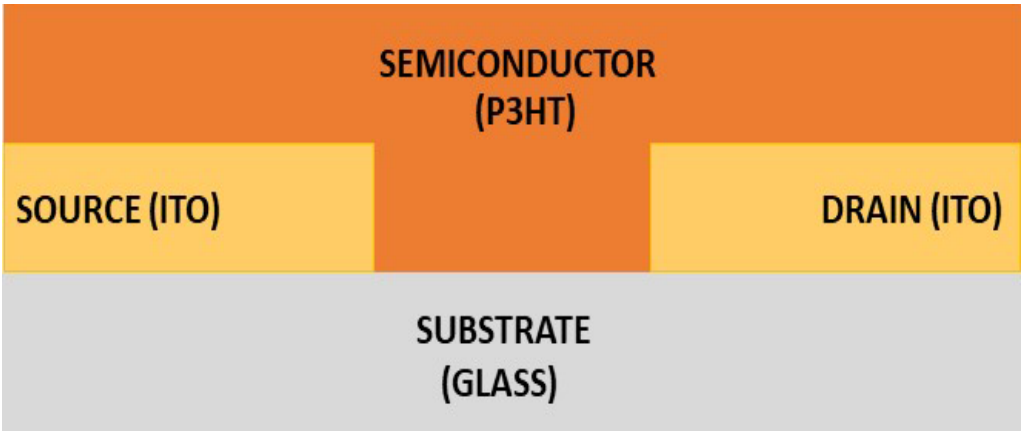

Figure 4.2: Device configuration for P3HT two-terminal measurements.

A range of annealing conditions were applied to P3HT films and their electrical properties were measured in an attempt to provide insight into the impact of thermal annealing on the properties of the film. Figure 4.3 shows the current-voltage (I-V) characteristics of the P3HT film deposited from a 15 mg/mL solution (a thickness of 71 nm as shown in the calibration curve in Figure 4.1), for samples that have undergone thermal treatments at various temperatures. After undergoing thermal treatment at 50 ºC, 70 ºC, 90 ºC, 110 ºC and 150 ºC for a period of 15 minutes each of the P3HT I-V curves are all almost linear, showing little diode behaviour. The lack of diode behaviour and very low currents shown for these films suggests that the P3HT is highly undoped and acts primarily as a resistor. The I-V curve slope (and hence the resistance) for these films is very similar, but on further increasing the annealing temperature

to 200 °C and then 250 °C the current drops and resistance increases as the P3HT film undergoes thermal degradation.

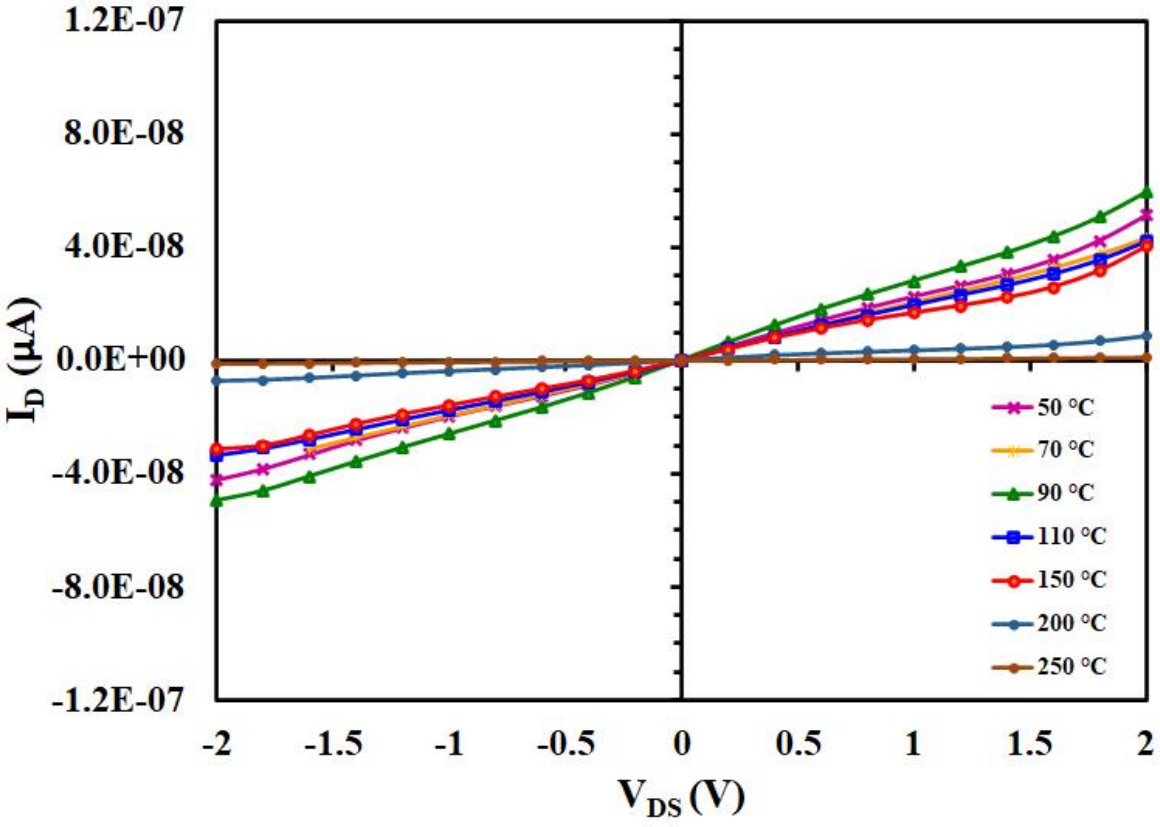

Figure 4.3: I-V characteristics of the 71 nm P3HT film with varying annealing temperatures (50 ºC, 70 ºC, 90 ºC, 110 ºC, 150 ºC, 200 ºC and 250 ºC).

Figure 4.4 shows the I-V characteristics of the P3HT films deposited from a 20 mg/mL solution (a thickness of 113 nm as shown in the calibration curve in Figure 4.1), for samples that have undergone thermal treatments at various temperatures. The increase in film thickness results in very little change to the I-V behaviour across this range of temperatures with similar currents and resistive behaviour observed to that of the 71 nm films.

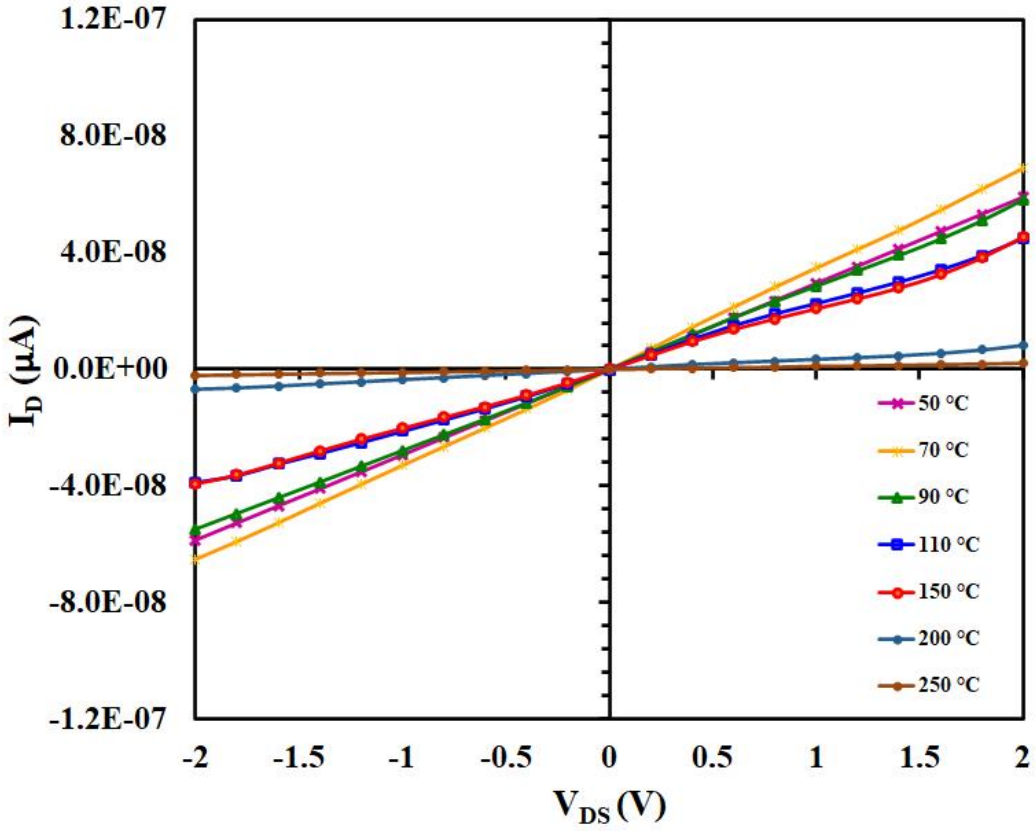

Figure 4.4: I-V characteristics of the 113 nm P3HT film with varying annealing temperatures (50 ºC, 70 ºC, 90 ºC, 110 ºC, 150 ºC, 200 ºC and 250 ºC).

Figure 4.5 shows the I-V characteristics of the P3HT films deposited from a 25 mg/mL solution (a thickness of 135 nm as shown in the calibration curve in Figure 4.1), for samples that have undergone thermal treatments at various temperatures. For this thickness of film, the I-V curves are again linear, showing little diode behaviour. Interestingly, an almost systematic increase in the film resistance is observed with increasing annealing temperature. This observation is contrary to what might be expected if heating of the film lead to higher film order and crystallinity.

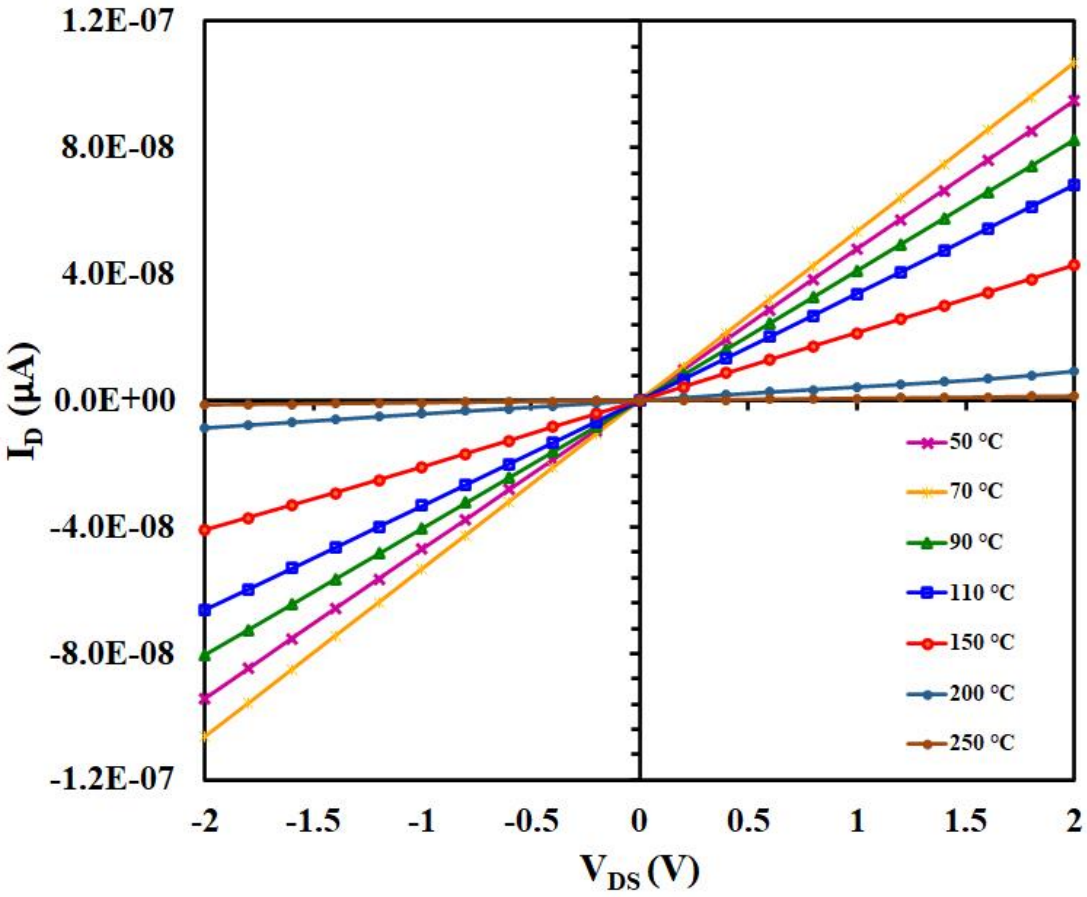

Figure 4.5: I-V characteristics of the 135 nm P3HT film with varying annealing temperatures (50 ºC, 70 ºC, 90 ºC, 110 ºC, 150 ºC, 200 ºC and 250 ºC).

As expected, we observe that the conductance of the P3HT films increases with thickness. In addition, the same overall trends for annealing conditions are observed across the three film thicknesses with a significant decrease in the conductivity of the P3HT observed at annealing temperatures at and above 200 °C.

4.3 Nafion Film Characterisation

As mentioned in Chapter 2, Nafion is an organic proton transport material which plays a significant role in devices such as fuel cells [279]. In this study, we measure the electrical properties of pure Nafion films as a function of thermal annealing temperature.

4.3.1 Nafion film thickness as a function of deposition conditions

In this experiment, we study the relationship between the spin speed of spin coated Nafion films and their thickness. As expected, we observe that with increased spin speed, the thickness of the films decreases as shown in Table 4.2 and Figure 4.6. We chose the 500 rpm spin condition (which gives a thickness of 575 nm) to produce Nafion films for all subsequent experiments.

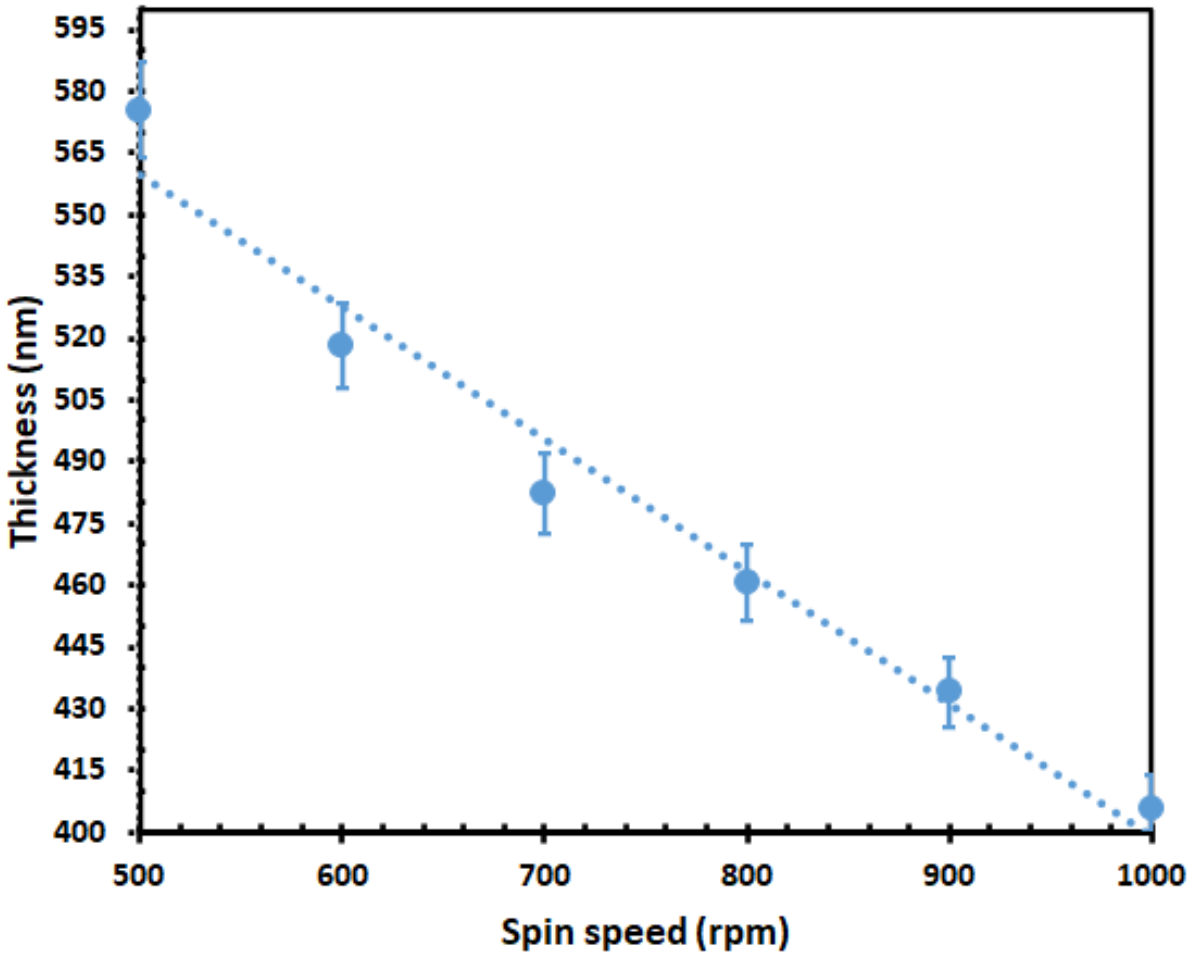

Figure 4.6: Thickness for spin-coated Nafion films as a function of spin-speed.

Table 4.2: Thickness for spin-coated Nafion films as a function of spin-speed.

Spin speed (rpm)	**Thickness (nm)**
500	575 ± 15
600	518 ± 17
700	482 ± 8
800	460 ± 16
900	433 ± 9
1000	405 ± 17

4.3.2 Electrical properties of Nafion as a function of annealing temperature

In this experiment, we measured the electrical properties of Nafion films as a function of annealing temperature. The architecture of the test device is displayed in Figure 4.7. The electrical properties were measured in order to understand the impact of annealing on the properties of the film. Films were annealed at temperatures ranging from 50 ºC to 250 ºC for 15 minutes. Figure 4.8 shows the I-V characteristics of the annealed Nafion films. All of the I-V relationships show diode-like behaviour with the film acting as an ionic semiconductor. The scan direction was from negative to positive voltage and the positive current observed across -1.5 V $\leq V_{DS} <$ 0 V can be attributed to polarisation of the positive charge carriers (protons) leading to a net positive charge in the film at the interface with the drain electrode for these low negative V_{DS} values. For the films annealed at 50 ºC, 70 ºC, 90 ºC, 110 ºC and 150 ºC the I-V curves are almost identical. At and above 200 ºC a slight increase in the conductivity of the material is observed as well as a reduction in the diode-like shape. This change in electrical properties may be due to changes in the water cluster sizes which have been observed upon annealing of Nafion [280]. Higher temperature above 200 ºC of Nafion led to loss the water resulting low conductivity then loss conductivity and efficiency [281].

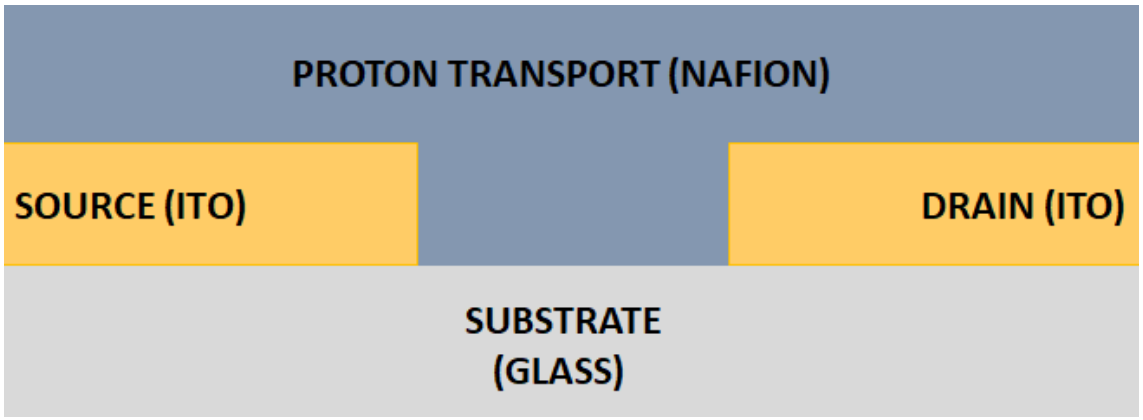

Figure 4.7: Device configuration for Nafion two-terminal measurements.

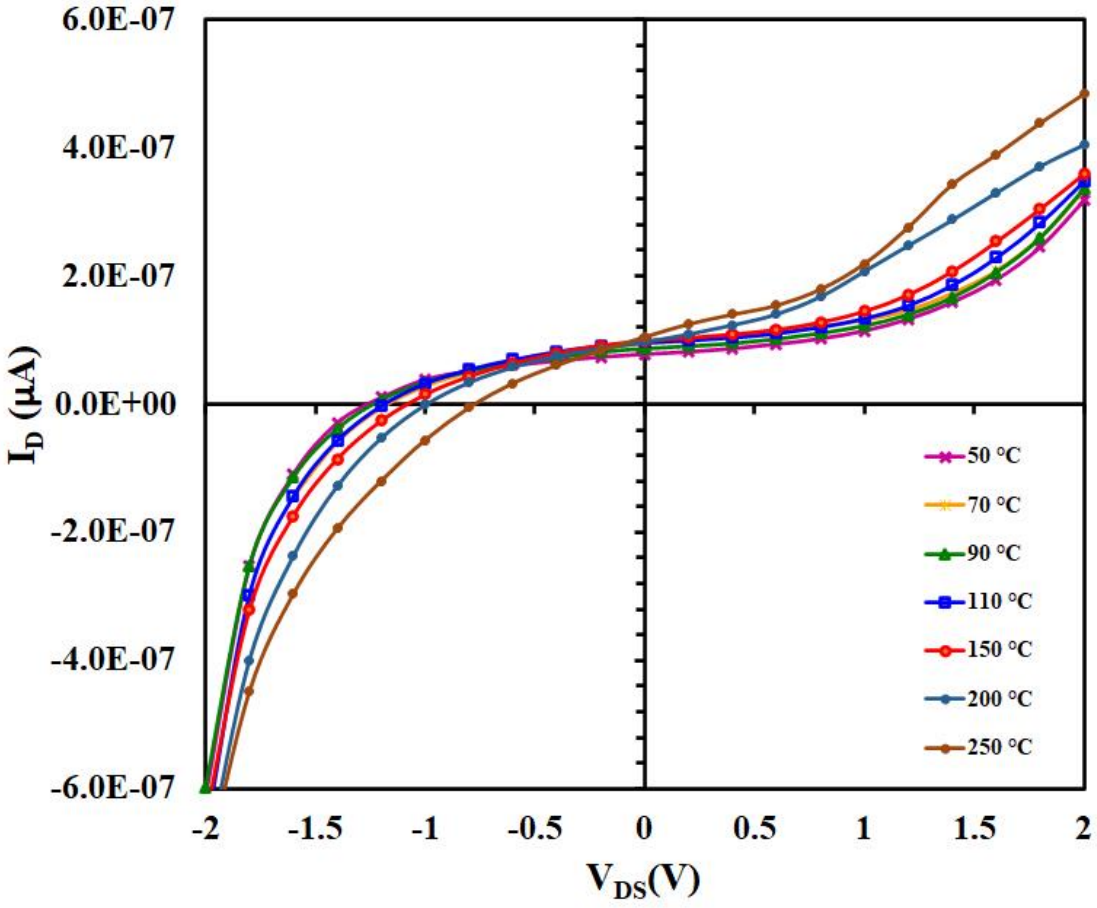

Figure 4.8: I-V characteristics of Nafion films, 575 nm with varying annealing temperatures (50 ºC, 70 ºC, 90 ºC, 110 ºC, 150 ºC, 200 ºC and 250 ºC).

4.4 P3HT/Nafion Bilayer Characterisation

Having established the effect of film thickness and annealing temperature upon the electrical properties of P3HT and Nafion layers, we now investigate the impact of these processing parameters on the electrical properties of P3HT/Nafion bilayers. For this purpose, we prepared P3HT/Nafion bilayer films (Figure 4.9) to measure the I-V characteristics as a function of annealing temperature.

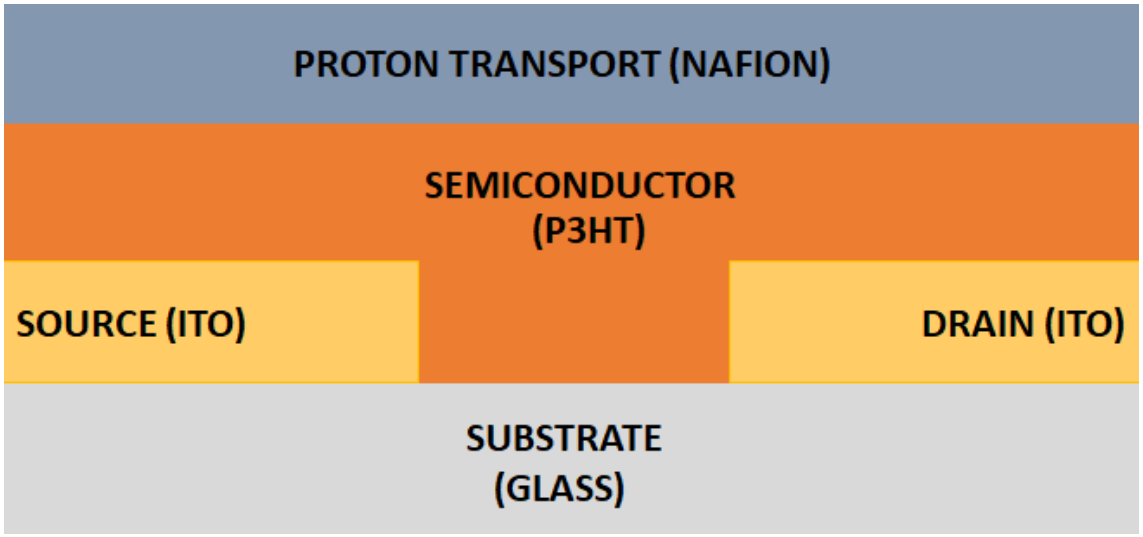

Figure 4.9: Device configuration for Nafion/P3HT two-terminal measurements.

4.4.1 Electrical properties of P3HT/Nafion Bilayer as a function of annealing temperature

In this experiment, bilayers of P3HT and Nafion were fabricated and their electrical properties as a function of P3HT thickness and annealing temperature were recorded. Figures 4.10 (t_{P3HT} = 71 nm), Figure 4.11 (t_{P3HT} = 113 nm) and Figure 4.12 (t_{P3HT} = 135 nm) show the I_D versus V_{DS} relationships after annealing at a range of annealing temperatures.

In general, we observe for all bilayer films, that there is a significant increase in the conductance (I_D at a given V_{DS}) compared with neat P3HT or Nafion films. We hypothesise that this change is due to intermixing of the two materials resulting in subsequent doping of the P3HT. For all three P3HT thicknesses, we observe a significant change in the I-V characteristics for P3HT/Nafion upon annealing. For temperatures up to 200 ºC, an increase in the conductance is observed with increasing temperature while at 250 ºC the conductance drops dramatically for all P3HT thicknesses. We hypothesise that this increase in conductance is consistent with an increase in the volume of the intermixed/doped P3HT/Nafion region near the interface as introduced above. This hypothesis is supported by the observation that for all P3HT thicknesses, the greatest increases in conductance are observed at annealing temperatures above 100 ºC which coincides well with the glass transition temperature (T_g) of Nafion (120 ºC) [281].

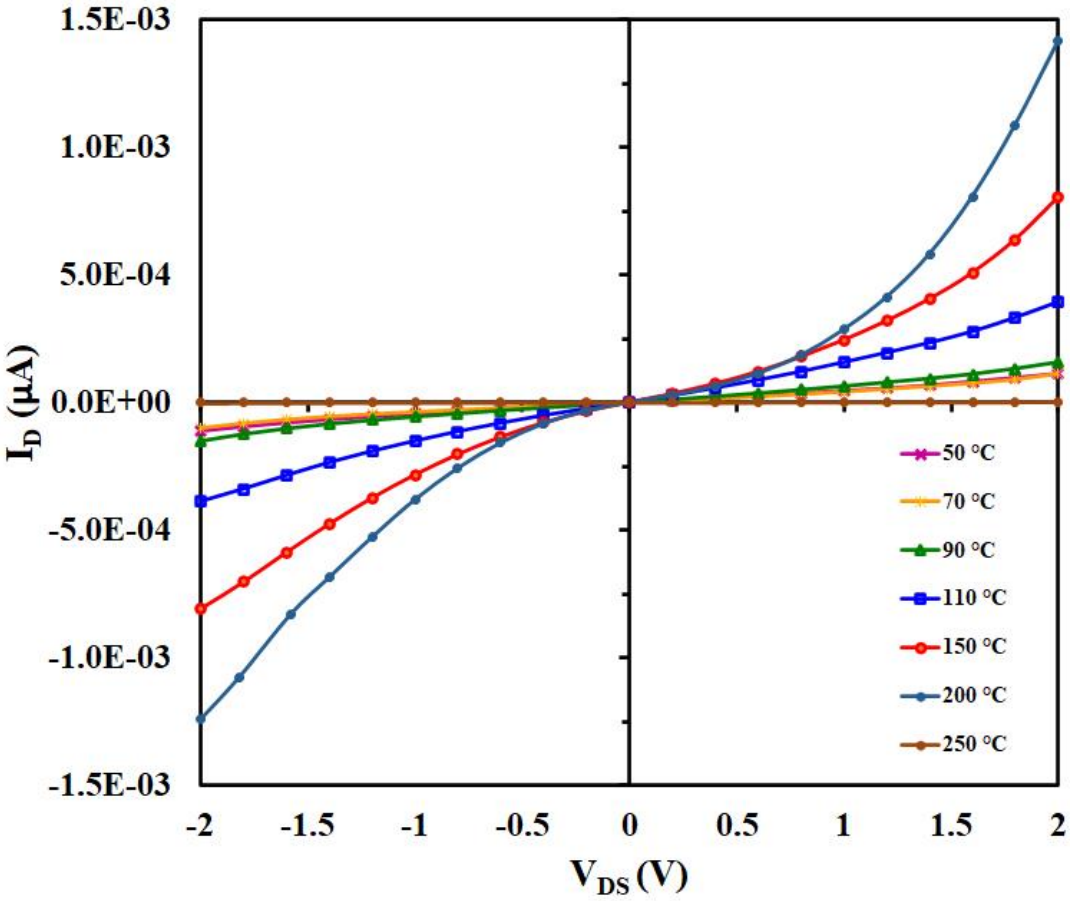

Figure 4.10: Output characteristics of the P3HT/Nafion at 71 nm with varying the temperatures (50 ºC, 70 ºC, 90 ºC, 110 ºC, 150 ºC, 200 and 250 ºC).

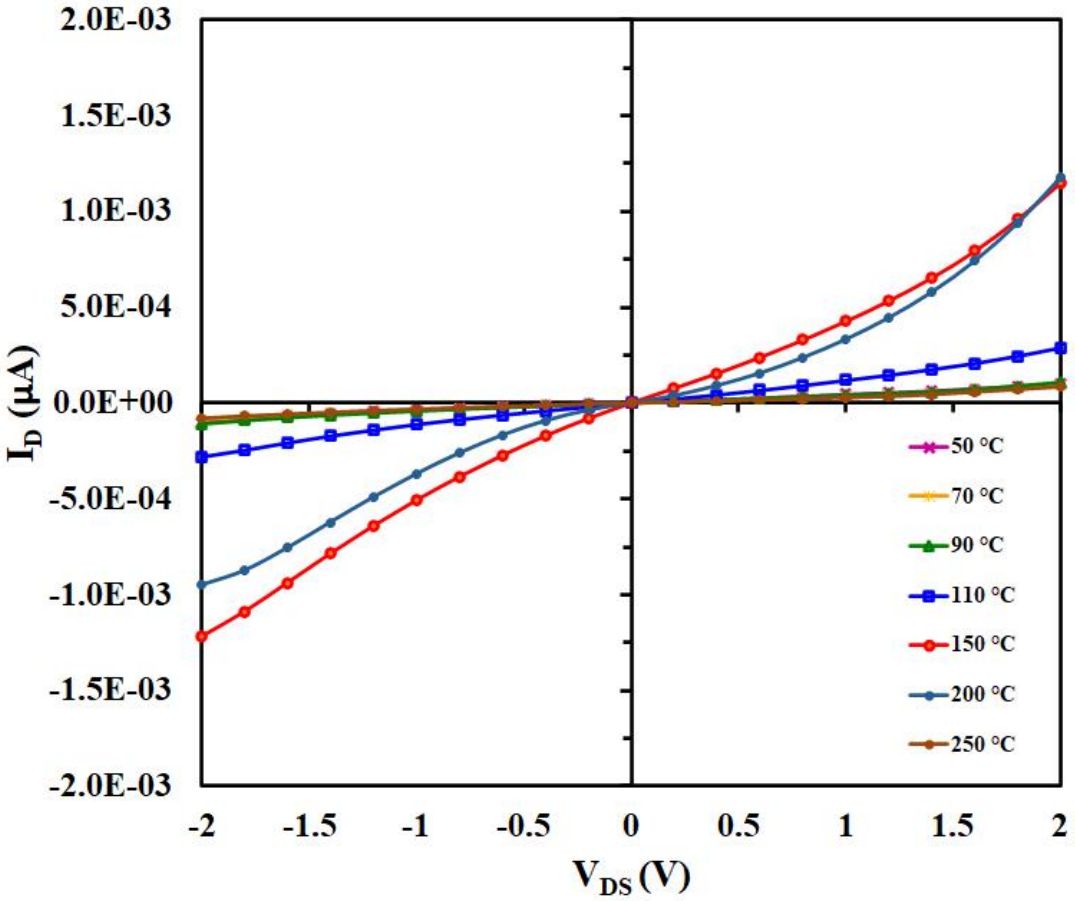

Figure 4.11: Output characteristics of the P3HT/Nafion at 113 nm with varying the temperatures (50 ºC, 70 ºC, 90 ºC, 110 ºC, 150 º C, 200 ºC and 250 ºC).

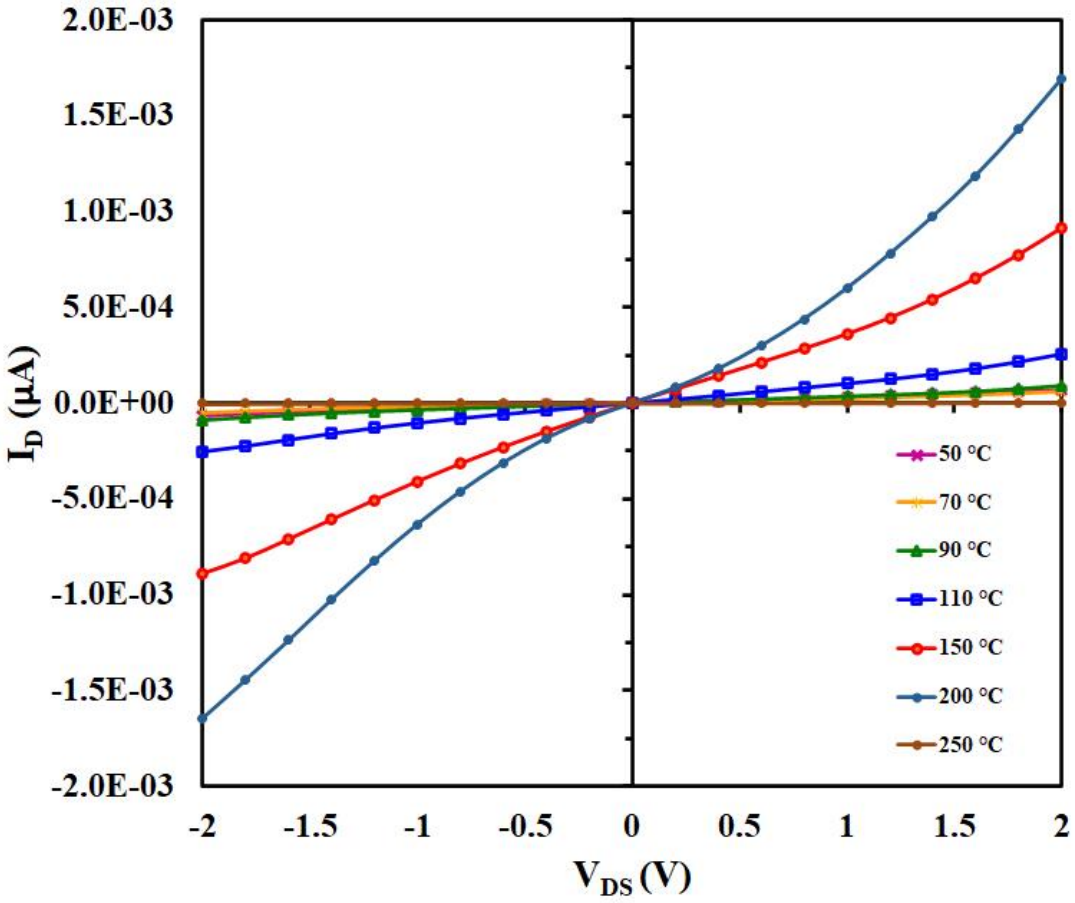

Figure 4.12: Output characteristics of the P3HT/Nafion, 135 nm with varying the temperatures (50 ºC, 70 ºC, 90 ºC, 110 ºC, 150 ºC, 200 ºC and 250 ºC).

The electrical properties of the P3HT/Nafion bilayers described above are consistent with a model in which the conductivity of the P3HT/Nafion bilayer is dominated by an interfacial doped P3HT region, the size of which does not change as the P3HT layer thickness varies across this thickness range (Figure 4.14). The slight decrease in conductivity with increasing P3HT thickness is consistent with an increased low conductivity pathway consisting of the undoped P3HT (Figure 4.13).

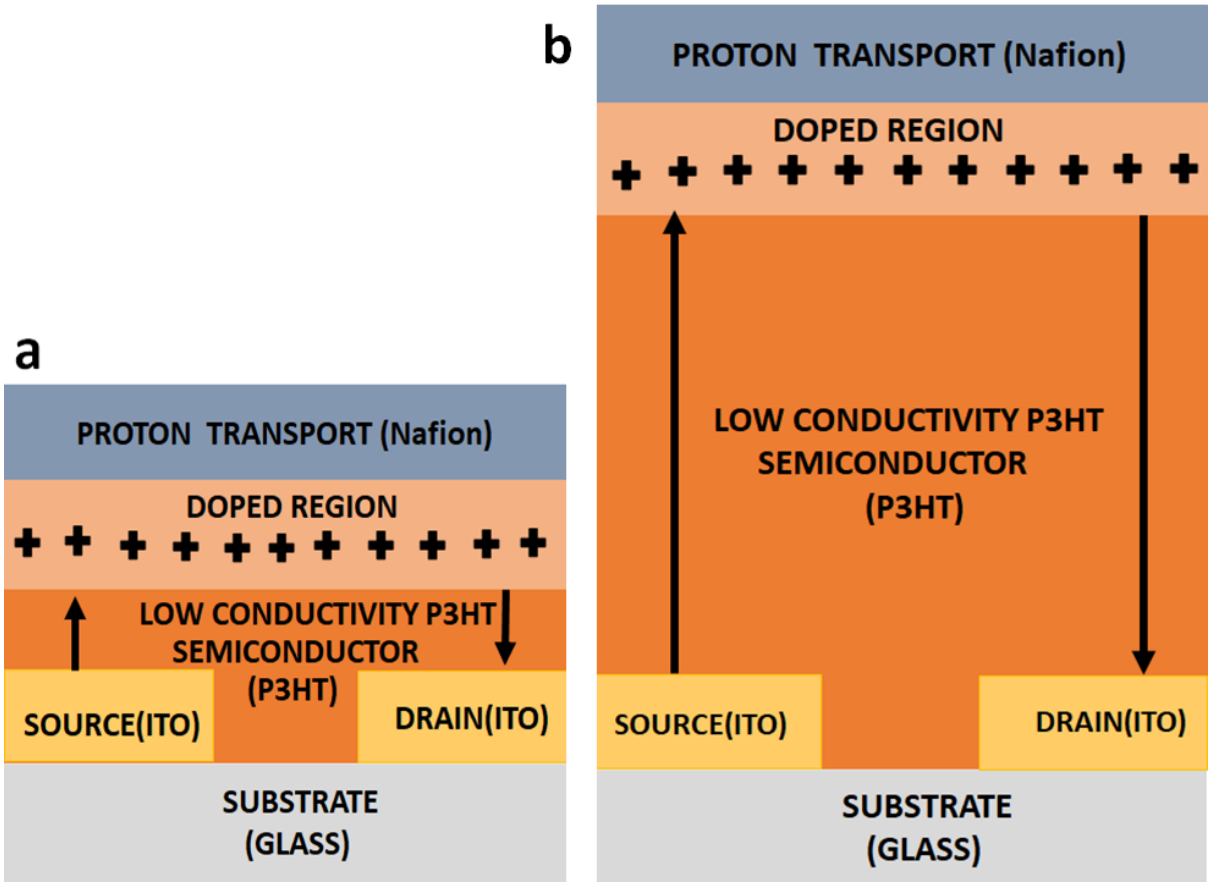

Figure 4.13: Schematic diagrams illustrating the difference in current pathways between devices with thick and thin P3HT layers: (a) thinner P3HT layer device and (b) thicker P3HT layer device.

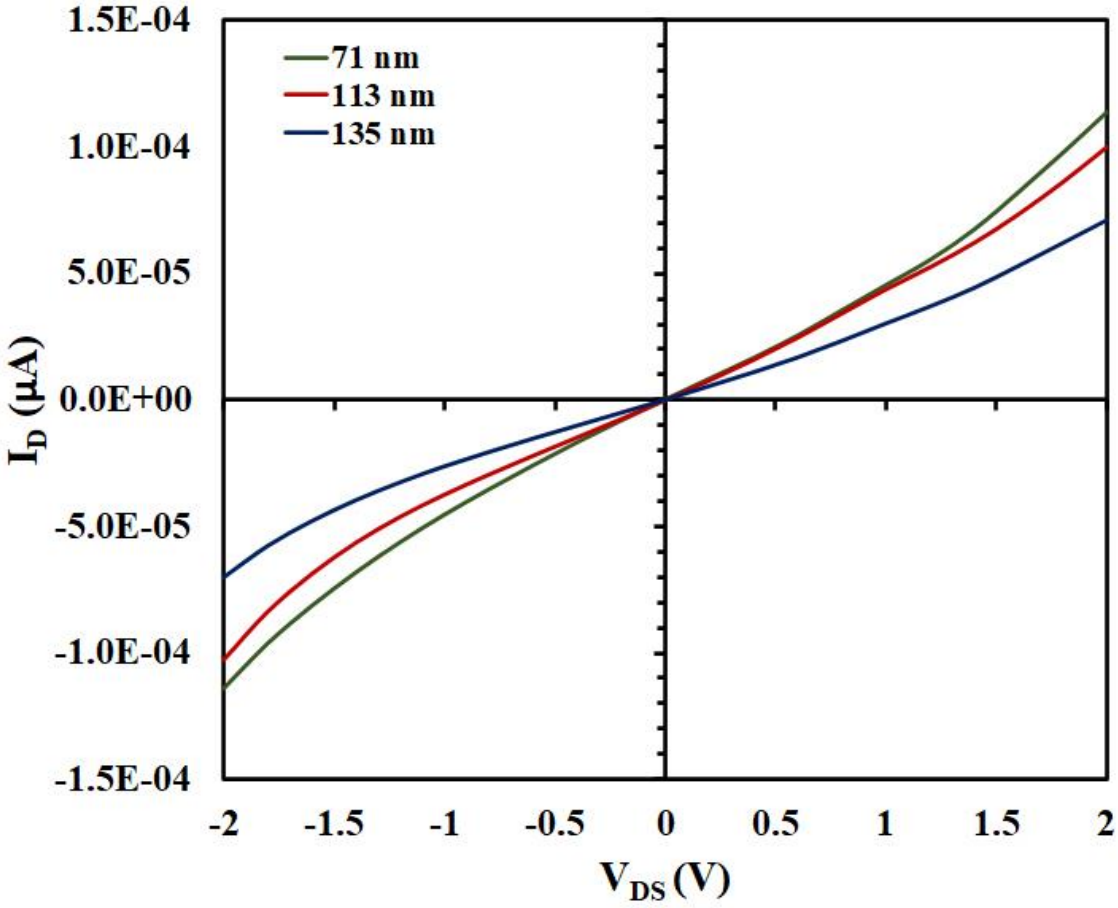

Figure 4.14: IV Characteristic of P3HT/Nafion bilayer film annealed at 50 °C with P3HT thickness 71 nm, 113 nm and 135 nm.

Further results are summarised in Table 4.3 and Figure 4.15 and show that the resistance values increase linearly with increasing thickness of the active layer.

Table 4.3: The average current and resistance of P3HT/Nafion bilayers with different P3HT thickness at V=1 V.

P3HT Concentration (mg/mL)	Thickness (nm)	Average I (A)	Average R (Ω)
10	51 ± 5	5.35×10^{-5}	1.93×10^{4}
14	71 ± 8	4.15×10^{-5}	2.50×10^{4}
20	113 ± 14	3.22×10^{-5}	3.29×10^{4}
25	135 ± 20	2.33×10^{-5}	4.28×10^{4}
30	225 ± 19	1.80×10^{-5}	5.90×10^{4}

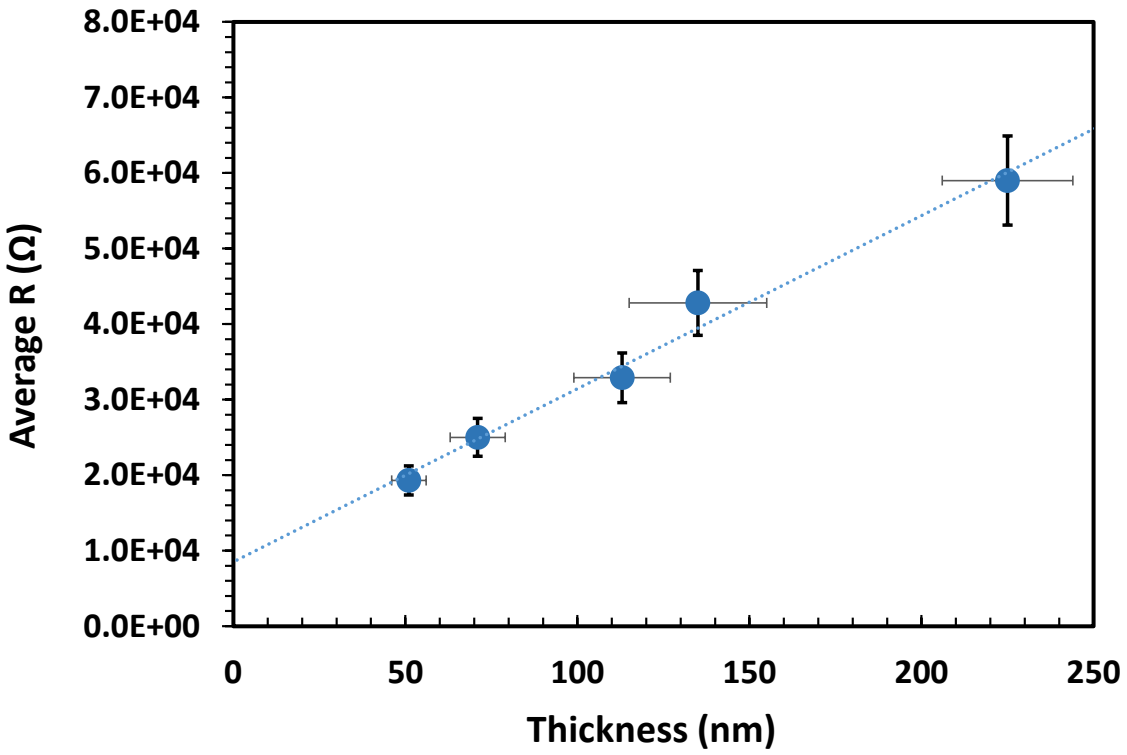

Figure 4.15: Relationship between thickness of P3HT and the P3HT/Nafion bilayer resistance. The resistance error is estimated to be 10 %.

4.5 Characterising the Effect of the Addition of Water to the Component Layers

The glucose sensors presented in this thesis are designed to test the glucose concentration of an aqueous solution, facilitating the use of saliva as an analyte. Consequently, it is important that we understand the effect of water on the electrical properties of the sensor architecture as well as the component layers. To achieve this goal, I-V curves were measured for the P3HT films, Nafion films and P3HT/Nafion bilayers onto which water has been deposited. P3HT layers of the three thicknesses determined in Section 4.4.1 were used, and all samples were annealed at temperatures ranging from 50 ºC to 250 °C as per the previous section.

4.5.1 Characterising the effect of the addition of water on P3HT films

Three sets of P3HT films of thickness 72 nm, 113 nm and 135 nm were deposited on substrates with ITO electrodes (defined as source and drain electrodes). The substrates were then heated at temperatures from 50 °C to 250 °C for 15 minutes. I_D-V_{DS} measurements were then conducted across a voltage range of -2 to 2 V. Figures 4.17, 4.18 and 4.19 show the I-V curves for standard 71 nm, 113 nm and 135 nm thick P3HT films, used in this study, respectively. For all experiments in Section 4.5, a 5 µL drop of deionised water was added over the gap between the electrodes immediately prior to measurement. Figure 4.16 shows the architecture of the P3HT/water samples that have been used in this study.

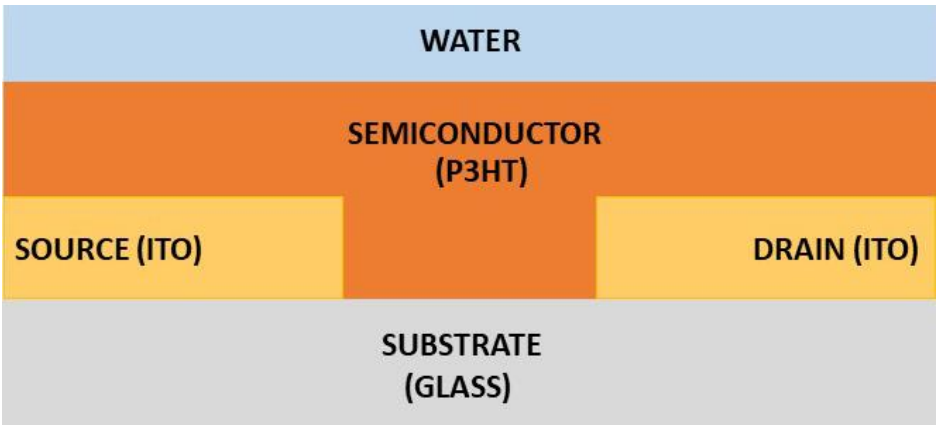

Figure 4.16: Cross-sectional schematic of P3HT sample with water addition as used in this study.

Water plays important role in the electronic transport and mobility properties in a more hydrated polymer film [282-284]. This experiment is designed to ascertain the change in the polymer properties upon hydration of the polymer

surface. In particular, hydration of crystalline polymers which have a high dry charge mobility can result in disruption of the conductivity [285]. Interfacial reactions between conducting polymers and water can produce pendant hydroxyl (OH) groups [286]. This results in a long term moisture effect on P3HT films stored in air [287]. Particularly during doping, swelling of the polymer can lead to water molecules being introduced into the P3HT layer. The penetration of water into the crystalline P3HT structure can lead to disruption of conductivity and destabilise the polymer structure [284, 287].

In this study, all three thicknesses show very similar diode behaviour and conductivities. However, there is a significant (approximately 100 times) increase in the current levels observed in comparison to the neat P3HT films, and a slight trend of lower current levels observed for increasing P3HT thickness. We hypothesise that this trend is due either to doping of the P3HT at the P3HT/water interface [251, 288] (in a similar but weaker effect to that caused by Nafion addition) or simply conductivity of the sample near the interface increasing due to current flowing through the water and the undoped (low conductivity) P3HT pathway increasing in length with thicker P3HT layers (similar to Figure 4.13). Additionally, as with the dry samples, the relative conductivities within each dataset are similar for annealing temperatures up to 150 °C and then decrease for higher temperatures.

In this experiment water appears to dope the P3HT itself – consistent with water dissociating into protons (and hydroxyls) and the protons subsequently doping the interface. The effect of this doping is significant (the conductance of the wet P3HT film is 100x that of the dry P3HT film) but is still much smaller than that produced by Nafion doping (the conductance of the P3HT/Nafion bilayer is 1000x that of the wet P3HT film), suggesting that [H+]water << [H+]Nafion. The relative size of these effects is not surprising. Nafion can be considered a superacid catalyst. The combination of fluorinated backbone, sulfonic acid

groups, and the stabilising polymer matrix make Nafion a very strong acid, with pKa ~ -6[289]. By contrast water is very weakly acidic with a dissociation constant of 10^{-14} and a pH of 7.

The shapes of the I-V curves may also be explained by the addition of the water. At $0 < V_{DS} < 1.2$ V, a linear relationship between I_D and V_{DS} is observed, indicating that the P3HT film is behaving as a resistor. As the VDS rises above 1.2 V a curved response is observed, resembling a diode. This voltage corresponds well with the potential at electrolysis of water occurs and the water decomposes into oxygen and hydrogen gases (1.23 V).

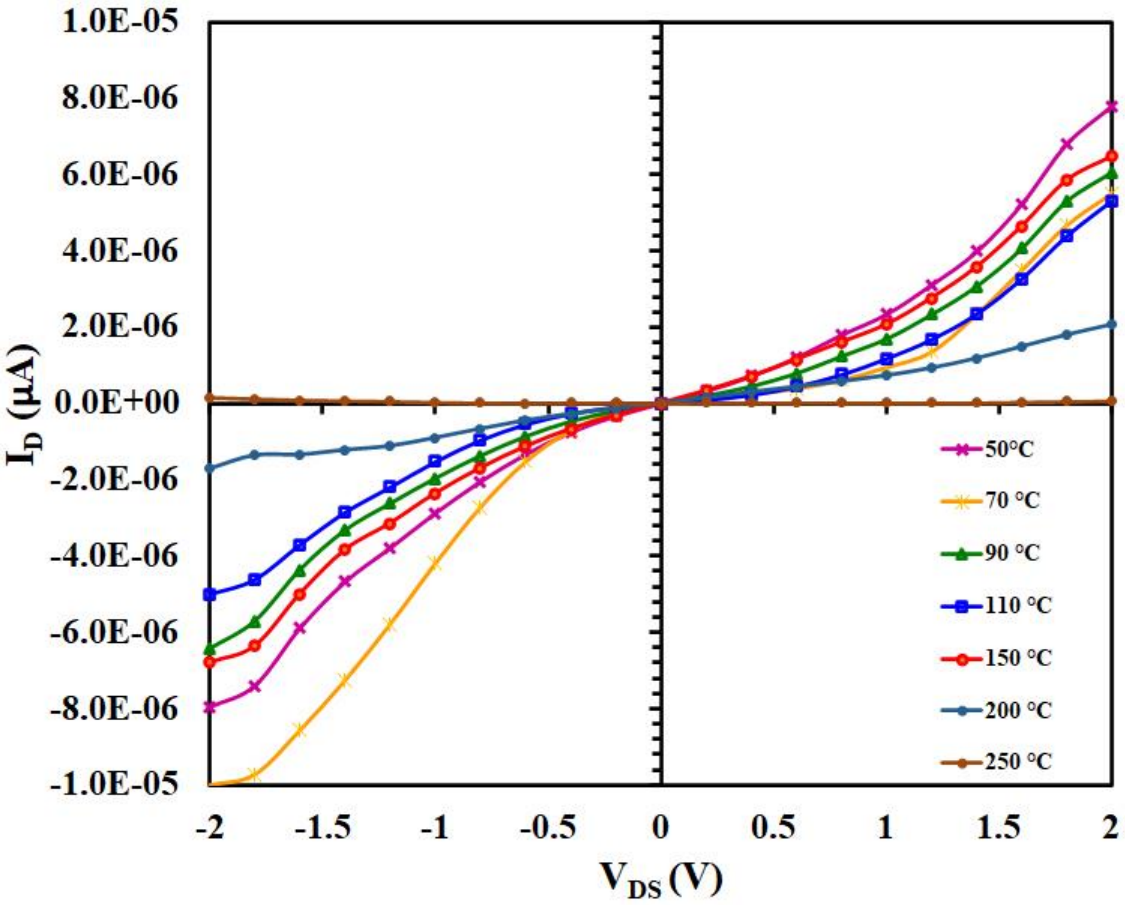

Figure 4.17: Output characteristics of the bilayers film P3HT/Water, P3HT 71 nm at the following annealing temperatures: 50 ºC, 70 ºC, 90 ºC, 110 ºC, 150 ºC, 200 ºC and 250 ºC.

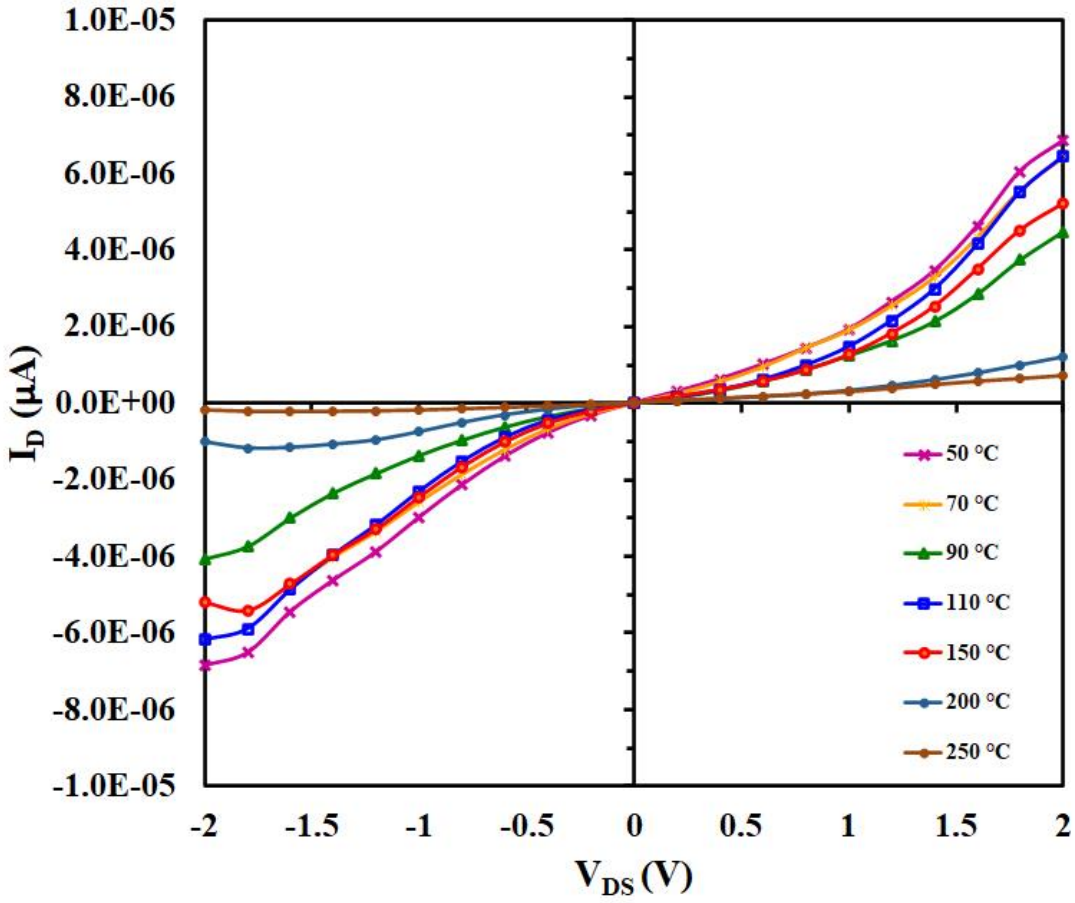

Figure 4.18: Output characteristics of the bilayers film P3HT/Water, P3HT 113 nm at the following annealing temperatures: 50 ºC, 70 ºC, 90 ºC, 110 ºC, 150 ºC, 200 ºC and 250 ºC.

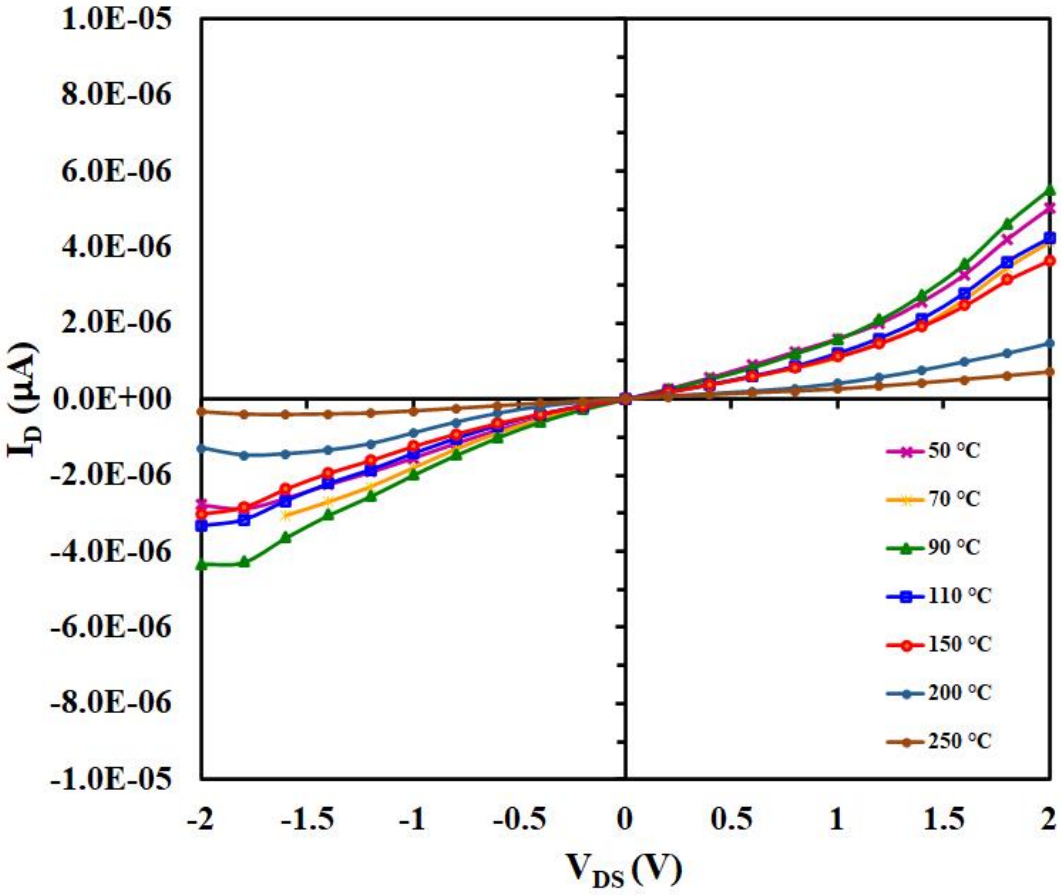

Figure 4.19: Output characteristics of the bilayers film P3HT/Water, P3HT 135 nm at the following annealing temperatures: 50 ºC, 70 ºC, 90 ºC, 110 ºC, 150 ºC, 200 ºC and 250 ºC.

4.5.2 Characterising the effect of the addition of water on Nafion films

Unlike P3HT, Nafion is a already hydrated polymer and as such the addition of water may be expected to have little or no effect on the polymer properties. Water content of the annealed membrane will decrease with increasing annealing temperature resulting in a change of the microstructure of the membranes. Figure 4.20 shows the architecture of the Nafion/water samples that have been used in this study. While Figure 4.21 shows the I-V curves of these samples as a function of annealing temperature.

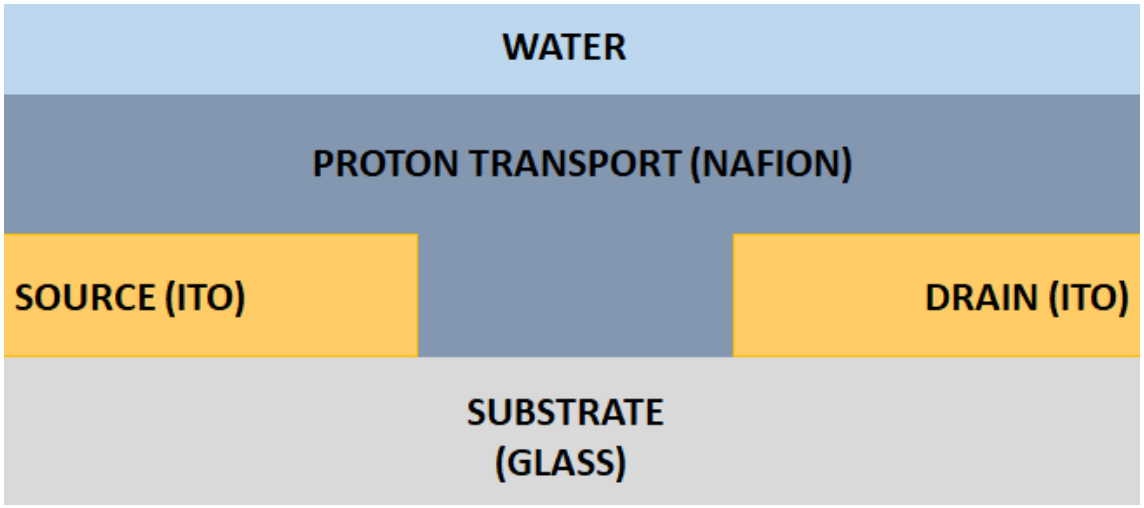

Figure 4.20: Cross-sectional schematic of Nafion samples with water addition as used in this study.

We would expect that annealing the Nafion films at or above 100 °C would result in dehydration and significant changes to the properties of the film. However, Figure 4.21 shows that there is very little impact of annealing temperature on the electrical characteristics of the Nafion/water samples up to the maximum annealing temperature used here of 250 °C. We speculate that this is due to uniform rehydration of the Nafion films following their dehydration to various degrees during annealing. If we compare Figure 4.21 with Figure 4.8, we can clearly see that there is little impact of the addition of water to Nafion as predicted.

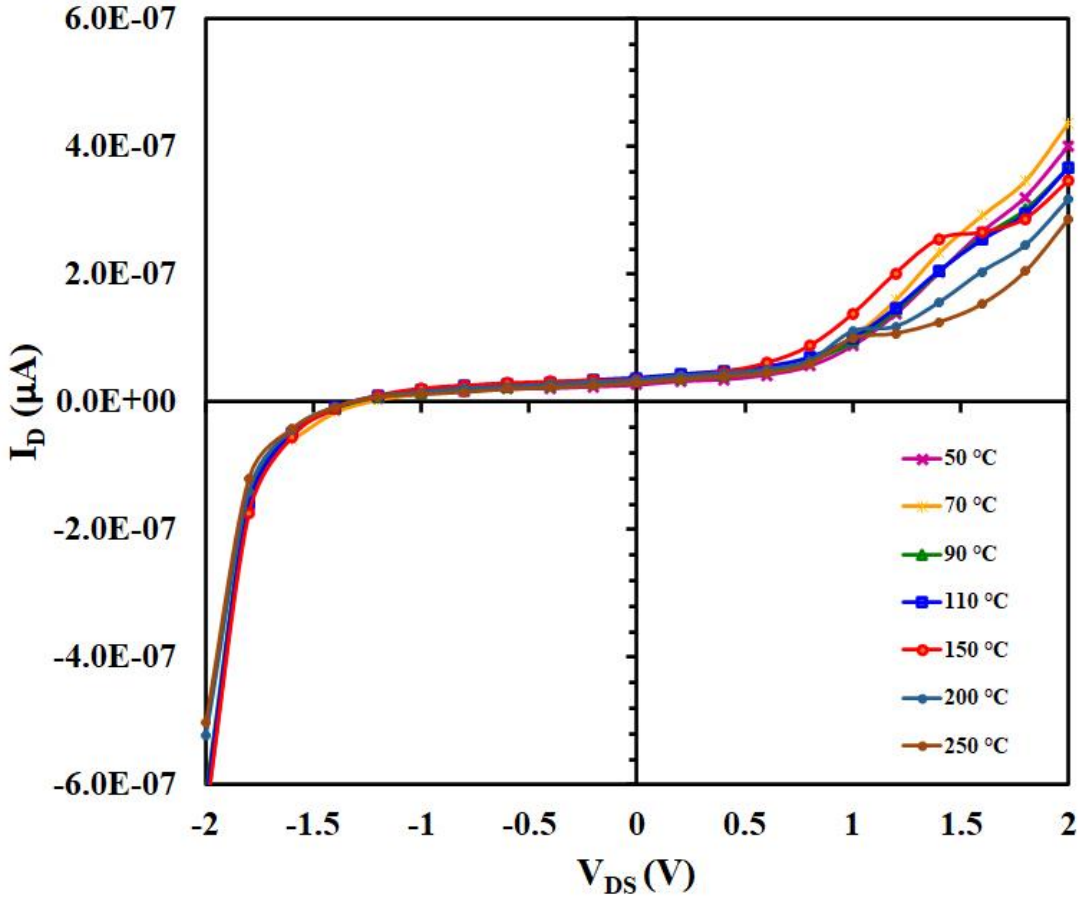

Figure 4.21: Output characteristics of the bilayers film Nafion/ Water with varying the temperatures (50 ºC, 70 ºC, 90 ºC,110 ºC,150 ºC,200 ºC and 250 ºC).

4.5.3 Characterising the effect of the addition of water on the P3HT/Nafion bilayers

In this section we quantify the effect of water upon the electrical properties of a P3HT/Nafion bilayer. This experiment simulates the effect of adding the water component of an analyte to the materials and thus provides us an opportunity to quantify the 'non-glucose' effects of an analyte sample. The structure of the prepared samples used in this study is shown in Figure 4.22.

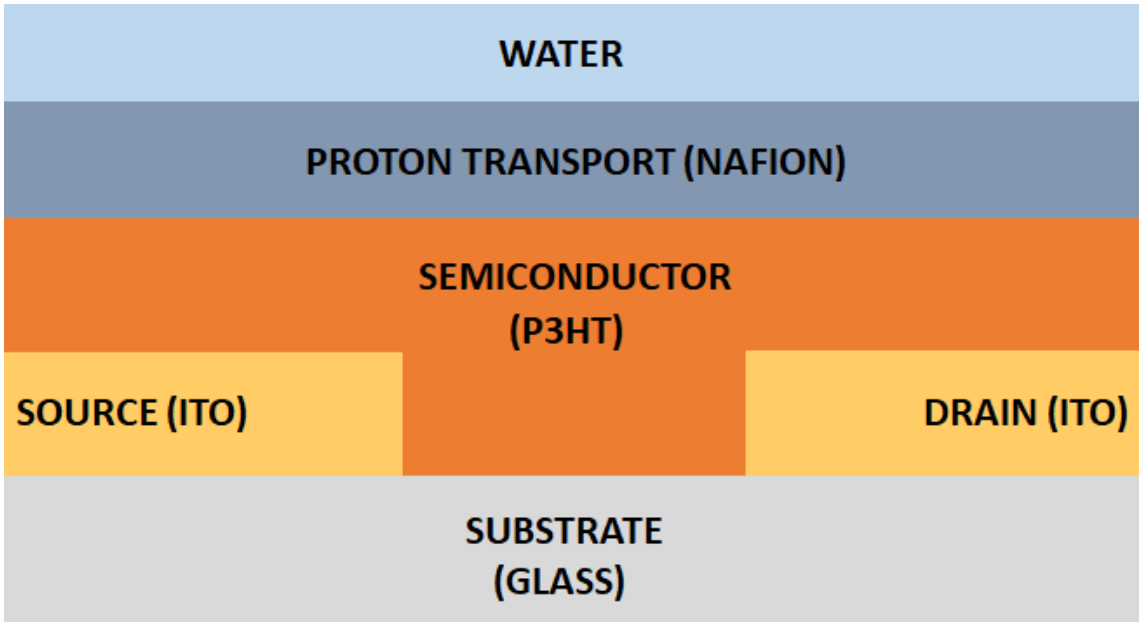

Figure 4.22: Cross-sectional schematic of P3HT/Nafion samples with water addition as used in this study.

As discussed previously, addition of Nafion enhances the current dramatically as compared to the neat P3HT films. This effect is clearly still present in the bilayers where water has been added, as shown in Figure 4.23, Figure 4.24 and Figure 4.25 Nafion, when saturated in water, has excellent proton conductivity [290-293] and so the hydrated P3HT/Nafion bilayer might be expected to have increased P3HT doping and higher conductivity. However, water addition will also lead to swelling of the Nafion and P3HT/Nafion interface which may lead to reduction of the doping density of the P3HT and reduced conductivity of the doped region. Figures 4.23, 4.24 and 4.25 however, show very little difference in their electrical properties in comparison to the equivalent "dry" samples (Figures 4.10, 4.11 and 4.12) and so these effects described above on the P3HT/Nafion bilayer appear to be negligible, as was the case in the neat Nafion films presented in Section 4.5.2. The one observable difference is that the "dry" samples (Figures 4.10, 4.11 and 4.12) show a maximum current at 200 °C, whilst the "wet" samples here show a maximum current at 150 °C. Otherwise the current magnitudes and trends are very similar.

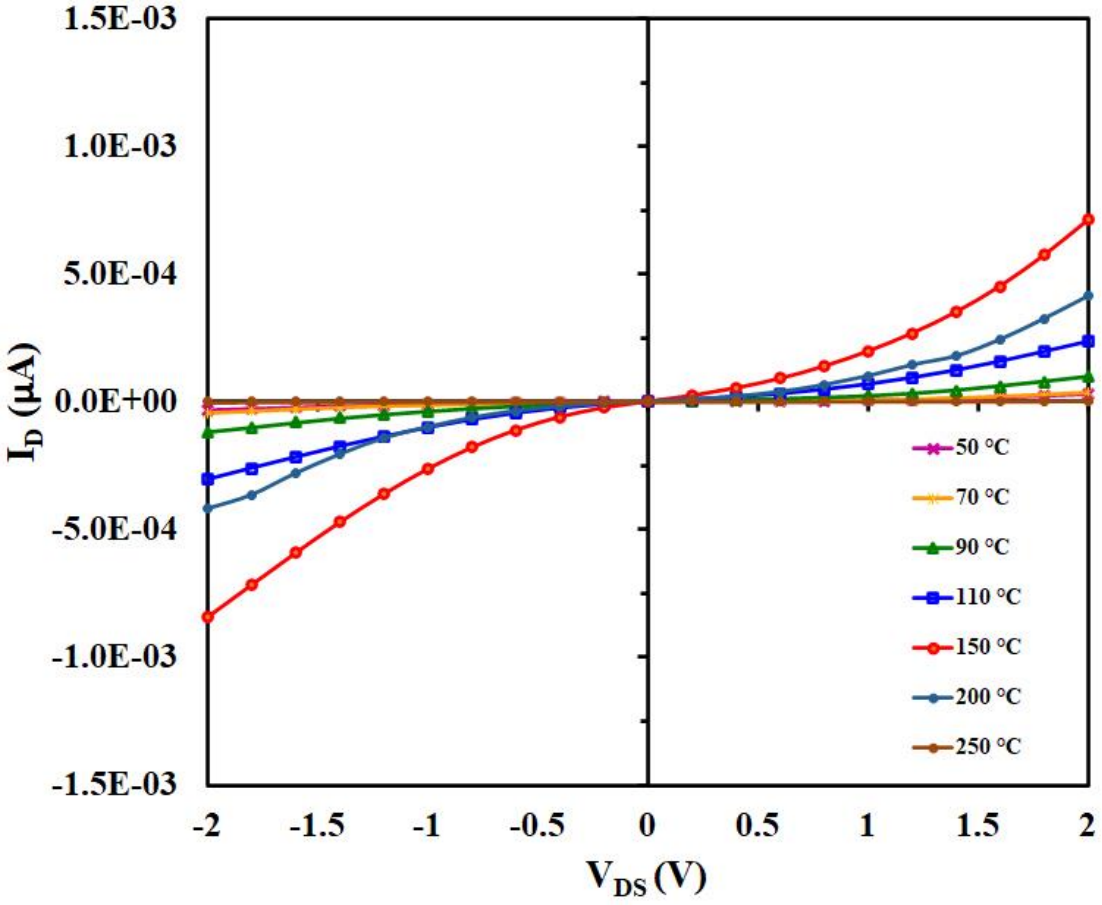

Figure 4.23: I-V characteristics of the P3HT/Nafion bilayer with /water addition for a 71 nm thick P3HT film. The bilayer was annealed at50 ºC, 70 ºC, 90 ºC, 110 ºC, 150 ºC, 200 ºC and 250 ºC.

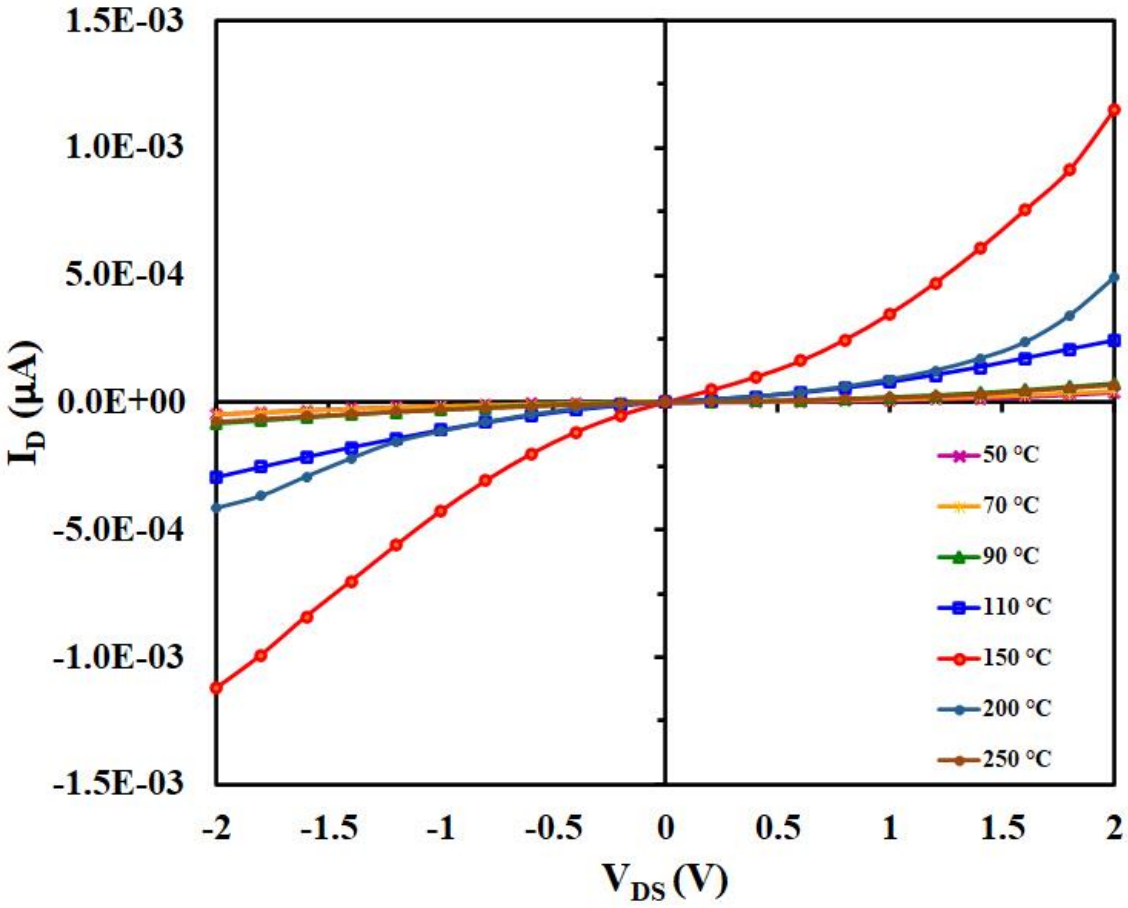

Figure 4.24: I-V characteristics of the P3HT/Nafion bilayer with /water addition for a 113 nm thick P3HT film. The bilayer was annealed at 50 ºC, 70 ºC, 90 ºC, 110 ºC, 150 ºC, 200 ºC and 250 ºC.

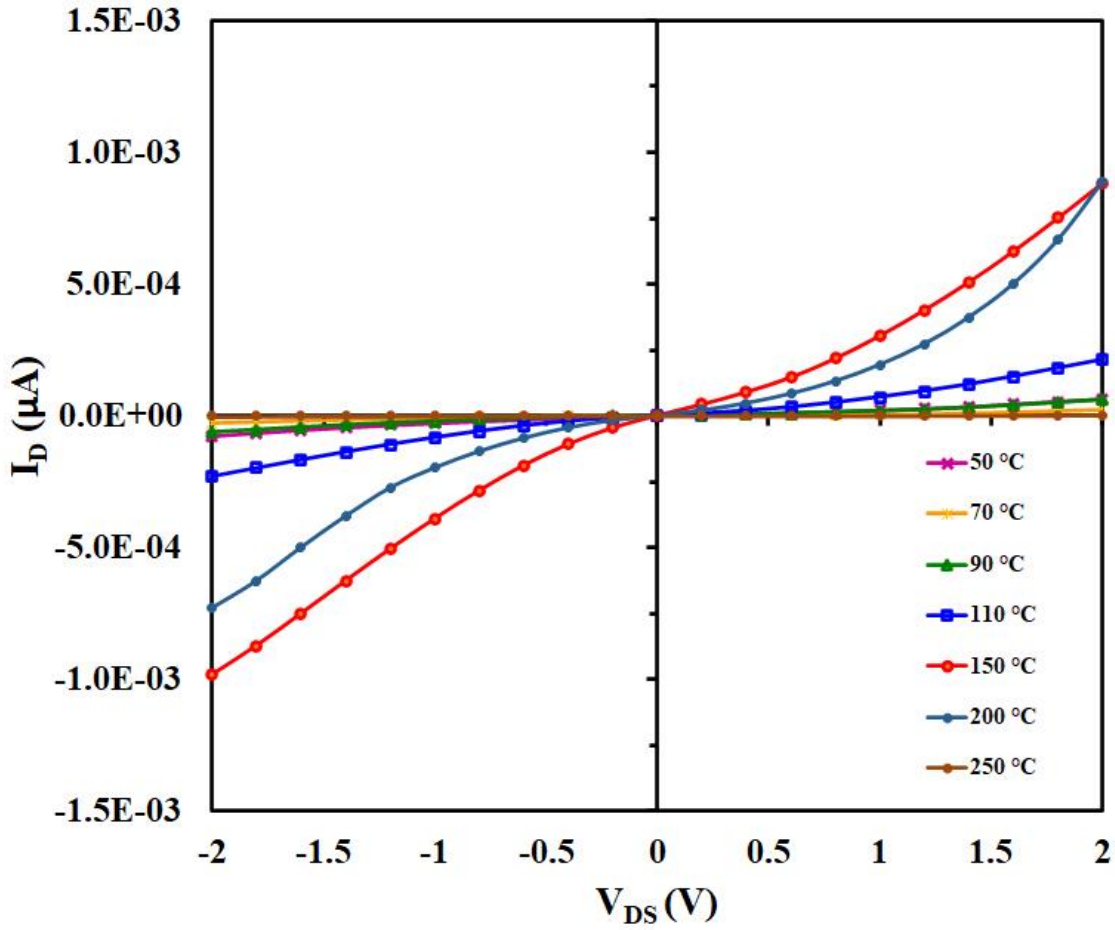

Figure 4.25: I-V characteristics of the P3HT/Nafion bilayer with water addition for a 135 nm thick P3HT film. The bilayer was annealed at 50 ºC, 70 ºC, 90 ºC, 110 ºC, 150 ºC, 200 ºC and 250 ºC.

4.6 Characterising the Effect on Sensor Characteristics of Device Annealing Temperature.

We have established the effect of annealing on the conductivity of component P3HT and Nafion films, and the P3HT:Nafion bilayer, as well as the effect of the subsequent addition of deionised water to the conductivity these films. In this Section we will establish how the annealing of the P3HT:Nafion bilayer effects the output of the complete GOX-based glucose sensor.

P3HT:Nafion bilayer devices were prepared as described in Section 4.2.2, except that a 20 mg/mL mixture of GOX in as-received Nafion solution was

drop-cast onto the P3HT layer, rather than just neat Nafion. These bilayer devices were then annealed at temperatures of 50 ºC, 70 ºC, 90 ºC, and 150 ºC for 2 minutes, cooled and treated with 10 µL of 0 mM, 0.01 mM, 0.1 mM, 1 mM or 10 mM glucose solutions in deionised water. V_{DS} was set at -1 V, V_{GS} at -0.3 V and the device drain current (I_D) was then monitored as a function of time.

Figures 4.26 a-d show calibration curves for devices annealed at 50 ºC, 70 ºC, 90 ºC, and 150 ºC and treated with 0 mM, 0.01 mM, 0.1 mM, 1 mM and 10 mM glucose solution, respectively. It was noted that the drop in I_D immediately after analyte addition (attributed to dedoping of the P3HT channel) was particularly variable in this set of data. We attribute this to variability in the hydration of the Nafion films – either as a result of a longer delay between device fabrication and measurement or changes in the ambient conditions. Consequently, a different FOM was chosen for this set of data. Instead of normalising to a point just prior to analyte addition, which means that the drop due to the water itself is included in the measurement, the minimum I_D (maximum negative current) reached after analyte addition was chosen as the point of normalisation. Thus, measurement of the change in I_D due to the water addition is minimised and the vast majority of the I_D change is due solely to the glucose. As such, the I_D data presented in the plots is normalised at $I_{D(max)}$ and the difference between this and the I_D at t = 800s is plotted. For all points the data is the average of a minimum 6 repeat samples.

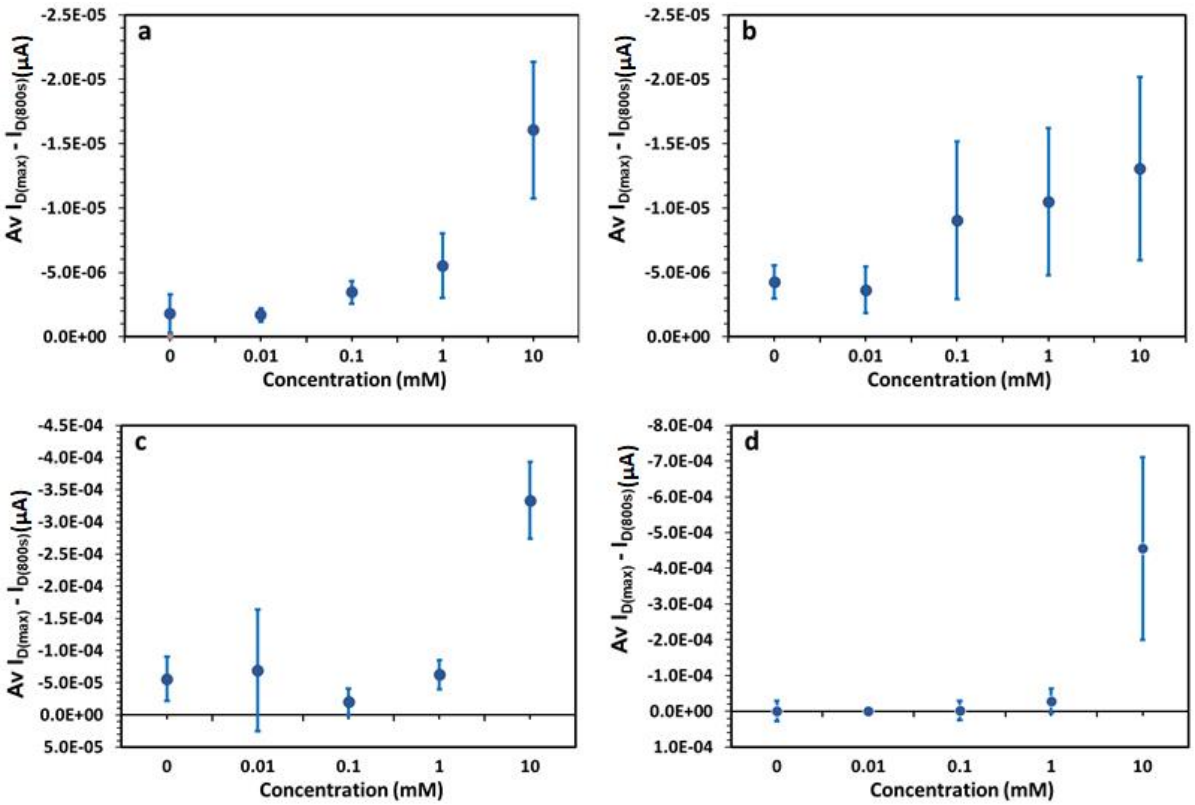

Figure 4.26: Plots of $I_{D\,(max)}$-$I_{D\,(800s)}$ as a function of glucose concentration (0 mM, 0.01 mM, 0.1 mM, 1 mM and 10 mM) for P3HT / Nafion: GOX devices annealed at a) 50°C, b) 90°C, c) 150°C and d) 200°C. Error bars represent one standard deviation for a minimum of 6 replicate measurements

If we focus on the data for 0 mM glucose (deionized water) we see that this data corresponds well with that presented in Section 4.5.3. The drain current starts low (~ $1x10^{-6}$ A) with 50 °C annealing, increases as the annealing temperature increases to 150 °C (~ $5x10^{-5}$ A), before dropping again at an annealing temperature of 200 °C (~ $1x10^{-7}$ A). At higher glucose concentrations we observe that $I_{D(max)}$-$I_{D(800s)}$ generally increases with increasing glucose concentration and annealing temperature. At low glucose concentrations (0 - 0.1 mM) there is little obvious correlation between the drain current and glucose concentration and, overall, the sensitivity across the higher annealing temperatures is not high, with the error bars associated with the currents exceeding the differences between I_D at sequential current in almost all cases. Interestingly, the error associated with drain current consistently increases as

the drain current increases, meaning that the calibration curves with the highest I_D currents are not necessarily the most sensitive, nor do they show the best correlation between I_D and glucose concentration. Indeed, whilst it shows a maximum I_D of only -1.5×10^{-5} A for 10 mM glucose, the devices annealed at 50 °C show the best sensitivity and correlation with glucose concentration. In addition, the use of a low energy process (such as low temperature annealing) is a distinct advantage in a fabrication which may be scaled to large production runs, especially where higher temperatures are known to degrade materials and change device morphology. Consequently, 50 °C was chosen as the annealing temperature for devices in subsequent experiments.

4.7 Conclusion

In this study, we characterised and optimised the annealing conditions for the OTFT based glucose sensors presented in this thesis. We demonstrated the effect of varying P3HT thickness on the conductivity of the P3HT/Nafion bilayer, the characteristics of which is crucial to device performance. We discovered that the addition of Nafion on to the P3HT channel results in an increase in conductance which is two orders of magnitude higher than either pure P3HT or Nafion. This increase is attributed to the formation of a doped intermixed layer which forms between the pure P3HT and Nafion domains.

Annealing of the bilayer, for temperatures up to 200 ºC results an increase in the conductance while at 250 ºC the conductance drops dramatically. We hypothesise that this increase in conductance is consistent with an increase in the volume of the intermixed/doped P3HT/Nafion region at the interface. This hypothesis is supported by the observation that the greatest increases in conductance are observed at annealing temperatures above 100 ºC which coincides well with the glass transition temperature of Nafion (114 ºC).

Addition of water to the annealed films appears to have little effect upon the conductance of the pure or bilayer films.

Finally, annealing of the full P3HT/Nafion:GOX sensor device at 50 °C appears to give the best correlation of I_D with glucose concentration. Whilst higher values of I_D are observed for devices annealed at higher temperatures, the errors associated with these values also increase (resulting in less sensitivity to the concentration) and the correlation between I_D and glucose concentration is no longer clearly monotonic.

Chapter 5: PAN Film Fabrication and PAN-mediated Devices

5.1 Introduction

Throughout Chapters 3 and 4 we have established a base sensor architecture for glucose sensing comprising ITO source and drain electrodes on a glass substrate, a film of P3HT as a conducting polymer channel material and a film of GOX embedded in Nafion as the sensing element, a binding layer and a proton transport material. Nafion is a polymer film that is commonly used in the preparation of glucose biosensors [294-296]. However, Nafion is unstable in aqueous solutions and, thus, the embedded enzyme molecules can be lost from the electrode surface. In addition, Nafion is a highly polar polymer and, as such, aqueous analytes will wet the film, spreading across its surface[297]. Consequently, much of the analyte may move from its initial location above the source-drain channel, which may in turn lower the magnitude and sensitivity of the sensing mechanism.

In order to address these issues, in this Chapter we investigate the use of a porous capping layer to sit on top of the Nafion. This layer is designed to absorb and embed the GOX, preventing its subsequent loss upon analyte addition, and to help to locate the analyte above the source-drain channel via wicking. Polyacrylonitrile (PAN) was initially chosen as a candidate for this capping material and its suitability is explored in this Chapter.

Polyacrylonitrile (PAN) is a non-conducting polymer that is widely used for producing membranes due to its good solvent resistance properties [298]. It is an important polymer in the manufacturing industry, is commonly applied in structural composites and is an the essential material for aerospace composites because of its hardness and strength [299, 300] .

PAN has attracted considerable research attention over the last decades not only due to its excellent mechanical and fibre forming properties for textiles [301, 302] and membranes [179, 303, 304], but also as precursors for carbon fibres [305, 306]. The chemical structure of PAN can be seen in Figure 5.1.

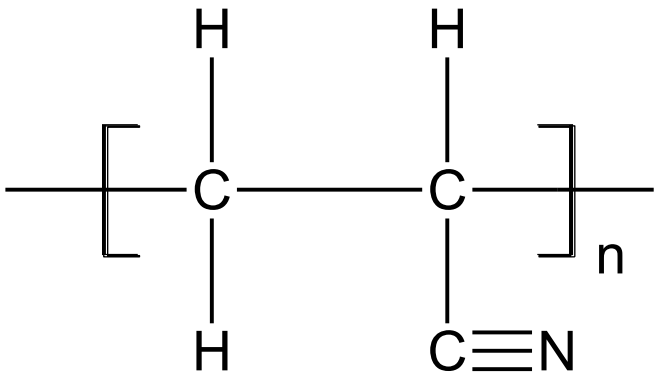

Figure 5.1: Chemical structure of PAN.

PAN membranes have attracted much attention due to a variety of excellent characteristics, such as the cost and large-scale commercial availability of the precursor material and the film's tolerance to most solvents [307, 308]. Moreover, PAN has an additional favourable attribute that contributes to its common usage; it has high wettability for aqueous solutions which allows water to spread evenly on the surface during processing [309]. As such, PAN was selected as an appropriate material for the enzyme-containing porous layer in this study due to its high chemical, mechanical and thermal durability [310] compared to other polymeric materials and its compatibility with the enzyme. In addition, PAN can easily be fabricated as a porous film with pore sizes suitable for enzyme incorporation [311-314]. PAN has a high melting point and a high degree of control over its molecule orientation is possible [315]. Modifications of PAN membranes have expanded its use into many biomedical fields [304].

In biomedical applications PAN is often used as a filament forming matrix for producing medicated fibers by dry spinning, wet spinning [316, 317] and electrospinning [318] . Previously, studies have been reported for PAN based biosensor designs; one of these studies used the electrochemical adsorption of glucose oxidase in a PAN film. Although a PAN biosensor was developed there were some limitations to the biosensor performance, such as low sensitivity and stability due to the hydrophobicity of the host (non-PAN) organic polymer [319]. These limitations were addressed by designing a modified biosensor which used pendant carboxyl groups (-COOH) to graft the glucose oxidase into the PAN film using acrylonitrile-co-acrylic acid [320].

Native PAN does not have active groups available for enzyme immobilisation [321]. However, chemically modified PAN has been used successfully to immobilise enzymes [313, 314, 322, 323]. Recent studies using this approach have investigated the incorporation of biomacromolecules such as heparin, chitosan and human serum albumin into PAN fibre membranes. These studies have aimed to improve the biocompatibility and the hydrophilicity of the PAN fibre-based membranes, where enzymes are immobilised onto PAN based membranes to improve their hemocompatibility [324, 325]. Similarly, different comonomers such as glycidyl methacrylate [326, 327] and phospholipid moieties have been incorporated into PAN to improve its biocompatibility and hydrophilicity [179]. In this study, the aim is to include GOX into the PAN layer without chemical modification of the PAN or covalent bonding between the polymer matrix and the enzyme. It is believed that the porosity of the PAN will facilitate entrapment of the enzyme and improve device performance.

The most commonly used polar organic solvents for the processing of PAN are dimethyl sulfone ($DMSO_2$), dimethyl sulfonate (DMSO), ethylene carbonate (EC), propene carbonate (PC), DMF, and N,N-dimethyl acetamide (DMAc)

[179, 182, 328, 329]. These organic solvents undergo dipole−dipole interactions with the nitrile groups of the PAN facilitating dissolution of the solid. The physical properties of PAN in the solid-state are then highly influenced by the interactions of these organic solvents [330, 331].

The fabrication of a highly porous organic film is not a trivial matter. The field of membrane science has undergone significant growth originating with the preparation of asymmetric type membranes by Loeb and Sourirajan [332]. Several techniques have been used significantly in synthetic membrane processing including spin coating, screen printing and conventional printing methods and phase inversion. The purpose is to process the material using a convenient technique to produce a membrane structure with a morphology appropriate for the specific application [333, 334]. As such, the phase inversion method has been commonly used for producing porous synthetic polymeric membranes [333, 335, 336]. In this process, the polymer membrane is prepared by immersing a highly concentrated, viscous solution of the polymer into a bath of a non-solvent which is miscible with the solvent used in the polymer solution. Exchange of the solvent and non-solvent leads to solidification of the polymer as a porous material [334, 337]. These exchanges are caused by interdiffusion of the casting solvent and the non-solvent and result in a phase transition by which the membranes are formed. When a conducting polymer is used Kim et al. noted the conductivity of the polymer film can be enhanced by the use of DMF or DMSO [155]. In this study, PAN membranes are prepared by the phase inversion process with post-treatment (annealing) from a casting solution of DMF and DMSO and a variety of non-solvents.

The initial idea of the phase inversion method was proposed and developed by Cohen et al. [338]. PAN is one of the polymers most commonly used for preparing membranes by phase inversion [339] owing to the physical and

chemical properties discussed above [339, 340]. For example, Musale et al. and Musale and Kumar have prepared chitosan composite ultrafiltration and nanofiltration membranes using PAN and the phase inversion technique [341, 342]. These films offer an alternative to films produced from inorganic materials such as silica or carbon and allow exquisite control of the pore shapes and size, which are of vital significance in many fields of technology such as separation processes, biocatalysts and heterogenous catalysis [343].

Polymer composite membranes have often been produced using polyacrylonitrile as a polymer fiber and DMF as a solvent while a flat sheet method is used for fabricating continuous PAN membranes. The flat sheet method uses the phase inversion process and involves templating the PAN solution on a flat plate during phase inversion resulting in a flat sheet. This type of highly porous membrane has been typically used in ultrafiltration processes since these films allow a high rate of water filtration, predominately due to the high porosity and interconnected pore structure [183, 344].

As stated above, we have focused our attention on DMF and DMSO as solvents for the phase inversion process [182, 345]. DMSO is a widely used solvent which has attracted attention in a variety of applications associated with biology, chemistry, industry and pharmacology [346]. It is often considered a super solvent because it can dissolve a wide range of organic and inorganic compounds well and therefore facilitates ease of fabrication [347]. DMF is also suitable for this purpose due to its wide solubility range for both organic and inorganic compounds, thermal stability, high polarity and wide liquid temperature range [348]. In addition is a less hazardous solvent to work with (than DMSO) and hence was preferred for the experiments described hereafter. Because of these unique properties, DMF has been used as a common solvent in the preparation of colloids [349-351] and many types of organic chemistry reactions [352].

In particular our study will describe the fabrication of phase inverted PAN films and the effect of temperature on the properties of the films produced by this method. The phase inversion method has been commonly used for the preparation of porous polymeric membranes [333, 336, 353] and was therefore considered ideal for the preparation of the enzyme-containing porous layer. Kesting et.al, 1985 have specifically noted that polymer solutions (PAN/DMF) or (PAN/DMSO) can be fabricated into porous membrane films by the phase inversion process [319]. We cast the PAN solution prior to phase inversion using two methods: a draw bar technique and spin coating. In the current work, spin-coating is found to result in more homogenous PAN films whereas the draw bar method can produce thicker films. For the formation of enzyme containing capping films it was felt that thicker (μm) films would be desirable. Post-phase inversion heat treatment was shown to affect the physical properties of the PAN films and was carefully adjusted to control pore size and defects in the PAN membrane.

There several factors which have an important influence on the properties of the PAN film. Key among these are: the spin coating conditions, wet film thickness, polymer solution volume and concentration, choice of non-solvent and washing procedures. Spin coating is widely employed for creating thin (<100 nm) films. However, in our study, we wanted to try to use spin coating to create thick polymer films. It was found that the spin speed and acceleration strongly influenced the thickness and morphology of the PAN film. In addition, increasing the concentration of the PAN solution led to increased viscosity and inhomogeneity of the resultant PAN film.

Another factor that plays an important role in PAN film fabrication is annealing. Consequently, annealing temperature was also investigated as an experimental lever to control the morphology of the PAN. It was hypothesised that significant changes in the PAN film morphology might be expected to be related to the polymer glass transition temperature (T_g = 150 °C). As we will show, at annealing temperatures at, or in excess, of the T_g, dramatic changes in the appearance of the PAN film and its properties were observed. In particular, the surface pore size of the PAN membranes was reduced upon post-formation thermal treatment, consistent with the literature [354, 355]. Annealing temperature will therefore affect analyte incorporation and the rate of interaction between the analyte and other materials in the device. Consequently, the specific aim of this study was to understand the effect of a range of fabrication parameters and post-fabrication annealing upon phase-inverted PAN film characteristics.

5.2 Experimental

5.2.1 Materials and method

Polyacrylonitrile (PAN) powder, (M_W 150 000 g/mol), DMF and DMSO were used as supplied (all purchased from Sigma Aldrich). The chemical structures for these materials are shown in Figure 5.2. Acetone, deionised water (H_2O), chloroform ($CHCl_3$), isopropanol (IPA), methanol and ethanol were used as non-solvents throughout these experiments (DI water was produced in-house, all other solvents were reagent grade and purchased from Sigma Aldrich). The experiments were carried out at room temperature in air.

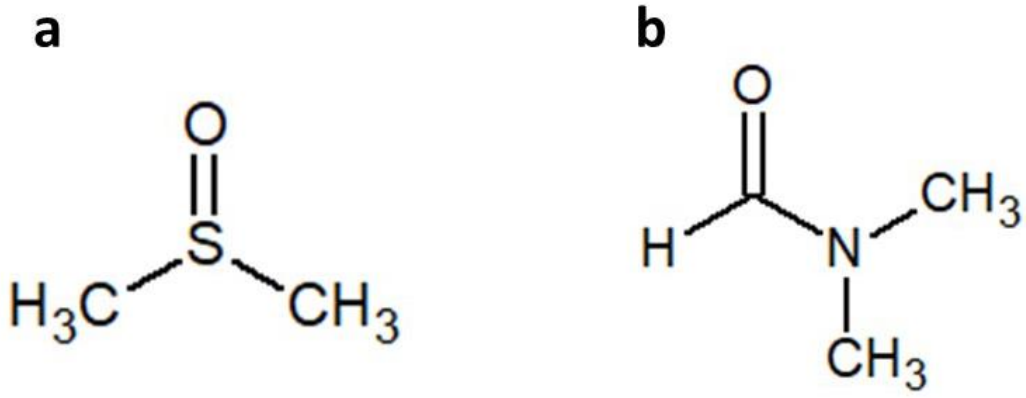

Figure 5.2: (a) Dimethyl sulfoxide (DMSO). (b) N, N-Dimethylformamide (DMF).

5.2.2 Preparation of the polymer (PAN) membrane

5.2.2.1 Preparation of wet PAN films using spin coating

As discussed above, PAN has been identified as a highly appropriate material for the enzyme-containing porous layer in glucose sensors and we propose used phase inversion to produce these films. Prior to phase inversion, "wet" PAN films consisting of the still-solvated polymer must be prepared and, in this work, we prepare such wet films using either spin coating (described here) or a drawbar method (described in Section 5.2.2.2).

Glass substrates of size 2 cm × 2 cm were cleaned before use according to the following method: (1) washing with detergent solution, (2) rinsing with distilled water, (3) use of N_2 gas to remove any surface dust. PAN powder was dissolved in DMF or DMSO at a concentration of 200 mg/mL and then the mixture was stirred at 30 ˚C until homogenous (which took approximately 5 hours). The polymer mixture (85 µL) was pipetted onto a clean glass slide and the slide was

then spun at 500 rpm at 1330 rpm/s^2 for 60 seconds using a Laurel WS-400 A-6 NPP/LITE (UK) to spread the polymer solution evenly.

To complete the phase inversion process, the wet polymer film is immersed with 90 mL of a non-solvent for 10 minutes with the non-solvents exchanged twice during that period to ensure removal of the residual solvent (DMSO or DMF). The non-solvents that were trialled for preparation of PAN films are ethanol, acetone, chloroform, water, isopropanol, and methanol. The steps for preparing the phase inverted, porous PAN film is summarised in Figure 5.3.

A challenge that we faced in these experiments was the difficulty to control the pore size of the resultant PAN film. These difficulties (specifically in reducing the pore size of the PAN film) typically result from the poor solubility of PAN with solvents, except for polar solvents (DMF and DMAc) [336]. Previously, successful attempts to modify the pores in PAN membranes were achieved by using NaOH and C_2H_5ONa to set the pore size and following pore formation cross-linking the film at high temperature to stabilise the pores [336]. In the current study, we have implemented annealing to evaluate the effect of thermal treatment on the pore size, using temperatures ranging from 50 ˚C to 250 ˚C. These results are presented in Section 5.3.

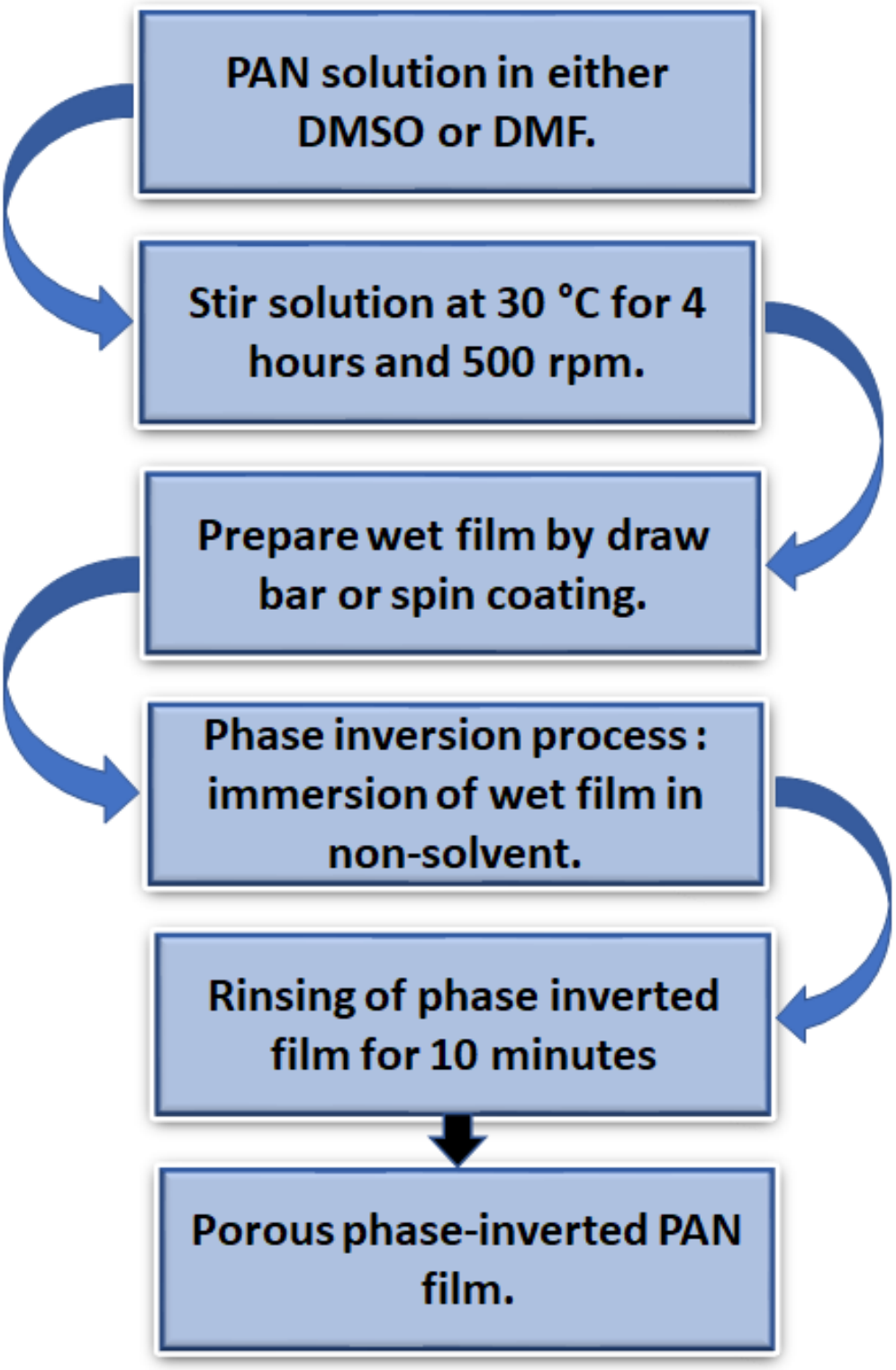

Figure 5.3: Schematic depicting the steps of preparing a thick phase inverted, porous PAN film

5.2.2.2 Preparation of wet PAN films using the drawing bar technique

The draw bar method is another method which was investigated for the making of the wet PAN films prior to phase inversion. The technique uses a glass substrate and tape as a depth guide for the glass rod which smooths the viscous PAN solution into a wet film prior to phase inversion by immersion in a reservoir of non-solvent [356]. Compared with other template syntheses, the draw bar method used here to prepare PAN membrane is very easy and straightforward. The PAN membranes were prepared by the following process:

1) The PAN solution is deposited onto a piece of PET (15 cm × 15 cm) which is temporarily adhered to a glass plate (20 cm × 20 cm) at room temperature as shown in Figure 5.4.

2) Strips of a polyacetate adhesive tape were used to make depth-defining guide rail for the draw bar. The number of layers used was 20, which gave a total rail thickness of 516 ± 3 μm.

3) A glass rod was used as the draw bar to distribute the solution evenly and uniformly across the surface of the glass plate.

4) The phase inversion was carried out by direct immersion of the wet polymer film and substrate in one of the following non solvents: The solvent diffuses into the non-solvent resulting in a porous polymer film. Care must be taken when controlling the glass rod to distribute the solution evenly and uniformly on the surface. The cross section of the draw bar technique can be seen in Figure 5.5.

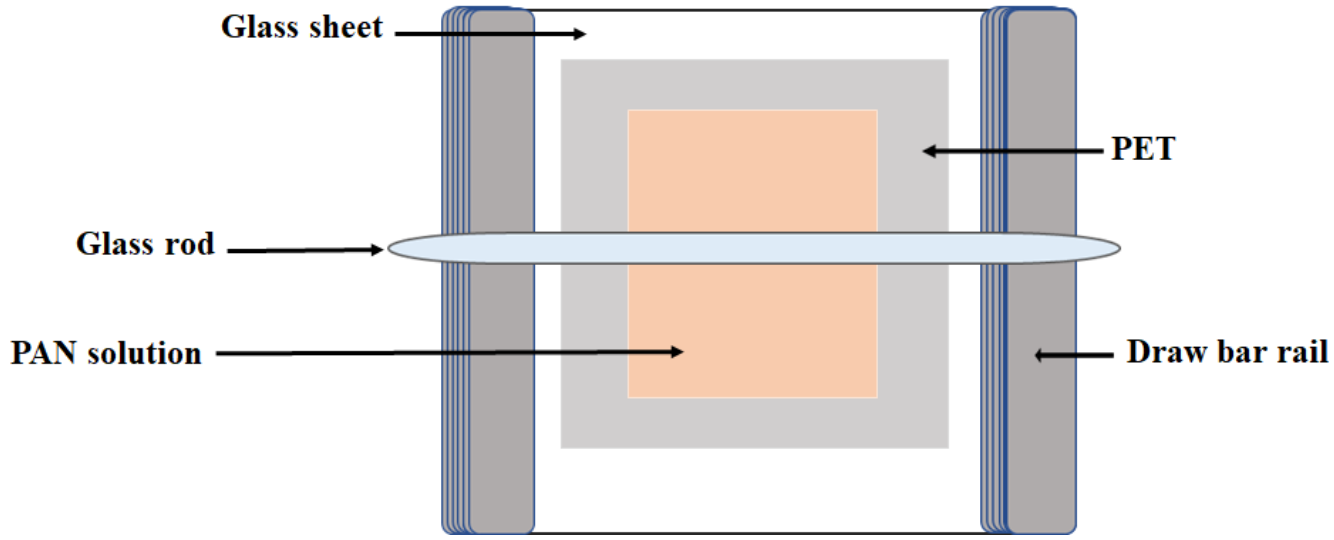

Figure 5.4: Schematic of the draw bar technique

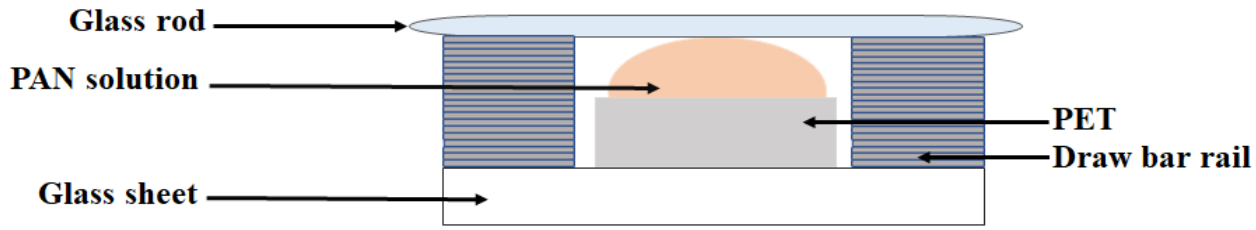

Figure 5.5: Schematic representation of the cross-section view of the draw bar technique.

5.3 Controlling and characterising the properties of the PAN film

There are a range of parameters that can be controlled in the fabrication of the phase inverted PAN film:

- Concentration of PAN in the chosen solvent
- The choice of solvent
- The choice of non-solvent
- Post-film formation annealing temperature
- Spin speed (for spin-coating)
- Height of guide rails (for draw bar)

By varying these parameters, we can modify the key PAN film characteristics of thickness and porosity. Several studies have highlighted that control of material properties such as polymer concentration is critical to PAN film morphology [357, 358].

In this section, the relationship between the temperature, thickness and concentration and the morphology of the PAN films prepared as described in Section 5.2 are characterised using atomic force microscopy (AFM) and scanning electron microscopy (SEM). In particular, the effect of the listed parameters on the porosity of the PAN films is qualitatively determined by this microscopy.

In this study, DMF was used as the solvent for PAN and water was used as the standard non-solvent. However, initially, a range of other non-solvents were tested to ascertain the morphology of the resulting films. The additional non-solvents trialled were acetone (C_3H_6O), chloroform ($CHCl_3$), methanol (CH_3OH), ethanol (CH_5OH), water (H_2O) and isopropanol (C_3H_8O). DMSO was also trialled as a solvent in this experiment.

Both scanning electron microscopy (SEM) and atomic force microscopy (AFM) have been used extensively to study the morphology of PAN membranes [355]. Initially, the surface morphology of PAN-DMF and PAN-DMSO membranes was examined by atomic force microscopy (AFM) for films prepared from a range of non-solvents. This technique was used as an initial survey of films to determine which solvent - non-solvent pair appeared most promising for the formation of porous PAN films.

The working principle of the AFM technique is based on a sharp tip that scans the device surface and measures the tip-surface interatomic forces. Three-dimensional morphology mapping of PAN – DMF films surface was determined by detecting the vibration frequency of the tip. Additionally, AFM can be used to quantify the interaction force between the membrane surface and the probe [359, 360]. As such, besides the surface morphology, additional information can be revealed; such as the electrical properties and the porosity of the surface [360, 361]. Primarily, however, AFM is used to provide the nanoscale lateral and vertical morphology of a film [359]. The choice of solvent and non-solvent is key to determining the membrane structure and interfacial characteristics. Different sets of compatible solvent and non- solvent pairs will have different and specific thermodynamic behaviour and miscibility [362, 363] leading to unique film morphology.

To evaluate the optimal solvent for solidifying PAN – DMF and PAN – DMSO films and governing surface and pore features, a range of non-solvents such as acetone, water, methanol, ethanol, propanol and chloroform were examined. In the current experiment, PAN – DMF and PAN – DMSO films were prepared by immersion of the wet film in the non-solvent for 10 minutes and then imaged by AFM. In this study, we aimed to evaluate the effect of various organic solvents on the surface features of PAN – DMF and PAN – DMSO membranes.

Figures 5.6 to 5.11 show 5 µm x 5 µm AFM images of DMF and DMSO based phase-inverted PAN films with non-solvents of acetone, chloroform, isopropanol, water, methanol and ethanol respectively. PAN films are immersed in these non-solvents for 10 minutes at 50 ºC. Tapping mode topography and the corresponding phase images of PAN films were recorded under ambient conditions to characterise the surface morphology of the films cast with the different non-solvents.

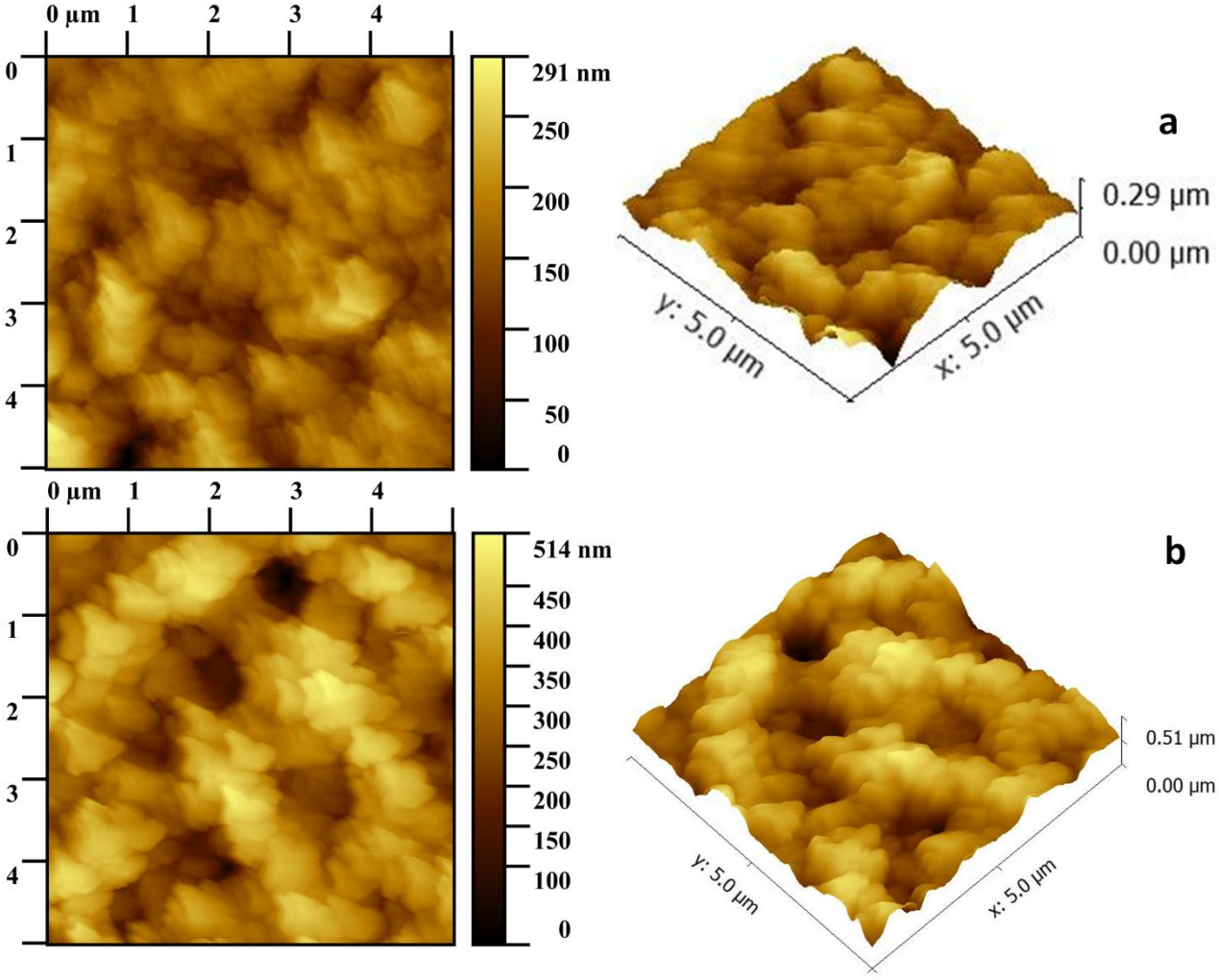

Figure 5.6: 5 µm × 5 µm scale topography and corresponding phase images of acetone treated PAN films by AFM in tapping mode (a) PAN-DMF and PAN- DMF 3D (b) PAN-DMSO and PAN -DMSO 3D.

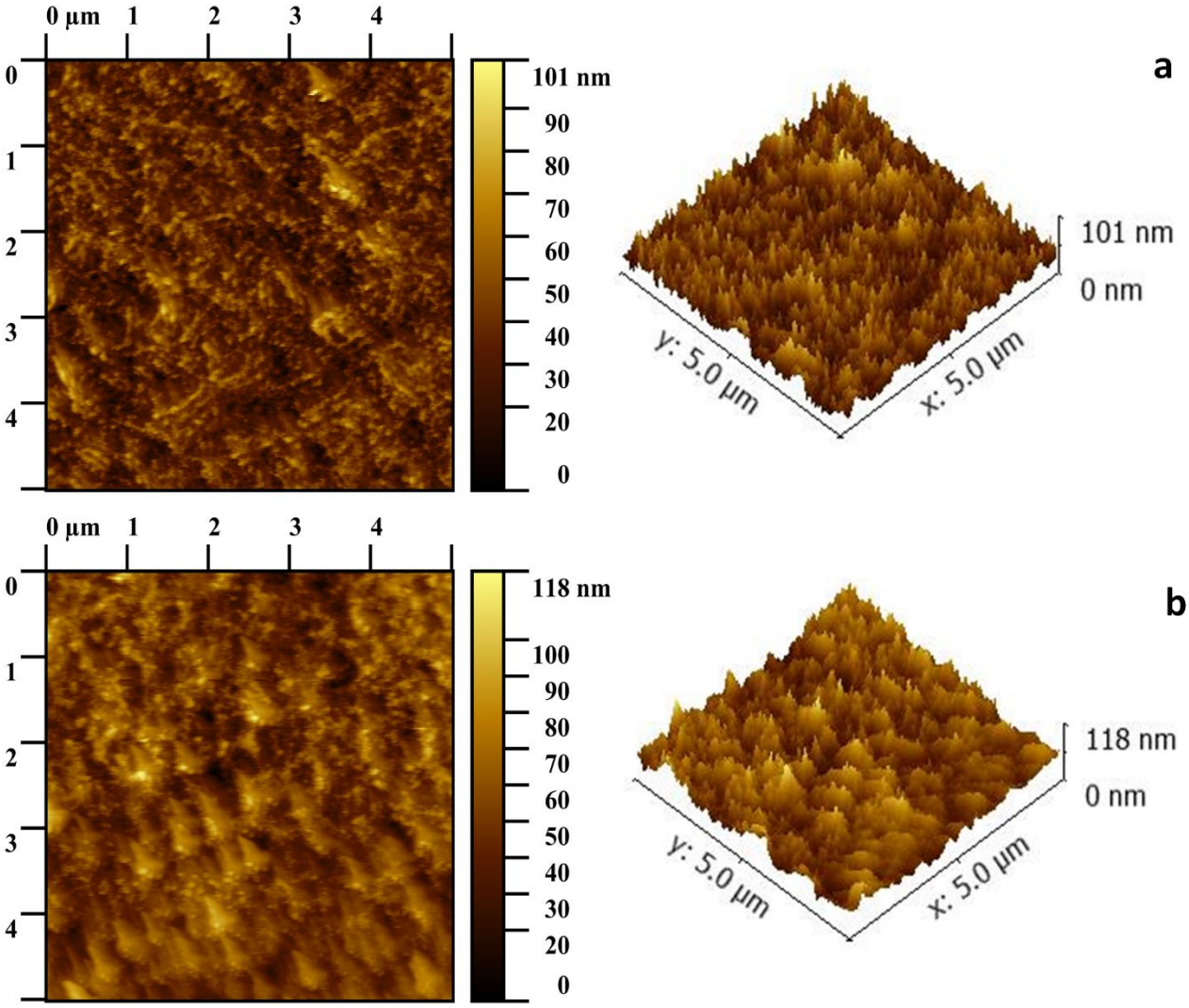

Figure 5.7: 5 µm × 5 µm scale topography and corresponding phase images of chloroform treated PAN films by AFM in tapping mode (a) PAN-DMF and PAN- DMF 3D (b) PAN-DMSO and PAN -DMSO 3D.

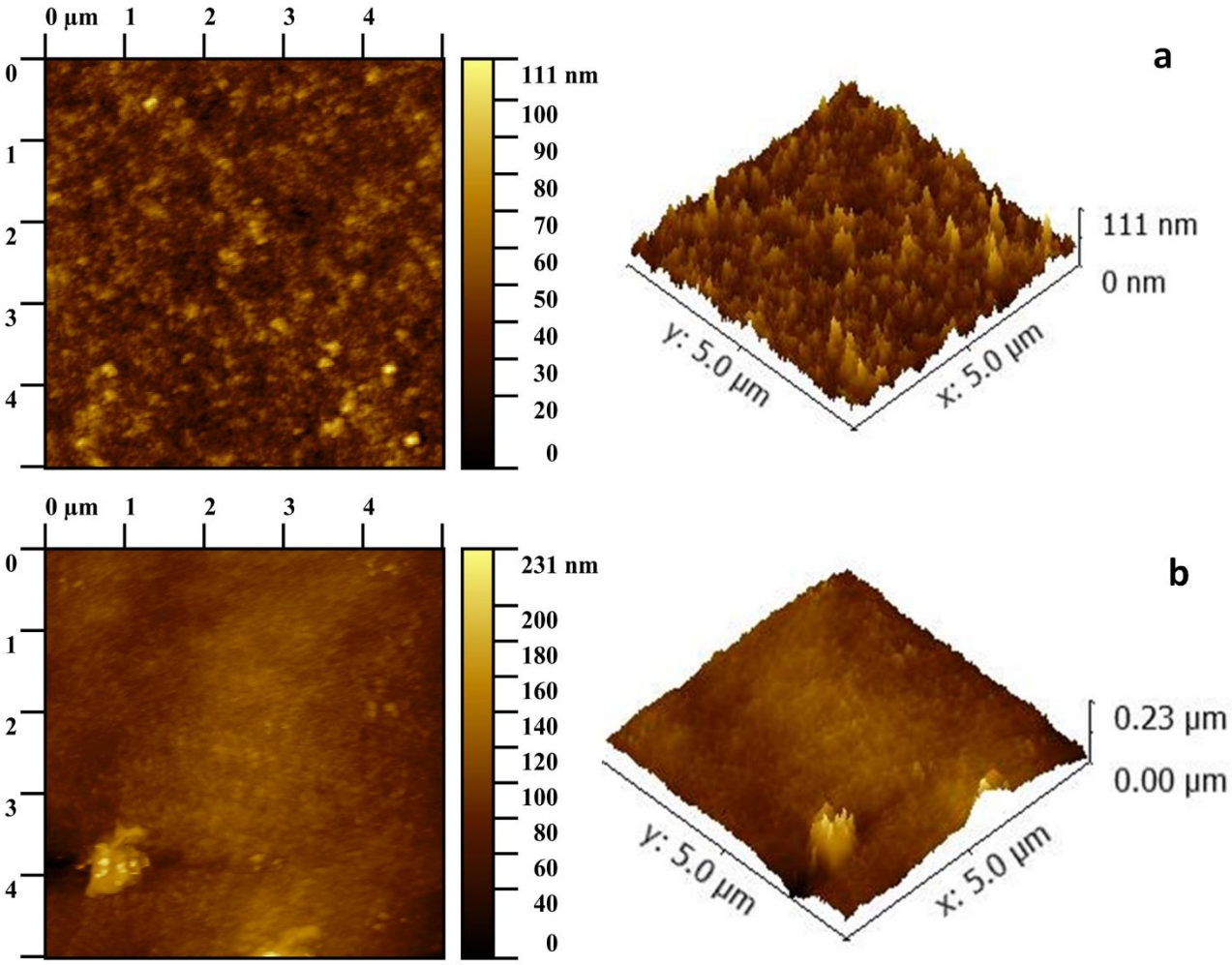

Figure 5.8: 5 µm × 5 µm scale topography and corresponding phase images of propanol treated PAN films by AFM in tapping mode (a) PAN-DMF and PAN- DMF 3D (b) PAN-DMSO and PAN -DMSO 3D.

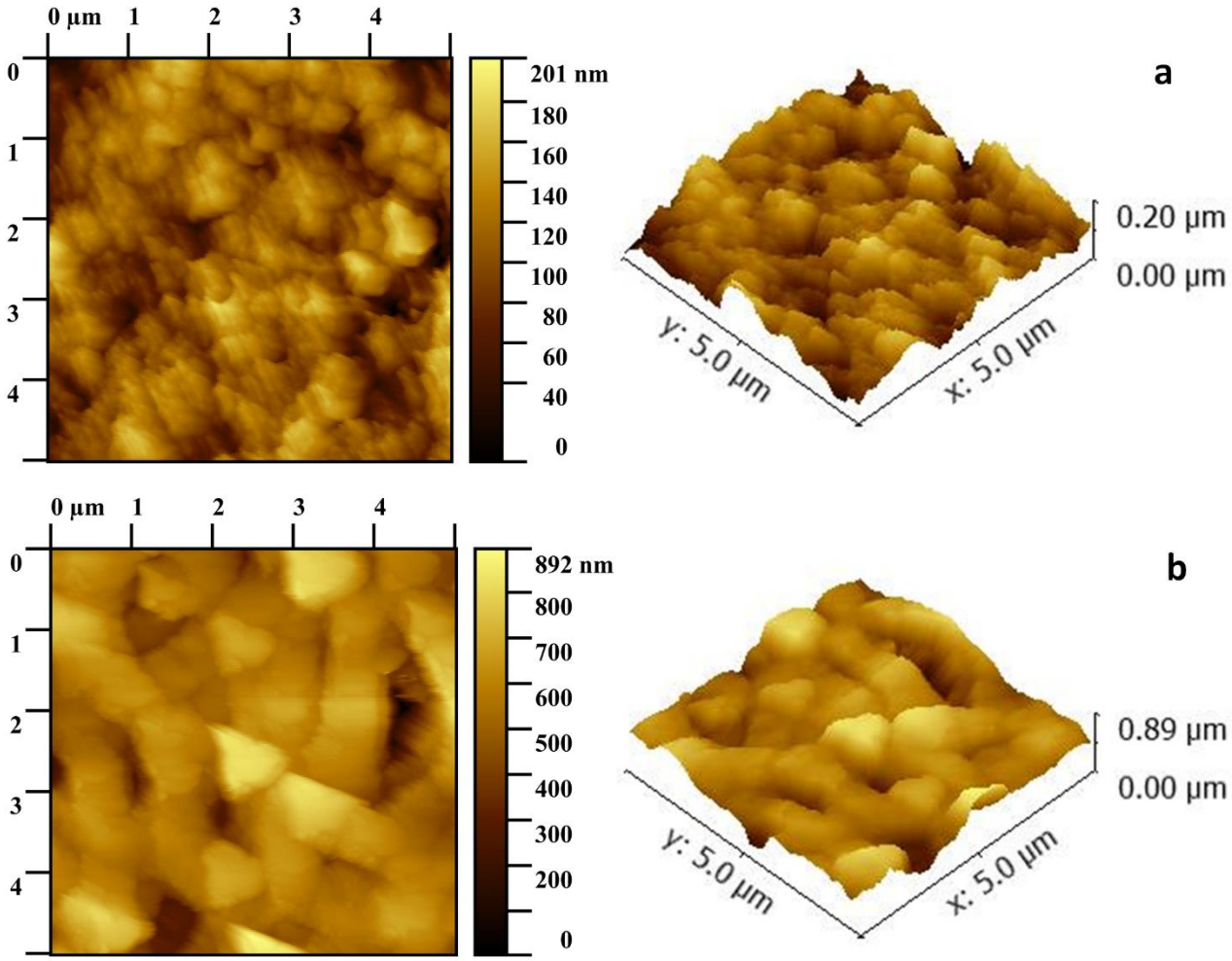

Figure 5.9: 5 µm × 5 µm scale topography and corresponding phase images of deionised water treated PAN films by AFM in tapping mode (a) PAN-DMF and PAN- DMF 3D (b) PAN-DMSO and PAN -DMSO.

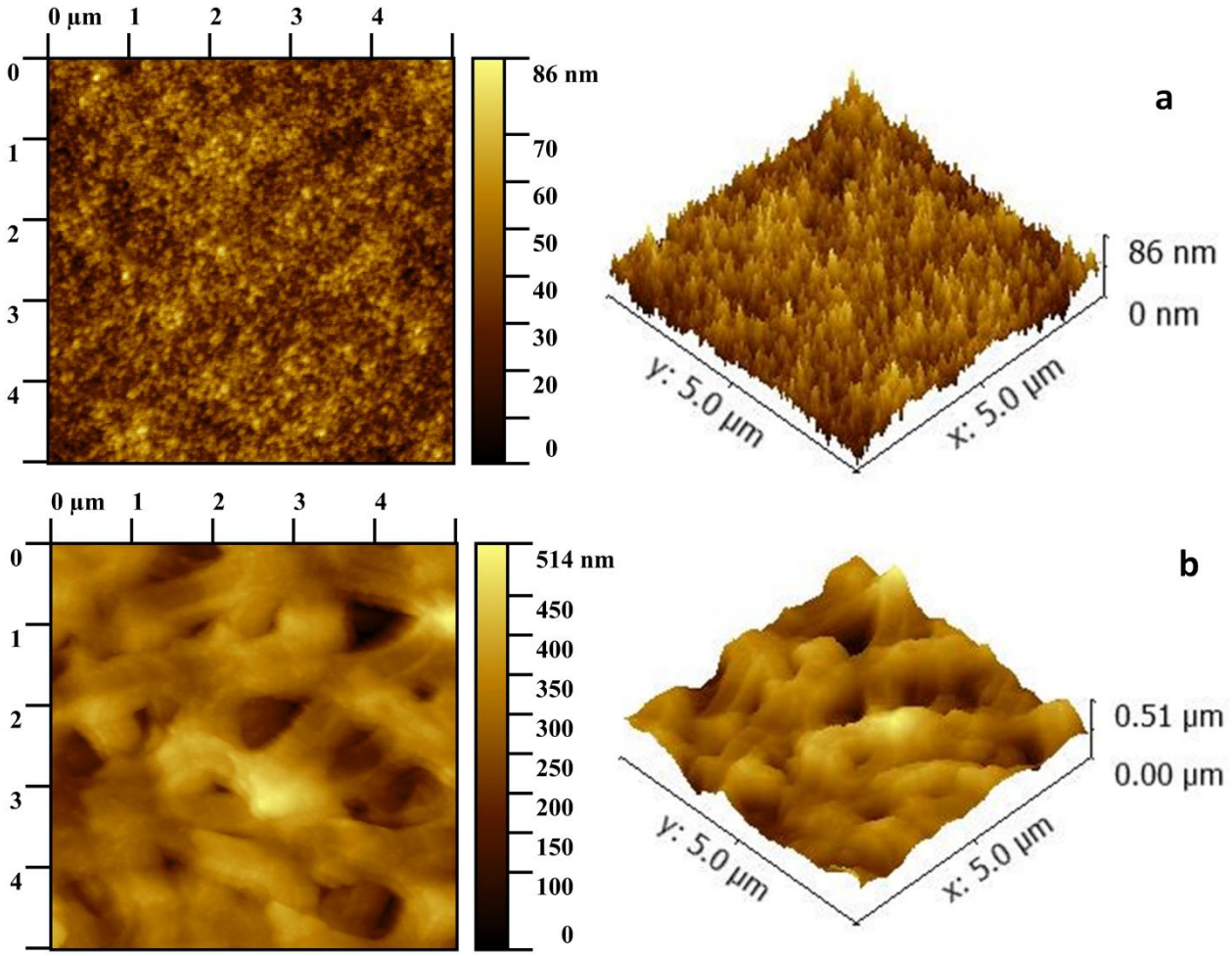

Figure 5.10: 5 µm × 5 µm scale topography and corresponding phase images of methanol treated PAN films by AFM in tapping mode (a) PAN-DMF and PAN- DMF 3D (b) PAN-DMSO and PAN -DMSO 3D.

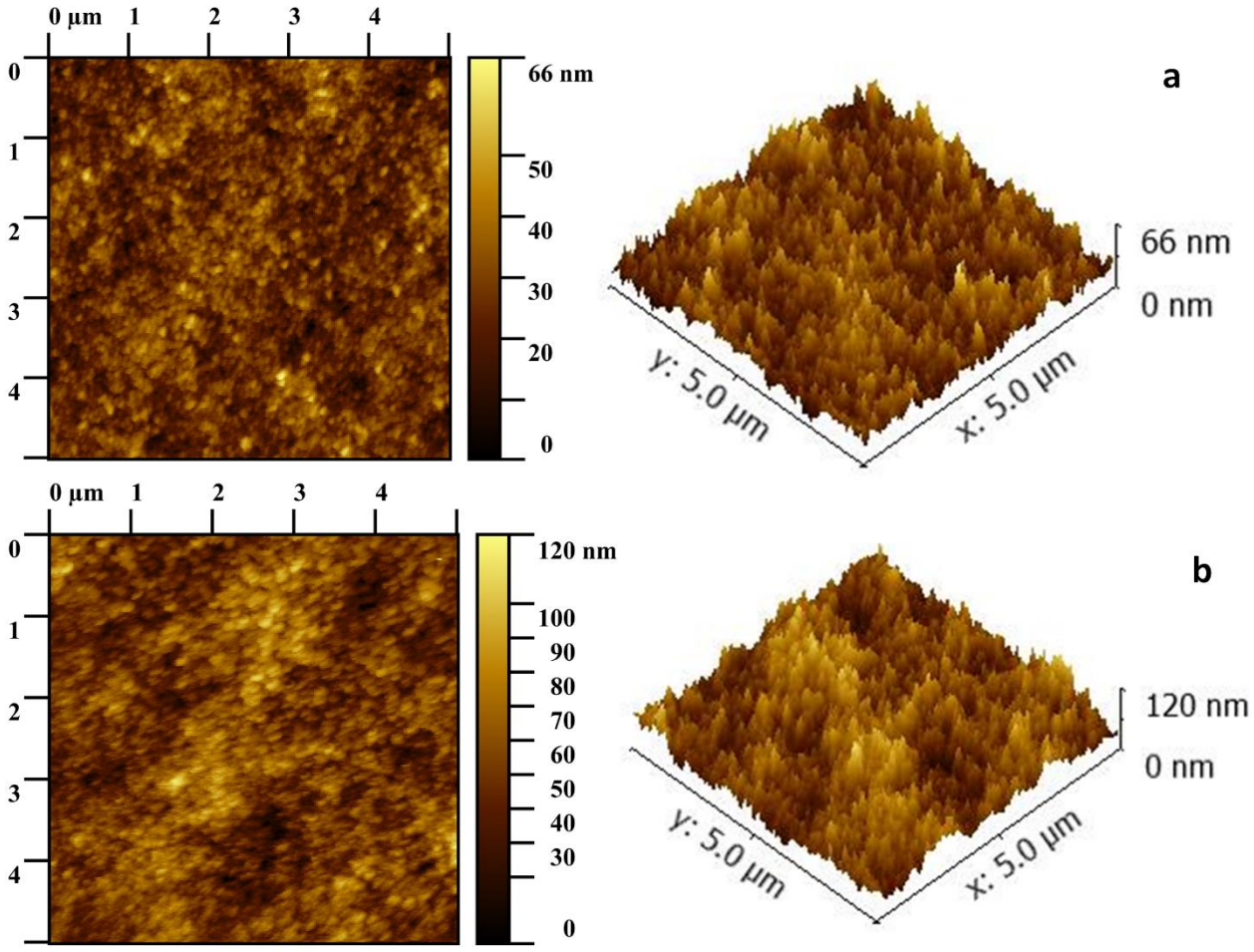

Figure 5.11: 5 µm × 5 µm scale topography and corresponding phase images of ethanol treated PAN films by AFM in tapping mode (a) PAN-DMF and PAN- DMF 3D (b) PAN-DMSO and PAN -DMSO 3D.

The variation of the morphology observed in the six non-solvents can be attributed to the differences in the non-solvents and the interactions between non-solvents and PAN films. The morphological changes in the six membranes can be correlated to the polymer-solvent interactions. There are three types of interactions in the polymer-solvent system: 1) polymer-polymer 2) solvent-solvent and 3) polymer-solvent; of these the polymer-solvent interactions is most dominant in determining morphology [364]. Significantly, the choice of non-solvent is known to determine polymer grain size. With more volatile non-solvents, rapid evaporation can result in the formation of free cavities inside the grains, leading to the formation of large grains [365].

We observe two distinct morphological types within the films examined. Firstly, fine structure, of the order of 10-100 nm, is observed on most of the films. However, underlying this structure a much larger grainsize (on the μm scale) is observed. This morphology is especially noticeable for the two acetone and water samples and the methanol sample treated with DMSO. This underlying large grain structure is indicative of large subsurface cavities and the desired high porosity of the film. In light of the preferable toxicity of DMF over DMSO, the DMF-deionised water solvent pair was chosen as an excellent candidate for further imaging.

SEM offers a much higher resolution imaging than AFM, which is useful for making a qualitative assessment of the films' porosity. The high resolution of SEM can be attributed to the short wavelength of an electron (~ 0.01 nm vs ~ 600 nm for visible light). Samples were prepared for SEM by spin coating 200 μL of PAN solution (500 rpm, 1 minute, acceleration of 1330 rpm/s) onto a glass substrate and then washing them in deionised water. SEM was conducted at cathode potential of 2 kV achieving a magnification of up to 200,000 times. In this study, SEM micrographs were employed to allow for observation of both the surface features of PAN membranes and cross-sectional morphology. The effect of annealing on the PAN films was investigated. SEM was used to provide a clear view of the overall structure of the membrane and it's the cross-section.

It is likely that the thermal treatment of the PAN films at different temperatures will result in changes to the porosity of the film structure. The temperature has a decisive influence on the solvent/polymer interaction and hence the morphology of the film. The samples were heated from 35 °C to 150 °C and the key temperatures which would be expected to affect the film's morphology are:

- The T_g of PAN (95 °C for the 150 kDa material used here)
- The boiling point (BP) of the non-solvent (100 °C for water)
- The BP of the solvent (153 °C for DMF) (although DMF should not be present in the film post-rinsing)
- The melting point (MP) of PAN (322 °C) (note that decomposition of PAN typically occurs at lower temperatures)

Figures 5.12, 5.13 and 5.14 show SEM micrographs of the surfaces of PAN membranes formed using DI and treated at 35 °C, 50 °C, 100 °C and 150 °C, at magnifications of 200 000 x, 100 000 x and 50 000 x respectively, using water as the non-solvent. From these images we observe that when annealed at 35 °C, a porous film is formed which has multiple ~50 nm pores breaking the surface. The PAN appears to be granular in nature with grain sizes of ~50-100 nm. For an annealing temperature of 50 °C, we observe that the porosity increases with pores now up to ~100 nm in diameter and an apparent increase in the overall roughness of the film. We speculate that this change may be a result of sub-BP expulsion of water from the internal pores. At an annealing temperature of 100 °C, we observe major smoothing of the film and collapse of the pores (both number of pores and size) with the pore size decreased from ~100 nm to <10 nm. This change is a direct result of reaching the T_g of the polymer and the resultant increase in polymer mobility. When annealing temperatures of 150 °C are applied, we observe further smoothing of the PAN film and an almost total loss of the surface pores.

Figure 5.15 shows cross-sectional SEM micrographs of the PAN films when annealed at 50 °C, 100 °C and 150 °C. These films were prepared by freezing the phase inverted films in liquid nitrogen and snapping them to obtain a clean fracture. Interestingly, the images show that the surface pores are insignificant compared to the massive voids observed within the PAN film at annealing

temperatures from 50 °C to 150 °C. Cavities in excess of 10 μm diameter dominate the morphology and the interstitial material is a honeycomb of smaller cavities. Very little change is observed in these films across the annealing temperature range used. As such, the phase inverted PAN film is a highly porous material with a void volume greatly in excess of the total volume of the PAN material present. Furthermore, for films annealed at 100 and 150 °C it is clear that a smooth skin of less porous PAN forms on the overall layer. At these processing temperatures skin formation may have a profound effect on analyte movement into the film and GOX immobilisation.

GOX is a dimeric globular protein having overall dimensions of 6.0 × 5.2 × 7.7 nm^3 [366]. Consequently, at RT and up to 100 °C annealing temperatures, GOX could enter the large cavities within the PAN films – if the films were subsequently annealed at ≥ 100 °C the surface pores would be closed and the GOX effectively trapped within the film.

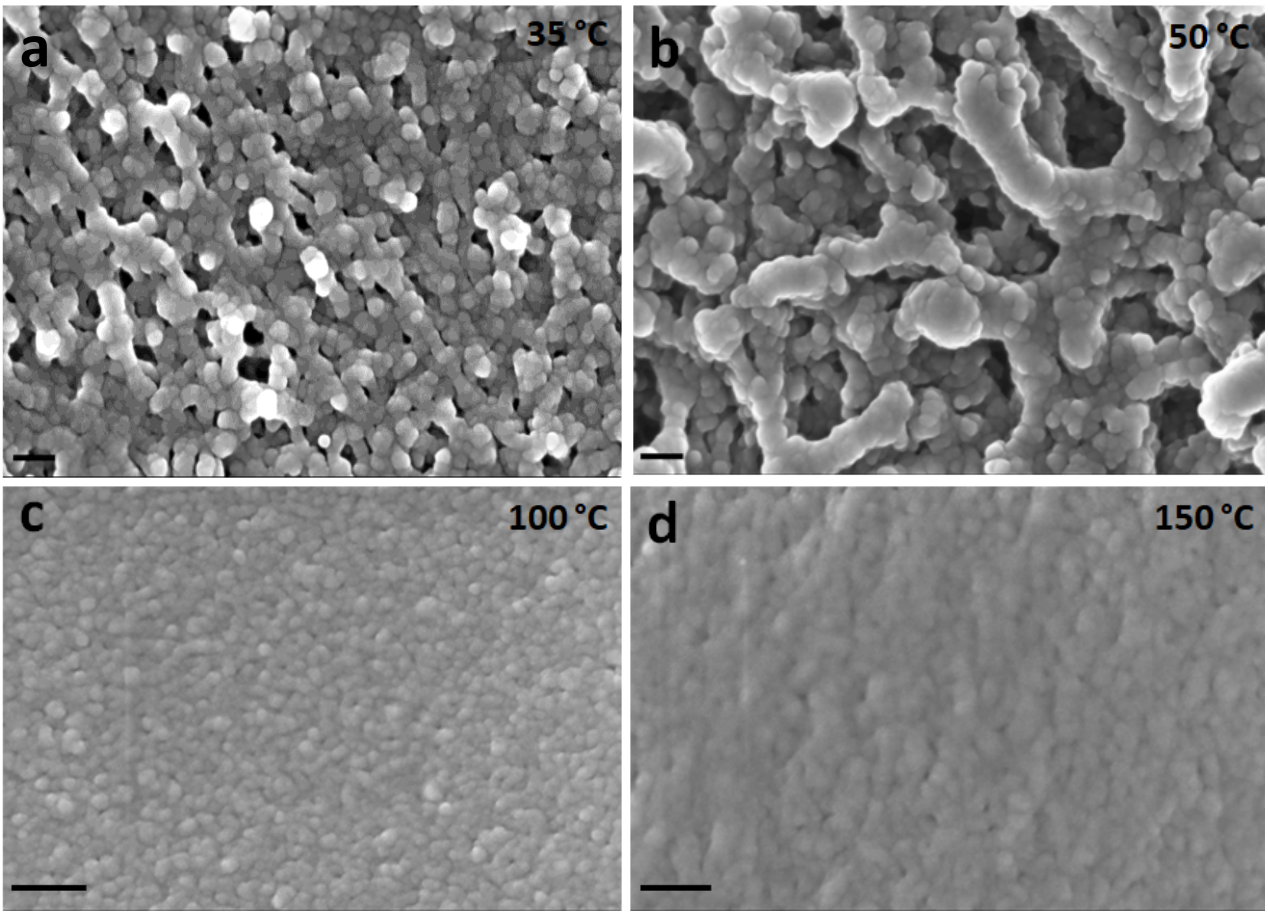

Figure 5.12: SEM micrographs (at 2 kV and 200, 000 x magnification) of PAN films using DMF as a solvent and water as a non – solvent annealed at: (a) 35 ºC (scale bar is 100 nm), (b) 50 ºC (Scale bar is 200 nm), (c) 100 ºC (scale bar is 100 nm), (d) 150 ºC (scale bar is 200 nm).

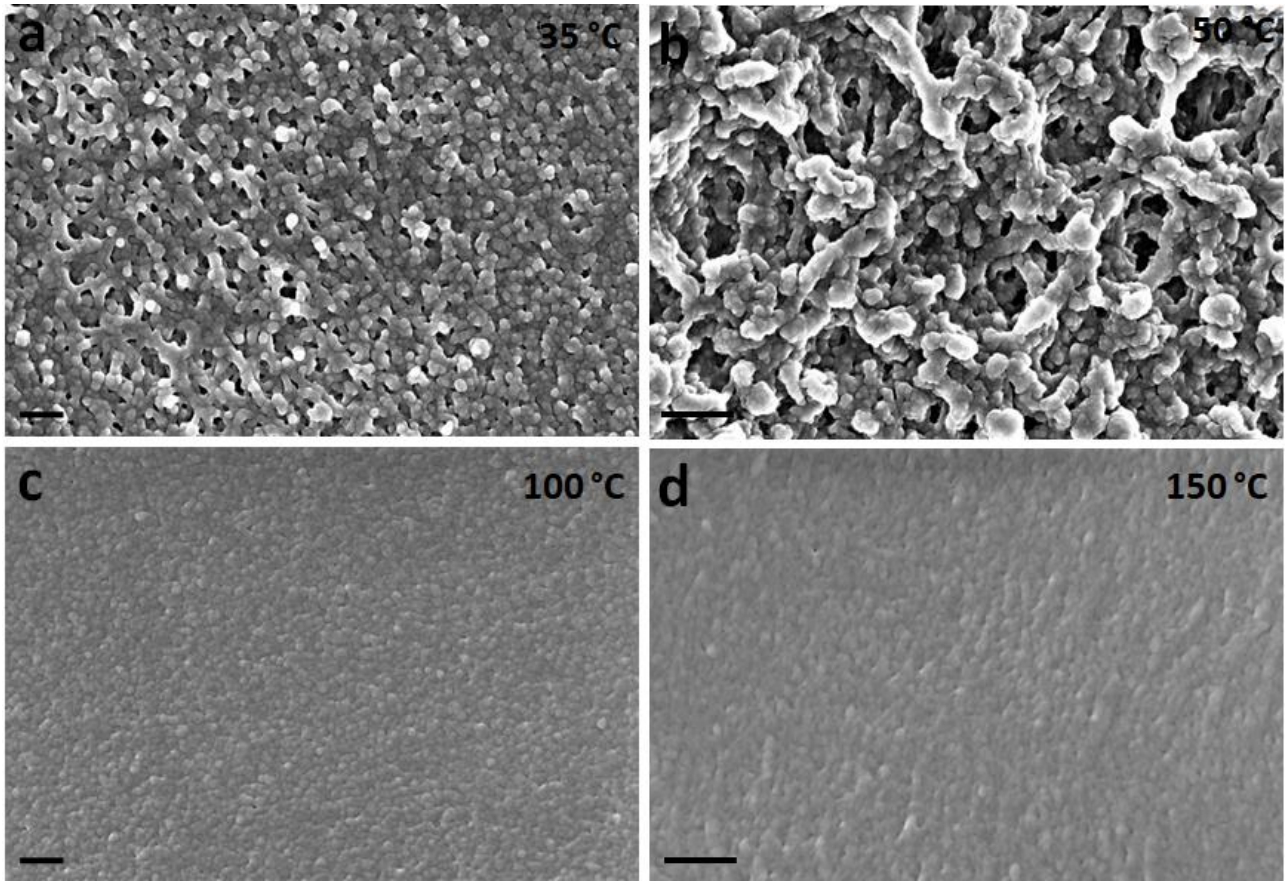

Figure 5.13: SEM micrographs (at 2 kV and 100, 000 x magnification) of PAN films using DMF as a solvent and water as a non – solvent annealed at: (a) 35 ºC (scale bar is 100 nm), (b) 50 ºC (scale bar is 200 nm), (c) 100 ºC (scale bar is 100 nm), (d) 150 ºC (scale bar is 200 nm).

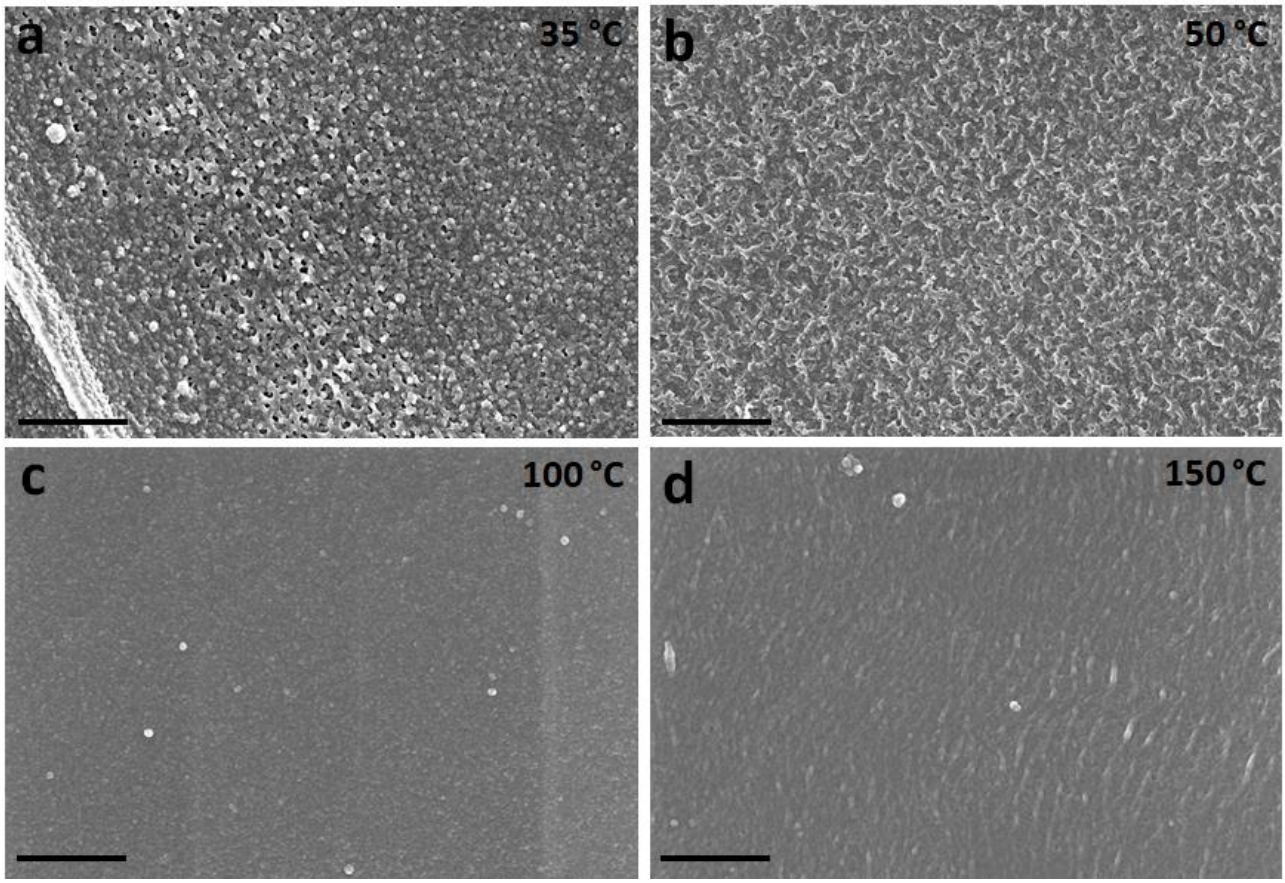

Figure 5.14: SEM micrographs (at 2 kV and the scale bars are 1 μm) of PAN films using DMF as a solvent and water as a non – solvent annealed at: (a) 35 ºC (magnification is 50, 000 x), (b) 50 ºC (magnification is 20, 000 x), (c) 100 ºC (magnification is 50, 000 x), (d) 150 ºC (magnification is 50, 000 x).

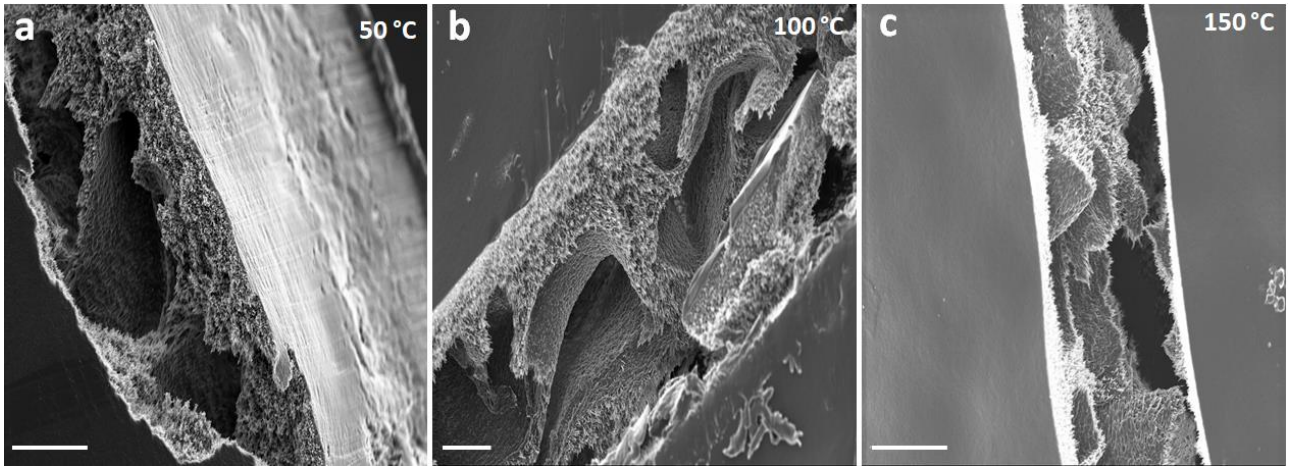

Figure 5.15: Cross-sectional SEM micrographs (at 2 kV) of PAN films using DMF as a solvent and water as a non-solvent annealed at: (a) 50 °C (magnification is 10, 000 x and the scale bar is 2 μm), (b) 100 °C (magnification is 10, 000 x and the scale bar is 1 μm) and (c) 150 °C (magnification is 12, 000 x and the scale bar is 2 μm).

Several studies have been performed to determine the effect of processing conditions such as temperature, stretching ratio and time on the shrinkage of PAN films and these studies indicated that physical shrinkage occurs because of disorientation of molecular chains cyclisation reactions at higher temperature[367-369]. In particular, thermal annealing involves heating the sample after deposition. When the kinetic energy is sufficient, the polymer chains increase movement and begin to move relative to each other. The polymer loses its glass-like properties and turns into a rubber-like leather [370, 371] . The temperature at which this occurs is termed the glass transition temperature (T_g). As such, the T_g plays a vital role in determining film morphology. Therefore, the T_g's of all polymer materials must be considered when choosing annealing conditions and sensor device fabrication procedures must be temperature controlled to obtain the optimum device film morphology. Notably, annealing a polymer above T_g causes melting of the crystalline thereby, the polymer chains is disrupted, and it becomes a disordered liquid. Solvent annealing is also possible, which involves placing the sample in a high

solvent vapour atmosphere so that the materials can achieve quasi- solvent state, which again allows the molecules to move easily.

Andrew and Kimmel have summarized the value of T_g of PAN which varies within the range ca. 80 – 145 ºC depending on processing and molecular weight [372, 373]. Our SEM studies show that for the DMF-deionised water solvent combination, most of the pores sizes were small (~10 nm), which is desirable for intercalation of molecules or ions. These results are in broad agreement with the studies of Amaral et al. and Kumar, Hashmi and Pandey [362, 374].

PAN – DMF films were prepared by spin coating 80 µL a OAN solution at 500 rpm and high acceleration in air. Following deposition, the film was dried with at 50 ºC, 100 ºC, 150 ºC, 200 ºC or 250 ºC) for 5 minutes. Photographs of these films were taken to image the large scale effects of thermal treatment on the morphology of the films. Figure 5.16 shows the films post-annealing.

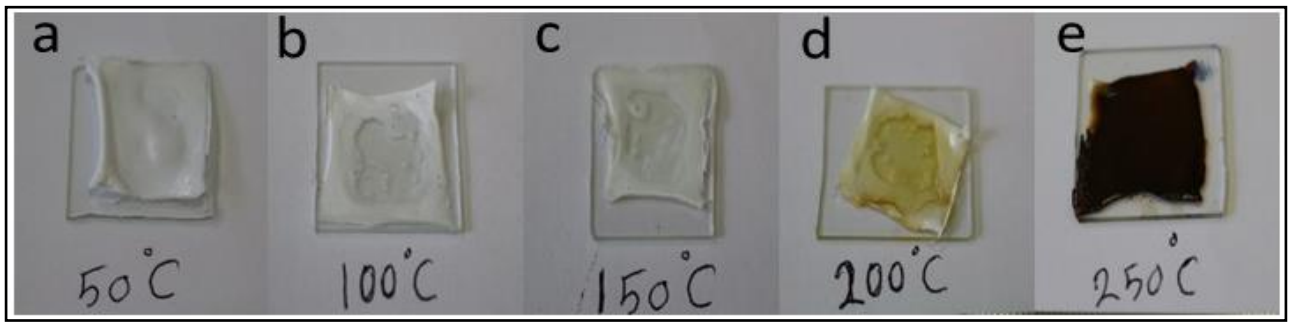

Figure 5.16: Effect of annealing on PAN membranes. a) Photograph of the PAN annealed at 50˚C, b) Photograph of the PAN annealed at 100˚C, c) Photograph of the PAN annealed at 150˚C d) Photograph of the PAN annealed at 200˚C, e) Photograph of the PAN annealed at 250˚C

As can be seen there are distinct changes in the appearance of the films upon annealing at different temperatures. At 50 ° C we observe swelling and deformation of the film. This remains largely unchanged until 200 ºC, although some minimal shrinking of the film is observed above the glass transition (125 ºC) due to entropic relaxation [375]. Whilst melting does not occur until >300 °C, thermal treatment of PAN above 200 ºC leads to changes in the physical properties of the material and decomposition and carbonisation is observed [375-377]. In this experiment we see that the PAN film begins to char and become brown at 200 °C and by 250 °C the film is black. Previous work has shown that for PAN fibres, higher temperatures can result in shrinkage attributed to cyclisation and crosslinking. However, neither sample weight or fibre diameter was dramatically affected through to 250 ºC [375].

A key property in the creation of effective PAN films for sensor applications is film thickness. When thermal annealing treatment are applied to PAN films, we found that the morphological changes which occur depend strongly on the polymer film thickness. Consequently, control of the wet PAN film thickness was critical to controlling the morphology of the PAN films and subsequent device performance. To allow for this control, experiments were conducted to vary wet PAN film thickness using both the spin coated and draw bar methods, by varying the volume of the solution added and the height of the draw bar rails, respectively.

Spin coated membranes were prepared from PAN (Mw =1500,000 g /mol) dissolved in N, N dimethylformide (DMF) and stirred for 4 hours at 30 °C to form a homogenous solution. Sample membranes were prepared by spin coating (200, 400, 600, 800 and 1000) μL of the PAN solution (500 rpm, 1 minute, 665 rpm /s) onto 2 × 2 mm^2 glass slides. The glass slides were immediately immersed in deionized water bath for 10 minutes at room temperature to

remove the remaining DMF solvent. Measurements were made at a minimum of 5 places on the PAN film. The effect of the volume of PAN solution on the film thickness is shown in Figure 5.17. It should be noted that it was difficult to get uniform thickness in the samples due to the viscosity of PAN solution, hence the high errors associated with the measurements. Figure 5.17, shows thickness of the film increases monotonically with the volume of PAN solution added, as expected, and that film thickness can readily be varied over the 30-80 μm range.

Draw bar coated PAN films were prepared as described in Section 5.2.2.2 of this chapter. However, the height of the guide rails was varied by changing the number of layers of tape applied. Post formation of the wet film, the PAN membrane was immersed with deionized water bath for 10 minutes at room temperature to remove the residual DMF solvent. The experiment was performed for various numbers of layers of tape (5, 10, 15 and 20). In order to measure the thickness of the film, small pieces were cut from each layer of the film and their thickness was measured resulting to reduce the variation in thickness of samples. Figure 5.18 shows the relationship between number of tape layers with the thickness of the phase inverted PAN film. The film thickness increases monotonically with increasing rail height (number of tape layers) and film thickness can readily be varied over the ~ 280-500 μm range. Note that 20 layers of tape gives a rail height of 516 ± 3 μm, so 5, 10 and 15 layers correlate to rail heights of 129 μm, 258 μm and 387 μm, respectively.

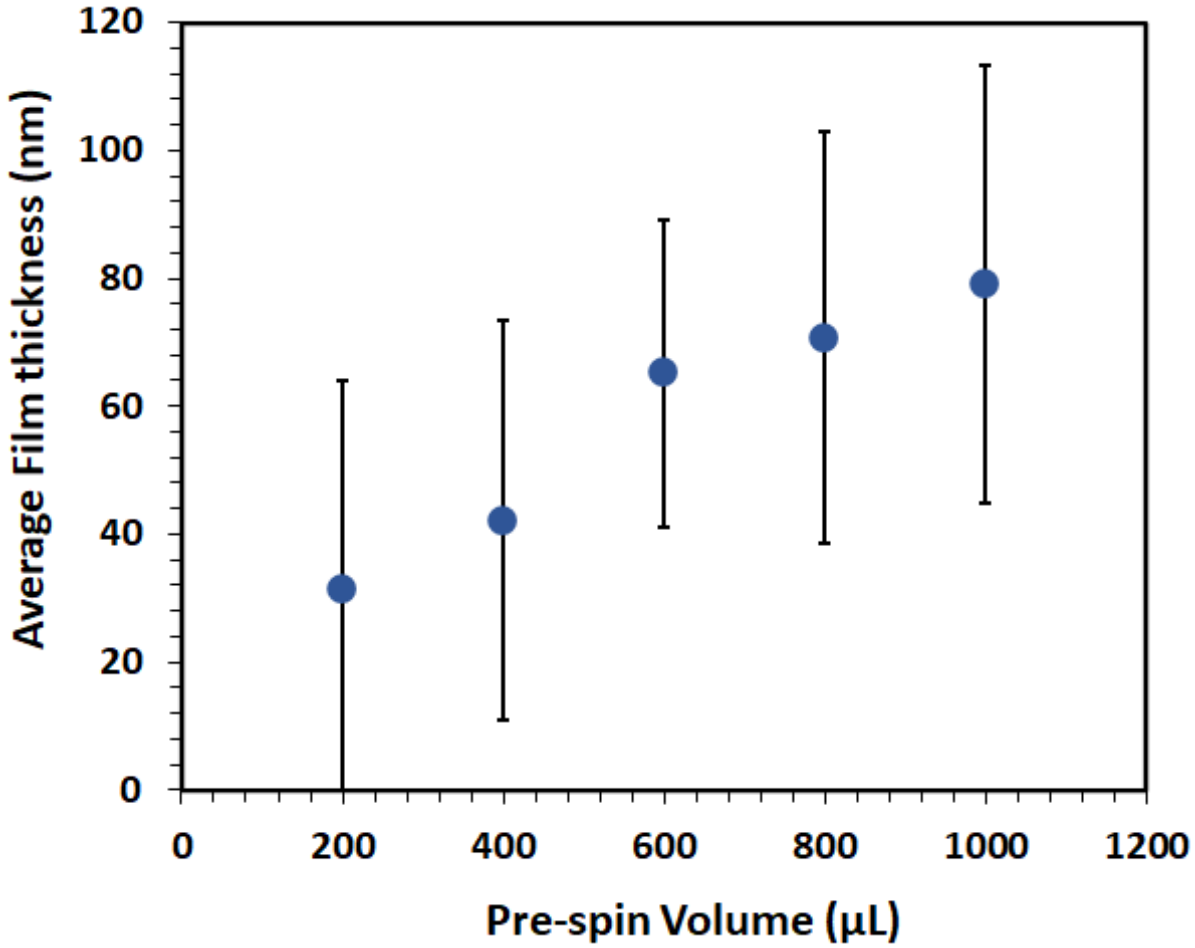

Figure 5.17: Effect of the volume of PAN solution on the thickness of spin coated PAN films. Errors are one standard deviation for a minimum of 5 measurements.

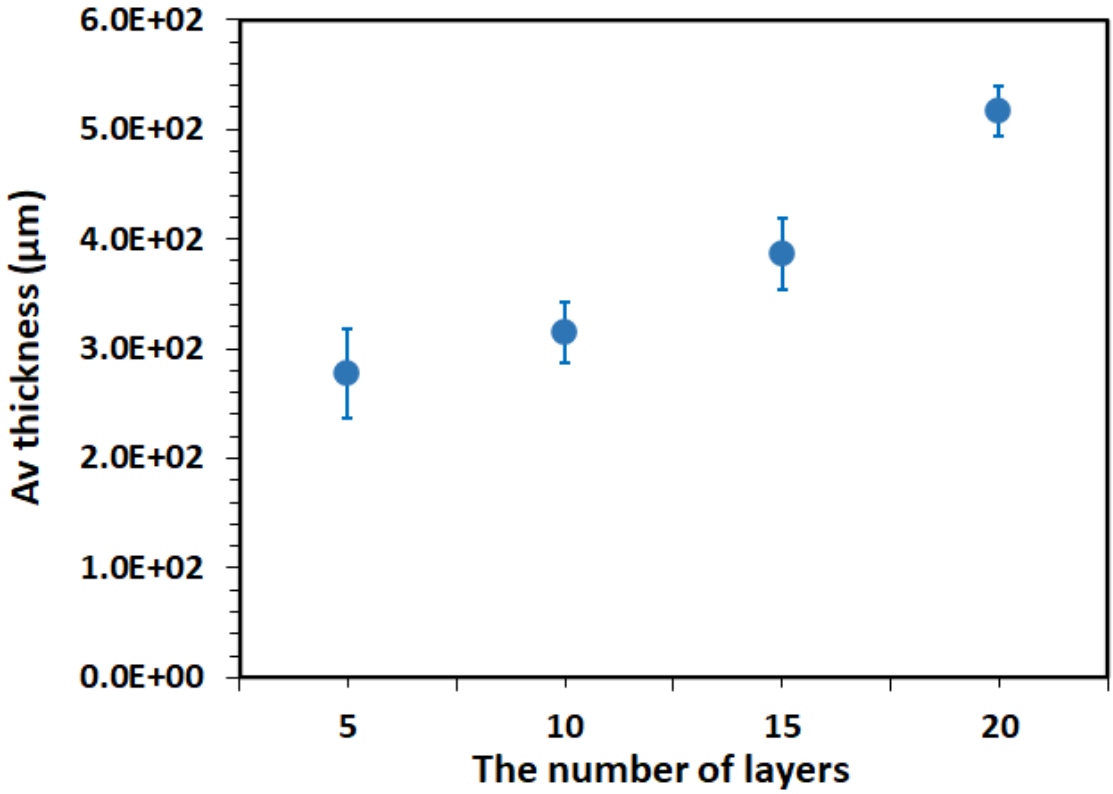

Figure 5.18: Effect of the number of layers of tape used in the draw bar guide rails on the thickness of PAN membrane. Errors are one standard deviation for a minimum of 5 measurements.

5.4 Effects of PAN on the response of devices to glucose solution addition

Having produced microporous PAN films with pore sizes suitable for enzyme immobilisation in the previous sections of this chapter we now apply these films as a capping layer for the glucose sensors developed in Chapter 4.

P3HT:Nafion bilayer devices were prepared as described in Section 4.2.2. No GOX was added to the Nafion prior to deposition. For PAN film fabrication, we used spin-coating instead of the draw bar technique. While thinner, this method created a more consistent film which plays a major role in homogenising device response and performance. Using the methodology developed in Section 5.2.2.2 phase inverted PAN films were prepared using DMF as the solvent and deionised water as the non-solvent. A dry PAN film thickness of ~80 μm was used.

To ensure consistent size and shape of the PAN layer, a hole punch (a tool designed to punch circular holes in paper) was used experiments to obtain regular small circular pieces of PAN film (diameter 20 mm). These film pieces were placed on top of the Nafion layer, between the source and the drain so that when a drop of glucose oxidase or glucose solution is placed on this piece, it will wick into the PAN and constrain the flow of the solution ensuring a consistent delivery. 10 μL of a solution of 20 mg/mL GOX in deionized water was dropped onto the PAN layer and the device was allowed to dry in air.

As previously (Section 4.6) the devices were then treated with 10 μL of a range of glucose solutions in deionised water. For this set of tests an extended glucose

analyte set was chosen, consisting of solutions of 0 µm, 0.001 µm, 0.01 µm, 0.03µm, 0.05 µm, 0.07 µm, 0.08 µm, 0.1 µm, 0.3 µm, 0.5 µm, 1 µm, 3 µm, 5 µm and 10 µm glucose concentration. Device V_{DS} was set at -1 V, V_{GS} at -0.3 V and the device drain current (I_D) was then monitored as a function of time. A minimum for 6 repeat measurements were recorded for each concentration. The FOM developed in Section 3.4.2 was used to analyse the I_D vs t curves, that is the data was normalised such that I_D at 240s (just prior to analyte addition) is zero and then the difference between I_D at 800s and I_D at 240s was plotted. Figure 5.19 shows typical I_D vs t plots for the normalised data and Figure 5.20 shows the calibration curve derived from the averaged data.

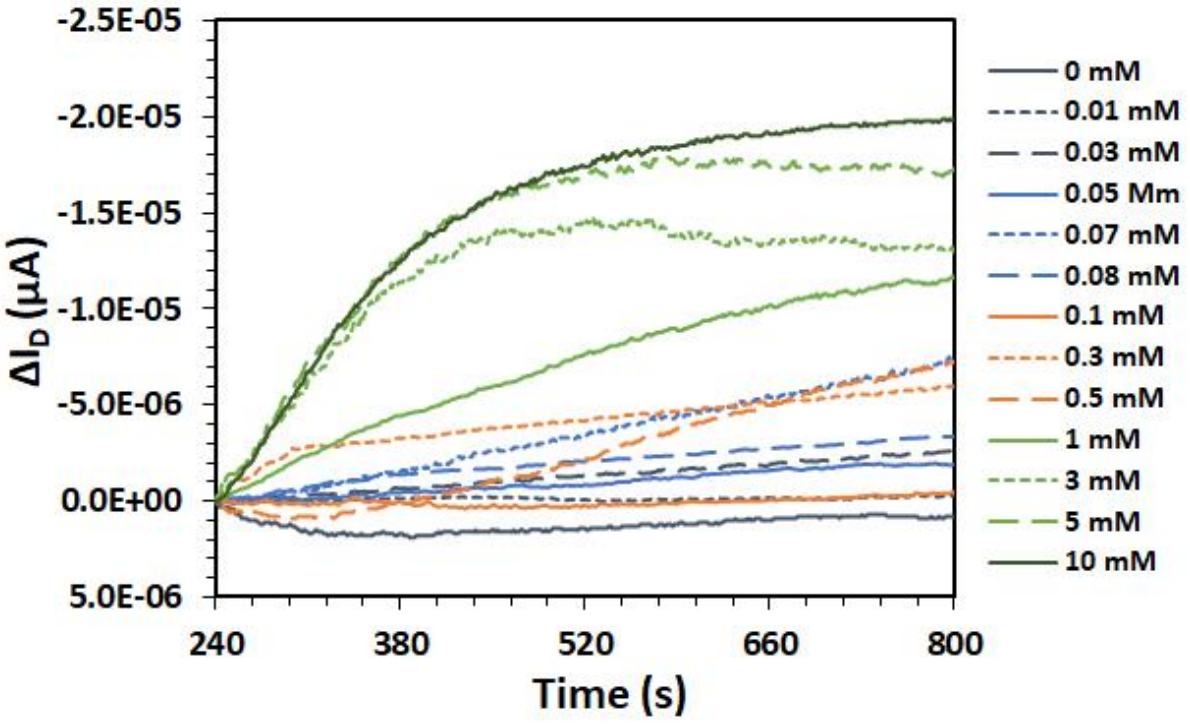

Figure 5.19: Typical I_D vs t curves for PAN containing glucose sensors treated with glucose of concentrations 0 µm to 10 µm.

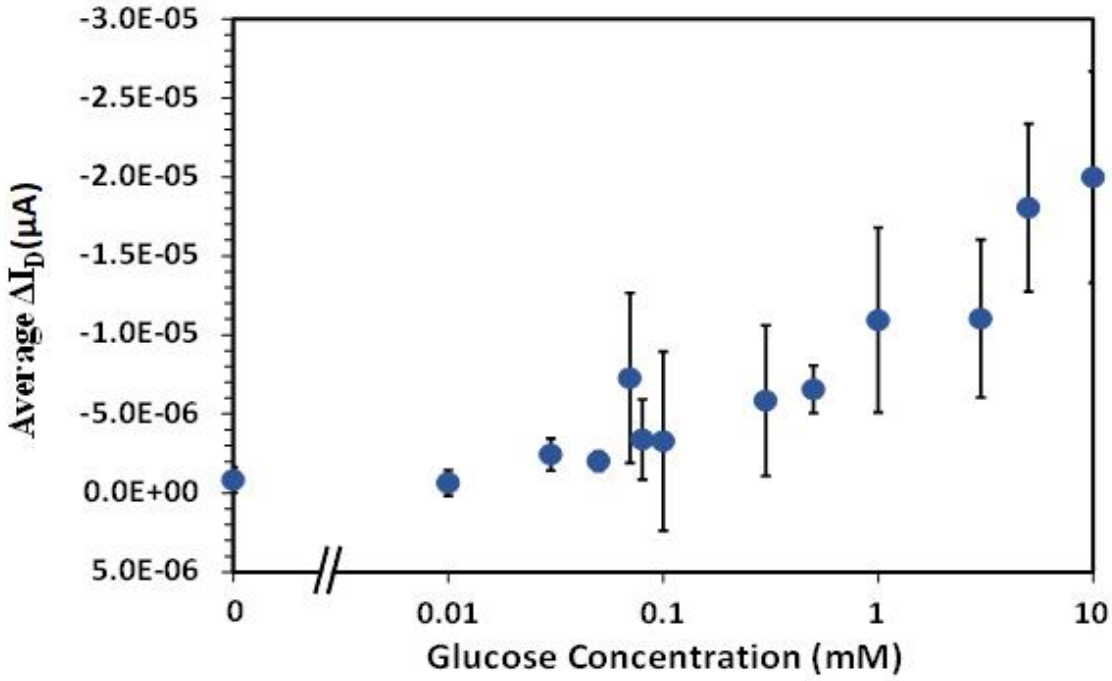

Figure 5.20: Calibration for PAN containing glucose sensors treated with glucose of concentrations 0 μm to 10 μm normalised to $I_{D\,(240s)} = 0$ A and using the I_D at t = 800 s as the FOM.

Figures 5.19 and 5.20 show a good correlation between the FOM (normalised I_D data at 800 s) and the glucose concentration. In general, the sensitivity, I_D change across the 0 μm to 10 μm concentration range and the error associated with the data are all improved over the non-PAN containing devices examined in Chapter 4. The data is largely monotonic (and within error of being so where it is not) and for the first time we begin to see some degree of sensitivity of the devices to glucose concentrations below 0.1 mM glucose, which we attribute to be due to the use of the porous PAN layer, which helped the enzyme and analyte be drawn closer to the P3HT-Nafion interface.

5.5 Conclusion

In this Chapter we have modified the glucose sensor design to include a porous PAN film capping layer on top of the Nafion. This modification was undertaken with the aim of entrapping the GOX within the PAN cavities, preventing it being washed out upon analyte addition, and confining the analyte above the source-drain channel via wicking of the solvent into the PAN film and the sensor results suggest that this aim may have been successful.

PAN was chosen as the polymer for this procedure due to its excellent chemical and physical properties. Both spin coating and a draw bar method were explored for deposition of an initial wet PAN film, the spin coated films were of higher quality, whereas the draw bar deposited films could be readily made thicker. The phase inversion technique was then used to produce highly porous PAN films by washing the wet films with a non-solvent. Imaging these films with AFM and SEM revealed that a solvent/non-solvent pairing of DMF/deionised water produced granular PAN films with regular surface pores of up to 50 nm in size. Cross-sections of these films revealed large (>10 μm) cavities within the film, making this an ideal porous material. Annealing the films closed up the surface pores but did not appear to dramatically alter the subsurface cavities.

Circular pieces of these PAN films were added to the P3HT: Nafion bilayer glucose sensor architecture and the devices tested with a range of glucose concentrations spanning the human saliva glucose range. An excellent calibration curve was obtained, indeed, for the first-time significant sensitivity to the glucose below 0.1 mM was observed.

Chapter 6: Modifying the Approach to Glucose Sensing to Mitigate Variance in Device Response

6.1 Introduction

Glucose sensors presented in previous chapters have shown high levels of device-to-device variability. In order to achieve the high levels of sensitivity required for saliva glucose detection, this variability must be minimised as much as possible. One possible way to reduce variability, which is explored in this chapter, is to adopt a "dual device" sensor architecture in which a reference device without a recognition element is incorporated alongside the active sensor. It is hoped that this approach will enable the mitigation of variation caused by small changes in layer thickness and composition arising during fabrication by using the reference device signal to normalise the data from the active sensor.

Sensor architecture comprising dual sensing components have been used previously in a range of sensing applications. Wang and Swensen suggested a dual-mode sensing method using a set of different and separated transduction signals for vapour detection. Luminescent organic semiconductors, that can produce both electrical and optical signals under gate modulation, were used as an active layer in their work. The authors found that these OTFT based sensors could be used to detect explosive vapours. However, the operation voltage was quite high (more than 50 V) [378]. Recently Zhang et al. demonstrated that this approach could be used to detect both glucose and oxygen via a triple sensor where one component acted as a null standard [379]. Ting Xu et al. have also successfully designed a novel dual sensor. CuO nanoparticles decorated polycaprolactone@polypyrrole fibers were deposited on to modified indium-tin oxide (CuO/PCL@PPy/ITO) using the electrospinning technique and used to

detect glucose in saliva at low concentration levels [380]. Piechotta et al. designed a dual sensor structure as a way of compensating for interference caused by species such as uric acid and paracetamol in glucose sensing. Thus only one sensor responds to glucose while both respond equally to the interferences [381].

In this work, we fabricate a dual device glucose sensor and will investigate if it can be successfully used for sensing low (saliva range) concentrations of glucose. In our work, we experimentally studied the efficacy of using this type of sensor for glucose monitoring. Such a dual device should ideally have at least the same or better accuracy and specificity as our previous sensor architectures and existing blood glucose sensing technology.

In this work, the dual device sensor was designed with two OTFT-based sensors fabricated on a single substrate. One device incorporated GOX, therefore acting as a glucose sensor, whilst the other device does not incorporate GOX and acts as the reference device for the measurement. The hypothesis is that comparison of the signals from these two devices should lead to a more accurate and sensitive glucose measurement independent of physical variations arising during fabrication. To determine the degree of cross talk between the two devices, dual device sensors were tested with both the active and references devices intact on the substrate (as fabricated) and also where the substrate was split into the two separate devices.

6.1.1 Potential sources of variation in device response

In this section, we will present and discuss several technical drawbacks that were encountered during the fabrication of devices. These technical limitations have origins in the conditions of manufacturing, variations in the layers of the

device inherent to the coating procedure, variations in device layers inherent to drop casting, variations caused by the PAN fabrication and variations in testing.

Variations due to the conditions of manufacturing can involve the influence of temperature and humidity on device performance, where controlling the temperature and humidity enhances the stability of the device. Issues associated with ambient humidity were previously observed and addressed in Section 4.6. Additionally, controlling these conditions was essential to understand the effects of temperature on the behaviour of the devices, specifically the effect on material conductivity, device response and lifetime. Practically, a high or low laboratory temperature will result in a variation in device performance. As these devices were prepared in ambient air, the variation in their performance can be attributed to the variation in ambient conditions. The ambient conditions for fabrication (such as temperature, humidity and light intensity) necessarily varied from time to time and season to season. The variation in environmental conditions is also expected to affect the properties of the materials used in preparation of these devices.

Variation in the layers of the device was also observed due to the spin coating process leading to changes in layer thickness. Especially at low spin rates, edge and “coffee stain” effects were apparent in the films. Notably, the layer thickness of the device has a significant effect on the analytical response to the device. It is worth noting that variation in the thickness of films is undesirable in manufacture and will have a negative effective on the device performance which may impact negatively on the response time of the sensor. Consequently, care must be taken to ensure reproducible films are obtained. The patterning and cleaning of deposited films to expose electrodes was also a process which, due to its manual nature, was a source of significant variation in the final device architecture. Elimination of variation due to this process was impossible, and consequently, great care was taken to minimise this effect. Variation in device

layers can also occur as a result of poor GOX distribution; the GOX position must be in centre of the device (between source and drain electrodes) and variation from this manual positioning can result in major changes to the device performance.

Another key factor in device performance is the PAN film fabrication where thicker layers of PAN will increase the physical pathway for reaction of the analyte with the other components of the device. Similarly, the size and shape of the PAN layer has a significant effect in the fabrication stages due to the high level of difficulty in obtaining a perfect circular shape and the affect this layer has in locating and "wicking" the analyte into the device.

Finally, the testing conditions are vitally important in the evaluation of device performance. This factor includes how well the devices were separated (in cases where a single substrate was broken into two prior to testing), variation in the quality of the electrical connections and variation in test conditions such as temperature and humidity. Many of the conditions listed above are controllable and can be minimised through careful fabrication and testing protocols and by controlling the laboratory conditions. This study will include the design and development of a prototype model of a dual glucose sensor, which is suitable for mobile devices. By having a standard for comparison, which is prepared on the same substrate utilising the same material layers, it is hoped that we will eliminate or minimise the majority of device-to-device variation observed previously. To achieve this target, we divide the device into two halves (dual sensor) that are identical in their materials and preparation and equal in size. Dual sensors of this type have been observed to provide fast response, high sensitivity and excellent repeatability while operating at room temperature [382]. We also aim to develop a dual glucose biosensor, which is not only sensitive enough to operate at room temperature, but which also can eliminate the influence of humidity on performance.

Table 6.1: The variations observed can be summarised in the table 6.1: as follows: B2B = batch to batch variation; D2D = device to device variation

Fabrication conditions	**Variation in materials**	**Variation in device layers inherent to spin coating**	**Variation in device layers inherent to drop casting**	**Variations caused by PAN fabrication**	**Testing**
Humidity, temperature etc.(B2B)	Batch to batch polymer variation (B2B)	Variation in thickness (substrate to substrate) (D2D)	Variation in device layers inherent to drop casting	PAN film thickness (D2D)	How well the devices were physically separated (D2D)
Cleaning variations (B2B/D2D)	Shelf-life issues (B2B)	Variation in thickness (across substrate e.g. coffee ring) (D2D)	GOX location (D2D)	PAN film size (D2D)	Variation in analyte solution deposition (D2D)
		Variation in patterning (D2D)(e.g.if material is not properly removed from the electrode)	GOX distribution (D2D)		Variation in electrical connection quality (D2D)
					Variation in testing conditions (temperature, humidity etc.) (D2D)

6.1.2 Possible approaches for mitigating sensor variation

As mentioned previously, we have encountered several technical limitations that affect the device performance, such as aspects of the manufacturing conditions and the effect of variations in film thickness and quality at manufacturing time. In this section, we have included and offer different practical methods to overcome and address these limitations.

The primary approach that we have adopted is the introduction of a dual device sensor which incorporates reference and sensing elements as described in Section 6.2. The dual device sensor will aim to help to mitigate device-to-device variation caused by factors including variance in film thickness and morphology, manufacture conditions and variation in ambient conditions during testing. In theory the use of an inbuilt reference device should also eliminate any issues due to the addition and dedoping effect of the water component of the analyte, as observed in Chapter 4.

Beyond the change in sensor design, we have adopted several measures to help mitigate those factors which are not reduced by the dual device sensor:

- To mitigate changes in device characteristics due to GOX activity, we instigated a measurement regime in which devices were characterised directly after drying the GOX film, since the activity of GOX film will drop over time. Furthermore, GOX was routinely tested for activity on a regular basis using a Sigma-Aldrich Glucose Oxidase Activity Assay Kit.
- To ensure that the test and reference devices are presented with the analyte solution at the same moment, we replaced the manual pipette with an electronic dual pipette, which is able to deposit two drops of glucose solution in the required two specific positions at the same time.
- For PAN fabrication, we used spin-coating instead of the draw bar technique. This method created a more consistent film which plays a major role in homogenising device response and performance.
- To ensure consistent size and shape of the PAN layer, a hole punch (a tool designed to punch circular holes in paper) was used in our experiments to obtain regular small circular pieces of PAN film (diameter 20 mm). These film pieces are placed between the source and the drain so that when a drop of glucose oxidase or glucose solution is placed on this

piece, it will constrain the flow of the solution ensuring a consistent delivery.

- Finally, we propose that devices be prepared, and measurements be carried out under controlled temperature and humidity in an air-conditioned laboratory environment since we hypothesise that controlling temperature and humidity will enhance the stability of the device.

However, despite these measures, there are still several challenges in the manufacture of these devices, and considerable effort is being made towards improving the reliability of glucose measurements.

6.2 Description of the adopted approach

The basis of the dual device sensor is the fabrication of a single substrate which has two devices on it - one of which does not respond to the analyte and one which does. This approach should eliminiate any device to device variations in fabrication (film thicknesses and defects) by providing an internal calibration for each and every measurement. In this case we build two identical devices but only one of the devices has GOX and thus any response from the other device is due to interferences inherent in the architecture and can be subtracted from the GOX signal. To improve analyte positioning and volume a dual electronic pipette was used to accurately deposit the analyte above the middle of the source and drain electrodes of each device. To avoid a potential issue with cross contamination of the analyte and electrical cross-talk between the two devices, tests were conducted with the subtrate intact (where both devices sit side by side when the analyte is added) and broken into two (where the GOX and No GOX standard devices are now separated upon addition of the analyte). Results of these experiments and discussion of the results are presented in this Chapter. Dual sensors have been shown to have several advantages, such as improved

signal to noise ratio and sensisitivity [383-385]. One of the most important advantages of the dual sensor was the absence of contact and therefore crosstalk between the device elements when the analyte was deposited on the device.

6.2.1 Experimental

The fabrication process started with polyacrylonitrile (PAN), as described in the experiments performed for Chapter 5. Several approaches for the preparation of PAN have been performed. As mentioned in Chapter 5 the draw bar was one of the techniques used in fabrication of PAN films. This technique starts by washing a 20 cm × 20 cm glass plate sequentially in isopropyl alcohol and methanol for 15 minutes each, then rinsing in distilled water for 5 minutes. A 15 cm × 15 cm sheet of polyethylene terephthalate (PET) substrate was washed in the same way, then placed on top of the glass sheet. Scotch tape was applied to the top of the glass sheet to form the rails for the draw bar which will set the thickness of the film. Then, a glass rod is used to distribute a PAN solution evenly across the PET substrate, as shown in Figure 5.4 and Figure 5.5.

The phase inversion process to fabricate a film of PAN was performed by immersion of the wet film in a non-solvent (deionised water). Following phase inversion, films were further washed twice with deionised water for 10 minutes. This step was performed to remove any contamination and residual solvent. The films were then stored in the dark at room temperature. A hole punch was used in our experiment to obtain circular pieces of PAN film (diameter 20 mm). These film pieces were positioned on top of the Nafion, in the middle of source/drain gap. This method enabled the drop of glucose to be positioned in the middle of the channel area because the analyte solution conforms to the PAN shape. Aside from the addition of PAN and the omission of GOX from the reference device, the devices fabricated here were otherwise identical to those described in Chapter 3. Where required, the devices (which are prepared two

per substrate) were physically separated by scoring through the P3HT and Nafion layers with a diamond glass cutter and snapping.

6.3 Dual Device Data With/Without PAN (DD1 and DD2)

This experiment was designed to determine the dual sensor response to glucose solution as a function of the presence or absence of a PAN layer, which has been shown in Chapter 5 to improve device performance. The dual device sensor structures were therefore fabricated with and without this PAN layer. We carried out this experiment with three different sensor designs. The first of them (DD1) involved deposition of a single drop of glucose solution of different concentrations (0 mM, 0.01 mM, 0.1 mM, 1mM and 10 mM) in the middle of the unbroken dual sensor (i.e. between the two set of electrodes), on to a PAN layer (Figures 6.1 and 6.2). The second design (DD2) was similar but did not contain the PAN layer. Two drops of the glucose solution were deposited on each of the test and reference devices (with the same concentrations). The two analyte drops were deposited simultaneously (Figure 6.7 and 6.8). For the third design (DD3), the test and reference devices were physically separated (by snapping the substrate) and circular 20 mm diameter PAN pieces were placed between each set of source-drain electrodes. As with the second design, the test and reference devices had their analytes deposited simultaneously across the same range of concentrations (Figure 6.12 and 6.13). In these experiments, PAN was used as a matrix material to hold the enzyme and analyte during testing with PAN film thickness of 516 ± 3 nm.

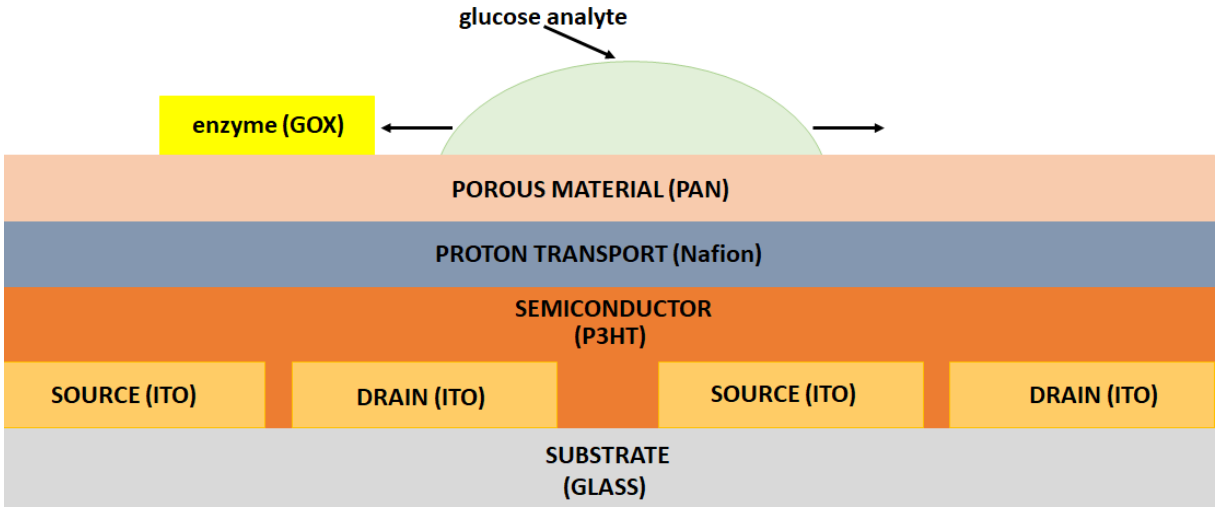

Figure 6.1: Device configuration for DD1 showing a single PAN layer spanning the full substrate. One of the sides contains GOX and the other side has no GOX. One drop of glucose analyte (0 Mm, 0.01 Mm, 0.1 mM, 1 mM and 10 mM) is deposited in the centre of the PAN layer.

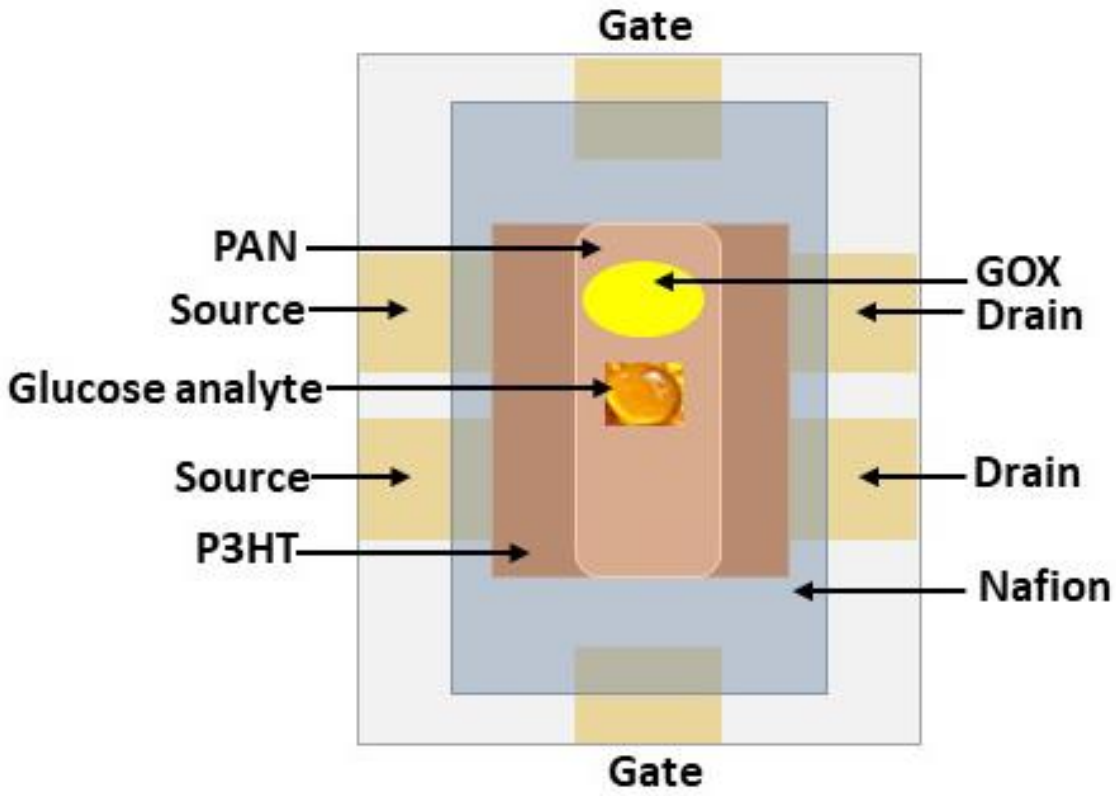

Figure 6.2: Top-down view of DD1.

To measure the response of the DD1 sensor device to a range of glucose concentrations, 10 µL of analyte solution was placed on the PAN layer and I_D was monitored as a function of time. V_{GS} was held at -0.3 V and V_{DS} was held at -1 V to ensure the electrochemical breakdown of the H_2O_2 . As discussed previously, the liberated H^+ interacts directly with the P3HT semiconductor material, doping it and altering its conductivity giving a measured response to the glucose analyte. A minimum of 6 measurements were conducted at each glucose concentration.

Prior to analyte addition, we observed that there is a significant (approximately one order of magnitude) difference between the current levels for the test and reference devices which is attributed to the addition of water to the device during deposition of the GOX. For all glucose concentrations, there is an initial change in current associated with the addition of the analyte which we also attribute to the hydration of the device and associated changes to the doping of the P3HT. To determine doping changes caused by the analyte, we focus on the region after this change has occurred (from t = 240 s). For a blank analyte solution, our results confirmed that there is very little difference in the I_D-time relationship for the reference and test devices in the t = 240 s to 800 s region as shown in Figure 6.3 a.

It is clear that the current time response curve obtained with the glucose biosensor was increased for DD1 with GOX at 1 mM and 10 mM (Figures 6.3 d and 6.3e), However, the current time response curve that was obtained for low concentration glucose (0.01 and 0.1 mM) show negligible response for DD1 with GOX and without GOX devices between 240 - 900 seconds. These results were summarised in Figures 6.3 b and 6.3 c.

The average initial current for DD1 sensors was recorded. For the test devices, this value was $-2.39 \pm 2 \times 10^{-6}$ A, whilst for the reference devices it was $-2.36 \pm 2 \times 10^{-5}$ A . The high variation in the initial current can be attributed to the

many factors that impact upon device performance as noted in Section 6.1.1. The order of magnitude difference between the average initial current of the test and reference devices in unclear but may be due to weak binding of ions in the device to the GOX moeity.

Figure 6.3 shows representative current-time relationships during glucose sensing for test and reference devices of the DD1 device type for glucose analytes of concentration 0 mM, 0.01 mM, 0.1 mM, 1 mM and 10 mM. The response of the reference device should ideally be consistent across all devices. However, it is clear from Figure 6.3 (d) and (e) that considerable crosstalk between the test and reference devices is occurring as the current-time relationship for the reference devices mimics that of the test device. This observation implies that GOX, H_2O_2 or protons generated during the sensing process are able to diffuse across the dual device sensor leading to doping of the P3HT layer in the reference device. This crosstalk is likely facilited by the physical coupling of the devices by the analyte containing PAN layer.

Figure 6.4 shows the difference plots between the test and reference device responses (normalised such that $\Delta I = 0$ at $t = 240$ seconds) , Figure 6.5 and Figure 6.6 shows a calibration curve using the calibration parameter equal to the difference in the ΔI plots at 800 s and 200 s. Despite the clear crosstalk between test and reference devices, we observe in Figure 6.6 a monotonic relationship between glucose concentration and this calibration parameter which can be attributed to the expected increase in P3HT doping in the test devices with increasing glucose concentration. However, only a somewhat monotonic relationship is observed for the glucose concentrations and the changes in current response for the device between 240 and 800 s and the errors involved in the measurements are larger than the difference in current between the samples. Consequently there is little sensitivity to glucose concentration in these devices. The data suggests that glucose detection is achieved at concentrations

higher than 0.1 mM which is towards the upper limit of salivary glucose concentrations (usually defined as 0.008 to 0.2 mM). However, because of the clear crosstalk between test and reference devices, the design was modifed in an attempt to alleviate this phenomenon by first removing the PAN layer (DD2) and subsequently by complete physical separation of the two devices (DD3).

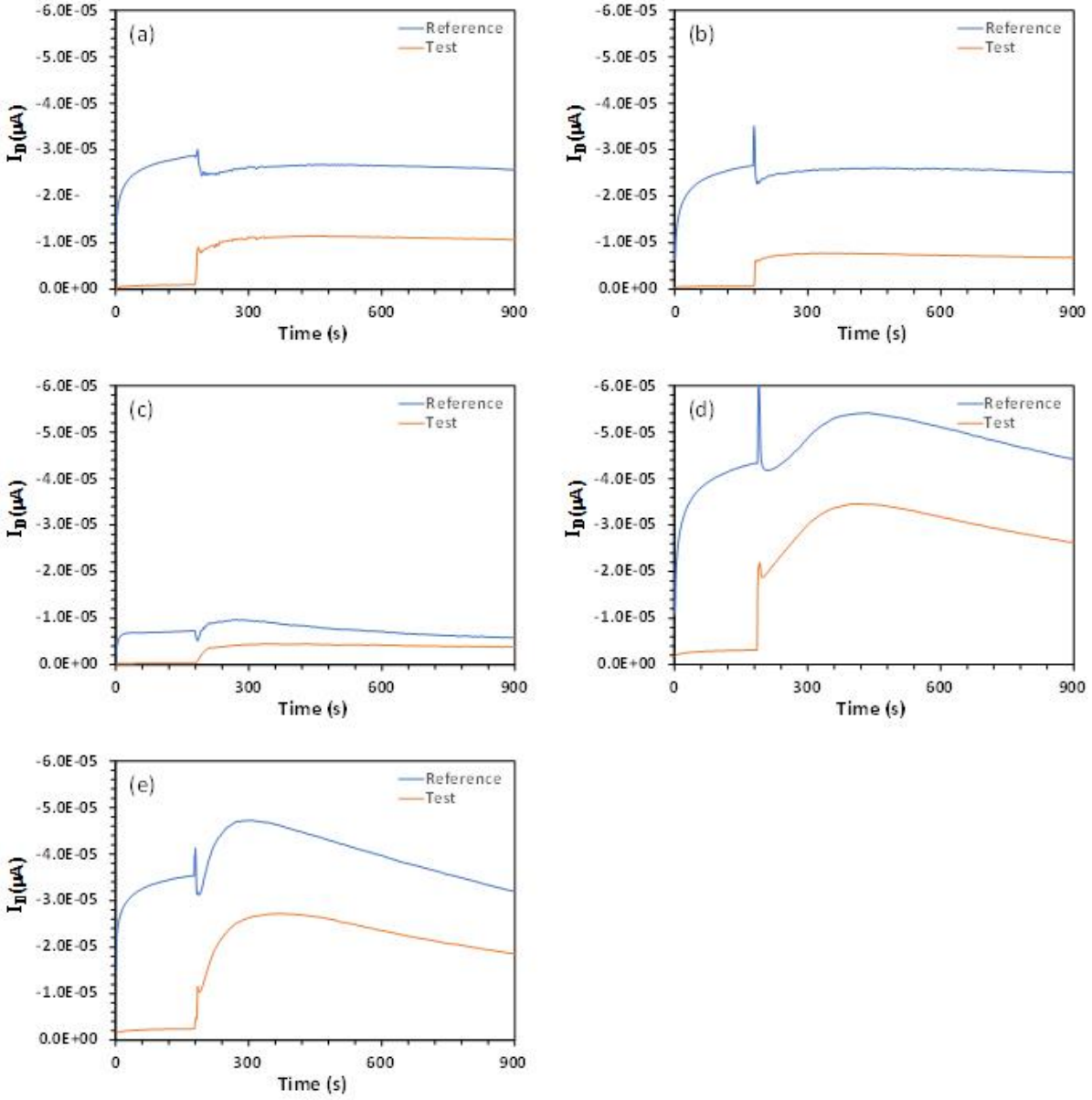

Figure 6.3: Typical I_D versus time for glucose concentrations a (0 mM), b (0.01 mM), c (0.1 mM), d (1 mM) and e (10 mM) (0 mM, 0.01 mM, 0.1 mM, 1 mM and 10 mM) where the glucose analyte is dropped in the middle of DD1 at t = 200s.

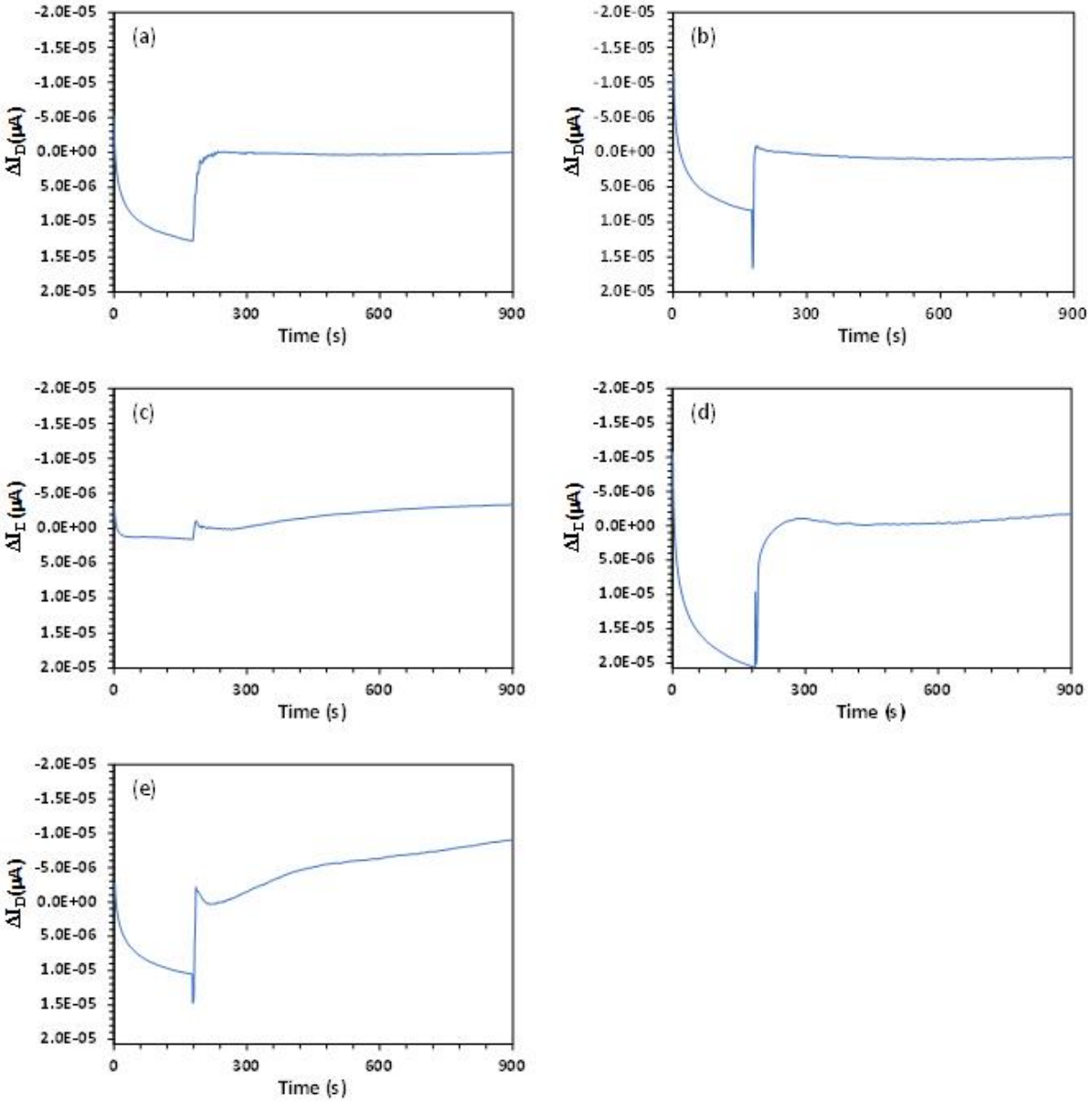

Figure 6.4: Typical DD1 current response versus time for glucose concentrations of; a 0 mM, b 0.01 mM, c 0.1 mM, d 1 mM and e 10 mM. The reference data has been subtracted from the test data and the resulting plot is normalised to $I_D = 0$ A at t = 240s seconds, just before glucose analyte addition.

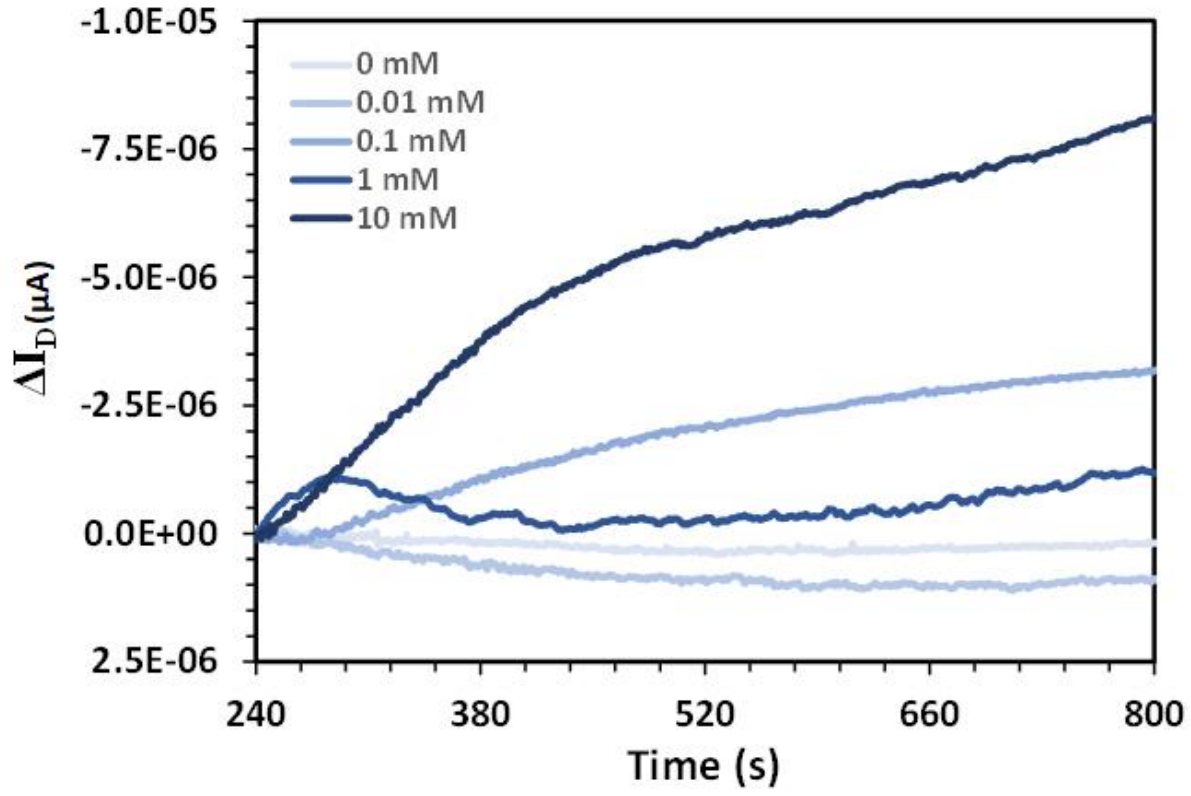

Figure 6.5: Typical ΔI_D vs t curves normalised to t = 240s for DD1.

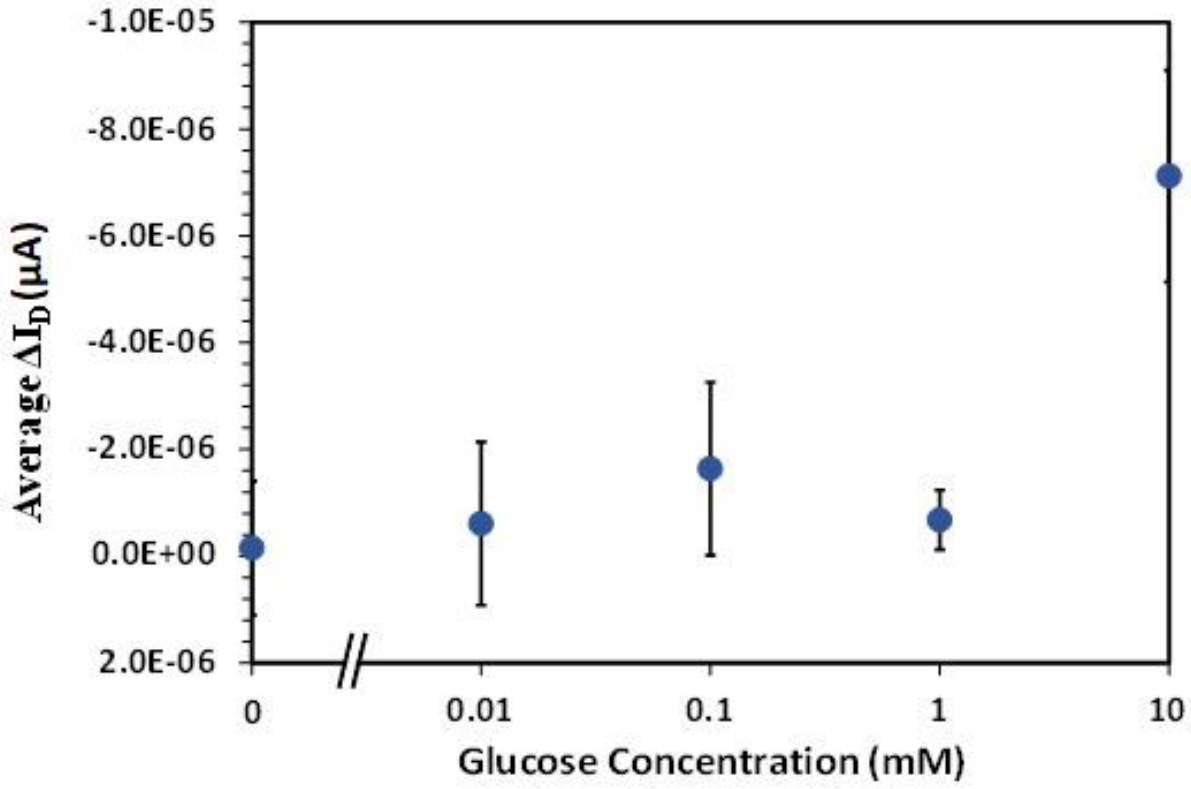

Figure 6.6: Calibration curve for DD1 glucose testing using the change in current at Av $\Delta I_{D,T=800s} - \Delta I_{D,t=240s}$ A after addition of 0 mM, 0.01 mM, 0.1 mM, 1 mM and 10 mM glucose

analyte, for a minimum of 6 tests at each glucose concentration. The error bars represent one standard deviation from the average.

The design for the DD2 sensor is depicted in Figures 6.7 and 6.8. In this design the PAN layer was removed (in an attempt to minimise crosstalk between the test and reference devices) and analyte was added simulatneously above both sets of source and drain electrodes.

The response of the DD2 sensor to glucose was measured in a similar manner as the DD1 devices. 10 µL of the analyte solution was placed on each side of the device and I_D was measured as a function of time. V_{GS} was set at – 0.3 V and V_{DS} was set at – 1 V. A minimum of 6 measurements were made for each glucose concentration.

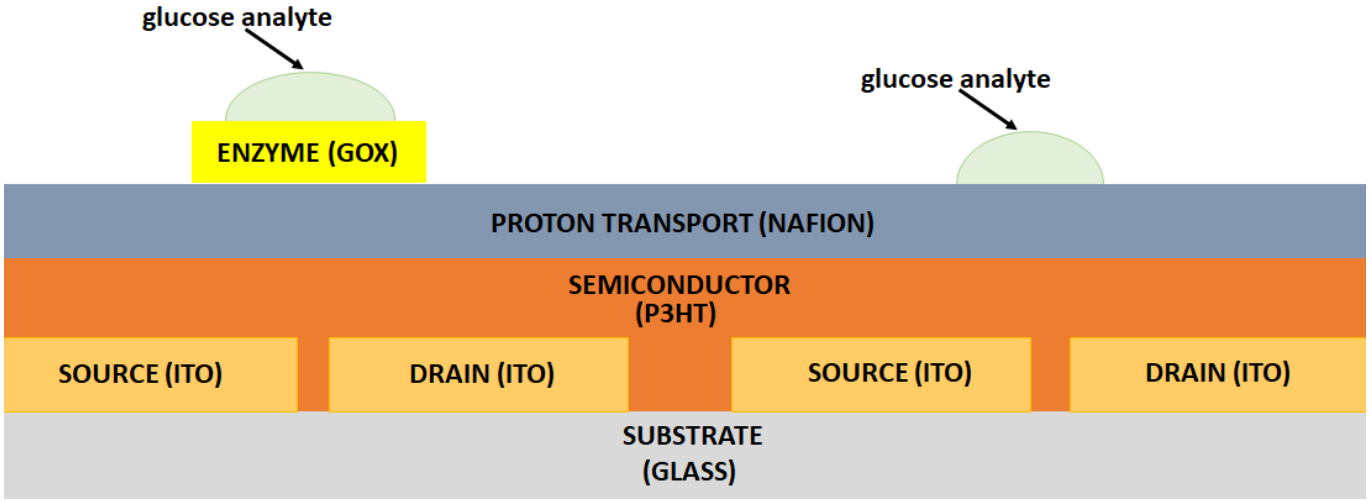

Figure 6.7: Device configuration for DD2. One of the sides contains GOX and the other side no GOX. One drops of glucose analyte (0 mM, 1 mM, 0.01 mM, 0.1 mM, 1 mM and 10 mM) is deposited on the top of each side of the device.

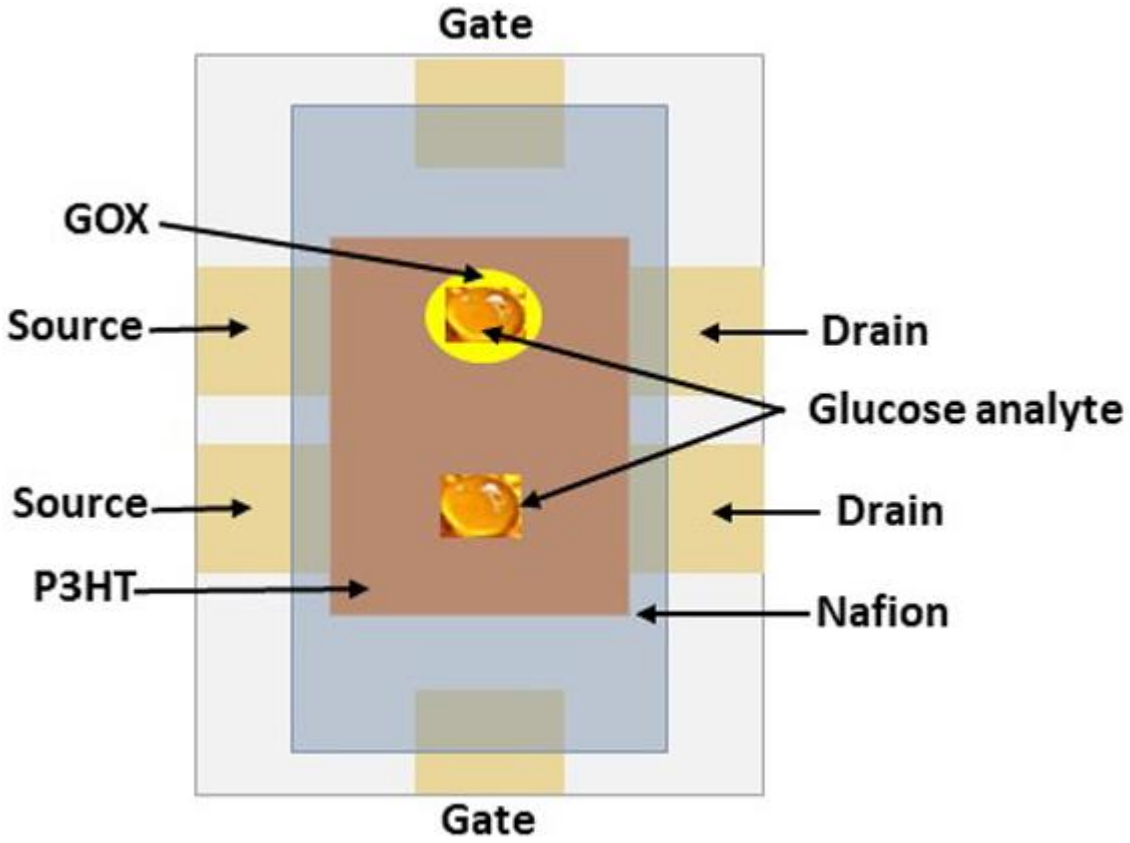

Figure 6.8: Top-down view of DD2. One of the sides contains GOX and the other side No GOX.

Our observation was that there was a major difference between the current levels for the test and reference devices before adding analyte. As mentioned previously, for all glucose concentrations there is initial change in current related with the addition of the analyte that appears to be due to the water and is related to changes in the doping levels of the P3HT. Thus addition of the GOX to the test side of the device will lead to some change in the native level of doping of the P3HT in the associated source-drain channel.

As previously, the difference between the test and reference data was taken, it was then normalised to $I_D = 0$ A at t = 240 s (just prior to analyte addition) and the I_D at t = 800 s was plotted as the figure of merit (FOM) for device output. Figure 6.9 shows typical difference plots between the test and reference data for each glucose concnetration and Figure 6.10 shows the these plots on the same

graph, nomalised at t – 240 s. Figure 6.11 shows the resultant calibration curve using I_D at t = 800 s as the output FOM. Again significant crosstalk was observed between the test and reference outputs, with the I_D plots mimicing each other, especially at higher concentrations. The data for DD2 show that the average initial current for all concentrations (0 mM, 0.01 mM, 0.1 mM, 1 mM, 10 mM) with GOX was -1.35 ± 1 x10^{-5} A whilst for without GOX was it was -6.39 ± 2 x10^{-5}.

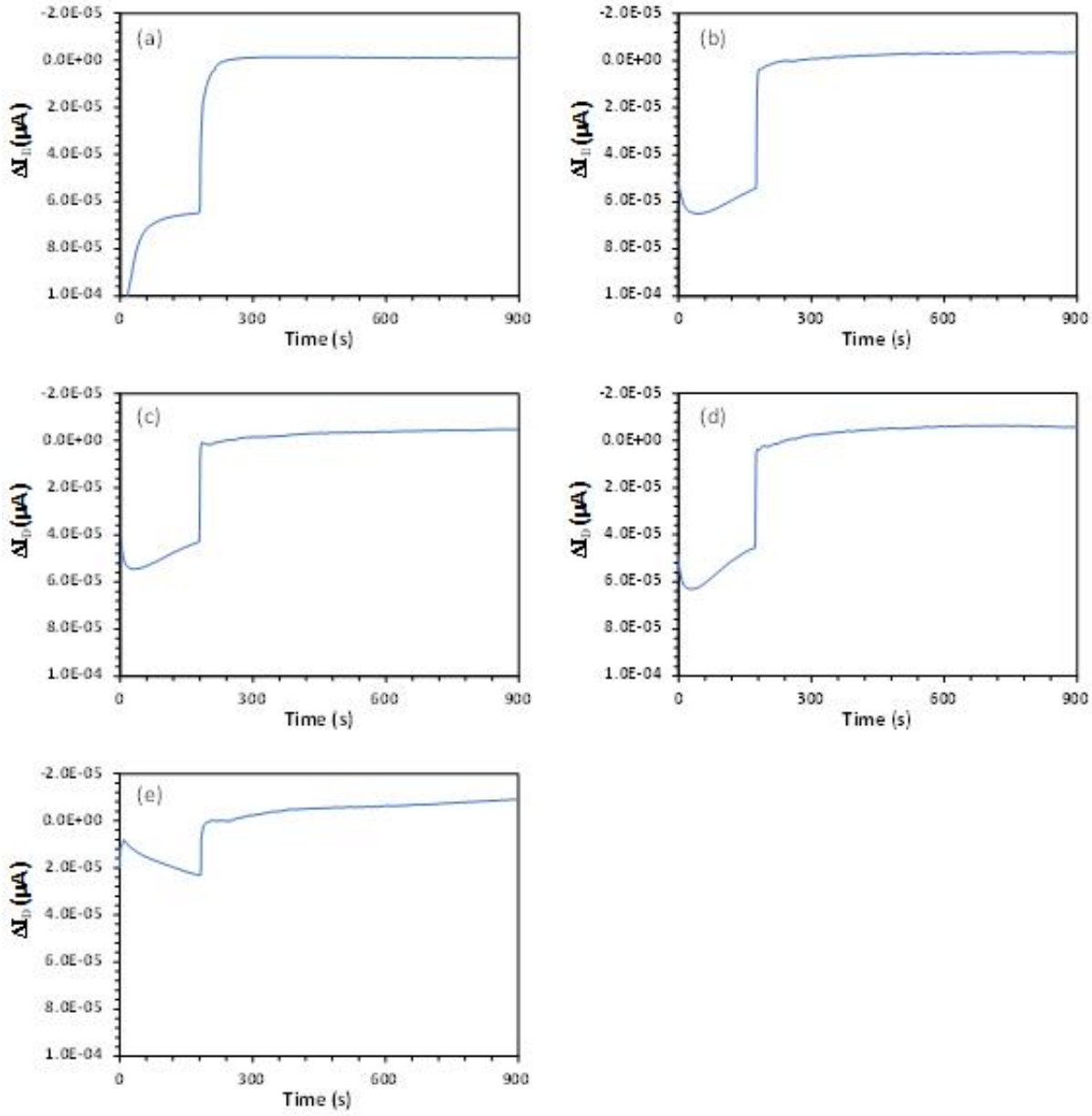

Figure 6.9: Typical DD2 current response versus time for glucose concentrations of; a 0 mM, b 0.01 mM, c 0.1 mM, d 1 mM and e 10 mM. The reference data has been subtracted from

the test data and the resulting plot is normalised to I_D = 0 A at t = 240s seconds, just before glucose analyte addition.

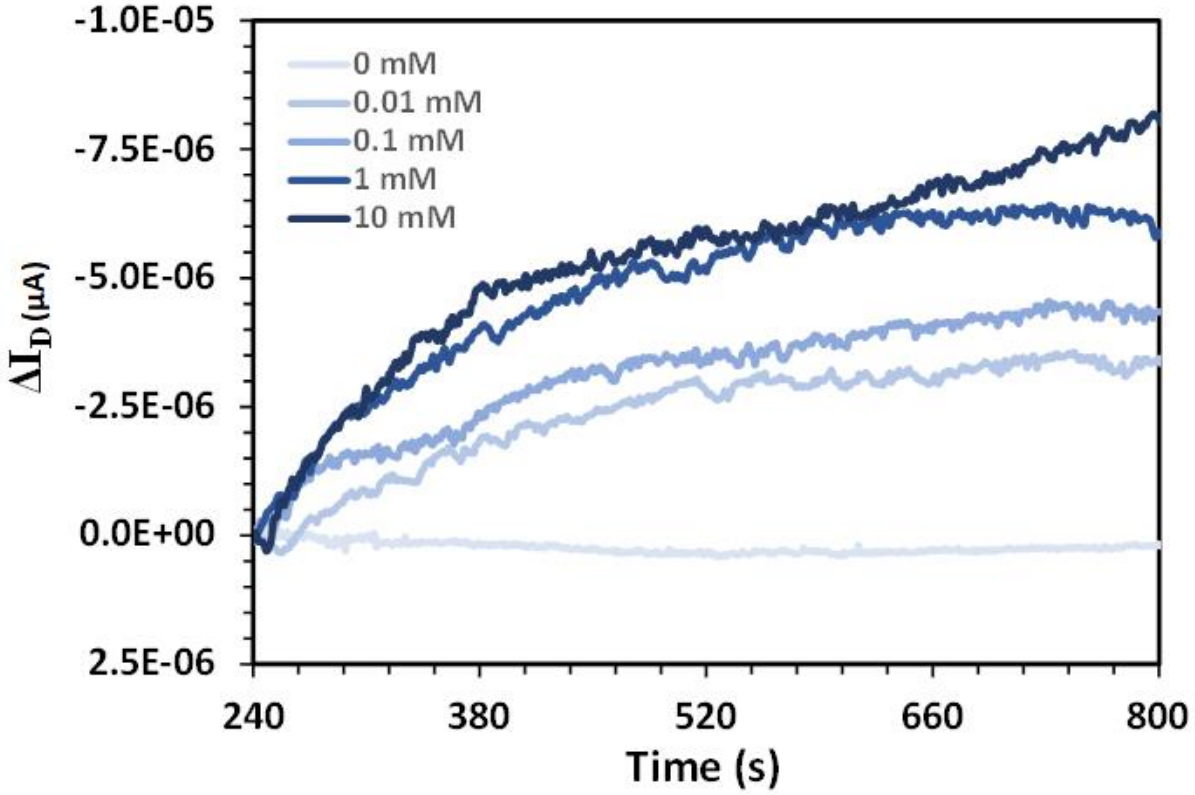

Figure 6.10 Typical ΔI_D vs t curves normalised to t = 240s for DD2.

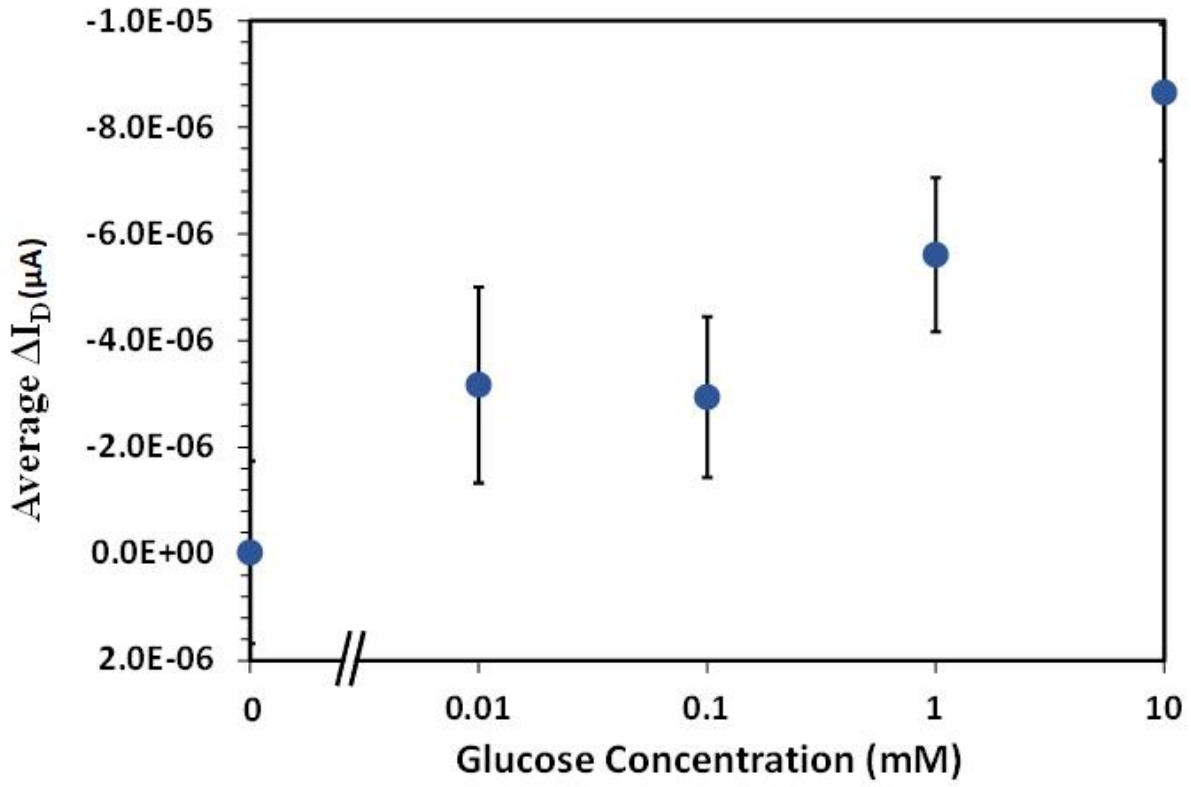

Figure 6.11: Calibration curve for DD2 glucose testing using the change in current at Av $\Delta I_{D,T=800s} - \Delta I_{D,t=240s}$ A after addition of 0 mM, 0.01 mM, 0.1 mM, 1 mM and 10 mM glucose analyte, for a minimum of 6 tests at each glucose concentration. The error bars represent one standard deviation from the average.

The measurements recorded for DD2 are both qualitatively and quantitatively very similar to those recorded for DD1. The data shown in Figure 6.10 exhibits ΔI_D values of ~0 for deionised water (0 mM glucose) across the entire testing period up to t = 800 s. The ΔI_D values at 800 s increase in an approximate monotonic fashion as the glucose concentration increases, up to a value of ~ -8 x 10^{-6} A for 10 mM glucose. As with DD1, the errors associated with the measurments in DD2 are large and suggest poor sensitivity to glucose at low concentrations[386] . As such, the presence or absence of a PAN layer seems to have little effect on the device output and crosstalk between the test and reference devices in the sensor.

In light of the continued clear crosstalk between test and reference devices we modified the measurement protocol by introducing total physical separation of the two devices prior to measurement (DD3).

6.4 Dual Device Data with Isolated Devices (DD3)

We designed this experiment to evaluate the effect of crosstalk between the test and reference devices in the DD1 and DD2 architectures. To achieve this aim, the glass substrate in the DD1 device design was scored prior to deposition of the layers and when the device fabrication was complete the test and reference devices were carefully separated by snapping the substrate prior to addition of the analyte and testing. PAN film circles (513 nm thick, 20 mm diameter) were also placed on top of the Nafion layer prior to GOX addition and testing. Thus, the test half of the device structure consisted of P3HT/Nafion/PAN/GOX and the reference half was P3HT/Nafion/PAN, as shown in Figures 6.12 and 6.13.

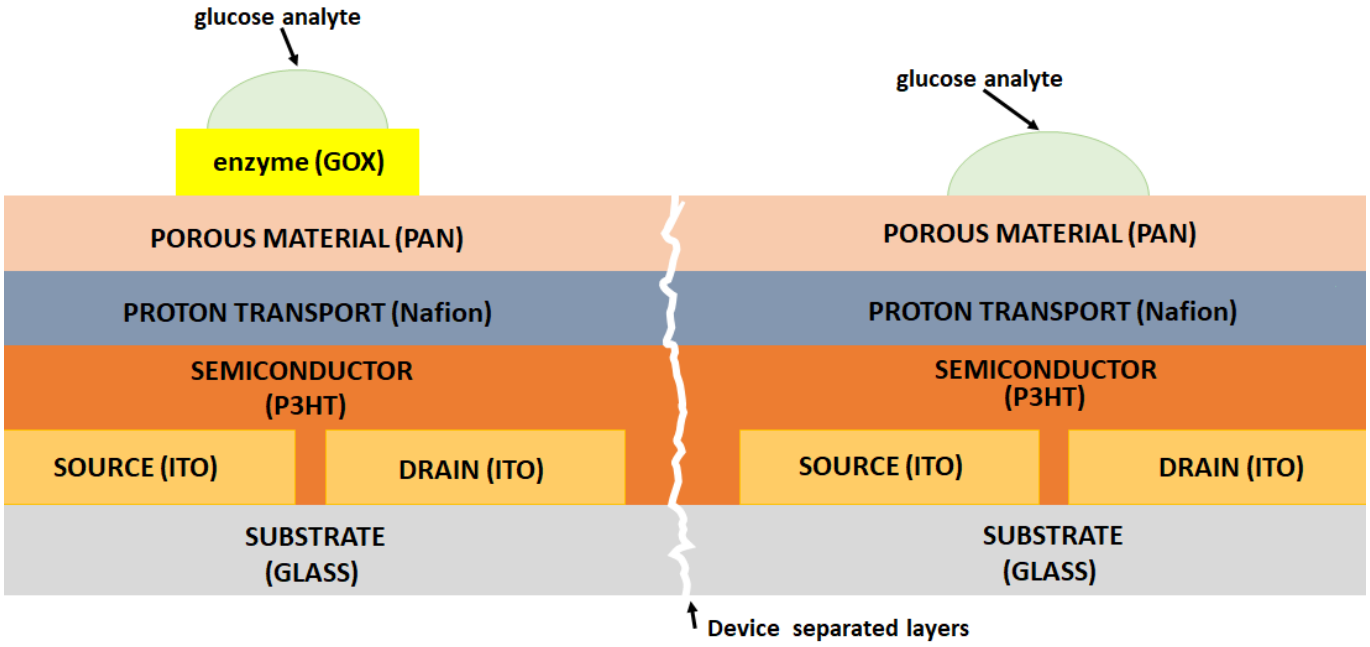

Figure 6.12 Device configuration for DD3 showing PAN layer on both sides. One of the sides contains GOX and the other side No GOX. One drop of glucose analyte (0 mM, 0.01 mM, 0.1, 1 mM and 10 mM) is deposited on the top of the PAN on each side of the separated device.

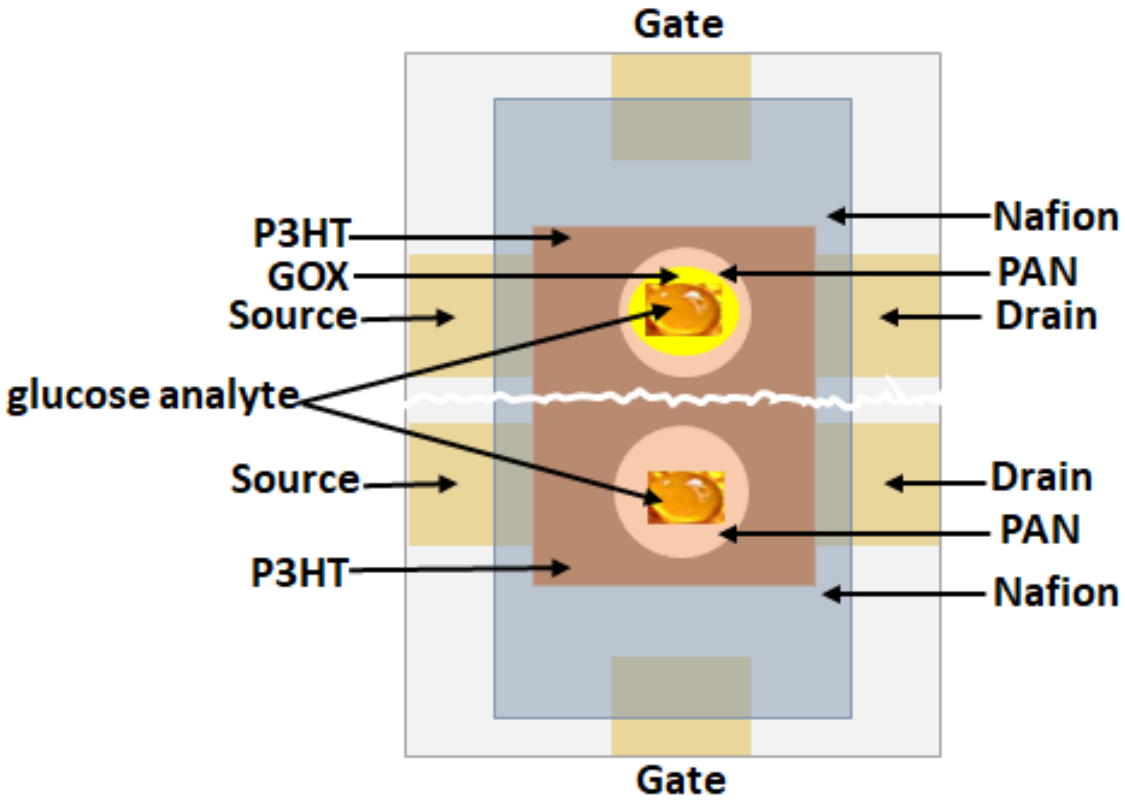

Figure 6.13: Top-down view of DD3.

Figure 6.14 shows typical DD3 current response versus time plots for glucose concentrations between 0 and 10 mM. The plots show the difference between the test and reference data sets and the I_D has been normalised to 0 A in each cast at t = 240 s. Figure 6.15 plots each of the curves in Figure 6.14 on the same graph for direct comparison. Figure 6.16 shows the resultant calibration curve using I_D at t = 800 s as the output FOM.

It is significant to note that in this experiment all of the reference measurements were essentially equivalent and they did not mimic the corresponding test measurement, suggesting that crosstalk was indeed responsible for the similar test and reference measurements in the DD1 and DD2 experiments. Obviously in this case, where the test and reference devices are physically separated crosstalk is no longer physically possible.

For the DD3 devices the average initial current for all concentrations for the test devices was -1.89 ± 9 x 10^{-6} A whilst for the reference devices the average initial current was -3.42 ± 2 x 10^{-5} A.

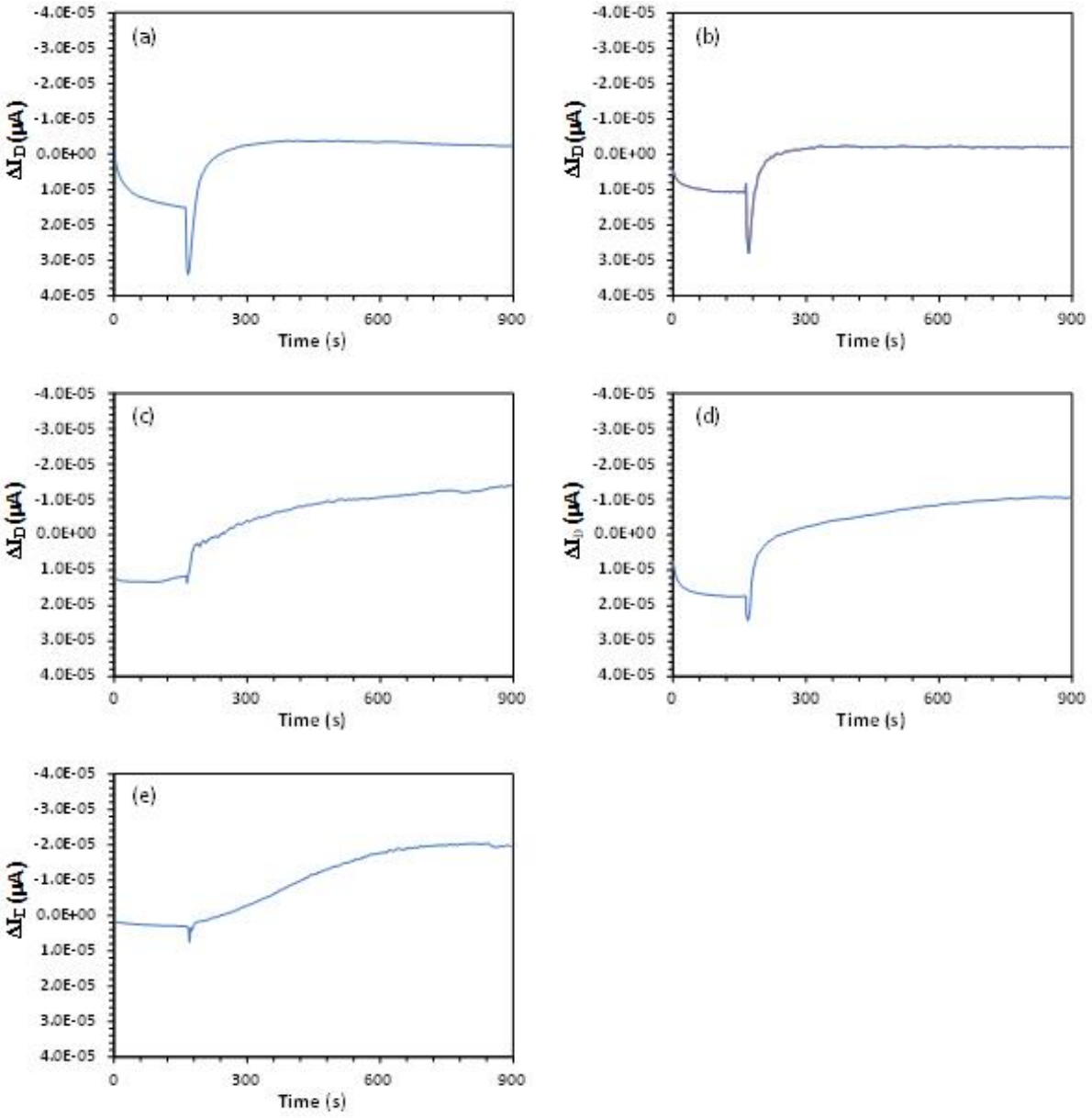

Figure 6.14: Typical DD3 current response versus time for glucose concentrations of; a 0 mM, b 0.01 mM, c 0.1 mM, d 1 mM and e 10 mM. The reference data has been subtracted from the test data and the resulting plot is normalised to I_D = 0 A at t = 240s seconds, just before glucose analyte addition.

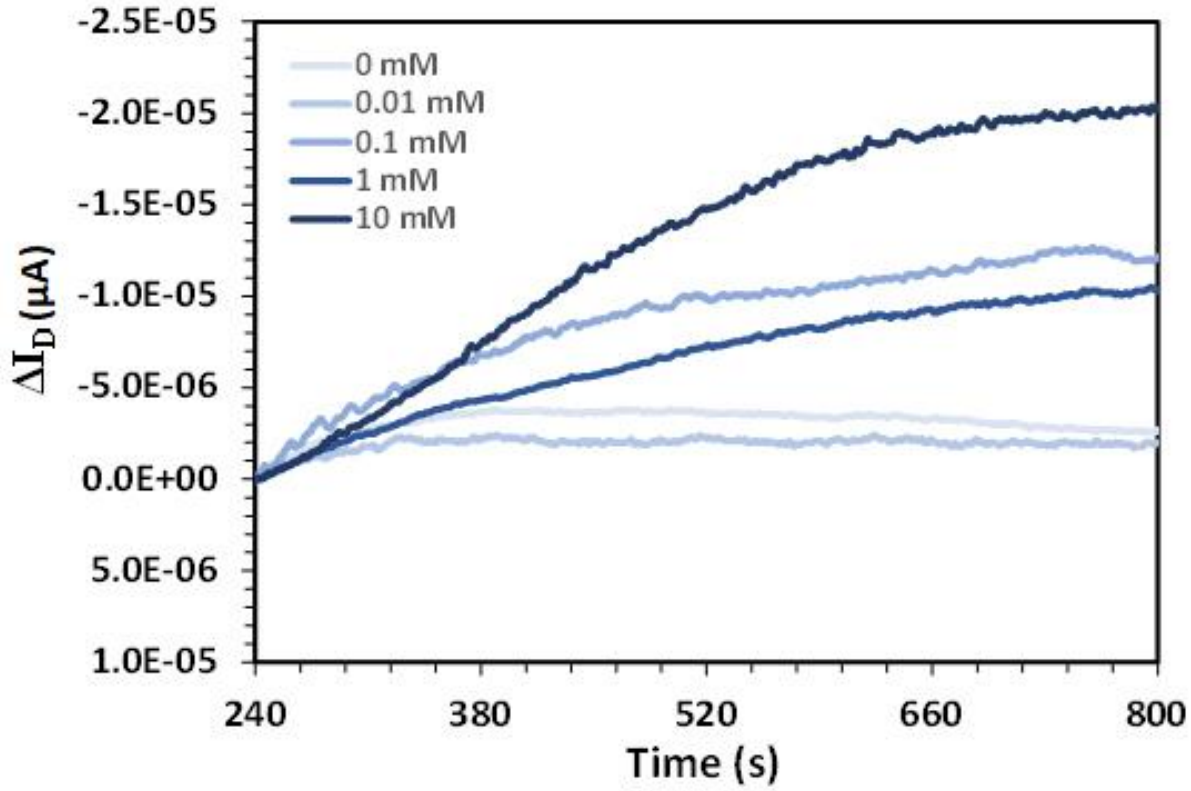

Figure 6.15: Typical ΔI_D vs t curves normalised to t = 240s for DD3.

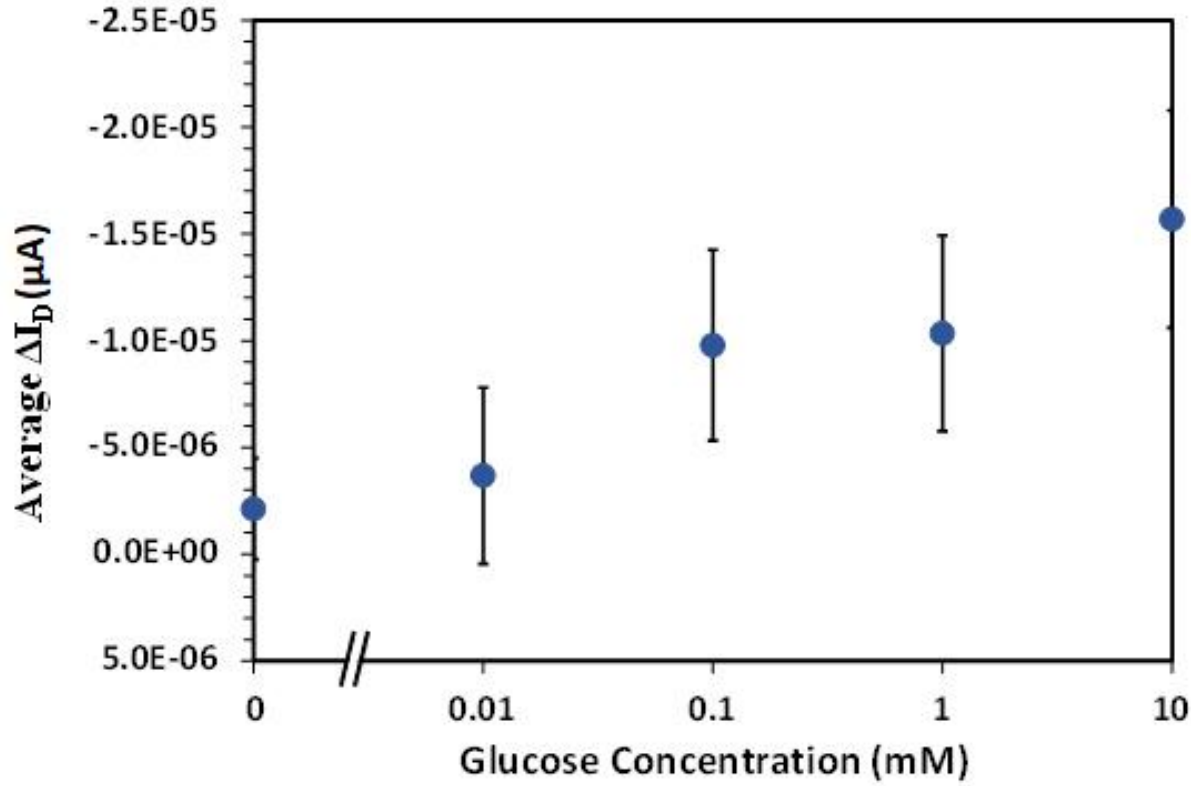

Figure 6.16: Calibration curve for DD3 glucose testing using the change in current at Av $\Delta I_{D,T=800s} - \Delta I_{D,t=240s}$ A after addition of 0 mM, 0.01 mM, 0.1 mM, 1 mM and 10 mM glucose

analyte, for a minimum of 6 tests at each glucose concentration. The error bars represent one standard deviation from the average.

Again, the results are qualitatively very similar to those obtained for DD1 and DD2 in the previous Section. The average $\Delta I_{D,T=800s} - \Delta I_{D,t=240s}$ values start off near 0 for deionised water and increase in a near monotonic manner as the glucose concentration increases. However, in the case of DD3 the initial current is higher (~ -2×10^{-6} A vs $< -5 \times 10^{-7}$ A for DD1 and DD2) and so is the current for the 10 mM glucose sample ($> -1.5 \times 10^{-5}$ A vs ~ -8×10^{-6} A for DD1 and DD2). Consequently, the current range which the glucose concentrations cover is higher, suggesting overall higher sensitivity of the device.

In order to better compare the output data of DD1, DD2, DD3 and the optimised non-referenced device presented in Section 5.4 (Figure 5.21), the four calibration curves are presented below on one graph (Figure 6.17). Dotted lines have been added to the plots. These represent a visual "best fit" and are present to guide the eye to the overall data trend. For the calibration curve from Chapter 5 only the I_D data corresponding to glucose concentrations 0 mM, 0.01 mM, 0.1 mM. 1 mM and 10 mM are plotted to simplify comparasion. Similarly, for the sake of clarity, the error bars have been left of the plots. Instead, for discussion purposes, a plot of concentration vs 1 standard deviation in each data point, for each calibration curve, have been plotted separately (Figure 6.18).

In Figure 6.17 the slope of the 'best fit" curves gives a visual indication of the relative sensitivity of the device to glucose at each glucose concentration. The steeper the slope the more sensitive the device is to changes in glucose at any given concentration (i.e. there is a greater change in the I_D of the test device relative to the reference device for the same change in glucose concentrations). We can see that, in this regard, DD3 performs better than DD2 which performs better than DD1. Furthermore, DD3 displays a greater ΔI_D value for a given glucose concentration than DD2, which again is higher than DD1. This simple

analysis suggests that DD3 is the superiorly performing sensor and that crosstalk in the conjoined devices (DD1 and DD2) may be a significant cause of variation.

Crosstalk between the test and reference devices will lead to significant changes in the responses of the two devices. On the one hand, crosstalk could result in diffusion of glucose from the reference device to the GOX in the test device, potentially resulting in an increase in the I_D of the test device after reaction. However, this diffusion will be slow, given that there are no specific drivers for this process beyond osmotic pressure (and the concentration of the glucose in both devices is the same). A more likely result is enhanced doping of the P3HT in the channel of the reference device by protons generated in the test device. This process will be fast (as proton transport in hydrated Nafion is by proton hopping - the Grotthuss mechanism) and driven by the relative potentials of the gate, source and drain electrodes in the conjoined device. Consequently, I_D in the reference device will be higher than expected and that of the test device will be correspondingly lower than expected. Since the FOM of these devices (ΔI_D at t = 800 s) is based on the difference between the reference and test outputs, a lower value will be recorded, as is observed for the conjoined devices in Figure 6.17.

Interestingly, the non-referenced PAN devices from Chapter 5 have a distinctly nonlinear calibration curve, with poor sensitivity at low concentrations but this improves rapidly at higher concentrations. This observation suggests that it may be possible to use a simple, non-referenced sensor device for saliva glucose detection but that the addition of a reference may assist in accurately differentiating concentrations at the low end of the human saliva glucose concentration range.

Figure 6.18 shows the errors associated with each of the data points in Figure 6.17 and is the other aspect of device response which must be considered to

assess device suitability. Figure 6.19 shows these values as a percentage error for the data points in Figure 6.17. In this plot guide lines at 50% and 100% have been added. In almost all cases for low glucose concentrations, the standard devication of the averaged data in very similar in value to the current itself. Indeed for the conjoined devices (DD1 and DD2) very large percentage errors are observed for the 0 mM samples. It is only for 1 mM and 10 mM samples that the errors become significantly lower (less than 50% of the value of the current output). This result suggests that improved sensitivity at lower concentrations is required before these devices could be relied upon to provide precise glucose reading at the low end of the human saliva glucose range. However, the uniformity of the errors as a percentage of the output current suggests that the non-referenced device from Chapter 5 may be a good candidate for further investigation, since whilst the output current at low glucose concentrations is generally lower than DD1, DD2 or DD3 the error in these values is also significantly smaller. This observation, coupled with the superior monotonic nature of this devices calibration curve make this device architecture the standout result of this work.

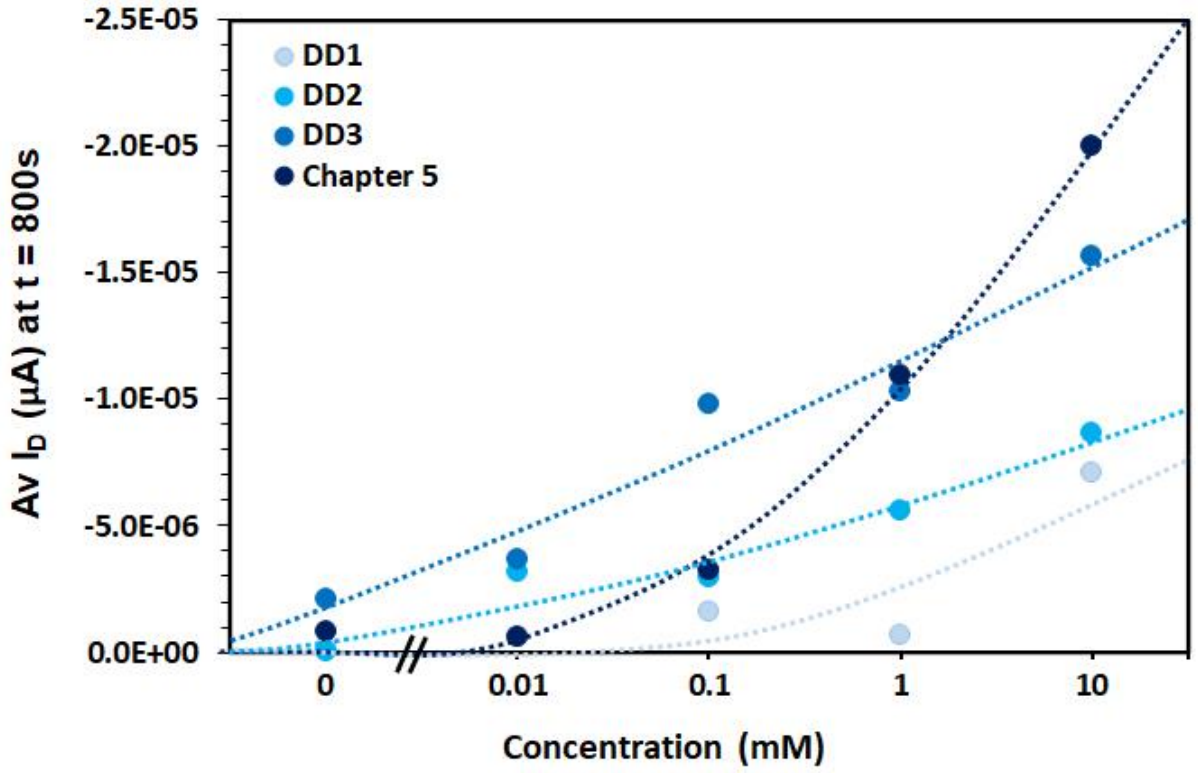

Figure 6.17: Comparison of glucose calibration curves for DD1 (light blue dots), DD2 (lighter blue dots), DD3 (blue dots) and the optimised device presented in Chapter 5 (dark blue dots). Error bars have been removed for clarity and dotted lines have been added to aid the eye.

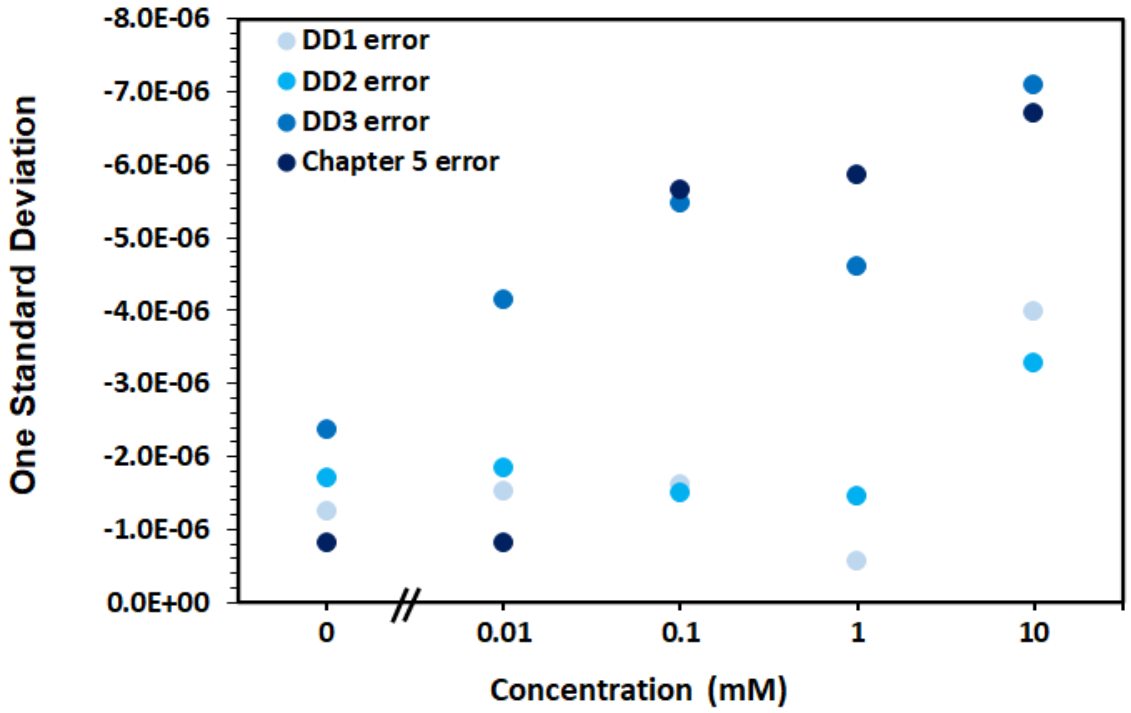

Figure 6.18: 1 standard deviation of the average I_D values as a function of glucose concentration for the data points presented in Figure 6.17.

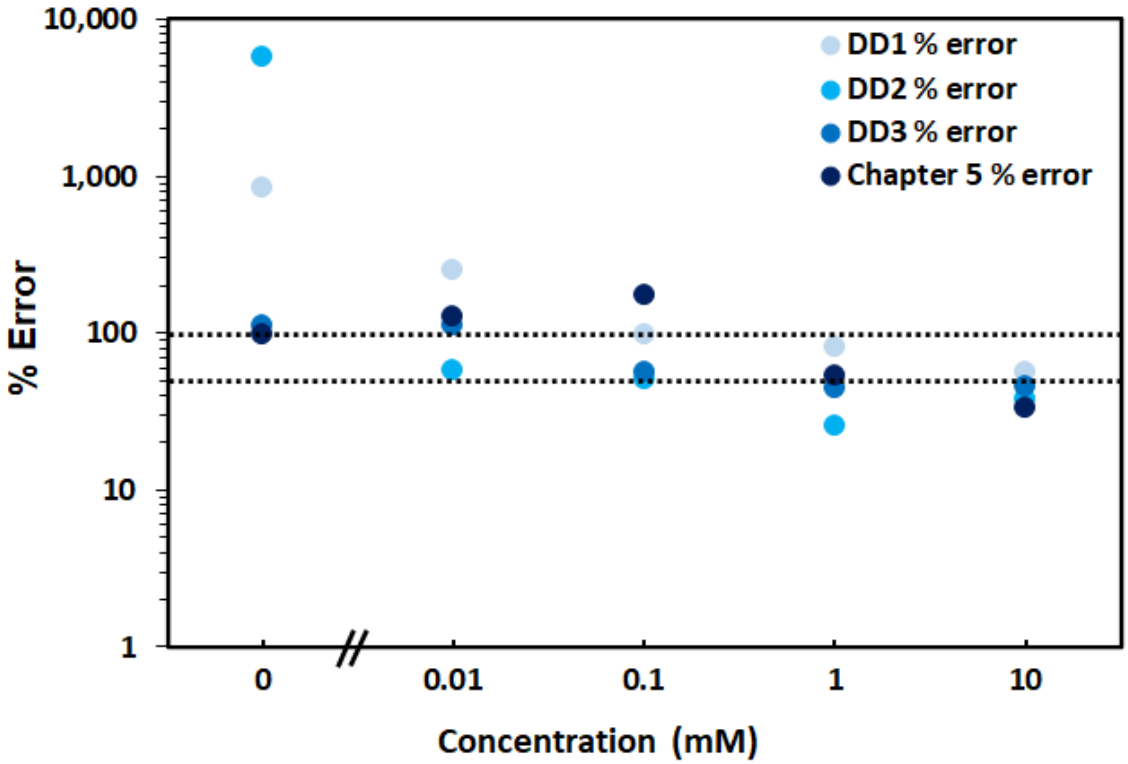

Figure 6.19: Data in Figure 6.18 presented as a percentage error of the data presented in Figure 6.17.

6.5 Conclusion

In this chapter we have explored the use of non-enzyme-containing reference devices to improve sensor sensitivity, the hypothesis being that a reference device, fabricated on the same substrate as the test device, will eliminate or mitigate variation due to the fabrication process. In Section 6.3 we found that, in architectures where the test and reference devices are conjoined during the testing process (DD1 and DD2), crosstalk between the two devices is a significant issue and results in a lower device FOM output than expected. The presence or absence of a PAN capping layer did not appear to alter the crosstalk.

When the test and reference are separated prior to testing (DD3) crosstalk necessarily cannot occur. A higher FOM output and better device sensitivity to glucose concentration, is observed for these devices. However, for all three device architectures, variance remains high and the errors associated with the glucose measurement are uniformly of a similar magnitude as the output itself. Indeed, when compared with the optimised non-reference device presented in Chapter 5, it is clear that DD1-3 do not offer an improvement in device output or sensitivity and that the non-referenced device is the best design for further investigation.

Chapter 7: Conclusions and Future work

7.1 Conclusions

This thesis focusses on the development of organic semiconductor-based glucose sensors built upon an organic thin film transistor (OTFT) architecture. Based upon the simplest architecture presented in Chapter 3, several variations and refinements to the devices are subsequently introduced in the following chapters and their characteristics discussed and analysed.

Chapter 3 gives a brief introduction to OTFTs and shows how they can be adapted for use in the types of glucose sensors presented in this thesis. The chapter systematically describes how, by exchanging certain materials and including an analyte specific recognition element, a previously used OTFT architecture can be used as a glucose sensor.

In Chapter 4, we electrically characterised the P3HT, Nafion and P3HT/Nafion bilayer films as a function of annealing temperature. We observe a significant increase in conductivity of the P3HT/Nafion bilayer and propose a mixing and doping mechanism to explain this increase. The impact of thermal annealing on the performance of the sensors was also explored.

In Chapter 5 we investigate the use of porous PAN films as a mechanism for controlling analyte placement and GOX retention in the devices. These porous films were fabricated using the phase inversion technique and their porosity was determined using microscopy. Devices containing PAN with subsequently characterised and their performance compared with those in Chpater 3 and 4. In this chapter we also identified the major sources of

variability in sensor fabrication and discussed methods for mitigating this variability.

In Chapter 6, the use of a reference device was explored as a method of reducing device fabrication variability. The reference was fabricated on the same substrate as the test device but did not contain the analyte recognition element (GOX).

7.2 Future work

This thesis has successfully demonstrated a prototype for an OTFT-based glucose sensor. However, the work undertaken has shown a number of areas that can be improved or need further work.

- Sensitivity: it is clear from the data presented from optimised devices in Chapter 5 that a further improvement in the sensitivity in the lower range of human salivary glucose is required. At current performance levels, the device may be suitable for use in a binary sensor to detect hyperglycaemia but are inadequate for use as an analytical glucose monitoring tool. The three main ways improve device performance would be to decrease the baseline current level ("off current"), increase the magnitude of current response to a given glucose concentration ("on current") and finally to reduce device-to-device variability (error). With lower variability, the analyte-based response for any given device would be more easily differentiated from any part of the response caused by other actors**.**

- Device fabrication automation: a major source of device fabrication variability is caused by the manual nature of this process. In order to reduce variability, we propose to automate each step of the device

fabrication process through the use of material deposition techniques such as roll-to-roll printing. In addition, automating the test procedure in the laboratory with a view to ultimately using an automated readout device which can control factors such as the location, volume and timing of the analyte addition would be desirable to minimise error.

- Stability
    - Materials: we note that the properties of key materials used in these devices are heavily dependent on their storage and treatment. Key properties such as the hydration level of Nafion, light-initiated oxidation of P3HT and the activity of GOX could lead to dramatic changes in device output. Whilst great care was taken throughout this thesis to ensure that materials were stored and treated appropriately, ensuring that the materials do not lose their function during fabrication, storage and testing will be critical to the long-term application of these devices.
    - Morphology: work in this thesis has shown that thermally driven intermixing of the Nafion and P3HT layers leads to dramatic changes in the material properties. Additionally, variation in the location of the GOX within the device over time in these devices could also lead to dramatic changes in device output. The long-term effects of exposure to ambient conditions (such as temperature and humidity) need to be measured to determine ways in which packaging could mitigate these effects.

- Porous PAN films: this work has shown that porous PAN films can be integrated into the glucose sensor device architecture. However, further work should be undertaken to utilise this layer to provide the most

efficient access to the enzyme by the analyte. Furthermore, quantitative free volumes studies on the PAN films should be undertaken with the aim of using these materials to provide an accurately metered volume of analyte solution to the device.

- Interfering moieties: beyond the scope of this thesis, but of key importance to the application of the devices presented here would be a study of device response to human saliva samples. Key to this study will be a determination of the effect of interring species within saliva upon device performance.

7.3 Summary

Across the course of this thesis, we have successfully demonstrated the fabrication and testing of prototype glucose sensors based on an OTFT architecture. Glucose concentration sensitivity has been demonstrated into the human salivary glucose range and a fundamental understanding of the device mechanism has been explored and discussed. Despite studies investigating the use of an integrated reference device, we have found that the optimal device architecture consists of a non-referenced multilayer stack of the following composition: ITO/P3HT/Nafion/PAN/GOX, using which some sensitivity down to glucose concentrations of 0.1 mM was observed. Going forward, it is envisioned that this sensor technology could provide the basis for a mass-produced glucose sensor for point-of-care management for sufferers of diabetes.

References

1. Herlogsson, L., *Electrolyte-Gated Organic Thin-Film Transistors*, in *Linköping Studies in Science and Technology*. 2011, Linköping.
2. Murat Atesa, Tolga Karazehira, and A.S. Saracb. *Conducting Polymers and their Applications.* Current Physical Chemistry. 2012; 2: 224-240.
3. Isaksson, J. *ORGANIC BIOELECTRONICS Electrochemical Devices based on Conjugated Polymers.* Linköping Studies in Science and Technology. Dissertations. 2007.
4. Elkington, D., *Fabrication and Characterisation of Organic Thin-Film Transistors for Sensing Applications*. 2013, The University of Newcastle.
5. Manju Gerard a, A.C.b., *, B.D. Malhotra b. *Application of conducting polymers to biosensors.* Biosensors & Bioelectronics. 2002; 17.
6. Berggren, M., D. Nilsson, and N.D. Robinson. *Organic materials for printed electronics.* Nat Mater. 2007; 6: 3-5.
7. Sirringhaus, H., T. Kawase, R. Friend, et al. *High-resolution inkjet printing of all-polymer transistor circuits.* Science. 2000; 290: 2123-2126.
8. Magliulo, M., M. Mulla, M. Singh, et al. *Printable and flexible electronics: from TFTs to bioelectronic devices.* Journal of Materials Chemistry C. 2015.
9. Mehrotra, P. *Biosensors and their applications – A review.* Journal of Oral Biology and Craniofacial Research. 2016; 6: 153-159.
10. Justino, C., A. Duarte, and T. Rocha-Santos. *Recent progress in biosensors for environmental monitoring: A review.* Sensors. 2017; 17: 2918.
11. Koklu, A., D. Ohayon, S. Wustoni, et al. *Microfluidics integrated n-type organic electrochemical transistor for metabolite sensing.* Sensors and Actuators B: Chemical. 2021; 329: 129251.
12. Yoo, E.-H. and S.-Y. Lee. *Glucose biosensors: an overview of use in clinical practice.* Sensors. 2010; 10: 4558-4576.
13. Gifford, R. *Continuous glucose monitoring: 40 Years, what we' ve learned and what's next.* ChemPhysChem. 2013; 14: 2032-2044.
14. Gruhl, F.J. and K. Länge. *Surface acoustic wave (SAW) biosensor for rapid and label-free detection of penicillin G in milk.* Food analytical methods. 2014; 7: 430-437.
15. Wang, Y., H. Xu, J. Zhang, and G. Li. *Electrochemical Sensors for Clinic Analysis.* Sensors (Basel, Switzerland). 2008; 8: 2043-2081.
16. Balakrishnan, S.R., U. Hashim, G.R. Letchumanan, et al. *Development of highly sensitive polysilicon nanogap with APTES/GOx based lab-on-chip biosensor to determine low levels of salivary glucose.* Sensors and Actuators A: Physical. 2014; 220: 101-111.
17. Yamaguchi, M., M. Mitsumori, and Y. Kano. *Noninvasively measuring blood glucose using saliva.* IEEE Engineering in Medicine and Biology Magazine. 1998; 17: 59-63.
18. Panchbhai, A.S. *Correlation of salivary glucose level with blood glucose level in diabetes mellitus.* Journal of oral & maxillofacial research. 2012; 3.
19. Zhang, J., W. Hodge, C. Hutnick, and X. Wang. *Noninvasive diagnostic devices for diabetes through measuring tear glucose.* Journal of diabetes science and technology. 2011; 5: 166-172.
20. Morgan, K.A., *Salivary testosterone and cortisol measurements in profesional elite rugby union players*. 2009: University of South Wales (United Kingdom).
21. Bartic, C., A. Campitelli, and S. Borghs. *Field-effect detection of chemical species with hybrid organic/inorganic transistors.* Applied Physics Letters. 2003; 82: 475-477.
22. Meshram, B., A. Agrawal, S. Adil, S. Ranvir, and K. Sande. *Biosensor and its application in food and dairy industry: A Review.* Int. J. Curr. Microbiol. Appl. Sci. 2018; 7: 3305-3324.
23. Horowitza, G. *Organic thin film transistors: From theory to real devices.* Denis-Didero. 2004.

24. Nikolou, M. and G.G. Malliaras. *Applications of poly(3,4-ethylenedioxythiophene) doped with poly(styrene sulfonic acid) transistors in chemical and biological sensors.* Chem Rec. 2008; 8: 13-22.
25. Mabeck, J.T. and G.G. Malliaras. *Chemical and biological sensors based on organic thin-film transistors.* Anal Bioanal Chem. 2006; 384: 343-53.
26. Cammann, K. *Bio-sensors based on ion-selective electrodes.* Fresenius' Zeitschrift für analytische Chemie. 1977; 287: 1-9.
27. Chiu, C.-W., *Interfacial Interactions between Implant Electrode and Biological Environment*. 2012.
28. Shkil, H., *Genetically modified yeast cells as a basis for biological recognition and sensing. evaluation of enzyme-based and cell-based electron transfer pathways*, in *Department of Analytical Chemistry*. 2011, Ruhr-Universität Bochum: Bochum.
29. Vo-Dinh, T. and B. Cullum. *Biosensors and biochips: advances in biological and medical diagnostics.* Fresenius' journal of analytical chemistry. 2000; 366: 540-551.
30. Perumal, V. and U. Hashim. *Advances in biosensors: Principle, architecture and applications.* Journal of Applied Biomedicine. 2014; 12: 1-15.
31. Jain, Y., C. Rana, A. Goyal, et al. *Biosensors, types and applications*. in *BEATS 2010: Proceedings of the 2010 International Conference on Biomedical Engineering and Assistive Technologies, Jalandhar, India*. 2010. BEATS.
32. Pejcic, G.P.B. *Using Biosensors to Detect Emerging Infectious Diseases.* Curtin university of Technology. 2005.
33. Warsinke, A., A. Benkert, and F. Scheller. *Electrochemical immunoassays.* Fresenius' journal of analytical chemistry. 2000; 366: 622-634.
34. Babkina, S., N. Ulakhovich, and Y.I. Zyavkina. *Amperometric DNA biosensor for the determination of auto-antibodies using DNA interaction with Pt (II) complex.* Analytica chimica acta. 2004; 502: 23-30.
35. Wang, J., A. Ibáñez, M.P. Chatrathi, and A. Escarpa. *Electrochemical enzyme immunoassays on microchip platforms.* Analytical chemistry. 2001; 73: 5323-5327.
36. Ivnitski, D., R. Sitdikov, and N. Ivnitski. *Non-invasive electrochemical hand-held biosensor as diagnostic indicator of dental diseases.* Electrochemistry Communications. 2003; 5: 225-229.
37. Palchetti, I., A. Cagnini, M. Del Carlo, et al. *Determination of anticholinesterase pesticides in real samples using a disposable biosensor.* Analytica Chimica Acta. 1997; 337: 315-321.
38. Dmitri Ivnitski, I.A.-H., Plamen Atanasov, Ebtisam Wilkins. *Biosensors for detection of pathogenic bacteria.* Biosensors & Bioelectronics 1999; 4: 599-624.
39. Thévenot, D.R., K. Toth, R.A. Durst, and G.S. Wilson. *Electrochemical biosensors: recommended definitions and classification.* Analytical Letters. 2001; 34: 635-659.
40. Bakker, E. and E. Pretsch. *Modern potentiometry.* Angewandte Chemie International Edition. 2007; 46: 5660-5668.
41. Bakker, E., D. Diamond, A. Lewenstam, and E. Pretsch. *Ion sensors: current limits and new trends.* Analytica Chimica Acta. 1999; 393: 11-18.
42. Rogers, K.R. and M. Mascini. *Biosensors for field analytical monitoring.* Field Analytical Chemistry & Technology. 1998; 2: 317-331.
43. Gerard, M., A. Chaubey, and B. Malhotra. *Application of conducting polymers to biosensors.* Biosensors and bioelectronics. 2002; 17: 345-359.
44. Luo, X.-L., J.-J. Xu, W. Zhao, and H.-Y. Chen. *Glucose biosensor based on ENFET doped with SiO2 nanoparticles.* Sensors and Actuators B: Chemical. 2004; 97: 249-255.
45. Sant, W., M. Pourciel, J. Launay, et al. *Development of chemical field effect transistors for the detection of urea.* Sensors and Actuators B: Chemical. 2003; 95: 309-314.
46. Fan, X., I.M. White, S.I. Shopova, et al. *Sensitive optical biosensors for unlabeled targets: A review.* analytica chimica acta. 2008; 620: 8-26.

47. Soldatkin, A., J. Montoriol, W. Sant, C. Martelet, and N. Jaffrezic-Renault. *A novel urea sensitive biosensor with extended dynamic range based on recombinant urease and ISFETs.* Biosensors and Bioelectronics. 2003; 19: 131-135.
48. Caygill, R.L., G.E. Blair, and P.A. Millner. *A review on viral biosensors to detect human pathogens.* Analytica Chimica Acta. 2010; 681: 8-15.
49. C. Steinem, A.J. *Piezoelectric sensors.* Springer. 2007; 5.
50. Leonard, P., S. Hearty, J. Brennan, et al. *Advances in biosensors for detection of pathogens in food and water.* Enzyme and Microbial Technology. 2003; 32: 3-13.
51. Cattrall, R.W., *Chemical sensors*. 1997, Oxford.
52. Nirschl, M., A. Blüher, C. Erler, et al. *Film bulk acoustic resonators for DNA and protein detection and investigation of in vitro bacterial S-layer formation.* Sensors and Actuators A: Physical. 2009; 156: 180-184.
53. Kim, J., S.-M. Chang, H. Muramatsu, and K. Isao. *The principles and applications of nano-diagnosis system for a nano-biosensor.* Korean Journal of Chemical Engineering. 2011; 28: 987-1008.
54. Somerse, V.S., *Mercaptobenzothiazole-on-Gold Biosensor Systems for Organophosphate and Carbamate Pesticide Compounds*. 2007, University of the Western Cape.
55. Xie, B., K. Ramanathan, and B. Danielsson, *Principles of Enzyme Thermistor Systems: Applications to Biomedical and Other Measurements*, in *Thermal Biosensors, Bioactivity, Bioaffinitty*, P.K. Bhatia, et al., Editors. 1999, Springer Berlin Heidelberg. p. 1-33.
56. Ahmad, L.M., B. Towe, A. Wolf, F. Mertens, and J. Lerchner. *Binding event measurement using a chip calorimeter coupled to magnetic beads.* Sensors and Actuators B: Chemical. 2010; 145: 239-245.
57. Watterson, J., P.A. Piunno, and U.J. Krull. *Practical physical aspects of interfacial nucleic acid oligomer hybridisation for biosensor design.* Analytica Chimica Acta. 2002; 469: 115-127.
58. Buurma, N.J. and I. Haq. *Calorimetric and spectroscopic studies of Hoechst 33258: self-association and binding to non-cognate DNA.* Journal of molecular biology. 2008; 381: 607-621.
59. Paul, P., M. Hossain, R.C. Yadav, and G.S. Kumar. *Biophysical studies on the base specificity and energetics of the DNA interaction of photoactive dye thionine: spectroscopic and calorimetric approach.* Biophysical Chemistry. 2010; 148: 93-103.
60. Xi, H., S. Kumar, L. Dosen-Micovic, and D.P. Arya. *Calorimetric and spectroscopic studies of aminoglycoside binding to AT-rich DNA triple helices.* Biochimie. 2010; 92: 514-529.
61. Upasham, S., I.K. Banga, B. Jagannath, et al. *Electrochemical impedimetric biosensors, featuring the use of Room Temperature Ionic Liquids (RTILs): Special focus on non-faradaic sensing.* Biosensors and Bioelectronics. 2021; 177: 112940.
62. Bard, A.J. and M.V. Mirkin, *Scanning electrochemical microscopy*. 2001: CRC Press.
63. Prodromidis, M.I. *Impedimetric immunosensors—A review.* Electrochimica Acta. 2010; 55: 4227-4233.
64. Chai, C. and S.-W. Oh. *Electrochemical impedimetric biosensors for food safety.* Food Science and Biotechnology. 2020; 29: 879-887.
65. Dzulkurnain, N.A., S.A. Hanifah, A. Ahmad, and N.S. Mohamed. *Characterization of random methacrylate copolymers synthesized using free-radical bulk polymerization method.* International Journal of Electrochemical Science. 2015; 10: 84-92.
66. Asrami, P.N., S.A. Mozaffari, M.S. Tehrani, and P.A. Azar. *A novel impedimetric glucose biosensor based on immobilized glucose oxidase on a CuO-Chitosan nanobiocomposite modified FTO electrode.* International journal of biological macromolecules. 2018; 118: 649-660.
67. Daniels, J.S. and N. Pourmand. *Label-free impedance biosensors: Opportunities and challenges.* Electroanalysis: An International Journal Devoted to Fundamental and Practical Aspects of Electroanalysis. 2007; 19: 1239-1257.

68. Wu, J., J.P. Park, K. Dooley, et al. *Rapid development of new protein biosensors utilizing peptides obtained via phage display.* PLoS One. 2011; 6: e24948.
69. Li, Y., M. Zhao, and H. Wang. *Label-free peptide aptamer based impedimetric biosensor for highly sensitive detection of TNT with a ternary assembly layer.* Analytical and bioanalytical chemistry. 2017; 409: 6371-6377.
70. He, Y., L. Zhou, L. Deng, et al. *An electrochemical impedimetric sensing platform based on a peptide aptamer identified by high-throughput molecular docking for sensitive L-arginine detection.* Bioelectrochemistry. 2021; 137: 107634.
71. Ahmad, R., M.-S. Ahn, and Y.-B. Hahn. *ZnO nanorods array based field-effect transistor biosensor for phosphate detection.* Journal of colloid and interface science. 2017; 498: 292-297.
72. Viter, R., A. Tereshchenko, V. Smyntyna, et al. *Toward development of optical biosensors based on photoluminescence of TiO2 nanoparticles for the detection of Salmonella.* Sensors and Actuators B: Chemical. 2017; 252: 95-102.
73. Tereshchenko, A., V. Fedorenko, V. Smyntyna, et al. *ZnO films formed by atomic layer deposition as an optical biosensor platform for the detection of Grapevine virus A-type proteins.* Biosensors and Bioelectronics. 2017; 92: 763-769.
74. Viter, R., I. Iatsunskyi, V. Fedorenko, et al. *Enhancement of electronic and optical properties of ZnO/Al2O3 nanolaminate coated electrospun nanofibers.* The Journal of Physical Chemistry C. 2016; 120: 5124-5132.
75. Humayun, Q., M. Kashif, and U. Hashim. *Area-selective ZnO thin film deposition on variable microgap electrodes and their impact on UV sensing.* Journal of Nanomaterials. 2013; 2013.
76. Lou, Z., J. Deng, L. Wang, et al. *A class of hierarchical nanostructures: ZnO surface-functionalized TiO 2 with enhanced sensing properties.* RSC advances. 2013; 3: 3131-3136.
77. Rahmanian, R., S.A. Mozaffari, H.S. Amoli, and M. Abedi. *Development of sensitive impedimetric urea biosensor using DC sputtered Nano-ZnO on TiO2 thin film as a novel hierarchical nanostructure transducer.* Sensors and Actuators B: Chemical. 2018; 256: 760-774.
78. Xu, S., Y. Dall'Agnese, G. Wei, et al. *Screen-printable microscale hybrid device based on MXene and layered double hydroxide electrodes for powering force sensors.* Nano energy. 2018; 50: 479-488.
79. Oliveira, J., V. Correia, H. Castro, P. Martins, and S. Lanceros-Mendez. *Polymer-based smart materials by printing technologies: Improving application and integration.* Additive Manufacturing. 2018; 21: 269-283.
80. Khan, S., L. Lorenzelli, and R.S. Dahiya. *Technologies for printing sensors and electronics over large flexible substrates: a review.* IEEE Sensors Journal. 2014; 15: 3164-3185.
81. Knieling, T., E. Nebling, L. Blohm, C. Beale, and M. Fahland. *Printed and Flexible Electrochemical Lactate Sensors for Wearable Applications.* Multidisciplinary Digital Publishing Institute Proceedings. 2017; 1: 828.
82. Yáñez-Sedeño, P., S. Campuzano, and J.M. Pingarrón. *Integrated affinity biosensing platforms on screen-printed electrodes electrografted with diazonium salts.* Sensors. 2018; 18: 675.
83. Khan, S., S. Ali, and A. Bermak. *Recent developments in printing flexible and wearable sensing electronics for healthcare applications.* Sensors. 2019; 19: 1230.
84. Khan, S., L. Lorenzelli, and R. Dahiya. *Flexible MISFET devices from transfer printed Si microwires and spray coating.* IEEE Journal of the Electron Devices Society. 2016; 4: 189-196.
85. Carey, T., S. Cacovich, G. Divitini, et al. *Fully inkjet-printed two-dimensional material field-effect heterojunctions for wearable and textile electronics.* Nature communications. 2017; 8: 1-11.
86. Khan, S., Y.H. Doh, A. Khan, et al. *Direct patterning and electrospray deposition through EHD for fabrication of printed thin film transistors.* Current applied physics. 2011; 11: S271-S279.

87. Seifert, T., E. Sowade, F. Roscher, et al. *Additive manufacturing technologies compared: morphology of deposits of silver ink using inkjet and aerosol jet printing.* Industrial & Engineering Chemistry Research. 2015; 54: 769-779.
88. Camilloni, L., E. Ferroni, B.J. Cendales, et al. *Methods to increase participation in organised screening programs: a systematic review.* BMC public health. 2013; 13: 464.
89. Kaya, H.O., A.E. Cetin, M. Azimzadeh, and S.N. Topkaya. *Pathogen detection with electrochemical biosensors: Advantages, challenges and future perspectives.* Journal of Electroanalytical Chemistry. 2021; 114989.
90. Gouvêa, C.M.C.P. *Biosensors for Health Applications.* Universidade Federal de Alfenas. 2011.
91. Liu, A., K. Wang, S. Weng, et al. *Development of electrochemical DNA biosensors.* TrAC Trends in Analytical Chemistry. 2012; 37: 101-111.
92. Nuggehalli M. Ravindra, C.P., Shanmugamurthy Fnu, Ivan Padronl, and Sushil K. Sikha. *Advances in the Manufacturing, Types, and Applications of Biosensors.* Energetic Thin Films. 2007; 59: 37-43.
93. Adetunji, C.O., W. Nwankwo, K.E. Ukhurebor, A.S. Olayinka, and A.S. Makinde. *Application of Biosensor for the Identification of Various Pathogens and Pests Mitigating Against the Agricultural Production: Recent Advances.* Biosensors in Agriculture: Recent Trends and Future Perspectives. 2021; 169-189.
94. Dennison, M. and A.P. Turner. *Biosensors for environmental monitoring.* Biotechnology advances. 1995; 13: 1-12.
95. Corcuera, J.I.R.D. and R.P. Cavalieri. *Biosensorss.* Encyclopedia of Agricultural, Food, and Biological Engineering. 2003.
96. Price, C.P. *Point-of-care testing in diabetes mellitus.* Clinical chemistry and laboratory medicine. 2003; 41: 1213-1219.
97. D'Costa, E.J., I.J. Higgins, and A.P.F. Turner. *Quinoprotein glucose dehydrogenase and its application in an amperometric glucose sensor.* Biosensors. 1986; 2: 71-87.
98. Yoo, E.H.L., S. Y. *Glucose biosensors: an overview of use in clinical practice.* Sensors (Basel). 2010; 10: 4558-76.
99. Md. Mahbubur Rahman 1, A.J.S.A., Joon-Hyung Jin , Sang Jung Ahn and Jae-Joon Lee *A Comprehensive Review of Glucose Biosensors Based on Nanostructured Metal-Oxides.* Sensors (Basel). 2010Sensors; 10: 4855-4886.
100. Elkington, D., W.J. Belcher, P.C. Dastoor, and X.J. Zhou. *Detection of saliva-range glucose concentrations using organic thin-film transistors.* Applied Physics Letters. 2014; 105: 043303.
101. Bankar, S.B., M.V. Bule, R.S. Singhal, and L. Ananthanarayan. *Glucose oxidase — An overview.* Biotechnology Advances. 2009; 27: 489-501.
102. Clark Jr, L.C. and C. Lyons. *Electrode systems for continuous monitoring in cardiovascular surgery.* Annals of the New York Academy of sciences. 1962; 102: 29-45.
103. Peterson, C.M., R.L. Jones, A. Dupuis, et al. *Feasibility of improved blood glucose control in patients with insulin-dependent diabetes mellitus.* Diabetes Care. 1979; 2: 329-335.
104. Sen, D. and G. Sarin. *Tear glucose levels in normal people and in diabetic patients.* British journal of ophthalmology. 1980; 64: 693-695.
105. Baca, J.T., D.N. Finegold, and S.A. Asher. *Tear glucose analysis for the noninvasive detection and monitoring of diabetes mellitus.* The ocular surface. 2007; 5: 280-293.
106. Gupta, S., M.T. Nayak, J. Sunitha, et al. *Correlation of salivary glucose level with blood glucose level in diabetes mellitus.* Journal of oral and maxillofacial pathology: JOMFP. 2017; 21: 334.
107. Liu, C., Y. Sheng, Y. Sun, et al. *A glucose oxidase-coupled DNAzyme sensor for glucose detection in tears and saliva.* Biosens Bioelectron. 2015; 70: 455-61.

108. Macaya, D.J., M. Nikolou, S. Takamatsu, et al. *Simple glucose sensors with micromolar sensitivity based on organic electrochemical transistors.* Sensors and Actuators B: Chemical. 2007; 123: 374-378.
109. Freckmann, G., C. Schmid, A. Baumstark, et al. *System accuracy evaluation of 43 blood glucose monitoring systems for self-monitoring of blood glucose according to DIN EN ISO 15197.* Journal of diabetes science and technology. 2012; 6: 1060-1075.
110. Zhang, W., Y. Du, and M.L. Wang. *Noninvasive glucose monitoring using saliva nano-biosensor.* Sensing and Bio-Sensing Research. 2015; 4: 23-29.
111. Liu, J., S. Sun, H. Shang, J. Lai, and L. Zhang. *Electrochemical Biosensor Based on Bienzyme and Carbon Nanotubes Incorporated into an Os-complex Thin Film for Continuous Glucose Detection in Human Saliva.* Electroanalysis. 2016; 28: 2016-2021.
112. Carlson, G.W. *The salivary glands: embryology, anatomy, and surgical applications.* Surgical Clinics. 2000; 80: 261-273.
113. Kaufman, E. and I.B. Lamster. *The diagnostic applications of saliva—a review.* Critical Reviews in oral biology & medicine. 2002; 13: 197-212.
114. Lagua, R.T. and V.S. Claudio, *Nutrition and diet therapy reference dictionary*. 2012: Springer Science & Business Media.
115. Amer, S., M. Yousuf, P. Siddqiui, and J. Alam. *Salivary glucose concentrations in patients with diabetes mellitus–a minimally invasive technique for monitoring blood glucose levels.* Pak J Pharm Sci. 2001; 14: 33-7.
116. Gupta, S., S.V. Sandhu, H. Bansal, and D. Sharma. *Comparison of salivary and serum glucose levels in diabetic patients.* Journal of diabetes science and technology. 2014; 9: 91-96.
117. Bandodkar, A.J., V.W. Hung, W. Jia, et al. *Tattoo-based potentiometric ion-selective sensors for epidermal pH monitoring.* Analyst. 2013; 138: 123-128.
118. Sista, R., V.K. Pamula, A. Sudarsan, et al., *Detection of cardiac markers on a droplet actuator*. 2014, Google Patents.
119. Tékus, É., M. Kaj, E. Szabó, et al. *Comparison of blood and saliva lactate level after maximum intensity exercise.* Acta Biologica Hungarica. 2012; 63: 89-98.
120. Yamaguchi, M., M. Mitsumori, and Y. Kano. *Development of noninvasive procedure for monitoring blood glucose levels using saliva*. in *Engineering in Medicine and Biology Society, 1998. Proceedings of the 20th Annual International Conference of the IEEE*. 1998. IEEE.
121. Panchbhai, A.S., S.S. Degwekar, and R.R. Bhowte. *Estimation of salivary glucose, salivary amylase, salivary total protein and salivary flow rate in diabetics in India.* Journal of oral science. 2010; 52: 359-368.
122. Bandodkar, A.J. and J. Wang. *Non-invasive wearable electrochemical sensors: a review.* Trends in biotechnology. 2014; 32: 363-371.
123. Kim, J., G. Valdés-Ramírez, A.J. Bandodkar, et al. *Non-invasive mouthguard biosensor for continuous salivary monitoring of metabolites.* Analyst. 2014; 139: 1632-1636.
124. Dimitrakopoulos, C.D. and P.R. Malenfant. *Organic thin film transistors for large area electronics.* Advanced materials. 2002; 14: 99-117.
125. Brabec, C., N. Sariciftci, and J. Hummelen. *Adv. Funct. Mater.* Adv. Funct. Mater. 2001; 11: 374.
126. Coakley, K.M. and M.D. McGehee. *Conjugated polymer photovoltaic cells.* Chemistry of materials. 2004; 16: 4533-4542.
127. Ullmann, A., J. Ficker, W. Fix, et al. *High performance organic field-effect transistors and integrated inverters.* MRS Online Proceedings Library Archive. 2001; 665.
128. Dou, L., J. You, Z. Hong, et al. *25th anniversary article: a decade of organic/polymeric photovoltaic research.* Advanced materials. 2013; 25: 6642-6671.
129. Po, R., A. Bernardi, A. Calabrese, et al. *From lab to fab: how must the polymer solar cell materials design change?–an industrial perspective.* Energy & Environmental Science. 2014; 7: 925-943.

130. Holliday, S., R.S. Ashraf, A. Wadsworth, et al. *High-efficiency and air-stable P3HT-based polymer solar cells with a new non-fullerene acceptor.* Nature communications. 2016; 7: 11585.
131. Campoy-Quiles, M., T. Ferenczi, T. Agostinelli, et al. *Morphology evolution via self-organization and lateral and vertical diffusion in polymer: fullerene solar cell blends.* Nature materials. 2008; 7: 158-164.
132. Holliday, S., J.E. Donaghey, and I. McCulloch. *Advances in charge carrier mobilities of semiconducting polymers used in organic transistors.* Chemistry of Materials. 2014; 26: 647-663.
133. Laird, D.W., S. Vaidya, S. Li, et al. *Advances in Plexcore active layer technology systems for organic photovoltaics: roof-top and accelerated lifetime analysis of high performance organic photovoltaic cells*. in *Organic Photovoltaics VIII*. 2007. International Society for Optics and Photonics.
134. Merlo, J.A. and C.D. Frisbie. *Field effect transport and trapping in regioregular polythiophene nanofibers.* The Journal of Physical Chemistry B. 2004; 108: 19169-19179.
135. Samitsu, S., T. Shimomura, S. Heike, T. Hashizume, and K. Ito. *Field-effect carrier transport in poly (3-alkylthiophene) nanofiber networks and isolated nanofibers.* Macromolecules. 2010; 43: 7891-7894.
136. Wu, Z., A. Petzold, T. Henze, et al. *Temperature and molecular weight dependent hierarchical equilibrium structures in semiconducting poly (3-hexylthiophene).* Macromolecules. 2010; 43: 4646-4653.
137. Ma, W., J.Y. Kim, K. Lee, and A.J. Heeger. *Effect of the molecular weight of poly (3-hexylthiophene) on the morphology and performance of polymer bulk heterojunction solar cells.* Macromolecular rapid communications. 2007; 28: 1776-1780.
138. Kline, R.J., M.D. McGehee, E.N. Kadnikova, J. Liu, and J.M. Frechet. *Controlling the field-effect mobility of regioregular polythiophene by changing the molecular weight.* Advanced Materials. 2003; 15: 1519-1522.
139. Kline, R.J., M.D. McGehee, E.N. Kadnikova, et al. *Dependence of regioregular poly (3-hexylthiophene) film morphology and field-effect mobility on molecular weight.* Macromolecules. 2005; 38: 3312-3319.
140. Schilinsky, P., U. Asawapirom, U. Scherf, M. Biele, and C.J. Brabec. *Influence of the molecular weight of poly (3-hexylthiophene) on the performance of bulk heterojunction solar cells.* Chemistry of Materials. 2005; 17: 2175-2180.
141. Bao, Z., A. Dodabalapur, and A.J. Lovinger. *Soluble and processable regioregular poly (3-hexylthiophene) for thin film field-effect transistor applications with high mobility.* Applied physics letters. 1996; 69: 4108-4110.
142. Raja, M., G. Lloyd, N. Sedghi, et al. *Conduction processes in conjugated, highly regio-regular, high molecular mass, poly (3-hexylthiophene) thin-film transistors.* Journal of applied physics. 2002; 92: 1441-1445.
143. Tu, G., A. Bilge, S. Adamczyk, et al. *The influence of interchain branches on solid state packing, hole mobility and photovoltaic properties of poly (3-hexylthiophene)(P3HT).* Macromolecular rapid communications. 2007; 28: 1781-1785.
144. Yang, C., F.P. Orfino, and S. Holdcroft. *A phenomenological model for predicting thermochromism of regioregular and nonregioregular poly (3-alkylthiophenes).* Macromolecules. 1996; 29: 6510-6517.
145. Kim, Y., S. Cook, S.M. Tuladhar, et al., *A strong regioregularity effect in self-organizing conjugated polymer films and high-efficiency polythiophene: fullerene solar cells*, in *Materials For Sustainable Energy: A Collection of Peer-Reviewed Research and Review Articles from Nature Publishing Group*. 2011, World Scientific. p. 63-69.
146. Skipidarov, S. and M. Nikitin. *Thermoelectrics for Power Generation-a Look at Trends in the Technology.* 2016.

147. Elschner, A., S. Kirchmeyer, W. Lovenich, U. Merker, and K. Reuter, *PEDOT: principles and applications of an intrinsically conductive polymer*. 2010: CRC press.
148. Jonas, F., W. Krafft, and B. Muys. *Poly (3, 4-ethylenedioxythiophene): Conductive coatings, technical applications and properties*. in *Macromolecular Symposia*. 1995. Wiley Online Library.
149. Ouyang, J. *"Secondary doping" methods to significantly enhance the conductivity of PEDOT: PSS for its application as transparent electrode of optoelectronic devices.* Displays. 2013; 34: 423-436.
150. Shi, H., C. Liu, Q. Jiang, and J. Xu. *Effective approaches to improve the electrical conductivity of PEDOT: PSS: a review.* Advanced Electronic Materials. 2015; 1: 1500017.
151. Zhang, F., M. Johansson, M.R. Andersson, J.C. Hummelen, and O. Inganäs. *Polymer photovoltaic cells with conducting polymer anodes.* Advanced Materials. 2002; 14: 662-665.
152. Lee, M.-W., M.-Y. Lee, J.-C. Choi, J.-S. Park, and C.-K. Song. *Fine patterning of glycerol-doped PEDOT: PSS on hydrophobic PVP dielectric with ink jet for source and drain electrode of OTFTs.* Organic Electronics. 2010; 11: 854-859.
153. Huang, J., P.F. Miller, J.C. de Mello, A.J. de Mello, and D.D. Bradley. *Influence of thermal treatment on the conductivity and morphology of PEDOT/PSS films.* Synthetic Metals. 2003; 139: 569-572.
154. Moujoud, A., S.H. Oh, H.S. Shin, and H.J. Kim. *On the mechanism of conductivity enhancement and work function control in PEDOT: PSS film through UV-light treatment.* physica status solidi (a). 2010; 207: 1704-1707.
155. Kim, J., J. Jung, D. Lee, and J. Joo. *Enhancement of electrical conductivity of poly (3, 4-ethylenedioxythiophene)/poly (4-styrenesulfonate) by a change of solvents.* Synthetic Metals. 2002; 126: 311-316.
156. Badre, C., L. Marquant, A.M. Alsayed, and L.A. Hough. *Highly conductive poly (3, 4-ethylenedioxythiophene): poly (styrenesulfonate) films using 1-ethyl-3-methylimidazolium tetracyanoborate ionic liquid.* Advanced Functional Materials. 2012; 22: 2723-2727.
157. Xia, Y. and J. Ouyang. *Significant conductivity enhancement of conductive poly (3, 4-ethylenedioxythiophene): poly (styrenesulfonate) films through a treatment with organic carboxylic acids and inorganic acids.* ACS applied materials & interfaces. 2010; 2: 474-483.
158. Sahu, A.K., S. Pitchumani, P. Sridhar, and A.K. Shukla. *Nafion and modified-Nafion membranes for polymer electrolyte fuel cells: An overview.* Bulletin of Materials Science. 2009; 32: 285-294.
159. Mauritz, K.A. and R.B. Moore. *State of understanding of Nafion.* Chemical reviews. 2004; 104: 4535-4586.
160. Yeo, S.C. and A. Eisenberg. *Physical properties and supermolecular structure of perfluorinated ion-containing (Nafion) polymers.* Journal of applied polymer science. 1977; 21: 875-898.
161. Huang, X., R. Solasi, Y. Zou, et al. *Mechanical endurance of polymer electrolyte membrane and PEM fuel cell durability.* Journal of Polymer Science Part B: Polymer Physics. 2006; 44: 2346-2357.
162. Bauer, F., S. Denneler, and M. Willert-Porada. *Influence of temperature and humidity on the mechanical properties of Nafion® 117 polymer electrolyte membrane.* Journal of Polymer Science Part B: Polymer Physics. 2005; 43: 786-795.
163. Majsztrik, P.W., A.B. Bocarsly, and J.B. Benziger. *Viscoelastic response of Nafion. Effects of temperature and hydration on tensile creep.* Macromolecules. 2008; 41: 9849-9862.
164. Tang, Y., A. Karlsson, and M. Santare. *G ilbert, M.; Cleghorn, S.; Johnson, WB Mater. S ci. Eng. a: S truct.* Mater. Properties Microstruct. Process. 2006; 425: 297-304.
165. Kim, M.A. and W.-Y. Lee. *Amperometric phenol biosensor based on sol–gel silicate/Nafion composite film.* Analytica Chimica Acta. 2003; 479: 143-150.

166. Zen, J.-M., J.-J. Jou, and A.S. Kumar. *A sensitive voltammetric method for the determination of parathion insecticide.* Analytica Chimica Acta. 1999; 396: 39-44.
167. de Betoño, S.F., A.A. Garcia, and J.F.A. Valentín. *UV-Spectrophotometry and square wave voltammetry at nafion-modified carbon-paste electrode for the determination of doxazosin in urine and formulations.* Journal of pharmaceutical and biomedical analysis. 1999; 20: 621-630.
168. Hu, S., K. Wu, H. Yi, and D. Cui. *Voltammetric behavior and determination of estrogens at Nafion-modified glassy carbon electrode in the presence of cetyltrimethylammonium bromide.* Analytica Chimica Acta. 2002; 464: 209-216.
169. Degrand, C., B. Limoges, and S. Rapicault. *Enzyme immunoassay technique using alkaline phosphatase enzyme labels and a Nafion electrode as sensor.* Journal of pharmaceutical and biomedical analysis. 1996; 14: 1343-1350.
170. Tsai, Y.-C., S.-C. Li, and J.-M. Chen. *Cast thin film biosensor design based on a nafion backbone, a multiwalled carbon nanotube conduit, and a glucose oxidase function.* Langmuir. 2005; 21: 3653-3658.
171. Satterfield, M.B. and J.B. Benziger. *Viscoelastic properties of Nafion at elevated temperature and humidity.* Journal of Polymer Science Part B: Polymer Physics. 2009; 47: 11-24.
172. Majsztrik, P.W., M.B. Satterfield, A.B. Bocarsly, and J.B. Benziger. *Water sorption, desorption and transport in Nafion membranes.* Journal of Membrane Science. 2007; 301: 93-106.
173. Satterfield, M.B. and J.B. Benziger. *Non-Fickian water vapor sorption dynamics by Nafion membranes.* The journal of physical chemistry B. 2008; 112: 3693-3704.
174. Wang, J., M. Musameh, and Y. Lin. *Solubilization of carbon nanotubes by Nafion toward the preparation of amperometric biosensors.* Journal of the American Chemical Society. 2003; 125: 2408-2409.
175. Fan, Z. and D.J. Harrison. *Permeability of glucose and other neutral species through recast perfluorosulfonated ionomer films.* Analytical Chemistry. 1992; 64: 1304-1311.
176. Fortier, G., M. Vaillancourt, and D. Bélanger. *Evaluation of nafion as media for glucose oxidase immobilization for the development of an amperometric glucose biosensor.* Electroanalysis. 1992; 4: 275-283.
177. Yu, D.-G., P. Lu, C. Branford-White, J.-H. Yang, and X. Wang. *Polyacrylonitrile nanofibers prepared using coaxial electrospinning with LiCl solution as sheath fluid.* Nanotechnology. 2011; 22: 435301.
178. Qian, W., D.-G. Yu, Y. Li, et al. *Triple-component drug-loaded nanocomposites prepared using a modified coaxial electrospinning.* Journal of Nanomaterials. 2013; 2013.
179. Wan, L.-S., Z.-K. Xu, X.-J. Huang, A.-F. Che, and Z.-G. Wang. *A novel process for the post-treatment of polyacrylonitrile-based membranes: Performance improvement and possible mechanism.* Journal of membrane science. 2006; 277: 157-164.
180. Ostrovskii, D., A. Brodin, L.M. Torell, G.B. Appetecchi, and B. Scrosati. *Molecular and ionic interactions in poly (acrylonitrile)-and poly (methylmetacrylate)-based gel electrolytes.* The Journal of chemical physics. 1998; 109: 7618-7624.
181. Wu, Q.-Y., L.-S. Wan, and Z.-K. Xu. *Structure and performance of polyacrylonitrile membranes prepared via thermally induced phase separation.* Journal of membrane science. 2012; 409: 355-364.
182. Wu, Q.-Y., X.-N. Chen, L.-S. Wan, and Z.-K. Xu. *Interactions between polyacrylonitrile and solvents: density functional theory study and two-dimensional infrared correlation analysis.* The Journal of Physical Chemistry B. 2012; 116: 8321-8330.
183. Thavasi, V., G. Singh, and S. Ramakrishna. *Electrospun nanofibers in energy and environmental applications.* Energy & Environmental Science. 2008; 1: 205-221.
184. Morgan, P., *Carbon fibers and their composites*. 2005: CRC press.

185. Zhang, H., H. Nie, D. Yu, et al. *Surface modification of electrospun polyacrylonitrile nanofiber towards developing an affinity membrane for bromelain adsorption.* Desalination. 2010; 256: 141-147.
186. Zhou, Z., C. Lai, L. Zhang, et al. *Development of carbon nanofibers from aligned electrospun polyacrylonitrile nanofiber bundles and characterization of their microstructural, electrical, and mechanical properties.* Polymer. 2009; 50: 2999-3006.
187. Atanassov, P., C. Apblett, S. Banta, et al. *Enzymatic biofuel cells.* Interface-Electrochemical Society. 2007; 16: 28-31.
188. Bahar, T. *Preparation of a ferrocene mediated bioanode for biofuel cells by MWCNTs, polyethylenimine and glutaraldehyde: glucose oxidase immobilization and characterization.* Asia-Pacific Journal of Chemical Engineering. 2016; 11: 981-988.
189. Bahar, T. and M.S. Yazici. *Immobilized glucose oxidase biofuel cell anode by MWCNTs, ferrocene, and polyethylenimine: Electrochemical performance.* Asia-Pacific Journal of Chemical Engineering. 2018; 13: e2149.
190. Ramanavicius, A., A. Kausaite, and A. Ramanaviciene. *Biofuel cell based on direct bioelectrocatalysis.* Biosensors and Bioelectronics. 2005; 20: 1962-1967.
191. Kavanagh, P. and D. Leech. *Mediated electron transfer in glucose oxidising enzyme electrodes for application to biofuel cells: recent progress and perspectives.* Physical Chemistry Chemical Physics. 2013; 15: 4859-4869.
192. Wilson, R. and A. Turner. *Glucose oxidase: an ideal enzyme.* Biosensors and Bioelectronics. 1992; 7: 165-185.
193. Bourdillon, C., J. Bourgeois, and D. Thomas. *Covalent linkage of glucose oxidase on modified glassy carbon electrodes. Kinetic phenomena.* Journal of the American Chemical Society. 1980; 102: 4231-4235.
194. Calvo, E.J. and A. Wolosiuk. *Supramolecular Architectures of Electrostatic Self-Assembled Glucose Oxidase Enzyme Electrodes.* ChemPhysChem. 2004; 5: 235-239.
195. Harper, A.C., *Modified electrodes for amperometric determination of glucose and glutamate using mediated electron transport*. 2005, Virginia Tech.
196. Heller, A. and B. Feldman. *Electrochemical glucose sensors and their applications in diabetes management.* Chemical reviews. 2008; 108: 2482-2505.
197. Bankar, S.B., M.V. Bule, R.S. Singhal, and L. Ananthanarayan. *Glucose oxidase—an overview.* Biotechnology advances. 2009; 27: 489-501.
198. Bankar, S.B. and M.V. Bule. *RekhaS.* Singhal, Laxmi Ananthanarayan. Glucose oxidase-An overview. 2009; 27: 489-501.
199. Hedborg, J., *A Printed Biosensor Based on an Organic Electrochemical Transistor with Mediated Gate Electrode*. 2012.
200. Wohlfahrt, G., S. Witt, J. Hendle, et al. *1.8 and 1.9 Å resolution structures of the Penicillium amagasakiense and Aspergillus niger glucose oxidases as a basis for modelling substrate complexes.* Acta Crystallographica Section D: Biological Crystallography. 1999; 55: 969-977.
201. Guilbault, G. and G. Lubrano. *An enzyme electrode for the amperometric determination of glucose.* Analytica chimica acta. 1973; 64: 439-455.
202. Yang, L., X. Ren, F. Tang, and L. Zhang. *A practical glucose biosensor based on Fe3O4 nanoparticles and chitosan/nafion composite film.* Biosensors and Bioelectronics. 2009; 25: 889-895.
203. Ang, L.F., L.Y. Por, and M.F. Yam. *Development of an amperometric-based glucose biosensor to measure the glucose content of fruit.* Plos One. 2015; 10: e0111859.
204. Nor, N.M., K.A. Razak, and Z. Lockman. *Physical and electrochemical properties of iron oxide nanoparticles-modified electrode for amperometric glucose detection.* Electrochimica Acta. 2017; 248: 160-168.

205. Peng, H.-P., R.-P. Liang, L. Zhang, and J.-D. Qiu. *Facile preparation of novel core–shell enzyme–Au–polydopamine–Fe3O4 magnetic bionanoparticles for glucosesensor.* Biosensors and Bioelectronics. 2013; 42: 293-299.
206. Essaidi, H., L. Cattin, Z. El Jouad, et al. *Indium free electrode, highly flexible, transparent and conductive for optoelectronic devices.* Vacuum. 2018; 153: 225-231.
207. Granqvist, C.G. *Transparent conductors as solar energy materials: A panoramic review.* Solar energy materials and solar cells. 2007; 91: 1529-1598.
208. Liu, H., V. Avrutin, N. Izyumskaya, Ü. Özgür, and H. Morkoç. *Transparent conducting oxides for electrode applications in light emitting and absorbing devices.* Superlattices and Microstructures. 2010; 48: 458-484.
209. Senol, S., A. Senol, O. Ozturk, and M. Erdem. *Effect of annealing time on the structural, optical and electrical characteristics of DC sputtered ITO thin films.* Journal of Materials Science: Materials in Electronics. 2014; 25: 4992-4999.
210. Gwamuri, J., A. Vora, J. Mayandi, et al. *A new method of preparing highly conductive ultra-thin indium tin oxide for plasmonic-enhanced thin film solar photovoltaic devices.* Solar Energy Materials and Solar Cells. 2016; 149: 250-257.
211. Baıa, I., M. Quintela, L. Mendes, P. Nunes, and R. Martins. *Performances exhibited by large area ITO layers produced by rf magnetron sputtering.* Thin Solid Films. 1999; 337: 171-175.
212. Kim, D. and S. Kim. *AFM observation of ITO thin films deposited on polycarbonate substrates by sputter type negative metal ion source.* Surface and coatings technology. 2003; 176: 23-29.
213. Pawar, P.S., K.E. Neerugatti, and J. Heo. *Effect of precursor concentration and post-annealing temperature on (040) oriented tin sulfide thin films deposited on SLG/Mo substrates by spin coating.* Current Applied Physics. 2021; 21: 89-95.
214. Göken, M. and M. Kempf. *Microstructural properties of superalloys investigated by nanoindentations in an atomic force microscope.* Acta Materialia. 1999; 47: 1043-1052.
215. Quate, C., C. Gerber, and C. Binnig. *Atomic force microscope.* Phys. Rev. Lett. 1986; 56: 930-933.
216. Liao, F., C. Chen, and V. Subramanian. *Organic TFTs as gas sensors for electronic nose applications.* Sensors and Actuators B: Chemical. 2005; 107: 849-855.
217. Krasnov, A.N. *High-contrast organic light-emitting diodes on flexible substrates.* Applied physics letters. 2002; 80: 3853-3855.
218. Sugimoto, A., H. Ochi, S. Fujimura, et al. *Flexible OLED displays using plastic substrates.* IEEE Journal of selected topics in quantum electronics. 2004; 10: 107-114.
219. Wang, L., D. Fine, D. Sharma, L. Torsi, and A. Dodabalapur. *Nanoscale organic and polymeric field-effect transistors as chemical sensors.* Analytical and bioanalytical chemistry. 2006; 384: 310-321.
220. Johnson, K.S., J.A. Needoba, S.C. Riser, and W.J. Showers. *Chemical sensor networks for the aquatic environment.* Chemical Reviews. 2007; 107: 623-640.
221. Shinar, R. and J. Shinar, *Organic electronics in sensors and biotechnology*. 2009: New York: McGraw-Hill.
222. Zaki, T., *Short-channel organic thin-film transistors: fabrication, characterization, modeling and circuit demonstration*. 2015: Springer.
223. Yan, F. and H. Tang. *Application of thin-film transistors in label-free DNA biosensors.* Expert review of molecular diagnostics. 2010; 10: 547-549.
224. Lin, P. and F. Yan. *Organic thin-film transistors for chemical and biological sensing.* Advanced materials. 2012; 24: 34-51.
225. Forrest, S.R. *The path to ubiquitous and low-cost organic electronic appliances on plastic.* Nature. 2004; 428: 911.
226. Berggren, M., D. Nilsson, and N.D. Robinson. *Organic materials for printed electronics.* Nature materials. 2007; 6: 3.

227. Saeedi, P., I. Petersohn, P. Salpea, et al. *Global and regional diabetes prevalence estimates for 2019 and projections for 2030 and 2045: Results from the International Diabetes Federation Diabetes Atlas.* Diabetes research and clinical practice. 2019; 157: 107843.
228. Shaw, J.E., R.A. Sicree, and P.Z. Zimmet. *Global estimates of the prevalence of diabetes for 2010 and 2030.* Diabetes research and clinical practice. 2010; 87: 4-14.
229. Hayford, J.T., J.A. Weydert, and R.G. Thompson. *Validity of urine glucose measurements for estimating plasma glucose concentration.* Diabetes Care. 1983; 6: 40-44.
230. Krynski, I. and J. Logan. *Dextrostix as a quantitative test for glucose in whole blood.* Canadian Medical Association Journal. 1967; 97: 1006.
231. Casselman, J., N. Onopa, and L. Khansa. *Wearable healthcare: Lessons from the past and a peek into the future.* Telematics and Informatics. 2017; 34: 1011-1023.
232. Olczuk, D. and R. Priefer. *A history of continuous glucose monitors (CGMs) in self-monitoring of diabetes mellitus.* Diabetes & Metabolic Syndrome: Clinical Research & Reviews. 2018; 12: 181-187.
233. Bruen, D., C. Delaney, L. Florea, and D. Diamond. *Glucose sensing for diabetes monitoring: recent developments.* Sensors. 2017; 17: 1866.
234. Kownacka, A.E., D. Vegelyte, M. Joosse, et al. *Clinical evidence for use of a noninvasive biosensor for tear glucose as an alternative to painful finger-prick for diabetes management utilizing a biopolymer coating.* Biomacromolecules. 2018; 19: 4504-4511.
235. Hoa, D., T.S. Kumar, N. Punekar, et al. *A biosensor based on conducting polymers.* Analytical chemistry. 1992; 64: 2645-2646.
236. Street, R. and A. Salleo. *Contact effects in polymer transistors.* Applied Physics Letters. 2002; 81: 2887-2889.
237. Gundlach, D., L. Zhou, J. Nichols, et al. *An experimental study of contact effects in organic thin film transistors.* Journal of Applied Physics. 2006; 100: 024509.
238. Eom, S.H., S. Senthilarasu, P. Uthirakumar, et al. *Polymer solar cells based on inkjet-printed PEDOT: PSS layer.* Organic Electronics. 2009; 10: 536-542.
239. Na, S.I., S.S. Kim, J. Jo, and D.Y. Kim. *Efficient and flexible ITO-free organic solar cells using highly conductive polymer anodes.* Advanced Materials. 2008; 20: 4061-4067.
240. Kavuri, H.A., S. Kihara, D.J. McGillivray, and G.R. Willmott. *Poly (vinyl pyrrolidone)-modified metal oxide anode interlayers for stable organic solar cells.* Journal of Photonics for Energy. 2020; 10: 042003.
241. Al-Mudhaffer, M.F., M.J. Griffith, K. Feron, et al. *The origin of performance limitations in miniemulsion nanoparticulate organic photovoltaic devices.* Solar Energy Materials and Solar Cells. 2018; 175: 77-88.
242. Jørgensen, M., K. Norrman, and F.C. Krebs. *Stability/degradation of polymer solar cells.* Solar energy materials and solar cells. 2008; 92: 686-714.
243. Sandberg, H.G., T.G. Bäcklund, R. Österbacka, and H. Stubb. *High-Performance All-Polymer Transistor Utilizing a Hygroscopic Insulator.* Advanced Materials. 2004; 16: 1112-1115.
244. Elkington, D., D. Darwis, X. Zhou, W. Belcher, and P.C. Dastoor. *The fabrication and characterization of poly (4-vinylpyridine)-based thin film transistors exhibiting enhanced ion modulation.* Organic Electronics. 2012; 13: 153-158.
245. Baeg, K.J., D. Khim, S.W. Jung, et al. *Polymer Dielectrics and Orthogonal Solvent Effects for High-Performance Inkjet-Printed Top-Gated P-Channel Polymer Field-Effect Transistors.* ETRI Journal. 2011; 33: 887-896.
246. Dimitrakopoulos, C.D. and P.R.L. Malenfant. *Organic Thin Film Transistors for Large Area Electronics.* Advanced Materials. 2002; 14: 99-117.
247. De Jong, M., L. Van Ijzendoorn, and M. De Voigt. *Stability of the interface between indium-tin-oxide and poly (3, 4-ethylenedioxythiophene)/poly (styrenesulfonate) in polymer light-emitting diodes.* Applied Physics Letters. 2000; 77: 2255-2257.

248. Velada, J., L.C. Cesteros, E. Meaurio, and I. Katime. *Highly interacting polymer blends: poly (monoethyl itaconate)/poly (vinylpyridine) s.* Polymer. 1995; 36: 2765-2772.
249. Pal, R.K., A.A. Farghaly, C. Wang, et al. *Conducting polymer-silk biocomposites for flexible and biodegradable electrochemical sensors.* Biosensors and Bioelectronics. 2016; 81: 294-302.
250. Nie, Z. and E. Kumacheva. *Patterning surfaces with functional polymers.* Nature materials. 2008; 7: 277-290.
251. Mauger, S.A., M.P. Glasser, B.J. Tremolet de Villers, et al. *Doped Interlayers for Improved Selectivity in Bulk Heterojunction Organic Photovoltaic Devices.* Advanced Materials Interfaces. 2016; 3: 1500346.
252. Manceau, M. and S. Berson. *Inverted polymer solar cells with Nafion® as the hole extraction layer: efficiency and lifetime studies.* Nanotechnology. 2013; 25: 014018.
253. Sandberg, H.G., T.G. Bäcklund, R. Österbacka, et al. *Applications of an all-polymer solution-processed high-performance, transistor.* Synthetic metals. 2005; 155: 662-665.
254. Sirringhaus, H., N. Tessler, and R. Friend. *Integrated, high-mobility polymer field-effect transistors driving polymer light-emitting diodes.* Synthetic Metals. 1999; 102: 857-860.
255. Cui, T., G. Liang, and J. Shi. *Fabrication of pentacene organic field-effect transistors containing SiO/sub 2/nanoparticle thin film as the gate dielectric*. in *IEEE International Electron Devices Meeting 2003*. 2003. IEEE.
256. Bäcklund, T., H.G. Sandberg, R. Österbacka, and H. Stubb. *Current modulation of a hygroscopic insulator organic field-effect transistor.* Applied physics letters. 2004; 85: 3887-3889.
257. Sandberg, H.G., T.G. Bäcklund, R. Österbacka, et al. *Insulators and device geometry in polymer field effect transistors.* Organic electronics. 2005; 6: 142-146.
258. Sirois, K., *Development of a Novel Organic Transistor Towards Microbiosensing of Glucose*. 2010, University of Newcastle.
259. Du, Y., W. Zhang, and M.L. Wang. *Sensing of salivary glucose using nano-structured biosensors.* Biosensors. 2016; 6: 10.
260. Elkington, D., W. Belcher, P. Dastoor, and X. Zhou. *Detection of saliva-range glucose concentrations using organic thin-film transistors.* Applied Physics Letters. 2014; 105: 112_1.
261. Bäcklund, T., R. Österbacka, H. Stubb, J. Bobacka, and A. Ivaska. *Operating principle of polymer insulator organic thin-film transistors exposed to moisture.* Journal of applied physics. 2005; 98: 074504.
262. Tao, Z., R.A. Raffel, A.-K. Souid, and J. Goodisman. *Kinetic studies on enzyme-catalyzed reactions: Oxidation of glucose, decomposition of hydrogen peroxide and their combination.* Biophysical journal. 2009; 96: 2977-2988.
263. Li, T., G. Zhong, R. Fu, and Y. Yang. *Synthesis and characterization of Nafion/cross-linked PVP semi-interpenetrating polymer network membrane for direct methanol fuel cell.* Journal of Membrane Science. 2010; 354: 189-197.
264. Liu, J., Y. Shi, and Y. Yang. *Solvation-induced morphology effects on the performance of polymer-based photovoltaic devices.* Advanced Functional Materials. 2001; 11: 420-424.
265. Hoppe, H., M. Niggemann, C. Winder, et al. *Nanoscale morphology of conjugated polymer/fullerene-based bulk-heterojunction solar cells.* Advanced Functional Materials. 2004; 14: 1005-1011.
266. Li, G., V. Shrotriya, Y. Yao, and Y. Yang. *Investigation of annealing effects and film thickness dependence of polymer solar cells based on poly (3-hexylthiophene).* Journal of Applied Physics. 2005; 98: 043704.
267. Kefala, G., A. Economou, and A. Voulgaropoulos. *A study of Nafion-coated bismuth-film electrodes for the determination of trace metals by anodic stripping voltammetry.* Analyst. 2004; 129: 1082-1090.
268. Hoyer, B., T.M. Florence, and G.E. Batley. *Application of polymer-coated glassy carbon electrodes in anodic stripping voltammetry.* Analytical chemistry. 1987; 59: 1608-1614.

269. Hajlaoui, M., F. Garnier, L. Hassine, F. Kouki, and H. Bouchriha. *Growth conditions effects on morphology and transport properties of an oligothiophene semiconductor.* Synthetic metals. 2002; 129: 215-220.
270. Jia, H., S. Gowrisanker, G.K. Pant, R.M. Wallace, and B.E. Gnade. *Effect of poly (3-hexylthiophene) film thickness on organic thin film transistor properties.* Journal of Vacuum Science & Technology A: Vacuum, Surfaces, and Films. 2006; 24: 1228-1232.
271. Lee, J., K. Kim, J.H. Kim, S. Im, and D.-Y. Jung. *Optimum channel thickness in pentacene-based thin-film transistors.* Applied physics letters. 2003; 82: 4169-4171.
272. Brixi, S., O.A. Melville, N.T. Boileau, and B.H. Lessard. *The influence of air and temperature on the performance of PBDB-T and P3HT in organic thin film transistors.* Journal of Materials Chemistry C. 2018; 6: 11972-11979.
273. Müller, C. *On the glass transition of polymer semiconductors and its impact on polymer solar cell stability.* Chemistry of Materials. 2015; 27: 2740-2754.
274. Strobl, G.R. and G.R. Strobl, *The physics of polymers*. Vol. 2. 1997: Springer.
275. Gutzow, I.S. and J.W. Schmelzer, *Non-equilibrium Thermodynamics and the Kinetics of Glass Transition and Stabilization*, in *The Vitreous State*. 2013, Springer. p. 69-125.
276. Boyce, M. and R. Haward. *The post-yield.* The Physics of Glassy Polymers. 1997; 213.
277. Alkhadra, M.A., *Convenient Approaches for Measuring the Glass Transition and Fracture Behavior of Semiconducting Polymers*. 2018, UC San Diego.
278. Beuth Jr, J. *Cracking of thin bonded films in residual tension.* International Journal of Solids and Structures. 1992; 29: 1657-1675.
279. Gagliardi, G.G., A. Ibrahim, D. Borello, and A. El-Kharouf. *Composite Polymers Development and Application for Polymer Electrolyte Membrane Technologies—A Review.* Molecules. 2020; 25: 1712.
280. Lyulin, A.V., S. Sengupta, A. Varughese, P. Komarov, and A. Venkatnathan. *Effect of annealing on structure and diffusion in hydrated Nafion membranes.* ACS Applied Polymer Materials. 2020; 2: 5058-5066.
281. Marques, J.L.d.S., A.P.S. Zanatta, M. Hattenberger, and M.M.d.C. Forte. *Nafion/sulfonated poly (indene) polyelectrolyte membranes for fuel cell application.* Polímeros. 2018; 28: 293-301.
282. Zhang, S., P. Kumar, A.S. Nouas, et al. *Solvent-induced changes in PEDOT: PSS films for organic electrochemical transistors.* APL materials. 2015; 3: 014911.
283. Kim, S.-M., C.-H. Kim, Y. Kim, et al. *Influence of PEDOT: PSS crystallinity and composition on electrochemical transistor performance and long-term stability.* Nature communications. 2018; 9: 1-9.
284. Savva, A., C. Cendra, A. Giugni, et al. *Influence of water on the performance of organic electrochemical transistors.* Chemistry of Materials. 2019; 31: 927-937.
285. Flagg, L.Q., C.G. Bischak, J.W. Onorato, et al. *Polymer crystallinity controls water uptake in glycol side-chain polymer organic electrochemical transistors.* Journal of the American Chemical Society. 2019; 141: 4345-4354.
286. Su, Z., R. Feng, L. Hu, et al. *Organic semiconductor/water interfaces for photoelectrical viscosity sensing.* Electrochemistry Communications. 2018; 95: 18-22.
287. Lin, B.-R., H.-L. Cheng, H.-H. Lin, et al. *Electrical stability study of polymer-based organic transistors in ambient air using an active semiconducting/insulating polyblend-based pseudo-bilayer.* Materials Chemistry Frontiers. 2020; 4: 1679-1688.
288. Mozer, A.J., N.S. Sariciftci, A. Pivrikas, et al. *Charge carrier mobility in regioregular poly (3-hexylthiophene) probed by transient conductivity techniques: A comparative study.* Physical Review B. 2005; 71: 035214.
289. Kreuer, K., M. Ise, A. Fuchs, and J. Maier. *Proton and water transport in nano-separated polymer membranes.* Le Journal de Physique IV. 2000; 10: Pr7-279-Pr7-281.

290. Cappadonia, M., J.W. Erning, S.M.S. Niaki, and U. Stimming. *Conductance of Nafion 117 membranes as a function of temperature and water content.* Solid State Ionics. 1995; 77: 65-69.
291. Commer, P., A. Cherstvy, E. Spohr, and A. Kornyshev. *The effect of water content on proton transport in polymer electrolyte membranes.* Fuel cells. 2002; 2: 127-136.
292. Tsuda, M., N.B. Arboleda Jr, and H. Kasai. *Initial driving force for proton transfer in Nafion.* Chemical physics. 2006; 324: 393-397.
293. Oh, K.S., D.H. Kim, and S. Park. *Behaviour of water molecules in Nafion 117 for polymer electrolyte membrane fuel cell by molecular dynamics simulation.* Molecular Simulation. 2008; 34: 1237-1244.
294. Tsai, Y.-C. and H.-Y. Chien. *Preparation of multiwalled carbon nanotubes-platinum-Nafion-glucose oxidase nanobiocomposite and its application to glucose biosensor.* Journal of nanoscience and nanotechnology. 2007; 7: 1611-1617.
295. Lim, S.H., J. Wei, J. Lin, Q. Li, and J. KuaYou. *A glucose biosensor based on electrodeposition of palladium nanoparticles and glucose oxidase onto Nafion-solubilized carbon nanotube electrode.* Biosensors and Bioelectronics. 2005; 20: 2341-2346.
296. Choi, H.N., M.A. Kim, and W.-Y. Lee. *Amperometric glucose biosensor based on sol–gel-derived metal oxide/Nafion composite films.* Analytica chimica acta. 2005; 537: 179-187.
297. Teixeira, F.C., A.I. de Sá, A.P. Teixeira, et al. *New modified Nafion-bisphosphonic acid composite membranes for enhanced proton conductivity and PEMFC performance.* International Journal of Hydrogen Energy. 2021; 46: 17562-17571.
298. Saufi, S.M. and A.F. Ismail. *Development and characterization of polyacrylonitrile (PAN) based carbon hollow fiber membrane.* Songklanakarin J. Sci. Technol. 2002; 24: 843-854.
299. Ouyang, Q., L. Cheng, H. Wang, and K. Li. *Mechanism and kinetics of the stabilization reactions of itaconic acid-modified polyacrylonitrile.* Polymer Degradation and Stability. 2008; 93: 1415-1421.
300. Abhiraman, A.S., *Precursor structure-fiber property relationships in polyacrylonitrile-based carbon fibers*. 1990, GEORGIA INST OF TECH ATLANTA SCHOOL OF CHEMICAL ENGINEERING.
301. Hussain, D., F. Loyal, A. Greiner, and J.H. Wendorff. *Structure property correlations for electrospun nanofiber nonwovens.* Polymer. 2010; 51: 3989-3997.
302. Zander, N.E., K.E. Strawhecker, J.A. Orlicki, A.M. Rawlett, and T.P. Beebe Jr. *Coaxial electrospun poly (methyl methacrylate)–polyacrylonitrile nanofibers: Atomic force microscopy and compositional characterization.* The Journal of Physical Chemistry B. 2011; 115: 12441-12447.
303. Tsai, H.-A., Y.-L. Ye, K.-R. Lee, et al. *Characterization and pervaporation dehydration of heat-treatment PAN hollow fiber membranes.* Journal of membrane science. 2011; 368: 254-263.
304. Wang, Z.-G., L.-S. Wan, and Z.-K. Xu. *Surface engineerings of polyacrylonitrile-based asymmetric membranes towards biomedical applications: An overview.* Journal of Membrane Science. 2007; 304: 8-23.
305. Osbeck, S., R. Bradley, C. Liu, H. Idriss, and S. Ward. *Effect of an ultraviolet/ozone treatment on the surface texture and functional groups on polyacrylonitrile carbon fibres.* Carbon. 2011; 49: 4322-4330.
306. Shen, W., S. Zhang, Y. He, J. Li, and W. Fan. *Hierarchical porous polyacrylonitrile-based activated carbon fibers for CO 2 capture.* Journal of Materials Chemistry. 2011; 21: 14036-14040.
307. Surianarayanan, M., R. Vijayaraghavan, and K. Raghavan. *Spectroscopic investigations of polyacrylonitrile thermal degradation.* Journal of Polymer Science Part A: Polymer Chemistry. 1998; 36: 2503-2512.
308. Semenistaya, T. and A. Ivanenko. *Electro-physical properties of thin films based on metal-containing polyacrylonitrile for application in low temperature gas sensors*. in *IOP Conference Series: Materials Science and Engineering*. 2017. IOP Publishing.

309. Marchetti, P., M. Mechelhoff, and A.G. Livingston. *Tunable-porosity membranes from discrete nanoparticles.* Scientific reports. 2015; 5: 17353.
310. Scharnagl, N. and H. Buschatz. *Polyacrylonitrile (PAN) membranes for ultra-and microfiltration.* Desalination. 2001; 139: 191-198.
311. Lachat, V., V. Varshney, A. Dhinojwala, and M.S. Yeganeh. *Molecular origin of solvent resistance of polyacrylonitrile.* Macromolecules. 2009; 42: 7103-7107.
312. Nenkova, R., D. Ivanova, J. Vladimirova, and T. Godjevargova. *New amperometric glucose biosensor based on cross-linking of glucose oxidase on silica gel/multiwalled carbon nanotubes/polyacrylonitrile nanocomposite film.* Sensors and Actuators B: Chemical. 2010; 148: 59-65.
313. Godjevargova, T. and K. Gabrovska. *Kinetic parameters of urease immobilized on modified acrylonitrile copolymer membranes in the presence and absence of Cu (II) ions.* Macromolecular bioscience. 2005; 5: 459-466.
314. Godjevargova, T., V. Konsulov, and A. Dimov. *Preparation of an ultrafiltration membrane from the copolymer of acrylonitrile–glycidylmethacrylate utilized for immobilization of glucose oxidase.* Journal of membrane science. 1999; 152: 235-240.
315. Fitzer, E. and L. Manocha, *Carbon Composites (Ch. 1)*. 2007, New York: Springer-Verlag.
316. Nie, H.-L., Z.-H. Ma, Z.-X. Fan, et al. *Polyacrylonitrile fibers efficiently loaded with tamoxifen citrate using wet-spinning from co-dissolving solution.* International journal of pharmaceutics. 2009; 373: 4-9.
317. Shen, X., D. Yu, X. Zhang, C. Branford-White, and L. Zhu. *Preparation and characterization of TAM-loaded HPMC/PAN composite fibers for improving drug-release profiles.* Journal of Biomaterials Science, Polymer Edition. 2011; 22: 2227-2240.
318. Zhang, X., D. Yu, S. Zhu, et al. *Investigation of electrospun acyclovir-loaded ultrafine fiber mats.* Journal of Textiles Research. 2009; 30: 1-4.
319. Zheng, H., H. Xue, Y. Zhang, and Z. Shen. *A glucose biosensor based on microporous polyacrylonitrile synthesized by single rare-earth catalyst.* Biosensors and Bioelectronics. 2002; 17: 541-545.
320. Shan, D., Y. He, S. Wang, H. Xue, and H. Zheng. *A porous poly (acrylonitrile-co-acrylic acid) film-based glucose biosensor constructed by electrochemical entrapment.* Analytical biochemistry. 2006; 356: 215-221.
321. Chiang, W.Y. and C.M. Hu. *Studies of reactions with polymers. VI. The modification of PAN with primary amines.* Journal of Polymer Science Part A: Polymer Chemistry. 1990; 28: 1623-1636.
322. Godjevargova, T. and K. Gabrovska. *Immobilization of urease onto chemically modified acrylonitrile copolymer membranes.* Journal of biotechnology. 2003; 103: 107-111.
323. Godjevargova, T., V. Konsulov, A. Dimov, and N. Vasileva. *Behavior of glucose oxidase immobilized on ultrafiltration membranes obtained by copolymerizing acrylonitrile and N-vinylimidazol.* Journal of Membrane Science. 2000; 172: 279-285.
324. Liu, T.-Y., W.-C. Lin, L.-Y. Huang, S.-Y. Chen, and M.-C. Yang. *Hemocompatibility and anaphylatoxin formation of protein-immobilizing polyacrylonitrile hemodialysis membrane.* Biomaterials. 2005; 26: 1437-1444.
325. Lin, W.-C., T.-Y. Liu, and M.-C. Yang. *Hemocompatibility of polyacrylonitrile dialysis membrane immobilized with chitosan and heparin conjugate.* Biomaterials. 2004; 25: 1947-1957.
326. Hicke, H.-G., I. Lehmann, G. Malsch, M. Ulbricht, and M. Becker. *Preparation and characterization of a novel solvent-resistant and autoclavable polymer membrane.* Journal of membrane science. 2002; 198: 187-196.
327. Huang, X.J., Z.K. Xu, L.S. Wan, Z.G. Wang, and J.L. Wang. *Novel Acrylonitrile-Based Copolymers Containing Phospholipid Moieties: Synthesis and Characterization.* Macromolecular bioscience. 2005; 5: 322-330.

328. Godshall, D., P. Rangarajan, D. Baird, et al. *Incorporation of methyl acrylate in acrylonitrile based copolymers: effects on melting behavior.* Polymer. 2003; 44: 4221-4228.
329. Deng, W., A. Lobovsky, S.T. Iacono, et al. *Poly (acrylonitrile–co-1-vinylimidazole): A new melt processable carbon fiber precursor.* Polymer. 2011; 52: 622-628.
330. Allen, R., I. Ward, and Z. Bashir. *An investigation into the possibility of measuring an 'X-ray modulus' and new evidence for hexagonal packing in polyacrylonitrile.* Polymer. 1994; 35: 2063-2071.
331. Bashir, Z., S. Church, and D. Price. *The formation of polymer-solvent complexes of polyacrylonitrile from organic solvents containing carbonyl groups.* Acta polymerica. 1993; 44: 211-218.
332. Loeb, S. and S. Sourirajan, *Sea water demineralization by means of an osmotic membrane*. 1962, ACS Publications.
333. Mulder, M., *Preparation of synthetic membranes*, in *Basic principles of membrane technology*. 1996, Springer. p. 71-156.
334. Young, T.-H. and L.-W. Chen. *Pore formation mechanism of membranes from phase inversion process.* Desalination. 1995; 103: 233-247.
335. Kesting, R., *Synthetic Polymeric Membranes (New York—Chichester—Brisbane*. 1985, Toronto—Singapore: J. Wiley.) p.
336. Kim, I.-C., H.-G. Yun, and K.-H. Lee. *Preparation of asymmetric polyacrylonitrile membrane with small pore size by phase inversion and post-treatment process.* Journal of Membrane Science. 2002; 199: 75-84.
337. Van de Witte, P., P. Dijkstra, J. Van den Berg, and J. Feijen. *Phase separation processes in polymer solutions in relation to membrane formation.* Journal of membrane science. 1996; 117: 1-31.
338. Cohen, C., G. Tanny, and S. Prager. *Diffusion-controlled formation of porous structures in ternary polymer systems.* Journal of Polymer Science: Polymer Physics Edition. 1979; 17: 477-489.
339. Mukherjee, R. and S. De. *Adsorptive removal of nitrate from aqueous solution by polyacrylonitrile–alumina nanoparticle mixed matrix hollow-fiber membrane.* Journal of membrane science. 2014; 466: 281-292.
340. Karmakar, S. and S. De. *Cold sterilization and process modeling of tender coconut water by hollow fibers.* Journal of food engineering. 2017; 200: 70-80.
341. Musale, D., A. Kumar, and G. Pleizier. *Formation and characterization of poly (acrylonitrile)/chitosan composite ultrafiltration membranes.* Journal of membrane science. 1999; 154: 163-173.
342. Musale, D.A. and A. Kumar. *Solvent and pH resistance of surface crosslinked chitosan/poly (acrylonitrile) composite nanofiltration membranes.* Journal of applied polymer science. 2000; 77: 1782-1793.
343. Bhattacharyya, S., G. Lelong, and M.-L. Saboungi. *Recent progress in the synthesis and selected applications of MCM-41: a short review.* Journal of Experimental Nanoscience. 2006; 1: 375-395.
344. Mataram, A., S. Nasution, M.L. Wijaya, and G.D. Septano. *Physical and mechanical properties of membrane Polyacrylonitrile*. in *MATEC Web of Conferences*. 2017. EDP Sciences.
345. Jung, B., J.K. Yoon, B. Kim, and H.-W. Rhee. *Effect of crystallization and annealing on polyacrylonitrile membranes for ultrafiltration.* Journal of membrane science. 2005; 246: 67-76.
346. Jacob, S., *Pharmacology of DMSO (Dimethyl Sulfoxide)*. 1971, Dekker, New York.
347. Marino, T., F. Galiano, S. Simone, and A. Figoli. *DMSO EVOL™ as novel non-toxic solvent for polyethersulfone membrane preparation.* Environmental Science and Pollution Research. 2019; 26: 14774-14785.

348. Riddick, J.A., W.B. Bunger, and T.K. Sakano. *Organic solvents: physical properties and methods of purification.* 1986.
349. Osakada, K., A. Taniguchi, E. Kubota, et al. *New organosols of copper (II) sulfide, cadmium sulfide, zinc sulfide, mercury (II) sulfide, nickel (II) sulfide and mixed metal sulfides in N, N-dimethylformamide and dimethyl sulfoxide. Preparation, characterization, and physical properties.* Chemistry of Materials. 1992; 4: 562-570.
350. Meier, M.A., M. Filali, J.-F. Gohy, and U.S. Schubert. *Star-shaped block copolymer stabilized palladium nanoparticles for efficient catalytic Heck cross-coupling reactions.* Journal of Materials Chemistry. 2006; 16: 3001-3006.
351. Pastoriza-Santos, I. and L.M. Liz-Marzán. *N, N-dimethylformamide as a reaction medium for metal nanoparticle synthesis.* Advanced Functional Materials. 2009; 19: 679-688.
352. Do, H.-Q. and O. Daugulis. *Copper-catalyzed arylation and alkenylation of polyfluoroarene C–H bonds.* Journal of the American Chemical Society. 2008; 130: 1128-1129.
353. Kesting, R.E. *Synthetic polymeric membranes: a structural perspectives.* 1985.
354. Gholami, M., S. Nasseri, C. Feng, T. Matsuura, and K. Khulbe. *The effect of heat-treatment on the ultrafiltration performance of polyethersulfone (PES) hollow-fiber membranes.* Desalination. 2003; 155: 293-301.
355. Tsai, H., Y. Ciou, C. Hu, et al. *Heat-treatment effect on the morphology and pervaporation performances of asymmetric PAN hollow fiber membranes.* Journal of membrane science. 2005; 255: 33-47.
356. Chinchillas-Chinchillas, M.J., V.M. Orozco-Carmona, C.G. Alvarado-Beltrán, et al. *Synthesis of recycled poly (ethylene terephthalate)/polyacrylonitrile/styrene composite nanofibers by electrospinning and their mechanical properties evaluation.* Journal of Polymers and the Environment. 2019; 27: 659-669.
357. Cho, T.-H., M. Tanaka, H. Onishi, et al. *Battery performances and thermal stability of polyacrylonitrile nano-fiber-based nonwoven separators for Li-ion battery.* Journal of Power Sources. 2008; 181: 155-160.
358. Dong, R., J. Zhao, Y. Zhang, and D. Pan. *Morphology control of polyacrylonitrile (PAN) fibers by phase separation technique.* Journal of Polymer Science Part B: Polymer Physics. 2009; 47: 261-275.
359. Guillen, G.R., Y. Pan, M. Li, and E.M. Hoek. *Preparation and characterization of membranes formed by nonsolvent induced phase separation: a review.* Industrial & Engineering Chemistry Research. 2011; 50: 3798-3817.
360. Kang, S. and M. Elimelech. *Bioinspired single bacterial cell force spectroscopy.* Langmuir. 2009; 25: 9656-9659.
361. Bowen, W.R. and T.A. Doneva. *Artefacts in AFM studies of membranes: correcting pore images using fast fourier transform filtering.* Journal of Membrane Science. 2000; 171: 141-147.
362. Amaral, F., R. Sousa, L. Morais, et al. *Preparation and characterization of the porous solid polymer electrolyte of PAN/PVA by phase inversion.* Journal of Applied Electrochemistry. 2015; 45: 809-820.
363. Mulder, M., *Basic principles of membrane technology*. 2012: Springer Science & Business Media.
364. Guan, R., H. Dai, C. Li, J. Liu, and J. Xu. *Effect of casting solvent on the morphology and performance of sulfonated polyethersulfone membranes.* Journal of Membrane Science. 2006; 277: 148-156.
365. Khulbe, K., B. Kruczek, G. Chowdhury, et al. *Characterization of membranes prepared from PPO by Raman scattering and atomic force microscopy.* Journal of membrane science. 1996; 111: 57-70.
366. Libertino, S., V. Aiello, A. Scandurra, M. Renis, and F. Sinatra. *Immobilization of the enzyme glucose oxidase on both bulk and porous SiO2 surfaces.* Sensors. 2008; 8: 5637-5648.

367. Warner, S., L. Peebles, and D.R. Uhlmann. *Oxidative stabilization of acrylic fibres.* Journal of Materials Science. 1979; 14: 556-564.
368. Wang, P. *Aspects on prestretching of PAN precursor: Shrinkage and thermal behavior.* Journal of applied polymer science. 1998; 67: 1185-1190.
369. Yu, M., C. Wang, Y. Bai, Y. Wang, and Y. Xu. *Influence of precursor properties on the thermal stabilization of polyacrylonitrile fibers.* Polymer Bulletin. 2006; 57: 757-763.
370. Stevens, M.P., *Polymer chemistry*. 1990: Oxford univ. press New York.
371. Bergqvist, J., C. Lindqvist, O. Bäcke, et al. *Sub-glass transition annealing enhances polymer solar cell performance.* Journal of Materials Chemistry A. 2014; 2: 6146-6152.
372. Minagawa, M., H. Kanoh, S. Tanno, and M. Satoh. *Glass-Transition Temperature (Tg) of Free-Radically Prepared Polyacrylonitrile by Inverse Gas Chromatography, 2. Molecular-Weight Dependence of Tg of Two Different Types of Aqueous Polymers.* Macromolecular Chemistry and Physics. 2002; 203: 2481-2487.
373. Kimmel, R. and R. Andrews. *Birefringence effects in acrylonitrile polymers. II. The nature of the 140 C transition.* Journal of Applied Physics. 1965; 36: 3063-3071.
374. Kumar, Y., S. Hashmi, and G. Pandey. *Lithium ion transport and ion–polymer interaction in PEO based polymer electrolyte plasticized with ionic liquid.* Solid State Ionics. 2011; 201: 73-80.
375. Iversen, C.B. *Characterization of polyacrylonitrile carbon fibers.* 2012.
376. Zhao, W., Y. Yamamoto, and S. Tagawa. *Regulation of the thermal reactions of polyacrylonitrile by γ-irradiation.* Chemistry of materials. 1999; 11: 1030-1034.
377. Jing, M., C.-g. Wang, Y.-j. Bai, B. Zhu, and Y.-x. Wang. *Effect of temperatures in the rearmost stabilization zone on structure and properties of PAN-based oxidized fibers.* Polymer Bulletin. 2007; 58: 541-551.
378. Wang, L. and J.S. Swensen. *Dual-transduction-mode sensing approach for chemical detection.* Sensors and Actuators B: Chemical. 2012; 174: 366-372.
379. Zhang, L., F. Su, S. Buizer, et al. *A dual sensor for real-time monitoring of glucose and oxygen.* Biomaterials. 2013; 34: 9779-9788.
380. Xu, T., W. Jin, Z. Wang, et al. *Electrospun CuO-nanoparticles-modified polycaprolactone@ polypyrrole fibers: An application to sensing glucose in saliva.* Nanomaterials. 2018; 8: 133.
381. Piechotta, G., J. Albers, and R. Hintsche. *Novel micromachined silicon sensor for continuous glucose monitoring.* Biosensors and Bioelectronics. 2005; 21: 802-808.
382. Huang, F.-C., Y.-Y. Chen, and T.-T. Wu. *A room temperature surface acoustic wave hydrogen sensor with Pt coated ZnO nanorods.* Nanotechnology. 2009; 20: 065501.
383. Bosse, E., J. Roy, and D. Grenier. *Data fusion concepts applied to a suite of dissimilar sensors*. in *Proceedings of 1996 Canadian Conference on Electrical and Computer Engineering*. 1996. IEEE.
384. Thomopoulos, S.C. *Sensor integration and data fusion.* Journal of Robotic Systems. 1990; 7: 337-372.
385. Chu, D., F. Li, X. Song, et al. *A novel dual-tasking hollow cube NiFe2O4-NiCo-LDH@ rGO hierarchical material for high preformance supercapacitor and glucose sensor.* Journal of Colloid and Interface Science. 2020; 568: 130-138.
386. Yao, H., A. Afanasiev, I. Lähdesmäki, and B.A. Parviz. *A dual microscale glucose sensor on a contact lens, tested in conditions mimicking the eye*. in *2011 Ieee 24th International Conference on Micro Electro Mechanical Systems*. 2011. IEEE.